8-31-2021

Feedstock powders for reactive structural materials

Daniel Hastings
New Jersey Institute of Technology

ABSTRACT

FEEDSTOCK POWDERS FOR REACTIVE STRUCTURAL MATERIALS

by
Daniel Hastings

Metals as fuels have higher energy density per unit mass or volume compared to any hydrocarbon. At the same time, metals are common structural materials. Exploring metals as reactive structural materials may combine their high energy density with attractive mechanical properties. Preparing such materials, however, is challenging. Requirements that need to be met for applications include density, strength, and stability enabling the component to sustain the structure during its desired operation; added requirements are the amount and rate of the energy release upon impact or shock. Powder technology and additive manufacturing are approaches considered for design of reactive structural materials. Respectively, feedstock powders are of critical importance. These feedstock powders must have the chemical composition ensuring, along with mechanical characteristics, a rapid initiation of the reactive material upon impact or shock, and high total energy release. They also must have the morphology suitable for processing.

In this work, several powders designed to serve as feedstock for manufacturing reactive structural materials are prepared, tuned, and characterized. High-energy mechanical milling is the common manufacturing approach for such powders in this study. The materials include elemental metals, such as aluminum, with the narrowly sized spherical porous powder and magnesium, with custom powder coating. Composite powders combining metals and metalloids, e.g., boron-titanium and boron-zirconium, with different structures and morphologies are also prepared and characterized. Milling

conditions are varied and it is shown that the structures, sizes, porosities, and shapes of the produced powder particles can be adjusted through such variation.

The experimental work includes characterizing ignition and combustion of the prepared powders. Custom experiments employing an electrically heated wire are used with all prepared materials. Particle combustion experiments, quantifying the particle burn time and temperatures are performed with selected materials. Additionally, thermal analysis is used extensively in addition to electron microscopy and x-ray powder diffraction. Microcalorimetry in oxidizing gas serves to quantify stability of the selected materials. Nitrogen adsorption is used for many prepared powders to characterize their specific surface area and respective porosity.

Prepared powders combine unique morphological properties making them amenable to additive manufacturing, in particular, with high reactivity and stability. It is expected that using them as feedstock will lead to design of a new generation of reactive structural materials.

FEEDSTOCK POWDERS FOR REACTIVE STRUCTURAL MATERIALS

by
Daniel Hastings

A Dissertation
Submitted to the Faculty of
New Jersey Institute of Technology
in Partial Fulfillment of the Requirements for the Degree of
Doctor of Philosophy in Chemical Engineering

Otto H. York Department of
Chemical and Materials Engineering

August 2021

APPROVAL PAGE

FEEDSTOCK POWDERS FOR REACTIVE STRUCTURAL MATERIALS

Daniel Hastings

Dr. Edward L. Dreizin, Dissertation Advisor — Date
Distinguished Professor of Chemical and Materials Engineering, NJIT

Dr. Mirko Schoenitz, Committee Member — Date
Associate Research Professor of Chemical and Materials Engineering, NJIT

Dr. Lisa B. Axe, Committee Member — Date
Professor and Chair of Chemical and Materials Engineering, NJIT

Dr. Rajesh Dave, Committee Member — Date
Distinguished Professor of Chemical and Materials Engineering, NJIT

Dr. Melissa A. Liberatore-Moretti, External Committee Member — Date
Research Chemist of the Propulsion R&D Branch Picatinny Arsenal Wharton, NJ

BIOGRAPHICAL SKETCH

Author: Daniel Hastings

Degree: Doctor of Philosophy

Date: August 2021

Undergraduate and Graduate Education:

- Doctor of Philosophy in Chemical Engineering,
  New Jersey Institute of Technology, Newark, NJ, 2021

- Bachelors of Science in Mechanical Engineering,
  New Jersey Institute of Technology, Newark, NJ, 2015

- Bachelor of Science in Information Technology,
  New Jersey Institute of Technology, Newark, NJ, 2015

Major: Chemical Engineering

Presentations and Publications

Publications:

Hastings, D., Schoenitz, M., Dreizin, E.L., Highly Reactive Spheroidal Milled Aluminum. Materialia 15 100959 (2021).

Hastings, D., Schoenitz, M., Dreizin, E.L. Zirconium-Boron Reactive Composite Powders Prepared by Arrested Reactive Milling. Journal of Energetic Materials 38(2), pp. 142-161 (2020).

M. Mursalat, D.L. Hastings, M. Schoenitz, E.L. Dreizin, Microspheres with Diverse Material Compositions can be Prepared by Mechanical Milling, Advanced Engineering Materials 22, p.1901204,1-4 (2020).

Hastings D. L., Schoenitz M., Ryan K.M., Dreizin, E.L., Krumpfer J.W. Stability And Ignition of a Siloxane-Coated Magnesium Powder. Propellants Explosives and Pyrotechnics 44 (2019).

Hastings, D.L., Dreizin, E.L., Reactive Structural Materials: Preparation and Characterization. Advanced Engineering Materials 20 (3) 1700631 (2018)

Hastings, D.L., Schoenitz, M., Dreizin, E.L., High Density Reactive Composite Powders. Journal of Alloys and Compounds 735 pp. 1863 – 1870 (2018)

Presentations:

D.L. Hastings, M. Schoenitz, E.L. Dreizin, Spherical Composite Powders of Metals and Alloys for Additive Manufacturing Of Reactive Structural Materials, presented at NJIT research Day 2019, Newark, NJ, November 2019 (Poster).

D.L. Hastings, M. Schoenitz, E.L. Dreizin, Spherical Composite Powders as Feedstock for Additive Manufacturing presented at the 2019 AIChE Annual Meeting, Orlando, FL, November 2019 (Presentation).

D.L. Hastings, M. Schoenitz, E.L. Dreizin, High Density Reactive Composite Powders, presented at the 2016 AIChE Meeting, San Francisco, CA, September 2016 (Poster).

D.L. Hastings, M. Schoenitz, E.L. Dreizin, High Density Reactive Composite Powders, presented at the Graduate Research Conference (GRC) Stowe, VT, June 2016 (Poster).

For my parents

Who have raised me all my life,
Who encouraged me to pursue my education
And without whom I would not be
the man I am today.

May I always make them proud.

ACKNOWLEDGMENT

My thanks extend to my advisors Dr. Edward Dreizin and Dr. Mirko Schoenitz for their hard work and guidance without which I would not have been able to prepare the work presented. In kind, I would like to thank the faculty and staff of NJIT for their engagement and support, including the committee which reviewed my thesis. NJIT doesn't run on its own and I could not have completed my work without the facilities available to me.

There were many former NJIT students who helped mentor me when I first came to our York Center lab, those that struggled with me before departing, and those I leave not far behind. Thank you for your guidance, friendship and help as I completed my PhD research projects, some of the most demanding experiences of my life. It never would have been the same without you.

I would also like to thank sponsors who have made the work thus far possible to include the NJIT Department of the Provost for providing the Provost's Doctorial Assistantship, which provided tuition and stipend funding for my first two years of academic research which were conducted. This work was also supported by the United States Defense Threat Reduction Agency, the Air Force Office of Scientific Research, the Navy and the Army for which I am most grateful.

And of course, I would be a fool not to thank my wife, Mehnaz. She is my best friend and my partner in life. Find someone who pushes you to be the best person you could be and you will never be disappointed. As for me, I like playing with fire and I could not have found a brighter flame.

TABLE OF CONTENTS

TABLE OF CONTENTS
(Continued)

TABLE OF CONTENTS
(Continued)

Chapter **Page**

TABLE OF CONTENTS
(Continued)

Chapter **Page**

LIST OF TABLES

LIST OF FIGURES

LIST OF FIGURES
(Continued)

Figure **Page**

LIST OF FIGURES
(Continued)

LIST OF FIGURES
(Continued)

LIST OF FIGURES
(Continued)

Figure **Page**

LIST OF FIGURES
(Continued)

LIST OF FIGURES
(Continued)

LIST OF FIGURES
(Continued)

CHAPTER 1

REACTIVE STRUCTURAL MATERIALS: PREPARATION AND CHARACTERIZATION

1.1 Introduction

Reactive Structural Materials (RSMs) are a relatively new group of materials designed to have structural strength and store energy to be released at a desired time [1-7]. Their typical applications are expected in such systems as kinetic penetrators [8], reactive fragments [9], reactive bullets [10], reactive armor [11, 12], and munition casings [13, 14]. Considering that most structural components in various munitions are based on steel, the utility of RSMs can be semi-quantitatively assessed from a diagram shown in **Figure 1.1**. The horizontal axis shows a mass fraction of a munition taken by an explosive charge. It is assumed, for simplicity, that the charge is TNT (trinitrotoluene) with the rest of the munition comprised of a metal casing, made of either steel or aluminum. Upon initiation, the case is assumed to oxidize releasing heat in addition to the heat generated by the TNT charge. The percentages of heat released by both TNT and case oxidation are shown for hypothetical scenarios with cases made of steel or aluminum. The estimate shows that for the common mass percentage of the explosive charge, around 30%, the heat release due to the combustion of the metal case can add from ca. 40 to 70% of the total chemical energy produced by the munition. For the common, chemically inert cases, this energy is not released. Thus, releasing even a portion of the total oxidation energy generated by the reacting case could substantially increase the total energy yield of the system. To maximize this additional heat release due to the metal case combustion, RSMs are typically based on metals with high heats of oxidation, such as aluminum, magnesium, zirconium, and

titanium. Alloys based on depleted uranium [15, 16] are also considered, in particular for kinetic penetrators, where both high density and high reactivity are important. However, because of radioactivity of uranium, its use in contemporary munitions systems is discouraged. Perhaps, the first reactive materials reported in literature were composites of aluminum and polytetrafluoroethylene (PTFE, also commonly referred to as Teflon1 [17, 18]). Although low density and strength of Al-PTFE composites severely limits their applications, such materials were studied rather extensively, representing a common reference system for many RSMs developed recently. In addition to metal-fluoropolymers, the types of RSMs described in the literature include thermites [19-21], reactive intermetallic systems, such as Al–Ni [22-24], metal-metalloid systems, including B–Ti, B–Zr [25-28], systems forming metal carbides [29], and various composites and alloys combining materials with different desired properties, for example, high density tungsten with relatively high reactivity metals such as zirconium or hafnium [30-36]. Along with the composition, design of composite RSMs and the methods used for their testing vary widely, depending on the intended application, properties of individual components, and capabilities available to the material designers. This review aims to offer an initial guidance to the potential users and researchers entering the field of RSMs. It first discusses thermodynamic foundations of selecting compo-sites suitable for RSMs, and then discusses some requirements.

1.2 RSM Compositions Based on the Heat Release and Density

Different types of exothermic reactions can be exploited to design an RSM. The initial selection of materials can be made accounting for their heat of oxidation. Other exothermic reactions, such as those leading to the formation of fluorides, borides, carbides, aluminides, and silicides are also commonly considered. The heats of reactions are readily available, either from such compilations as NIST - JANNAF tables [37] (available online as NIST Chemistry webbook), summary by Fischer and Grubelich [38], and other sources. An overview shown in **Figure 1.2** was prepared using, in addition to the above databases, data from references [39-42]. It presents heats of reaction normalized per gram and per cubic centimeter of metal fuels for formation of fluorides, oxides, borides, and carbides. Other reactions that have been exploited for RSM produce silicides, sulfides, and aluminides. Two trends apparent in **Figure 1.2** are that reactions of fluorination and oxidation are substantially more exothermic than any other reactions and that, in general, metals with lower densities have greater gravimetric heats of reaction. There appears to be a much weaker difference between different metals when their volumetric heats of reaction are compared to one another. Dashed lines in each plot mark the heat of oxidation for iron, which was used to estimate the percentages of heat release shown in **Figure 1.2**. Metals/reactions with close or higher values of heat release are of potential interest in RSM. It thus appears that almost any metal could be attractive for the applications, where the volume needs to be minimized, while greater mass is acceptable. In particular, volumetric heats of oxidation of relatively high-density metals, such as Mo, Nb, Hf, Ta, and W are greater than those of iron. Therefore, it could be possible to extract from RSMs energies greater than shown in **Figure 1.1** for the munitions, in which steel cases are replaced with reactive materials based on the above metals. Of course, reaction enthalpies, such as shown

in **Figure 1.2**, offer only the initial assessment, while the ability to reach the rate of heat release necessary to make the exothermicity useful is another important consideration that needs to be accounted for while designing RSMs.

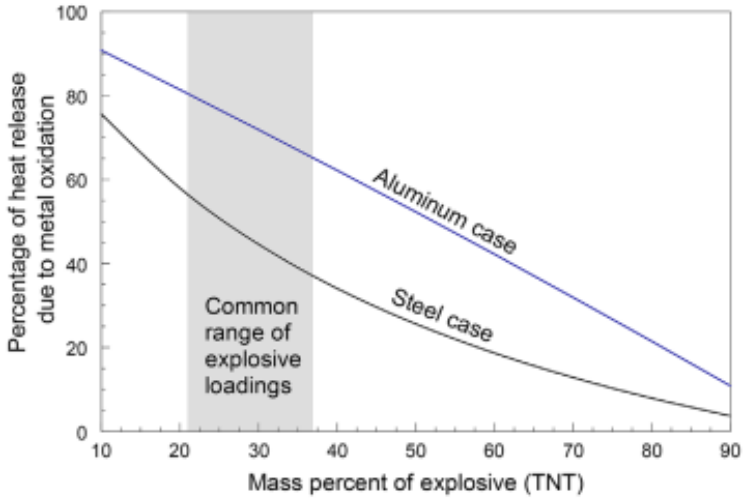

Figure 1.1 Estimated fraction of heat release due to complete oxidation of a metal case for a hypothetical munition containing varied mass percent of TNT as an explosive.

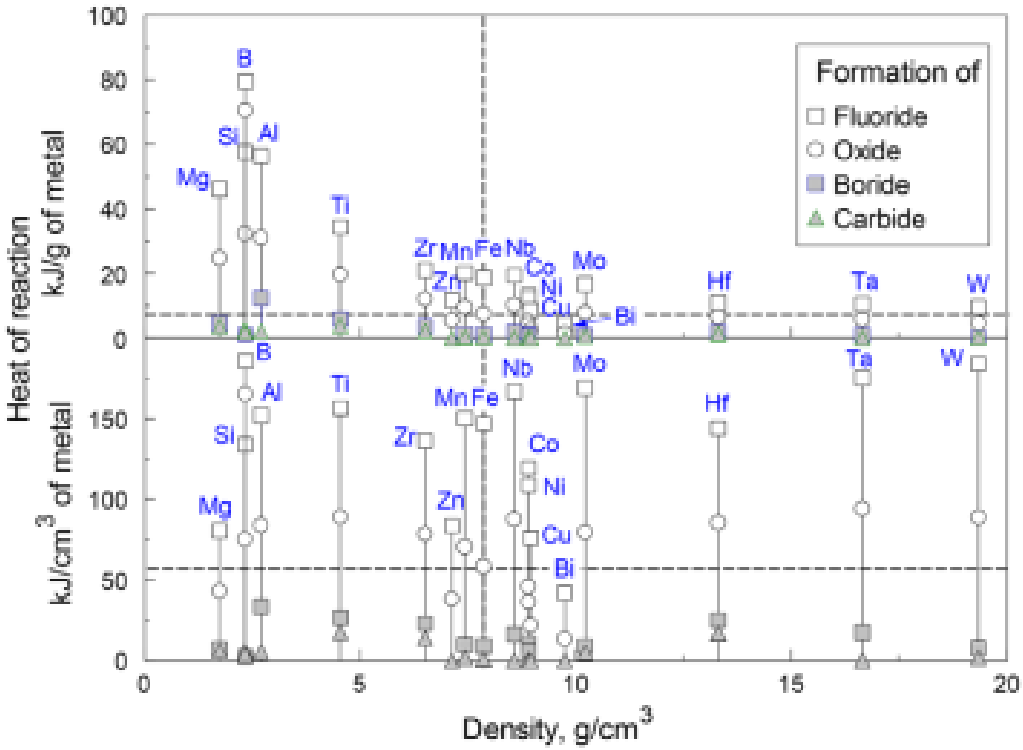

Figure 1.2 Gravimetric and volumetric heats of reaction for selected metals as functions of the metal densities.

1.3 Rates of Heat Release for RSMs

Taking full advantage of the heat of oxidation or other reactions involving material components used in RSMs is difficult; it requires heterogeneous reactions with fast kinetics and breaking of the structural parts into fine fragments, which can burn in time scales defined by the specific application. Each specific application defines its own range of the acceptable time scales; these scales range from minutes, in the case of signal flares [43], to milliseconds for blast charges [44], or down to microseconds for kinetic penetrators [45]. Some specific examples are considered here to illustrate an approach guiding the designs of RSMs for specific time scale requirements.

The shortest reaction time scales are necessary for armor piercing projectiles, which impact targets at speeds in the range of 1800–2900 m^{-1} [45]. Assuming the penetration depth $d \approx 100$ mm, the time for the reaction to occur for the chemical energy to be coupled with the kinetic energy of the impact, can be estimated as, $t \approx d/v$. Thus, the timescales are on the order 35–55 μs. These times are shorter than any reported times of combustion for metal particles or nanoparticles in gaseous oxidizers; besides, the gaseous oxidizers may not be readily available in many practical scenarios, for example, involving impacts in upper atmospheric layers or underwater. Thus, the reaction for such applications must occur between the components of RSM; it would occur heterogeneously and be rate controlled by mass transport of the reactive components toward each other. To crudely estimate appropriate reaction rates, consider characteristic diffusion coefficients in various metal oxide and intermetallic phases, which range typically from 10^{-10} to 10^{-3} cm^2/s [46-49]. Note, however, that the diffusion coefficient is a strong function of temperature; it can also change dramatically for different diffusion mechanisms [50]. For example, diffusion coefficients as high as 10^{-8} cm^2/s are reported for the grain boundary diffusion in alumina

[51], a common product of thermite reaction. The diffusion coefficient, D, can be used to estimate the characteristic reaction time as $t = L^2/D$, where L is the diffusion length. The diffusion length may be evaluated as the scale of mixing between the reacting components, and plugging in the characteristic diffusion coefficients and times above, the range of mixing estimated varies from 0.02 to 7.5 nm. Clearly, the lower bound, obtained using $D = 10^{-13}$ cm^2/s is not physical; however, the upper bound approaching 10 nm and relying on the rapid, grain boundary diffusion is achievable for the materials mixed on the nanoscale and having multiple defects and grain boundaries in the layers separating reactive components. The same estimate suggests that coarser scales of mixing, ca. 30 nm and above may be useful when the characteristic reaction times exceed 1 ms.

For applications where external oxidizer is available, initial heterogeneous reactions may only be needed to ignite RSM fragments; the continued combustion of such fragments may occur at much longer time scales, for example 10–50 ms [44]. In such cases, the reaction may occur either on the surface of the produced fragments or in the vapor phase and be primarily controlled by the fragment sizes. Clearly, the rates of combustion will depend on the oxidizing environment and pressure, flow conditions, and fragment materials. For the initial guidance in selecting the appropriate fragment size, one can consider burn times of typical metal particles reported in the literature. A summary of such data is shown in **Figure 1.3**. Because a comprehensive summary of many published datasets for different metals cannot be clearly represented in a single plot, only selected results are shown. For each metal, the burn times are shown for two ranges of particle sizes, representing coarser and finer powders. For each range of particle sizes, a descriptive trend expressing the burn time proportional to the particle size in the power n is shown as a

dashed line, with the symbols representing the ends of the respective particle size ranges. Some of the trends shown are based on more than one set of measurements reported in the literature. The data for aluminum come from references [52, 53], for boron, from references [54-56], for titanium, from references [57-59], and for magnesium, from references [60-63]. It is apparent that there are discrepancies between the trends for coarse and fine particles for all metals, which is likely associated with errors in measurements. Despite the errors, the trends shown can be used for the initial assessment of the burn times for the fragments with the specified dimensions. It is observed that for all particle sizes, boron particles have the longest burn times, while the shortest burn times are reported for particles of magnesium. Burn times for the same size aluminum and titanium particles are very close to each other. The data summarized in **Figure 1.3** suggest that magnesium particles as coarse as 200–300 μm diameter can still be useful if the reaction times can be extended to 50 ms. However, the particle sizes for boron must be finer than ca. 50 μm in order for them to react in the same time.

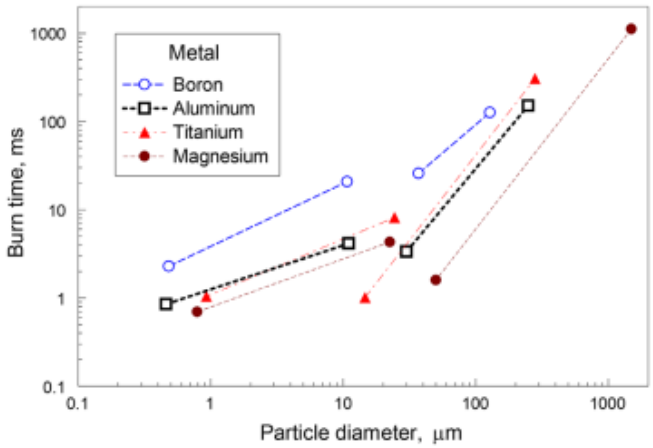

Figure 1.3 Characteristic burn times of particles of different sizes for selected metal fuels reported in the literature: aluminum, boron, titanium, and magnesium
Sources: [52, 53], [54-56], [57-59] and [60-63], respectively

1.4 Structures of RSM and Methods of Their Preparation

1.4.1 Reinforced Composites with Micron- and Coarser Components

Composites combining aluminum powder with PTFE were proposed as RSMs more than a decade ago [64], probably building on the well-known Mg/PTFE composites used in pyrotechnics. The most common composition is the stoichiometric mixture comprising 26.5 wt% of Al and 73.5 wt% of PTFE. Typically, such composites are prepared by blending powders of Al and PTFE and consolidating them by uniaxial or isostatic compression. An elevated temperature, typically between 375 and 385˚C, is used during consolidation to ensure the structural integrity [65]. The methodology is refined in further work, for example, references [66-68]. The materials can be pressed to more than 99% of their theoretical maximum density (TMD), which is approximately 2.33 g/cm^3 for the stoichiometric composition. PTFE is a very attractive oxidizer thermodynamically, and the interest in metal-PTFE composites as RSM has been maintained over the years. More recently, composites incorporating other metals, such as titanium, zirconium, tungsten, and others in addition to, or instead of aluminum were prepared and characterized [68-72].

Composites prepared as consolidated blends of metal powders have substantially higher densities, but are less reactive than Al/PTFE. Perhaps the most studied composition is based on nickel and aluminum with the TMD of 6.95 g/cm^3 for the stoichiometric composition containing 31.5 wt% of Al and 68.5 wt% of Ni. The composites were prepared by cold pressing, with densities in the mid to low of 90% of TMD [73], radial forging [74], and by cold spray, although the powders were ball-milled prior to spraying [24]. A combination of hot isostatic pressing (HIP) with monitoring heat release in the consolidated sample [75] was used to prepare low-porosity, RSM components, while retaining their micro-structure and reactivity in the consolidated shapes. The cold spray may also be

interesting as a technique enabling consolidation of RSMs from powders without substantial heating necessary and leading to a relatively high product density [76]. It was also applied to consolidate Al–CuO thermite [19]. Other reactive composite systems were prepared by hot pressing elemental powders, for example, W–Zr [30].

More recently, control of fragmentation of the RSM was attempted by varying the particle size[70] and, even more interestingly, structure of the composite material, which can be changed replacing a powder with fibers [77]. Composites with tungsten fibers embedded in aluminum were prepared using a combination of cold isostatic pressing (CIP) and HIP, which could be followed by an additional heat treatment to harden the aluminum matrix [78]. Prepared materials contained mesostructures including tungsten fibers embedded in aluminum while being placed strategically in both hoop and axial directions, as shown in **Figure 1.4** [79]. When loaded dynamically, the structure fails when tungsten fibers oriented in the axial direction buckle, which is facilitated by the initial fracture of the circumferential fibers [79]. Thus, materials with mesostructures offer additional capabilities for the pre-programmed break up upon its shock loading.

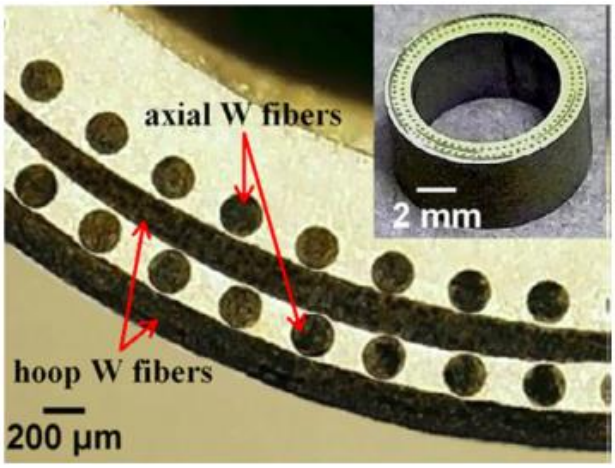

Figure 1.4 Composite reactive materials with tungsten fibers embedded in aluminum matrix. Microstructure Al-composite tube (see inset) with W fibers in hoop and axial directions.
Source: [79]

1.4.2 Composites with Nano-Sized Components

Availability of metal nanopowders led to significant research efforts dedicated to preparation and testing structures with nanoparticles replacing regular metal particles in composites. Following up on the work with coarser powders, Al-PTFE composites were prepared and characterized using nano-powders of aluminum [80-82]. The focus has been on reaction mechanisms and rates rather than mechanical and structural properties of such composites. Substantial efforts were also dedicated to preparing and characterizing various nano-thermite type materials starting with the nanopowders of metal fuels and oxidizers. The powder mixing is commonly achieved via ultrasonication of the starting components [83]. The products are commonly loose powders, which are difficult to consolidate as necessary for most RSM applications. However, ultrasonic vibrations, similar to those used in ultrasonic welding, have been successfully used to consolidate samples of nickel–aluminum[84] and nano-thermites with binary and more complex, for example, Al–Ni–CuO and Al–Ni–Fe2O3 composites [85, 86]. Other methods, including sol-gel chemistry [87-90] and self-assembly [91-94] were used to prepare nano-composite thermites;

typically the products are highly porous and may include additional components, such as chemicals used to functionalize metal surface, resulting in a reduced energy density. Continuous, uniform, and flexible laminate structures containing a nanothermite with a polymer binder was recently prepared by electro-spray deposition [95]. A good review of different types of reactive nanocomposites is available in reference [96].

Recently, additive manufacturing approaches have been explored to generate controlled architectures of RMs, for which burn rate and gas generation can be tuned while using the same nanocomposite thermite [97, 98]. Nanothermite structures comprising micro-channels and hurdles were created starting from nanopowders of Al and CuO. Compared to a non-patterned material, the flame propagation velocity was tripled and halved for channels and hurdles, respectively.

While significant progress has been made preparing various shapes and morphologies of RMs using nanoparticles of starting materials, most of the prepared continuous structures were limited to relatively thin, quasi two-dimensional layers; three-dimensional items prepared were typically very porous and had low strength, limiting their applications in RSMs.

1.4.3 Layered and Nano-Layered Systems

Fully dense composites suitable for RSM applications have been prepared by mechanical processing bulk metals or packed powders using swaging, a cold forging process reducing diameter of tubes [74, 99]. The scale of mixing achieved in such a processing and the structure of the layered system are illustrated in **Figure 1.5** for a composite prepared from nickel flakes with powders of aluminum and magnesium. The mixing scale achieved is rather coarse, with the thickness of about 1 μm for the finest Ni layers. Minor porosity is

also observed, although most of the sample is fully packed. Based on density measurements, the volume fraction of voids was estimated to be within 0–5%.

A variety of RMs were prepared as nanolayered systems, using vacuum deposition based techniques [100]. The structure of such materials can be precisely controlled and the layer thickness can be as small as 10 nm. Earlier work focused on intermetallic systems, such as Al–Zr, Ni–Al, and others [101-104]; more recently, significant progress has been made preparing various thermite-type materials [105-109]. RMs with planar, well-defined layers of individual composites and with essentially no porosity serve as a convenient model material for studies of reaction mechanisms. Varying the thickness of the deposited layers enables one to manipulate directly the mixing scale between the components. It has been recognized, however, that poorly defined phases exist at the interfaces between the reactive components deposited on top of each other by sputtering. To avoid uncontrollable formation of the intermediate reaction products, additional layers were formed between the reactive components by atomic layer deposition [110-112]. Such layers, although still serving as diffusion barriers, can be better controlled, leading to a more predictable behavior of the RM system. An example of such a custom-engineered RM is shown in **Figure 1.6**. Although the added intermediate phases create diffusion barriers between the reactants, slowing down the rate of heat release, this effect may be tuned by adjusting the thickness and type of the added interfacial layers.

Various approaches were explored for preparing optimized layered systems; for example, the order in which the metal and oxidizer are layered, and which material ends up on the surface, can affect how the material ages over time. Depositing aluminum or magnesium onto preliminarily grown, ordered nano-columns of an oxide (e.g., CuO or

Co_3O_4) leads to interesting morphologies, for which the reaction rate is different than for a planar layered system [113, 114]. Further, such systems can be modified by added layers of fluorocarbon [115, 116], making the surface of the prepared material hydrophobic.

1.4.4 Mechanochemically Prepared or Mechanoactivated Materials

Composite powders were prepared mechanically milling starting components, present as micron-sized particles, flakes, or even bulk pieces [117, 118]. This technique, developed initially for preparation of mechanically alloyed and dispersion strengthened composites [119, 120], was extended to process materials of interest to RSMs. Such materials include reactive metals and intermetallic systems, such as aluminum, magnesium, nickel, zirconium, titanium, etc., and composites, including all types of chemistries discussed above, as well as metals with even more aggressive oxidizers, such as $KClO_4$, NH_4ClO_4, etc. [121]. Mechanical milling typically yields powders with particle sizes in the order of 1–100 μm. Each powder particle is a nearly fully dense composite. The components are mixed within such particles on the scale of ca. 100 nm. The interfaces formed in mechanochemically prepared particles form because of interaction between the components during milling. Such interactions mostly involve mechanically induced shear accompanied by pressing the components together by colliding milling media. These interactions occur at the milling temperature, which is typically just slightly higher than the room temperature. Thus, the components are rather inert chemically, so that the interfacial layers produced may be thinner than for the composites prepared by vacuum deposition or than surface oxide layers, such as amorphous alumina, always present on the metal particles exposed to an oxidizing environment. Using such powders for preparing RSMs has its advantages and drawbacks. The advantages are the relatively coarse particle

size, combined with the fine mixing scale for the reactive composites, making handling such powders easier than that of the nanopowders with the same or comparable scale of mixing. It is also important for the mixing scale and morphology to be preserved while the powder is being handled. However, mechanochemically prepared powders are typically work hardened (or less ductile), making it more difficult to consolidate them into bulk items.

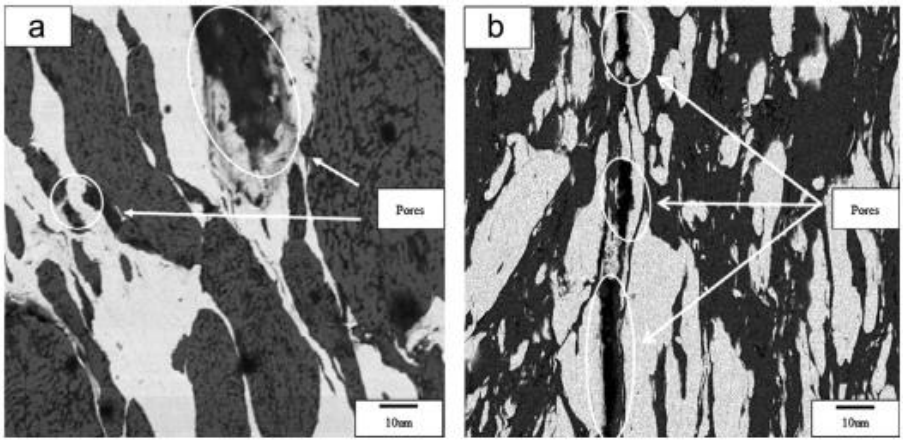

Figure 1.5 Microstructures of the composite prepared by swaging using powders of Al and Mg with flakes of Ni. Minor porosity is observed. Most of pores appear between Ni flakes and at boundaries between Ni and Al.
Source: [74]

Consolidated shapes were readily prepared using mechanochemically prepared metal-fluoropolymer composites by slightly pressing them [122, 123]. These highly energetic materials have relatively low density and strength. Fuel-rich thermites were consolidated by uniaxial pressing, achieving densities close to 90% of TMD without binders [124]. Added binders, either polymers or low-melting metals improved mechanical properties, but reduced the energy density of the consolidated composites.

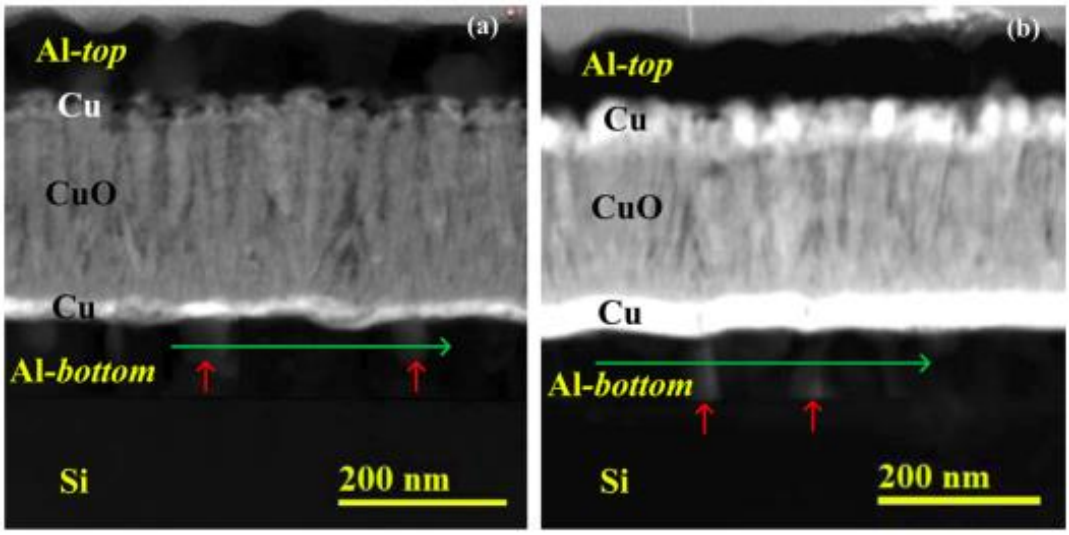

Figure 1.6 High-angle annular dark-field scanning transmission electron microscopy images of Al–CuO nanocomposites prepared by magnetron sputtering and including 41 wt% Cu a) and 63 wt% of Cu b) between Al and CuO layers.
Source: [111]

1.5 Characterization of RSMs

1.5.1 Mechanical Properties

As for any structural materials, mechanical properties are of critical importance for RSMs. Static mechanical properties, such as tensile, yield, compressive, or flexural strength are routinely measured using standard tests [125]. However, in many cases, prepared RSMs may not be available in the form of specimen required for the most common standardized tensile yield test; sometime preparing such specimen is problematic because the composites are brittle. In such cases, often compressive strength of RSMs is measured instead using so-called Brazilian test, in which a disk-like specimen is compressed with a continuously increasing load until it fails [126]. Static tests, while important, are not specific for RSMs and will not be discussed here in further detail.

Dynamic mechanical properties of RSMs are measured using Split Hopkinson Pressure Bar (SHPB) [127]. SHPB is probably the most common test enabling one to

characterize dynamic response of a material. The achievable strain rates vary from 50 to 10^4 s^{-1}. The experimental setup is shown schematically in Figure 1.7 [128]. The sample or specimen is placed between input and output bars. The input bar is loaded by a striker bar, which can be accelerated using a gas gun. An incident pulse (or stress wave) propagates through the input bar toward the specimen where it splits into transmitted and reflected pulses. The transmitted pulse may deform the sample plastically. Thus, it can be substantially changed as it travels through the sample and into the output bar. The reflected pulse travels back down the input bar. There are strain gauges in both input and output bars, which measure strains caused by the traveling waves; an analytical model is used to process the output of the strain gauge readings and recover mechanical properties of the material. Additional optical measurements can be used to detect an exothermic reaction initiated in an RM sample by the impact.

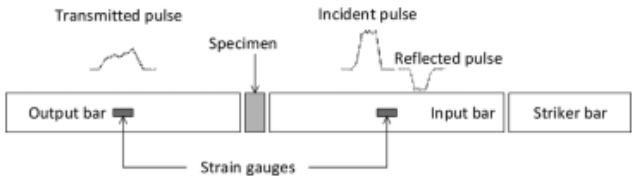

Figure 1.7 Schematic of the SHPB
Source: [130]

Multiple examples of the SHPB-based experiments characterizing RSMs were reported in the literature, such as [31, 79, 129-133]. For example, Al-PTFE composite materials were found to be sensitive to the strain rate; it was further reported that the compressive strength is maximized at the aluminum fraction of 35 wt% [132].

An example of a sequence of high-speed video frames taken during an SHPB experiment with a hot pressed RSM comprising 33 wt % of W and 66 wt% of Zr is shown in **Figure 1.8** [31]. Processing the recorded video along with the analysis of the incident,

transmitted, and reflected pulses recorded by strain gauges enabled researchers to determine that the dynamically measured compressive strength of the sample was higher than that measured in static tests. It was also observed that the specimen failed at only about 2% of strain, behaving as a typical brittle material. Different type fragments formed upon the sample failure and exhibited different combustion regimes, identified from the video.

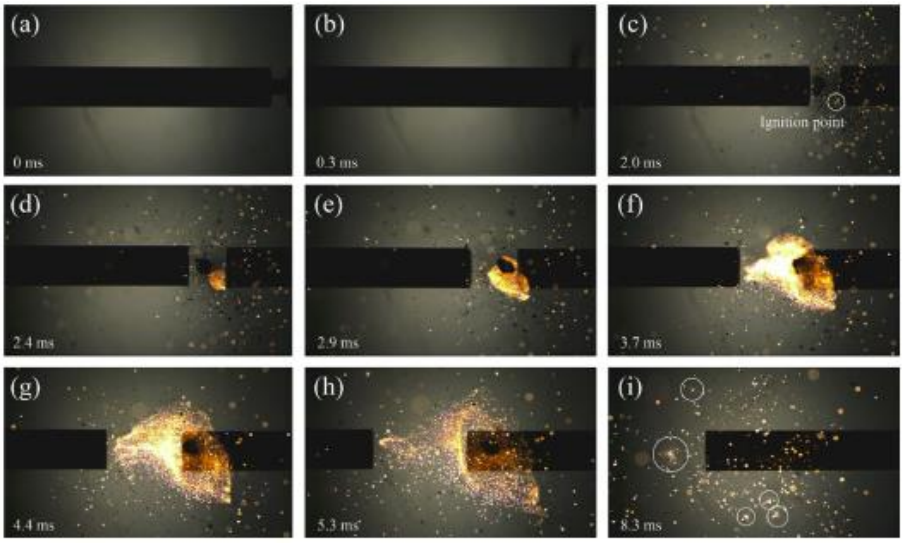

Figure 1.8 Selected frames from a high-speed video record of ignition and propagation of a Zr–W samples in a SHPB test at 23.53 m/s. A record rate of 30000 frames s^{-1} and shutter speed of 1/40000 s were used. The timestamp of each frame is measured from the start of deformation.
Source: [31]

Other dynamic tests include Taylor impact, in which a cylindrical projectile made of the material being tested impacts onto a large flat plate, or anvil [134]. The impact velocities a round 100–200 m/s cause a non-uniform deformation of the projectile. Strain rates exceed 10^5 s^{-1}, and thus are higher than those in the SHPB test. A model is available that correlates the residual geometry of the deformed projectile with the dynamic yield strength. A more detailed modeling involving state of the art hydrocodes, such as CTH [135, 136], are also used to interpret such tests for RMs [23]. High-speed videos are used to detect the ignition and record changes in the sample shape while it is being deformed.

Such videos help recovering dynamic values of the yield stress during the test; such measurements are particularly valuable if the sample ignites and thus changes its shape before being recovered. Results of Taylor tests showed that a cold sprayed Ni–Al composite is more reactive than the same composite consolidated by explosive compaction [23]. Sometime, a reverse Taylor test is performed, in which the RM cylinder is stationary and the projectile serves as the anvil [137]. Modifications of this test are also being developed using instrumented plates, high-speed video, and post-mortem analysis of the compacted and initiated samples [138, 139].

1.5.2 Thermal Analysis

Thermal analysis has become the most common and versatile technique for studying thermally activated chemical reactions, which are of critical importance to RSMs. Aging of such materials is certainly governed by the reactions occurring both at their surfaces, interacting with the environment, and at the internal interfaces between reactive components. It can also be argued that the thermally activated reactions are critical for ignition of RSMs even when the practical ignition stimuli are the shock or impact. In those cases, multiple models have been developed to predict formation of so-called hot spots, caused by various defects and irregularities in the loaded structures [140-146]. Once such defects are developed, they self-heat, leading to ignition, which then can be described as a developing thermally activated reaction. Thus, the importance of thermo-analytical measurements, including thermo-gravimetry (TG) and differential scanning calorimetry (DSC) cannot be overestimated. Not surprisingly, most researchers developing RSMs or relevant compositions have applied DSC and TG to characterize their materials. A review

describing relevance of such measurements to ignition mechanisms of aluminum-based RMs is available [147]. Ideas discussed there are also applicable to other types of RMs.

Measurements performed at different heating rates are routinely used to establish kinetics of various reactions. Various isoconversion processing techniques are used; recently, useful recommendations for the data processing were proposed, which are fully applicable for studies of RSMs [148]. Similarly, recommendations are available for collecting the thermo-analytical data [149].

Without reviewing a very extensive set of references, where thermo-analytical measurements were used to characterize various RSMs and relevant structure, one overarching observation can be made coming from the authors own studies [117, 118, 150]. While multi-step exothermic reactions are commonly observed in DSC traces, it is most commonly the very first, low-temperature reaction step that governs the ignition behavior of the material, when it is heated rapidly. This initial step may not necessarily be the strongest among different reactions observed. However, accounting for it becomes critically important when one attempts interpreting ignition of both thermites and intermetallic-based RM composites.

New experimental methods, expanding the capabilities of conventional thermo-analytical measurements take advantage of miniaturized heating elements, which can achieve heating rates exceeding 10^4 K/s, approaching those expected in the RSM ignition scenarios [151]. Such measurements, limited to very small samples and affected by possible temperature gradients in the heated material are useful to bridge the understanding of reaction mechanisms obtained from DSC with the processes occurring in ignition, as discussed below.

1.6 Ignition and Combustion

1.6.1 Ignition Experiments

Ignition and combustion measurements are performed for both consolidated RSMs and for powders used to prepare RSMs. It is commonly assumed that if an RSM fragments upon initiation, ignition and combustion of the produced fragments is reasonably well represented in studies dealing with the powder particles.

Ignition of small amounts of RM powders is commonly studied using an electrically heated metal filament with a thin deposit of an RM powder [152]. The filament temperature may be monitored using an infrared pyrometer, or it can be obtained from the filament's resistance, calculated using the measured current and voltage [153, 154]. The ignition instant is detected optically and the measured temperature of the filament is treated as the ignition temperature. The heating rate may be varied to observe a shift in the ignition temperature, suitable for quantifying the respective reaction activation energy. Depending on the filament diameter and the power supply, the heating rates attainable are from 100 to 10^6 K/s. This method was used extensively to determine how the ignition temperature changes as a function of the heating rate for a broad range of RMs prepared by mechanical milling, for example [155-160], as well as for other types of RMs [161-164]. In a variant of this experiment, the powder-coated wire is mounted in a vacuum chamber connected to the inlet of a time of flight mass spectrometer (TOF-MS) [154, 165-168]. Thus, release of gaseous species emitted by the heated and ignited RM is described in real time. A characteristic result is illustrated in Figure 1.9, where the RM sample is prepared by vacuum layer deposition of Al and CuO nanolayers directly onto a platinum filament [161]. The vertical dashed line indicates ignition observed in a high speed video. An oxygen peak occurs before ignition, whereas onsets of peaks of Al, Al_2O, and Cu coincide with the

ignition instant. The early oxygen release was proposed to be associated with decomposition of the heated CuO, which was confirmed by separate experiments [169]. A similar behavior was observed for nanothermites with several other oxides used as oxidizers. A qualitatively similar oxide decomposition was observed to precede ignition for fully-dense thermites prepared by mechanical milling, although the experiments were not performed in a high vacuum so that no CuO decomposition was detected without the presence of Al. It was proposed that for the milled materials, pre-ignition heterogeneous reaction between Al and CuO partially reduces CuO prior to ignition, yielding a metastable CuO1–x phase (1>x>0), which decomposes upon heating [158].

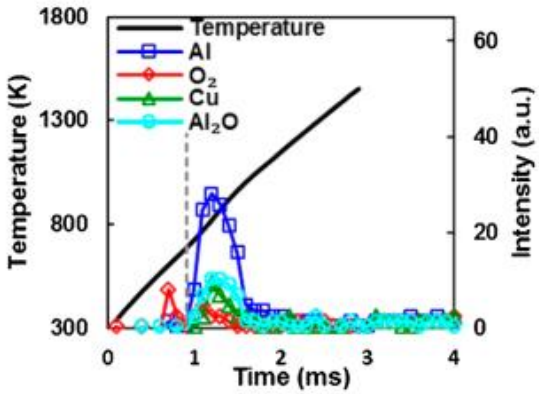

Figure 1.9 TOF-MS results from experiments for a reactive Al–CuO nanofoil prepared by vacuum deposition with six bilayers.
Source: [161]

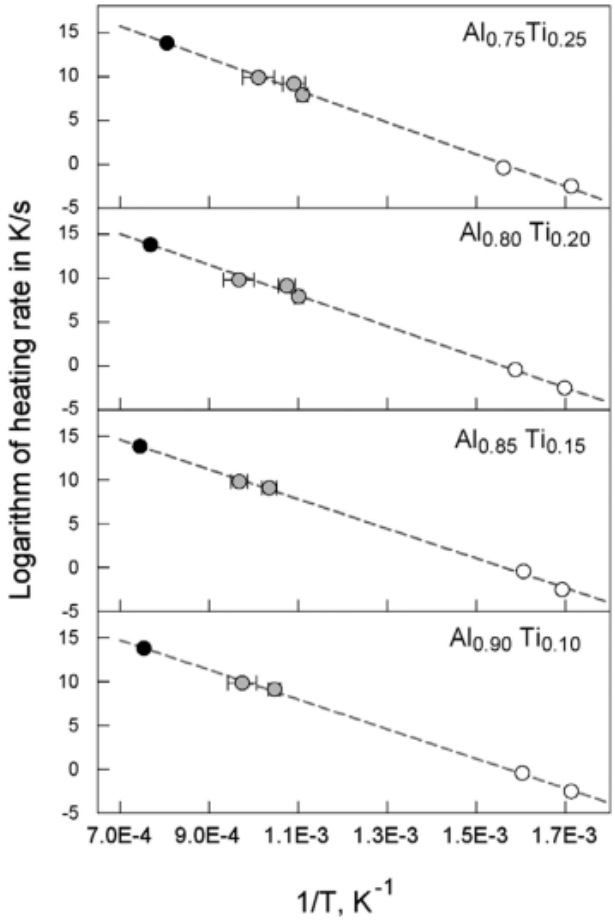

Figure 1.10 Arrhenius plots combining different measurements for mechanically alloyed Al Ti powders. Results of thermo-analytical measurements representing formation of $L1_2$ phase of Al_3Ti are shown as open circles. Ignition temperatures measured using the electrically heated filament shown as gray circles. Ignition temperatures, estimated for the heating rate 10^6 K/s expected in the laminar lifted flame experiments are shown as black circles.
Source: [160]

An idea of correlating the ignition with intermetallic exothermic reactions in an RM, discussed in detail in reference [147] is illustrated in **Figure 1.10** [160]. For comparison, the positions of exothermic peaks from thermo-analytical measurements and ignition temperatures obtained from the heated filament experiments are plotted in the same Arrhenius coordinates for the same mechanically alloyed Al-Ti powders. The peaks in DSC traces were assigned to a weakly exothermic intermetallic reaction producing L12 phase of Al_3Ti. The results of the ignition experiments correlate well with the trend-line for the DSC

measurements. Extrapolating this trend-line to even higher heating rates enables one to predict an ignition temperature (shown by filled black symbols) in more practical scenarios.

Other techniques used for thermal initiation of RMs include use of laser heating for individual particles[170, 171] and for pressed bulk samples [147, 172]. Heating rates approaching 10^6 K/s are achieved. If used for the same materials, ignition temperatures observed in the laser heating experiments can be compared to those expected from the kinetic trends obtained from thermal analysis and/or from the heated filament experiments. Still higher heating rates, in the range of 10^9 K/s are achievable in the experiments using an electrostatic discharge (spark) as an ignition source [173-176]. An increase in the heating rate can cause a qualitative change in how the reaction propagates [177]. At very high heating rates, substantial temperature gradients develop across RM domains. This can cause localized reactions to occur while the rest of the material is being heated and/or melts. Thus, the fine structure of the composite material may be preserved to much higher temperatures and through greater reaction progress than anticipated for low-heating rate events, in which melting of the material components results in a loss of the initial structure and scale of mixing.

A methodology for studying shock initiation of thin RM layers using a very short laser pulse was developed [178-182]. A picosecond laser flash heating vaporized the surface of an RM target. The RM, typically a nano-aluminum/reactive binder composite, reacts involving surrounding oxidizing environment. A spherical shock wave is generated while its pressure drops rapidly. The shock decomposes the binder (nitrocellulose or Teflon1) down to a characteristic diameter of reaction. That diameter was measured as a function of the laser energy. A hydrodynamic model was developed to interpret results; the

model assumed that chemical reactions occur when a threshold pressure applied for a given time duration. A similar technique was recently used to study shock initiation of RM samples based on porous Si [183].

Microscopic samples of various RMs were impact initiated in recent experiments using metal foil-based flyer plates [176, 181, 182, 184-186]. In a typical experiment, illustrated in **Figure 1.11**, a thin copper foil is used as a flyer plate; aluminum foils were also used. The foil is initially epoxied to a glass and is accelerated by a pulse from an Nd:YAG laser. The impact produces a planar shock in the target material, in this case, an Al-PTFE nanocomposite. The speed of the flyer can exceed several km/s. The shock duration is varied around 10 ns; it depends on the material impacted by the flyer. Prior to the launch of the foil, the target material is placed at the impact location using an optical microscope. High-speed optical probes track emission, and, in the most recent experimental development, spectra emitted by the impact-initiated target material with ps resolution [186, 187]. Time-resolved details of shock-compression initiation can be detected, which are not currently accessible by any other techniques. These experiments serve to establish mechanisms of shock initiation, hot spot formation, etc. However, because the flyer plate typically quenches the initiated reaction, the reaction at longer time scales may not compare well with that expected in a practical configuration.

A new generation of measurements of initiation mechanisms in RSMs take advantage of the advanced analytical techniques, such as dynamic transmission electron microscopy (DTEM) [188, 189] or time-resolved X-ray diffraction studies enabled by high intensity X-ray beams produced by synchrotron radiation [190]. Such measurements enable direct observation of changes in morphology and structure of the RM particles

initiated directly under the microscope or in the diffractometer. It was observed, for example, that for the thermites prepared as mixed nanopowders, condensed phase and interfacial reactions, as opposed to gas release, are fast enough to serve as dominant combustion mechanisms [188].

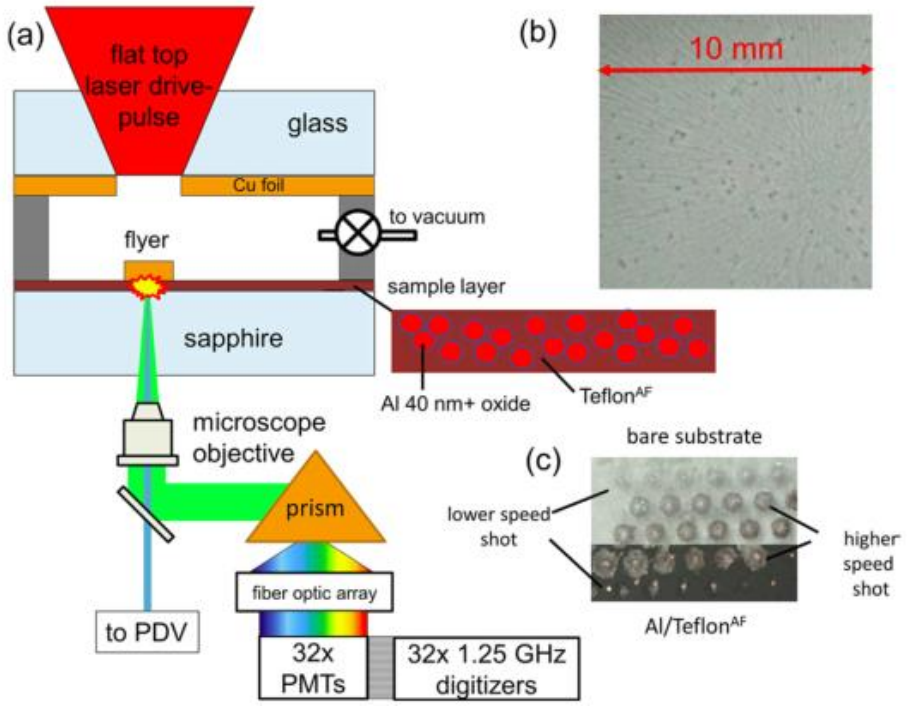

Figure 1.11 a) Schematic of the apparatus using laser-launched 25 μm thick Cu flyers to shock a 3 μm thick film of Al/Teflon. b) Optical micrograph of Al/Teflon film on sapphire. c) A sample after the experiment. Prior the experiment, a portion of the Al/Teflon film is scraped away to yield a bare region which was used to precisely calibrate flyer velocity versus launch laser energy. The darker region with Al/Teflon shows reacted regions for lower speed (0.7 km/s) and higher-speed (1.5 km/s) shots. The reaction produced with the higher-speed shots extends several mm beyond the 0.5-mm diameter flyer. The impact areas are 4 mm from one another.
Source: [186]

1.6.2 Combustion of RM Particles and Particle Clouds

These experiments follow, generally, the same methods as used to study combustion of individual metal particles or powder clouds. Particles are ignited, typically by a laser beam [171, 191] or while being injected in a flame [192-195]; their combustion times and temperatures are measured based on their optical emission. Different methods were used to correlate the particle sizes and their combustion times. Recently, such correlations were obtained by comparing the measured statistical distributions of particle sizes and their burn times [171]. In that processing, larger particles are assumed to burn longer than smaller ones. It is assumed that larger particles burn longer. Results with multiple RM particles ignited in a reflected shock wave were also reported [196, 197]. In such experiments, the burn times are usually obtained measuring the width of the optical emission pulse. The obtained burn time is correlated with the average particle size for the powder used in experiments.

In other experiments, typically performed with the RMs comprising mixed nanopowders, combustion of a loosely packed RM sample in an open tube is studied [198-201]. Although most measurements focused on the apparent flame propagation rate, it was understood recently that this rate is superficial and is associated with incandescent particles moving along the tube [202, 203]. It was reported that the nanoparticles agglomerate rapidly and form mesoparticles, which burn in the time scales comparable to those for common micron-sized metal particles.

Constant volume explosion experiments are rather common [155, 162, 171, 191, 194, 204]; they can be performed in vessels of different sizes, with different powders initiated using a heated wire, pyrotechnic igniter, or a spark. Pressure is usually measured in real time and the maximum achieved pressure is associated with the total energy release.

The reaction rate is quantified based on the recorded rate of pressure rise. Because not all powder is ignited and because a fraction of the ignited particles is quenched on the vessel walls, the efficiency of combustion may be low. However, this technique is useful for comparing different RM powders to one another. When interpreting these experiments, it is necessary to account for differences in flowability of different powders, which can substantially affect formation of the aerosolized cloud and thus its combustion dynamics.

Examples of luminous streaks produced by Al Mg alloy particles ignited by a CO_2 laser beam are shown in **Figure 1.12** [203]. The particles were fed vertically up crossing the laser beam directed horizontally. Once ignited, they burned in ambient air. Labels in each image show the Al/Mg atomic ratios for different samples. The streaks include two bright parts; the first, associated with the selective combustion of Mg followed by the second, produced by predominantly Al combustion. Pressure traces measured in the constant volume explosion experiments in air for the same mechanically alloyed Al Mg powders are shown in **Figure 1.13** [205]. The results show that the maximum pressures are almost the same for all materials and for the pure aluminum. However, the rates of pressure rise are substantially increased for the mechanically alloyed powders.

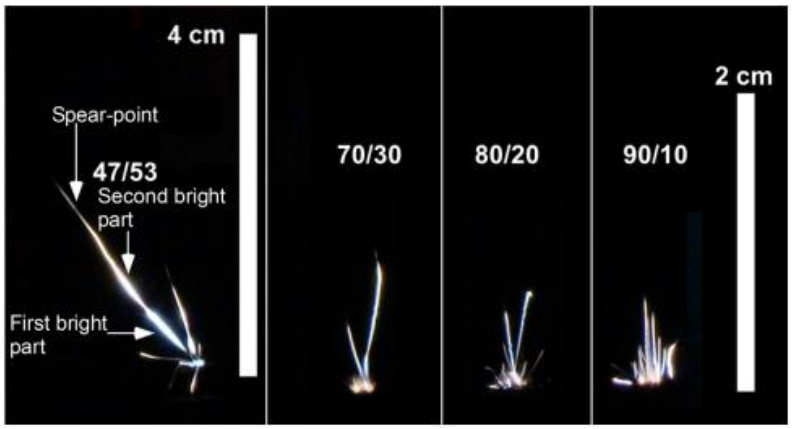

Figure 1.12 Streaks of burning particles of mechanically alloyed Al Mg powders ignited by the CO_2 laser beam; scale bar for 70/30, 80/20, and 90/10 compositions is the same.
Source: [205]

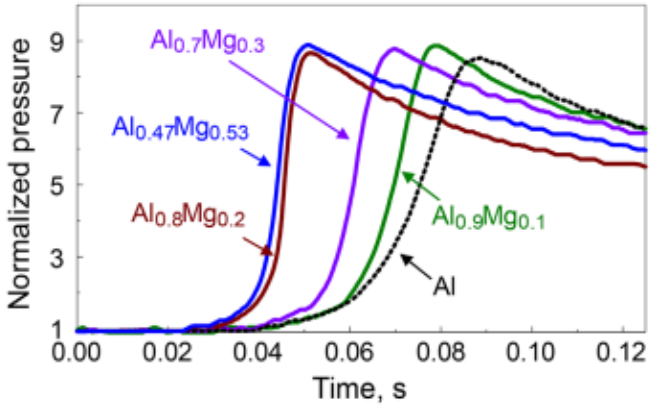

Figure 1.13 Pressure traces measured in the constant volume explosion experiments for mechanically alloyed Al Mg powders burning in air. The igniter, a heated wire, is initiated at the time zero.
Source: [205]

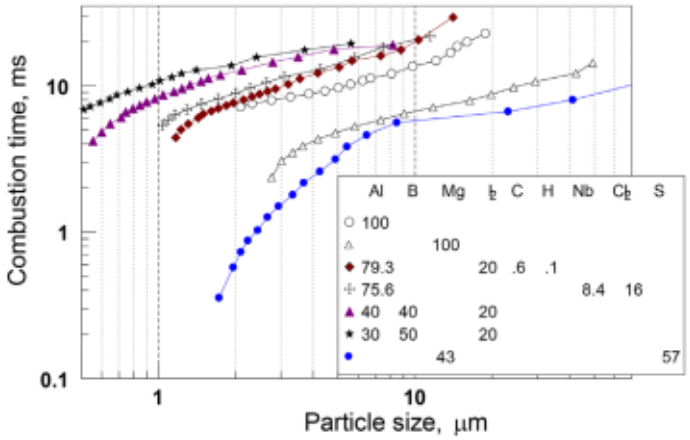

Figure 1.14 Burn times as a function of particle sizes for some RM powders containing biocidal additives, I_2, Cl_2, or S, burning while being injected in an air-acetylene flame. Results for pure Al and Mg are shown for reference.
Source: [206, 207]

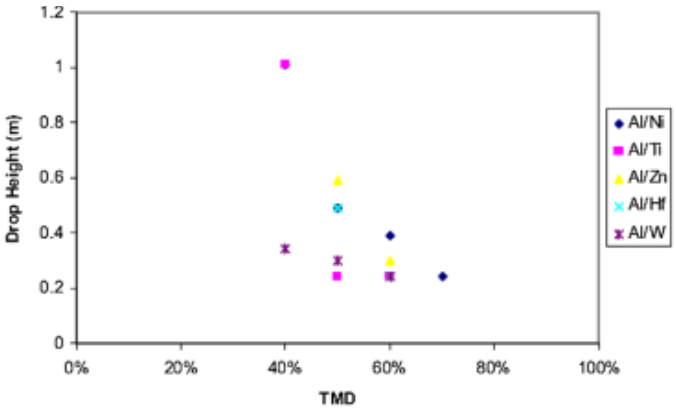

Figure 1.15 Impact sensitivity of intermetallics measured in air as a function of bulk theoretical maximum density of a pressed sample.
Source: [208]

Burn times measured for several nanocomposite RM powders prepared by mechanical milling and injected in an air-acetylene flame are shown in **Figure 1.14** [206, 207]. These RMs contain such additives as I_2, Cl_2, or S, expected to generate biocidal combustion products aimed to inactivate biological agents, such as anthrax-laced powders. They can be used as liners in the respective munition systems. The results, obtained from a correlation between the measured statistical distributions of particle sizes and burn times are compared to those for pure aluminum and magnesium. It is observed that only one of the prepared materials, Mg S composite, burned faster than pure Mg (and thus, faster than any other metal, compare to **Figure 1.3**). All aluminum-based powders burned slower, than the pure Al.

1.6.3 Impact Initiation of Bulk RSMS

Experiments on impact initiation of bulk RSM samples are often designed to reproduce scenarios expected in the practical applications. For example, it may be important to establish that the material survives launch of a projectile, penetration through a protective layer, and/or capable of coupling the released chemical energy with that of the mechanical impact. It also often desired to characterize the fragmentation of the RSM upon impact and assess the reactivity of the produced fragments.

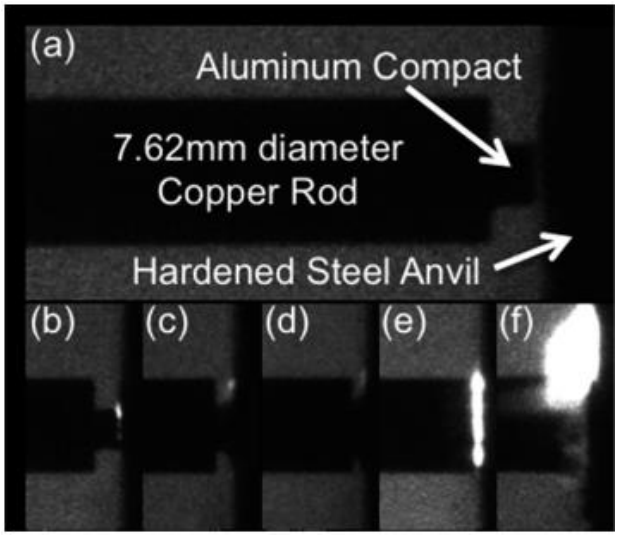

Figure 1.16 High-speed images of an impact of an RSM projectile onto a hardened steel anvil at 302 m/s. The RSM is a mechanically milled aluminum compact attached to a copper cylinder. Times corresponding to different frames: a) immediately prior to impact; b–d) 0.05–2.5 μs; e) 6.5 μs; and f) 9.5 μs. Pellet is compacted and deformed in frames b–e). The copper cylinder contacts the anvil in frame (f).
Source: [138]

A very simple experimental testing of the impact sensitivity of reactive composites is possible using a commercial drop weight impact tester, where a pellet is placed on an anvil and hit by a weight falling from a pre-set height [208]. The impact energies may reach several J. Ignition was detected monitoring the infrared emission from the impacted samples. Pellets of several aluminum-based intermetallic composites were pressed and tested. For the relatively low compaction achieved by uniaxial pressing (less than 80% TMD), the results suggested an increased sensitivity to ignition at greater compaction, as illustrated in **Figure 1.15**. It was also reported that the size of Al particles used in the compacts had only marginal effect on the measured ignition sensitivity, in contrast with laser ignition studies, where the particle size of aluminum affects the ignition temperature of composite RMs substantially. It was proposed that ignition was caused by piercing aluminum particles by harder particles of higher density metals, which broke down the protective alumina shell and exposed aluminum to the external oxidizer. Variations in the

drop weight impact techniques, for example, when a sample is used to characterize several Ni-Al composite and nanocomposite materials more recently [209-211]. A sample is placed on a support plate; a plunger with a flat impact surface rests on top of the sample. The plunger is hit by a flyer plate accelerated by a gas gun so that it is rapidly pressed into the sample. The impact energies are in the range of hundreds of J. The setup is installed in a windowed chamber so that the ignition can be monitored using a high-speed video camera. In different experiments, impact sensitivities were compared for mixed nanopowders, composites prepared by high-energy ball milling, and for nano-layered composites with the structures generated by magnetron sputtering. It was observed that the porosity and hardness of the samples significantly affected their impact ignition sensitivity, even when their ignition temperatures measured for the heated samples were nearly identical.

In another experimental technique, based on the Taylor test discussed above, a gas gun is used to accelerate a sample of RSM, which impacts onto a stationary anvil [138, 139, 212]. An RSM sample is attached to a metal carrier rod using custom-manufactured copper capsule fixtures. The powder compact may be pressed into or epoxied to the driver. The flyer plate is made of copper, tungsten, or tungsten heavy alloy, depending on the desired impact stress. The flyer plate is carried by aluminum sabots. The impact velocity is monitored using sequential shorting pins. Polyvinylidene fluoride (PVDF) stress gauge packages are built onto the driver and backer plates to monitor the stress state and wave arrival times at the front and back of the powder. An example of a series of high-speed images for an impact initiation experiment is shown in **Figure 1.16** [138]. The initiation threshold in terms of impact energy was found for different RM samples. Results for

materials prepared as mixtures of regular (not ball milled) powders, suggest that composites of tungsten/aluminum and tantalum/aluminum reacted in both air and vacuum. Composites of nickel/aluminum and aluminum compacts only reacted in air [6]; composites of tungsten/aluminum and tantalum/aluminum reacted in both air and vacuum. A higher reactivity was observed for tantalum/aluminum composite. Its reactivity threshold in air was 718 kJ, which was about 195 kJ lower than the next lowest threshold of 913 kJ observed for aluminum. Composites of tungsten/aluminum and nickel/ aluminum (at a higher packing density) all react in air at around 1000 kJ. This suggests that aluminum oxidation with surrounding air defines the reaction threshold for all composites except for tantalum/aluminum ones. The intermetallic anaerobic reaction was suggested to be driving tantalum/aluminum compacts. In vacuum, the tantalum/aluminum initiation threshold was 863 kJ, which was 348 kJ lower than that for tungsten/aluminum composite (1211 kJ).

An interesting effect of particle size was observed for nickel/ aluminum composites. Samples prepared using powders with different sizes, 325 mesh and +325–200 mesh, exhibited similar trends for the effects of packing density. However, the samples prepared from a coarser powder (+325–200 mesh) were substantially more reactive and initiated at a lower energy than samples prepared using finer, 325 mesh powders.

A customized impact initiation testing methodology was developed a decade ago [213, 214] and modified and used in many more recent studies [4, 215-221]. In this method, as schematically shown in **Figure 1.17** [213], a consolidated RSM compact (which could have spherical, cylindrical, or cubic shape) is used as a projectile. The sample needs to survive launch from a ballistic gun at speeds varied from ca. 500–2500 m/s. Aluminum foils are used to measure the speed of the projectile. A pressure sensor mounted in the test

chamber is not shown. The projectile first hits a "target skin," which is typically a thin sheet of mild steel [213] or an aluminum plate. Some recent experiments are focused on the interaction of RSM with aluminum plates of different thicknesses, production of fragments, and their ignition [220]. Upon passing through the target skin, the RSM projectile is disintegrated. A portion of the material may be left outside the test chamber, while fragments continue moving towards the center of the chamber and impact upon a heavy anvil plate. Ignition occurs upon the impact, resulting in a shock wave and rapid combustion of pulverized material. Although the chamber cannot be sealed because its wall is punctured through by the projectile, the pressure rise in the chamber occurs sufficiently fast to make the pressure measurement meaningful. The quasistatic pressure (QSP) measured in the chamber upon impact is translated into the energy released. This energy is interpreted considering the theoretical energy release expected from the RSM projectile upon its complete combustion.

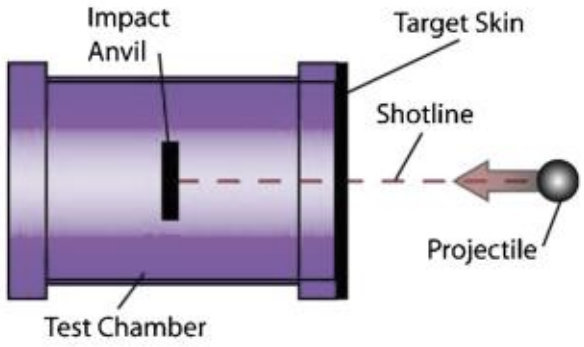

Figure 1.17 Schematic diagram of an experimental chamber used in the impact initiation experiments by Ames.
Source: [213]

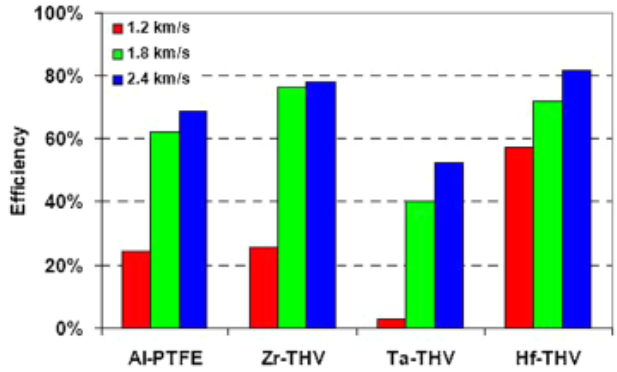

Figure 1.18 Typical reaction efficiencies for impact initiated RM samples.
Source: [214]

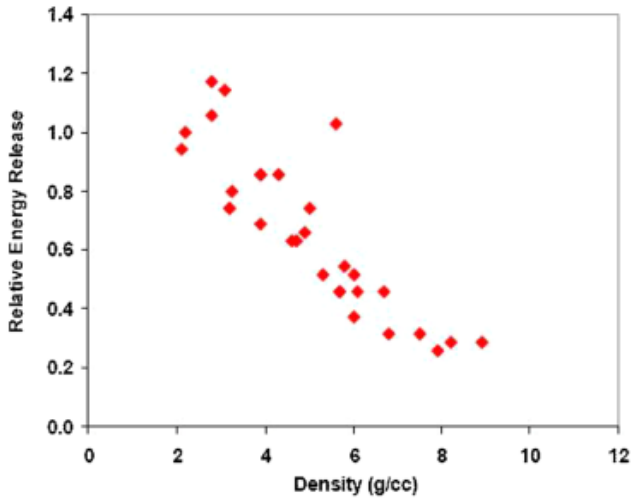

Figure 1.19 Energy released by different reactive material samples as a function of the material density. The reaction is initiated by a 6,000 ft/s impact; the energy is normalized by that released by Al-PTFE with TMD of 2.4.
Source: [214]

Selected results are illustrated in **Figure 1.18** and **Figure 1.19** [214]. Reaction efficiency, measured based on the QSP, increases markedly with increase in the impact speed (**Figure 1.18**). The effect of density on the reaction efficiency is also very strong, and overarching for a wide range of materials (**Figure 1.19**). However, all samples represented in **Figure 1.19** were prepared as compacted commercial powders; they do not include more advanced nanocomposite materials.

In addition to the energy release, the minimum impact pressure necessary for ignition of an RSM projectile is identified. For example, the initial critical impact initiated velocity is about 650 m/s for W/Zr alloy [221]. **Table 1.1** shows reaction characteristics, including reaction efficiencies for several impact initiated RSM samples. In calculating the kinetic energy, it was assumed that the samples entered the chamber at 90% of their initial kinetic energy after passing through the target skin.

In recent experiments following the same general approach, the RSM was packed into a reactive bullet, as a reactive fragment inside a steel shell [222]. The impact initiation behavior of Al/PTFE RSMs with added tungsten was investigated. It was found that a greater reaction efficiency was achieved at higher impact velocity. Samples with greater porosities and with greater concentration of tungsten were more reactive. Tungsten was not observed to participate in the reaction, however.

Table 1.1 Reaction Characteristics, Including Chemical Reaction Efficiency for Different RM Compositions Tested using an Impact of Accelerated RM Projectile

Material	Impact velocity (m/s)	Quasi-static pressure (Mpa)	Total energy (kJ)	Kinetic energy (kJ)	Chemical energy (kJ)	Total chemical energy (kJ)	Reaction efficiency (%)	Impact pressure (GPa)
W/Zr	752	0.14	5.46	1.575	3.885	29.145	13.3	12.57
W/Zr	1094	0.21	8.19	3.384	4.806	29.895	16.1	19.29
W/Zr	1335	0.45	17.55	5.004	12.546	29.359	42.7	24.40
Al/PTFE	847	0.10	3.90	2.124	1.776	25.314	7.0	5.49
Al/PTFE	934	0.19	7.41	2.520	4.890	24.041	20.0	6.19
Al/PTFE	1004	0.30	11.70	3.141	8.559	26.021	32.9	6.76
Al/PTFE	1203	0.68	26.52	4.320	22.200	25.879	85.8	8.49
Al/PTFE	1481	0.23	8.97	6.867	2.103	26.304	8.0	11.09
Al	1049	0.07	2.73	3.456	...	...	...	...
Al	1169	0.08	3.12	4.311	...	...	...	...

Source: [221]

1.6.4 Explosive Imitation of RSMs

Initiation of RSM samples using an explosive is aimed to imitate a scenario when the RSM serves as a case or liner for a munition carrying an explosive charge. Efforts [223, 224] was aimed to observe detonations in consolidated RSM samples. Qualitatively similar

experimental configurations were used, as shown schematically in **Figure 1.20**. An RSM sample was constrained in a thick-walled container. To minimize the effect of reflected sound waves on the measurements dealing with Zn–S composition, the container was made of a porous composite with a low sound speed [224]. In both studies [223, 224], the results were inferred from the velocity measurements for the propagating combustion wave. It was concluded that a detonation wave was possible for an RSM system with the minimized gas release, for which both reactants and products were condensed phases.

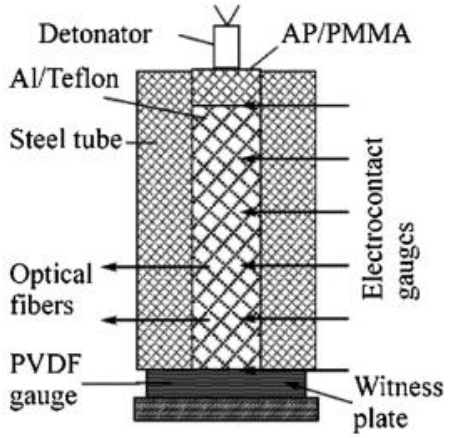

Figure 1.20 An experiment studying an explosive-driven deto.nation in an aluminum-PTFE composite.
Source: [223]

In other studies [225, 226], a qualitatively similar experimental setup was built and used to consider a detonation-induced reaction in the Zn–S samples prepared at different nominal densities, as illustrated in **Figure 1.21**. Dimensions of the RSM samples were increased to enable recovery and analysis of the materials after the experiments. Despite the larger sample size, no self-accelerated reaction rates were observed. It was, therefore, concluded that no evidence for gasless detonation currently exists.

A set of experiments described in references [227, 228] followed up on extensive earlier work aimed to identify the mechanism of initiation and propagation of a shock initiated reaction in a condensed phase RSM. The general focus of this work was to establish the size of the area directly initiated by the shock, often referred to as a hot spot, and to determine the mechanism of the reaction propagation through the rest of material. Two experimental configurations shown in **Figure 1.22** were used [227]. In both cases, an RSM sample was constrained in a cylindrical steel capsule. An explosive placed on top of the capsule was detonated. In one of the configurations, **Figure 1.22**a, both thermocouple and light sensor were used to monitor reaction. In this case, a polycarbonate window was used as part of the sample enclosure; the explosive charge in this case was limited to 130 g of nitromethane (NM) sensitized with 5 wt% of diethylenetriamine. It was expected that the optical signal will show when local high temperatures occur, for example, when hot spots are formed. Conversely, the thermocouples were expected to describe the rise in the bulk sample temperature when the reactions propagate. In the configuration shown in **Figure 1.22**b, only thermocouples were used and the window was replaced by a steel part. In the latter case, the explosive was 450g of commercial pentolite. Yet another experimental configuration was used, when only optical signal was collected. For these experiments, the light passed through a hole drilled in a steel component, while the entire capsule was placed in a water pool. After experiments, samples were recovered to observe the extent of reaction. Some of the recovered samples were completely reacted; for others, no evidence of bulk initiation was observed. No partially reacted materials were found.

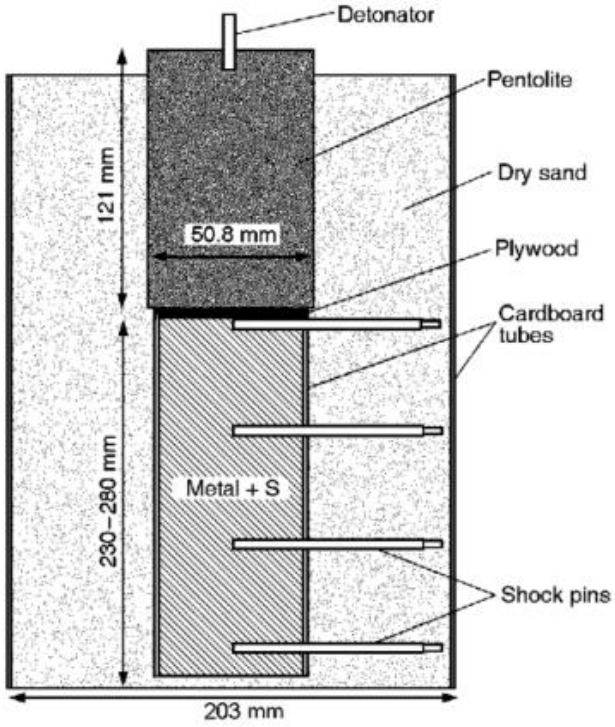

Figure 1.21 Experimental setup used to study an explosive driven reaction in different RMs.
Source: [226]

Based on results of the experiments, it was concluded that the initiation of hot spots occurs in the time scale of μs, comparable to the time of shock compression. Conversely, reaction propagation occurs at a much longer time scale, from ms to hundreds of ms. The burn rate in such materials was found to be largely pressure-independent.

In a complementary study [228], shock initiation was studied for a broad range of samples with the focus on correlation between thermal and shock initiation processes. The process of ball-milling or mechanical activation was found to increase both thermal and shock sensitivity. It was further found that the increased thermal sensitivity was not caused by shock compression alone. For samples shocked at pressures just lower than necessary for ignition, the ignition threshold was found to be indistinguishable from the equivalent un-shocked samples.

Shock initiation of laminate Ni–Al composite samples was studied using so called "Thick-Walled Cylinder Method" presented schematically in **Figure 1.23** [229, 230]. A cylindrical RSM sample is placed inside a copper tube. The assembly is placed inside PVC container filled with an explosive. The information about reaction initiation is obtained by recovery and examination of the samples following the experiments. The focus is on the mechanical processes leading to chemical reactions. It was established that instabilities during the collapse of the Ni–Al-corrugated laminate composites triggered three main mechanisms of plastic strain accommodation. The inside facing wedge-shaped regions at the inner surface of the laminate were extruded. There was a small number of non-uniformly distributed local/global trans-layer shear bands. The initial locally concentric layers experienced cooperative buckling. These mechanisms were specific to the configuration studied and different from shear localization processes involving plastic deformation and discussed in earlier work with fully dense or granular materials.

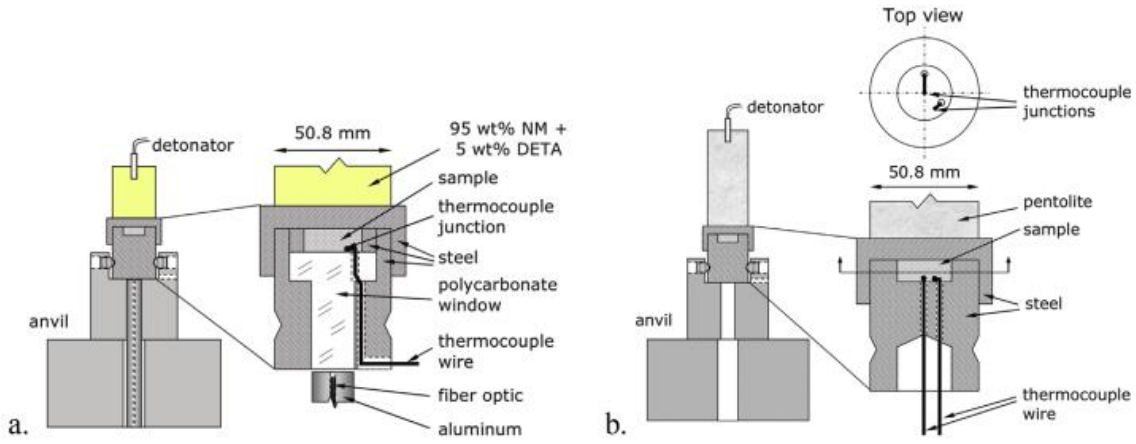

Figure 1.22 Experimental configurations used in ref. for explosive-initiated experiments with RMs. A) Experiments with photo-multiplier tubes and thermocouples; b) experiments with thermocouples.
Source: [227]

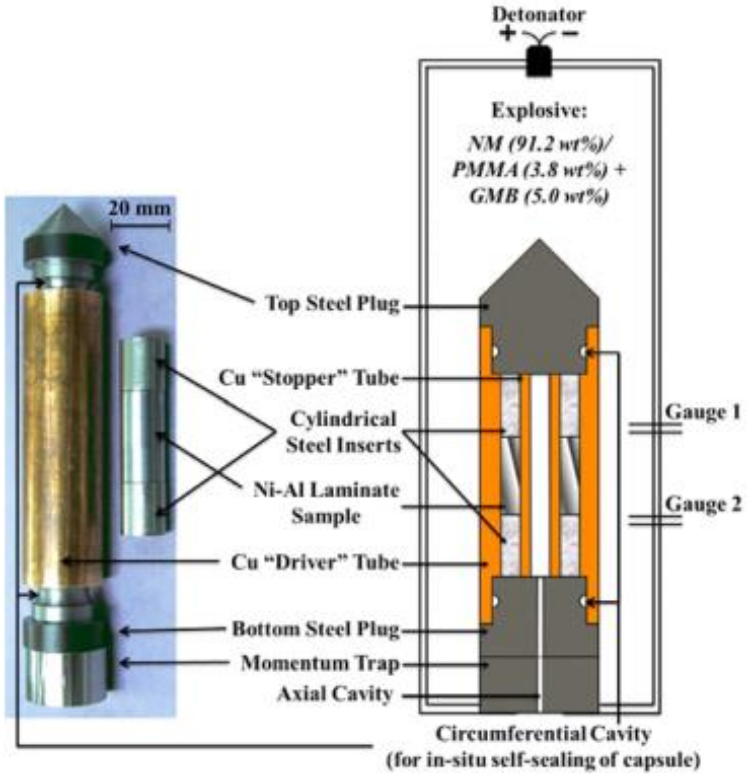

Figure 1.23 Experimental configuration for the thick-walled cylinder method. See https://doi.org/10.1080/14786435.2014.948524 for details.
Source: [229, 230]

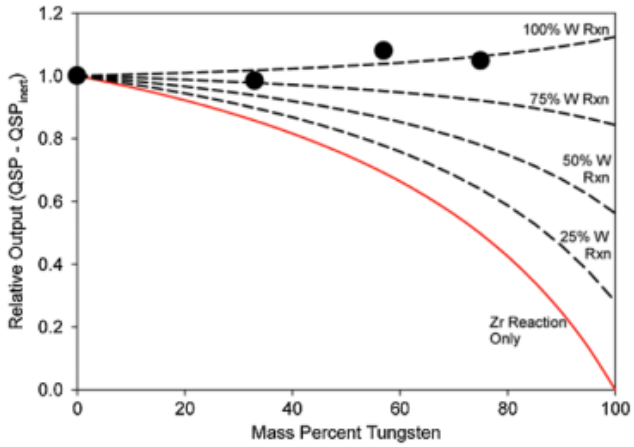

Figure 1.24 Net QSP is the total QSP minus that of the test with inert (WO3) pellets. Measured net QSP produced by W–Zr alloys normalized to the pure Zr case. Dashed lines show expected net QSP for different degrees of tungsten reaction.
Source: [35]

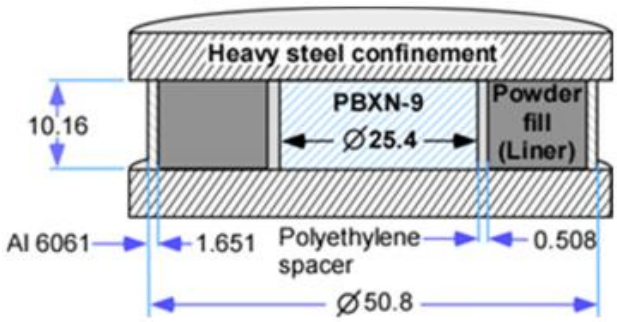

Figure 1.25 Charge configuration for reactive liners with a PBXN-9 booster used in experiments. Dimensions are in mm.
Source: [231]

A different set of experiments with shock-initiated RSMs addresses applications, in which an RSM is dispersed and initiated by interaction with a shock wave produced by a high explosive (HE) [25, 35, 231]. In one of the experiments, a pressed pellet of mechanically alloyed B–Ti powder was placed directly on top of an HE pellet. The experiments were performed in a chamber with optical ports for high speed video and spectroscopy. The chamber was also equipped with both transient and QSP transducers. It was observed that the mechanically alloyed materials produced greater pressure and greater energy release than other samples with the same bulk compositions (blended powders or titanium boride). The method used to prepare mechanically alloyed material was found to be critical to ensure the best performance. In other experiments, a conceptually similar configuration generating a more spatially uniform explosion was used for testing mechanically alloyed W-Zr samples [35]. Disk-shaped 12.7-mm diameter pellets of RSM pressed to 60-70%TMD were arranged to form a dodecahedron. An 18-g nitromethane charge used to initiate the RSM was located at the geometrical center. Experiments were performed inside a 1.2 m x 1.2 m x 1.2 m steel blast chamber. Both transient and QSP measurements were made. Results were processed to estimate the completeness of tungsten combustion based on the net QSP-implied energy release. The net QSP was obtained by

reducing the measured QSP by that obtained in tests with the nitromethane charge and inert tungsten oxide pellets instead of RSM. A bare Zr case was used as a reference for RSM assessment. In the reference experiment, QSP suggested that approximately 86% of the theoretical energy of Zr combustion was released. The calculated and measured energy release is illustrated in **Figure 1.24** [35]. If the only reaction is that of Zr, the calculated energy release becomes smaller when W is added. The decay as a function of W concentration is predicted even if 75% of the added W combusts. The present results suggest no decay, or, in fact a slight increase in the QSP with tungsten combustion. Thus, a nearly 100% reaction efficiency is implied. This reaction occurs in the time scale of 20–100 ms (**Figure 1.24**).

In recent studies [35, 231, 232], an experimental configuration involving a cylindrical liner of an RM powder initiated by a centrally placed explosive charge, as shown in **Figure 1.25** was explored. Fragmentation of a pressed aluminum case was studied in reference [232], while both aluminum and differently prepared Al–Mg composites were used in the reactive liners in reference [231]. It was found that the explosion leads to compaction of the aluminum powder to near solid density, and its subsequent fracture into fragments that are several centimeters long and less than a centimeter thick [232]. Reactive liners were prepared with pure aluminum, cast alloyed and mechanically alloyed Al Mg powders, and with blended Al and Mg powders. For reference, liners were also prepared filled with inert Al_2O_3 powder. All liners filled with reactive powders produced higher QSP than the inert reference; they also exhibited a stronger initial pressure peak occurring in the sub-millisecond time scale, important for improvement of the air blast characteristics. In particular, both time of arrival of the pressure peak and its

amplitude were improved in experiments with reactive liners. The mechanically alloyed powder showed the most significant improvement in the early blast characteristics, although it did not offer substantial benefits in terms of QSP, as compared to the pure Al. These results are interesting as direct indicators that a very rapid reaction is possible for RSMs, which could usefully contribute to the early blast development. The mechanisms of such prompt metal combustion are not understood presently and further work is desired to determine such mechanisms and exploit them for design of optimized RSMs.

1.7 Summary and Future Work

Metal-based compositions capable of various self-sustaining exothermic reactions have been prepared and tested for potential use in applications requiring both structural strength and ability to generate chemical energy upon initiation by heat, impact, or shock. Such materials, referred to as reactive structural materials, emerged as an important group of composites, prepared by multiple methods and required customized characterization approaches. The composites can react forming oxides, fluorides, carbides, borides, sulfides, silicides, and aluminides. They are prepared by mixing starting powders or nanopowders, employing binders, mechanically refining bulk metals or powders of starting materials, and by layered deposition of starting elements or molecules. Consolidating composites prepared as powders is an important step in designing RSMs, where both high density and reactivity are desired. Contemporary approaches, such as involving additive manufacturing and enabling design of customized material architectures are of particular interest.

Chemically, the most reactive systems are those relying on the reactions of oxidation and fluorination; however, typically materials relying on such reactions have relatively low densities or require an external oxidizer. Including a high-density additive,

such as tungsten, is relatively common; however, such additive is chemically inert in most cases. Advanced refining methods, such as high energy mechanical milling or preparation of layered structures by magnetron sputtering generates useful, high density morphologies, which hold promise of combining the high density and reactivity for the future RSMs.

Both mechanical and energetic properties of RSMs must be characterized. Traditional characterization methods, such as static mechanical testing and thermal analysis are necessary, but must be supplemented by dynamic experiments. In mechanical tests, such as using SHPB, initiation of RSMs is probed in addition to recovery of their dynamic mechanical properties. In addition, customized test methods, addressing, for example, fragmentation of the RSMs upon impact and reactivity of the produced fragments are developed and used for a broad range of RSM compositions. These experiments are usefully supplemented with the studies focused on ignition and combustion of individual particles and meso-particles, used to prepare consolidated RSMs and expected to re-emerge upon the RSM fragmentation. Results of the latter studies may be used to predict the behavior of RSM fragments in various practical scenarios. Little is presently done to characterize long-term stability and aging of RSM composites, and work is expected in that direction, involving advanced thermal analysis and microcalorimetry.

Dynamic initiation experiments for RSMs described in the literature currently can be seen as two distinct groups: one, dealing with microscopic samples and involving very fine spatial and temporal scales, and the other, dealing with relatively large consolidated samples exposed to conditions expected in a practical application. Presently, there is essentially no link between the outputs of these different types of experiments. It is hoped

that a better connection can be developed in the future. In particular, using the same types of RSMs in different types of tests and comparing results systematically should be useful.

The theoretical ideas describing fragmentation and reactions in RSMs are much less developed presently and were not reviewed here. Such descriptions are necessary, however, and future experiments should be designed to enable and support development of the relevant models. The models should describe both mechanical and energetic properties of the new materials and must be compatible with the state of the art hydrodynamic codes describing munition systems in which the use of RSMs is anticipated.

The work aimed at developing new RSM compositions is expected to continue and focus on ternary and more complex materials systems. It is further expected that advanced materials processing and consolidation techniques, such as mechanical milling, layered deposition, controlled isostatic pressing, cold spray, and others will be combined to prepare final advanced RSM structures. Materials with modulated densities and tunable heat release kinetics are of particular interest.

CHAPTER 2

HIGH DENSITY REACTIVE COMPOSITE POWDERS

2.1 Introduction

Reactive materials do not detonate but burn rapidly with a gravimetric and volumetric heat release comparable to or exceeding that of conventional propellants and explosives [19]. They can be used as fuels or customized fuel additives [4], reactive liners [233], weapons casings [192, 234, 235], as reactive solders or brazes [236, 237], and as components of pyrotechnic devices [238, 239]. Most of such materials are based on metals, such as Al, Mg, B, Ti, Zr, etc. Both absolute heat release and rate of reaction are important while utilizing reactive materials in all practical systems. For an important class of applications involving kinetic penetrators[240-242], it is also necessary for the reactive structures to have high density to maximize the momentum of the projectile. The combination of high heat release, high burn rate, and high density is difficult to find while considering individual metals with high heats of combustion; however, such a combination may be achieved in composite structures.

Although aluminum is by far the most common metal fuel additive [83, 243, 244], when selecting components for a composite material, it is natural to consider boron, which possesses the highest volumetric theoretical heat of oxidation of any element at ca. 147 kJ/ cm^3 [245]. Limitations of boron include its low density (2.5 g/cm^3), long ignition delays and relatively low burn rates [83]. It has been shown that combining boron with titanium yields a composite with an accelerated burn rate and increased material density [25, 28, 244, 246-249]. The composites were prepared as mixed powders [26], titanium coatings on boron powders [250], and fully-dense composite powders prepared mechanochemically

(or via ball milling) [27, 28, 250]. The latter approach is most versatile and practical; it also enables one to readily control the composition of the prepared composite. Upon initiation, boron begins reacting with titanium forming TiB and/or TiB_2 generating 10.7 and/or 21.6 kJ/cm^3, respectively [25]. These are some of the most exothermic intermetallic reactions. Although they are not matching the oxidation heat release of either boron or titanium, they serve to rapidly raise the temperature of the composite. When such a fast and nearly volumetric heating occurs in an oxidizing environment, the material goes on to oxidize rapidly and completely [25, 28], generating more heat per unit volume than burning aluminum, 103.5 or 111.5 kJ/cm^3 for B·Ti and 2B·Ti, respectively (compare to 83.8 kJ/cm^3 for aluminum combustion [28]). The densities of B-Ti composites (3.9 and 3.6 g/cm^3 for B·Ti and 2B·Ti, respectively), exceed that of aluminum (2.7 g/cm^3).

Despite energetic and density advantages, B-Ti composites do not match the density of common structural materials, such as steel, used to construct munition casings. To increase the density of reactive composite material used for kinetic energy penetrators or similar applications, highly reactive B-Ti composites can be combined with tungsten (density of 19.3 g/cm^3). Tungsten heavy materials are widely used or explored for the penetrators [25, 28, 38]; however, they commonly do not rely on tungsten combustion. Combustion of tungsten is used in selected pyrotechnic devices [251, 252]; however, tungsten is known to be difficult to ignite and have low burn rates, which mostly restricts the current uses of its combustion to slow-burning delay mixtures [253]. Recently, it was shown that combustion of tungsten can be catalyzed by preparing its composite with zirconium, another readily burning metal [254]. The approach involving catalyzing tungsten combustion is promising for the reactive structural materials and is explored here

by combining tungsten with a boron-titanium composite. The composition selected for this study is that having the density of steel, 7.8 g/cm^3. It is achieved by combining boron, titanium, and tungsten with the mole percentages of 53, 26, and 21, respectively. The total energy of the intermetallic reaction in this composite is 9.36 kJ/cm^3 (formation of TiB_2); its total heat of combustion (or complete oxidation of all metals) is 108 kJ/cm^3. The paper describes mechanochemical preparation of the composite powder and its characterization involving electron microscopy, thermal analysis, and combustion experiments.

2.2 Experimental

2.2.1 Materials

Starting materials and the overall composition of the prepared composites are described in **Table 2.1**. The particular composition used here was chosen in part to maximize the energy release by the TiB2 formation, using a 2:1 B:Ti atomic ratio. The amount of tungsten was chosen to yield a final theoretical maximum density equaling that of steel, or 7.8 g/cm3. After an initial set of composites prepared with -325 mesh tungsten, a different, finer, tungsten powder was used in order to improve refinement of the components. Binary B·Ti and B··W composites were prepared with the respective component ratios from **Table 2.1**. Composite B-Ti-W powders were prepared by mechanical milling. A SPEX 8000D shaker mill was primarily used. Five grams of powder were milled with 25 g of 3/800 (9.53 mm) balls, giving a ball-to-powder ratio of 5. Milling was performed under argon, and 10 mL of hexane were used as process control agent. Milling vials and media of hardened steel, and of stabilized zirconia were both used. Milling with steel media introduced noticeable levels of iron contamination in the resulting composite. While not necessarily detrimental

to performance, this did make sample analysis more challenging due to the formation of iron-bearing phases. The compositions characterized in detail here were therefore prepared using zirconia vials and milling media.

Two general milling protocols were followed: in one set of experiments, the component powders were loaded into the milling vials together, and then milled for varying periods of time. Materials prepared using this single-step milling protocol will be denoted as B·Ti·W. In a second set of experiments, boron and tungsten powders were milled first in order to minimize the reaction between boron and titanium during milling. Combining mechanically harder boron and tungsten in the first milling step also helped achieving a more homogeneous distribution of tungsten in the final composite material. This first milling step produced binary B·W composites. Titanium powder was added later. Composites prepared using this two-stage milling protocol are designated as (B·W)·Ti. Milling times varied in the 2-7 h range based on experience from prior work [255, 256]. For comparison of combustion behavior, a reference material was prepared by blending elemental tungsten with a preliminarily prepared B·Ti binary composite; this reference blend is labeled (B·Ti)·W.

Table 2.1 Elemental Composition

Composition of W-B-Ti				Description
	Atomic %	Mass %	Volume %	
Tungsten	21%	68%	27%	Atlantic Equipment Engineers, 99.9%, −325 mesh (<44 μm) Alfa Aesar, 99.9%, 1−5 μm
Boron	53%	10%	34%	SB Boron, SB-95, 95%, nominal size −325 mesh (<44 μm)
Titanium	26%	22%	39%	Atlantic Equipment Engineers, 99.7%, −325 mesh (<44 μm)

2.2.2 Characterization

Morphology of, and elemental distribution in the prepared composites were examined on a LEO 1530 VP scanning electron microscope operating at 10 kV, and using a back-scattered electron detector.

Particle size distributions were determined using a Beckman Coulter LS230 particle analyzer. Suspensions were prepared in ethylene glycol. Measurements were repeated three times, and ultrasonic agitation was used for the final repetition. Size distributions were accepted as stable only when all repetitions coincided.

Reactive properties were characterized by differential thermal analysis using a Netzsch STA409-PG thermal analyzer. Samples were heated from 50 to 1100 ˚C under argon at a rate of 10˚ per minute, allowed to cool and then reheated. The second heating of the sample was subtracted from the first to compensate for baseline effects. Onset temperatures of exothermic reactions and the net heat release over the observable temperature range were used to compare materials against each other as well as with the literature values. These comparisons also were used to guide the details of the milling protocol.

X-ray diffraction on a PANalytical Empyrean diffractometer with unfiltered Cu-Ka radiation was used to assess reaction products formed during thermal analysis.

Bulk energy release upon combustion, and combustion rate in an oxygen atmosphere were assessed in a custom constant volume chamber shown schematically in **Figure 2.1**. In practical applications, reactive materials are expected to be ignited using booster charges or similar high-energy ignition sources. Such igniters are difficult to imitate in the small-scale laboratory tests. Thus, in order to achieve the most reliable ignition, pure oxygen was chosen as an oxidizing environment in these tests. Oxygen was also helpful in

maximizing the pressure rise from the relatively small sample masses used. Samples with masses up to 0.3 g were contained in a brass plate with a 3.05 mm diameter, 0.635 mm deep machined recess. This sample holder was covered with a mask that only leaves the recess open, and placed under a 140 mesh (106 mm) sieve. Small amounts of powder were then passed through the sieve. This procedure avoided any incidental compaction of the powder, ensuring even dispersal during ignition and combustion. The sample holder was weighed on a Mettler Toledo AX205 Delta Range microbalance before and after loading, and after the combustion test in order to determine initial and final sample masses. The loaded sample holder was then placed in the combustion chamber. The chamber was sealed and pressurized with oxygen to about 3.5 atm, and bled again to atmospheric pressure. The pressurization/bleeding cycle was repeated five times in order to ensure an atmosphere of >99% O_2. For sample ignition, a modified model 931 firing test system by Electro-Tech Systems, Inc. was used. Samples were initiated by discharging a 2000 pF capacitor charged to 12 kV, and the chamber pressure was measured with a factory-calibrated ICP 113B28 pressure sensor with a 0-50 psi pressure range and acceleration compensation, and recorded using a RIGOL DS1054 oscilloscope. From the pressure-time records, maximum chamber pressure and time to peak pressure were determined. For reference, the adiabatic chamber pressure assuming the complete combustion generating thermodynamically equilibrated products was calculated using NASA CEA code [257]. In preliminary experiments, a stoichiometric 2Al·3CuO nanocomposite thermite prepared by arrested reactive milling and known to be highly reactive [204, 258] was ignited in this chamber. The measured pressures reached nearly 50% of those predicted by the NASA CEA code.

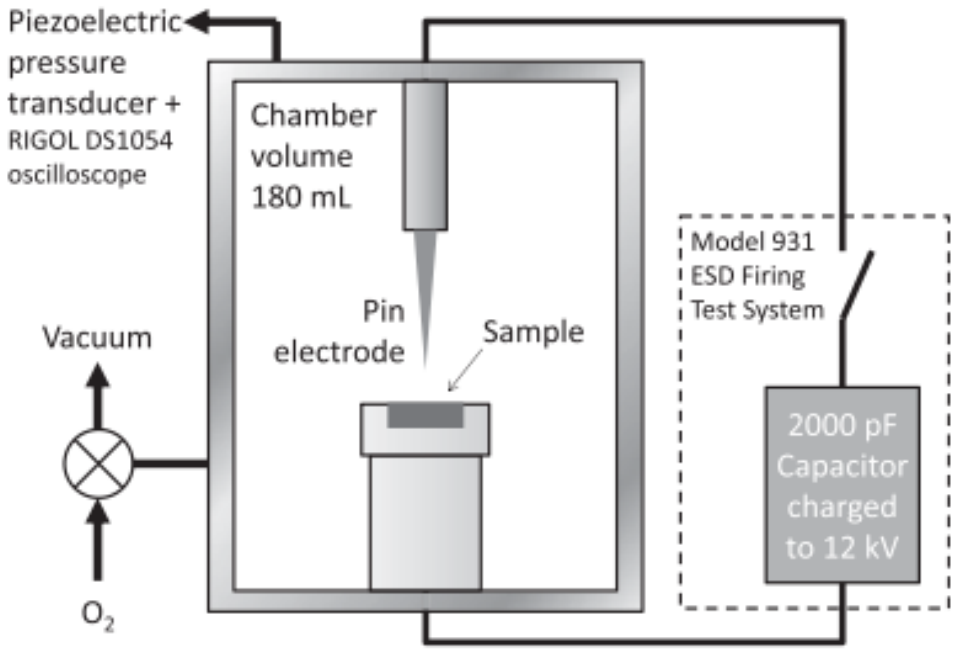

Figure 2.1 ESD constant volume combustion chamber.

2.3 Results

Figure 2.2 and **Figure 2.3** show backscattered electron images of the prepared composites. **Figure 2.2** shows the binary composites B·Ti and B·W. In both materials boron forms isolated inclusions in a continuous matrix consisting of Ti, and W, respectively. The images at slightly lower magnification on the left show that the B·Ti composite particles are overall less porous. In contrast, the tungsten matrix is less continuous; some individual deformed and rarely even undeformed particles of tungsten can be distinguished even after 4 h of milling.

Figure 2.3 shows ternary milled composites and, for reference, also a partial blend. The first composite is an example of the direct/ straight milling protocol, where all components were milled for the entire duration. The second composite, with the same composition, was milled in stages: the binary B·W composite shown in **Figure 2.2** was milled for an additional 2 h with the addition of titanium. While boron is recognizable as

micron to submicron sized dark inclusions in both materials, titanium and tungsten are less readily distinguished, suggesting intimate mixing using either milling protocol. Finally, the third material consists of a blend of the binary B·Ti composite shown in **Figure 2.2**, and the original 1e5 mm tungsten powder. All materials shown in **Figure 2.3** have the same bulk composition and differ only in the method of milling and blending.

Size analysis using light scattering showed that materials had relatively broad size distributions with average sizes of less than 10 mm and upper limits near 50 mm. Based on SEM images, there was no significant particle size differences between any of the prepared powders. An example of the size distribution is shown in **Figure 2.4**.

Figure 2.5 shows the results of differential scanning calorimetry. The progression of DSC curves with milling time for composite milled in a single stage is shown in **Figure 2.5**A. **Figure 2.5**B and C show the DSC curves for the initial and final stages of the two-stage milling protocol. Most DSC curves show a pronounced exothermic effect near 1000˚C. An endothermic effect near 400-500 ˚C develops for ternary composites at longer milling times. Besides these localized effects, there is a broad exothermic background indicating gradual formation reactions of intermetallic equilibrium phases. Integration of these curves is challenging due to the wide temperature interval. As a first approximation, the curves can be integrated by drawing a linear baseline between the temperature limit. This gives a semi-quantitative measure of the exothermic enthalpy released during heating.

A summary plot for the cases shown in **Figure 2.5** is shown in **Figure 2.6**. The stars show data for the materials obtained by the two-stage milling, the inset axis in **Figure 2.6** shows the duration of the second milling step, which is added to the times scale shown in the main time axis. Observed exothermic enthalpies for all materials exhibit a maximum

at intermediate milling times. At short milling times, the components are still poorly mixed, limiting the reaction by long diffusion distances. At long milling times, equilibrium intermetallics or their precursors form during milling, limiting the enthalpy available during heating. Within the resolution shown in **Figure 2.6**, the optimum milling times are 2 h for the single-stage milling protocol, and 4 h for the first and 2 h for the second stages of the two-stage milling protocol.

To confirm the state of the materials after milling, and after annealing, selected samples were analyzed by x-ray diffraction. **Figure 2.7** shows samples prepared by single-step milling with 1, and 2 h milling time, in the as-milled state, and after recovery from the DSC analysis shown in **Figure 2.5**A. As expected, elemental component Ti is still seen after one hour of milling. After two hours its crystallinity and grain size has decreased enough to be no longer detectable. Tungsten remains visible, although peaks do become slightly weaker. Boron is nominally amorphous and is therefore never detected in the as-milled materials. A small peak observed around 30˚ is contamination by zirconia from the milling tools. After annealing to 1100 ˚C during thermal analysis, elemental tungsten is still present, although in smaller amounts. The WB intermetallic phase is a major reaction product in both materials, as is TiB_2. The W_2B intermetallic phase is only present in the material milled for 2 h.

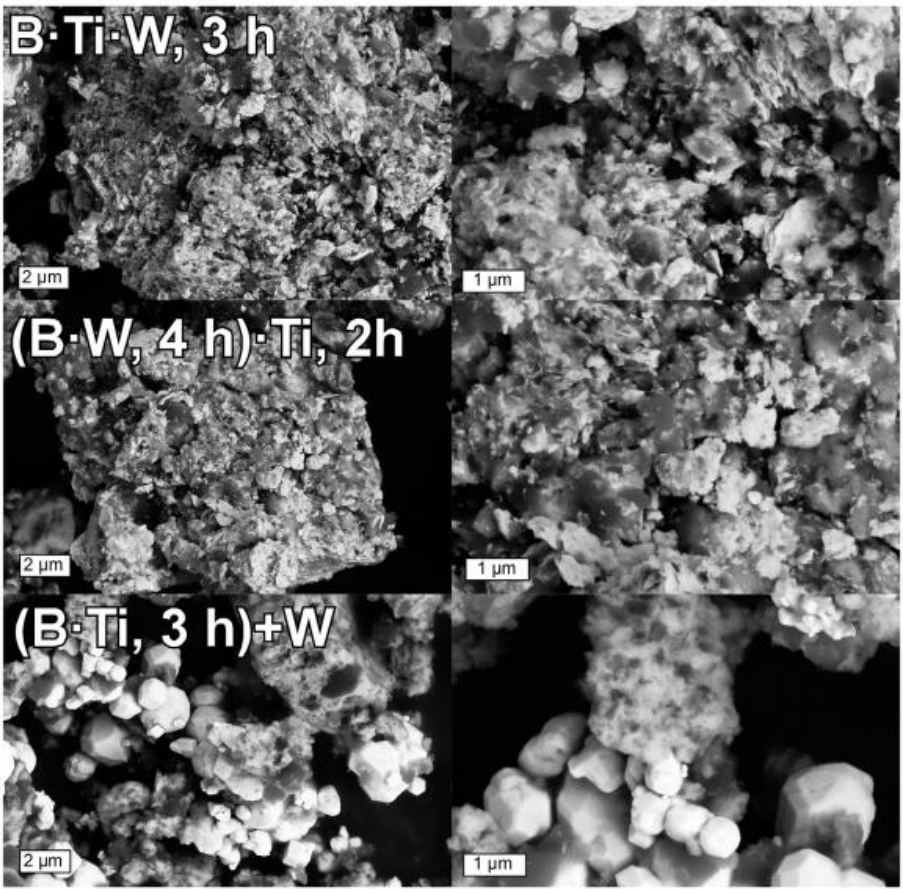

Figure 2.2 Backscattered electron images of the binary composites B·Ti and B·W with respective compositions as indicated in **Table 2.1**. The darker inclusions are boron in either composite, and the brighter matrix is titanium and tungsten, respectively.

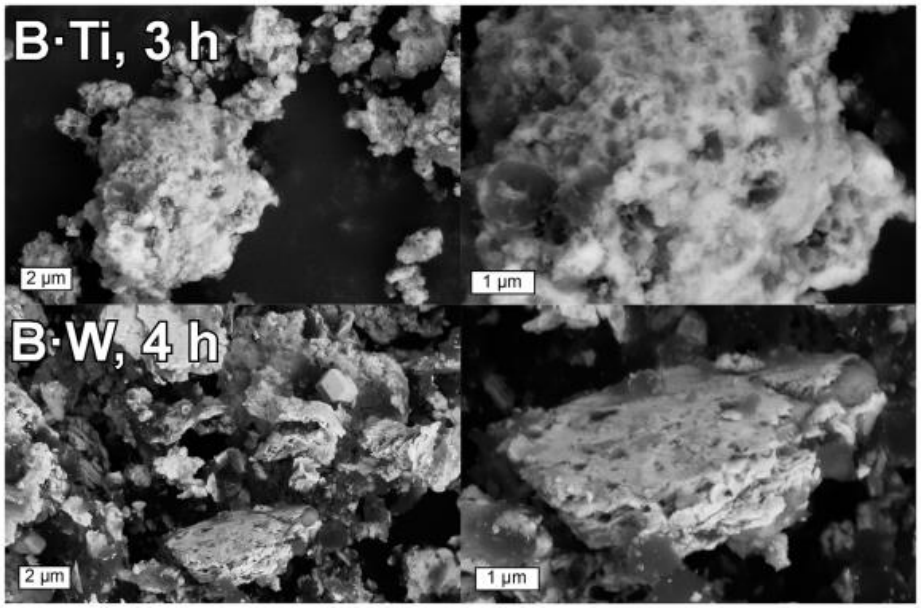

Figure 2.3 Backscattered electron images of ternary B·Ti·W composites with composition shown in **Table 2.1**. The top two sets represent milled composites and the bottom set a partially blended composite or reference. The first composite was milled with all components directly, while the second composite was milled in two stages. The darker inclusions are boron in all cases. Both, titanium and tungsten are relatively brighter and not well distinguished in the milled composites. Tungsten is seen as the well-crystallized, blended component in the partial blend.

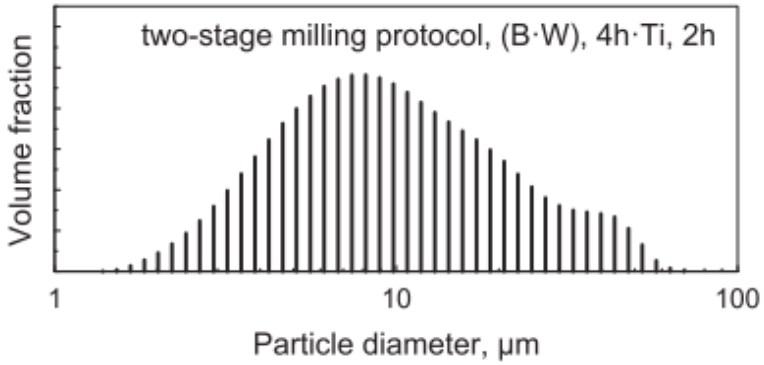

Figure 2.4 Particle size distribution of a B·Ti·W composite prepared by the two-stage milling protocol.

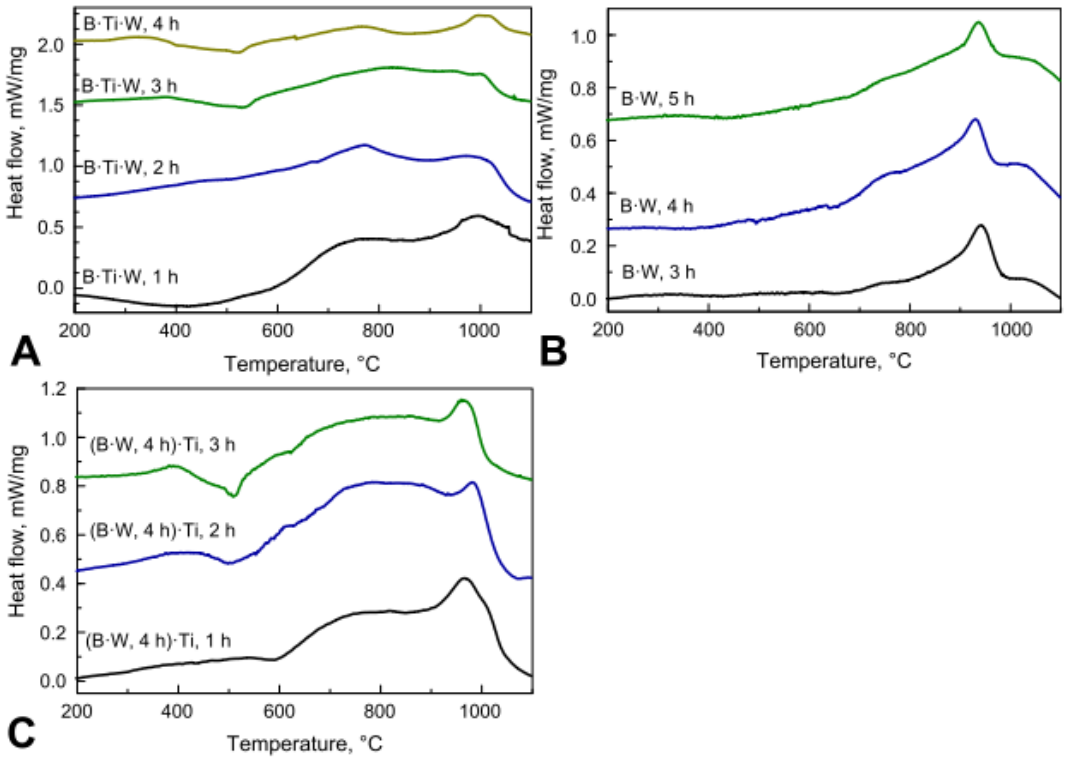

Figure 2.5 DSC measurements of B·Ti·W composites.

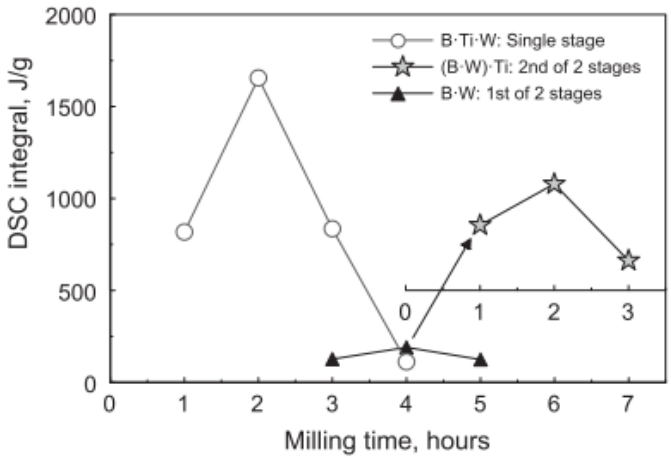

Figure 2.6 DSC integrals of binary and ternary composites as function of milling time.

The prepared powders were initiated by an electrostatic discharge in a constant-volume chamber under pure oxygen. Records of the chamber pressure vs. time were the only diagnostic signal. Examples of the raw results are shown in **Figure 2.8**. All traces shown in **Figure 2.8** are from the same material. The pressure pulses are all relatively slow,

typically peaking after more than 40 ms with some times sharper, some times more flattened maxima. There was a relatively strong variability.

The data shown in **Figure 2.8** were reduced to extract the peak pressure value, and the peak value of the pressure-time derivative. The peak pressure is interpreted as proportional to the total heat release from combustion and the pressure derivative served as an indicator of the reaction rate. These reduced results are shown in **Figure 2.9** as plots of peak pressure vs. the amount of sample loaded and ignited. **Figure 2.9** shows the component binary B·Ti material for reference, and selected ternary composites prepared using the single-stage protocol and the optimum material prepared using the two-stage milling protocol. In order to meaningfully compare the component B·Ti material with the ternary tungsten-containing materials, the sample volume was chosen as common axis. In addition, **Figure 2.9** shows maximum pressures for adiabatic combustion of the materials calculated using NASA CEA code. In calculations, the initial reactants were entered as B, Ti, W, and O_2. The products predicted were mostly limited to three condensed oxides, B_2O_3, TiO_2, and WO_3 with O_2 being the only gas. As previously suggested by **Figure 2.8**, there is substantial scatter in the observed peak pressure. The values obtained for the ternary composite prepared using the two-step protocol appear to be somewhat higher than all others, however. All observed peak pressures are substantially less than the theoretical adiabatic limits due to a combination of incomplete combustion and non-adiabatic conditions. Peak pressurization rates, or maxima of the pressure-time derivatives, are shown in **Figure 2.10**. Here, too, the ternary material prepared by the two-stage protocol appears to be faster than all other materials, although there is also strong scatter in the results.

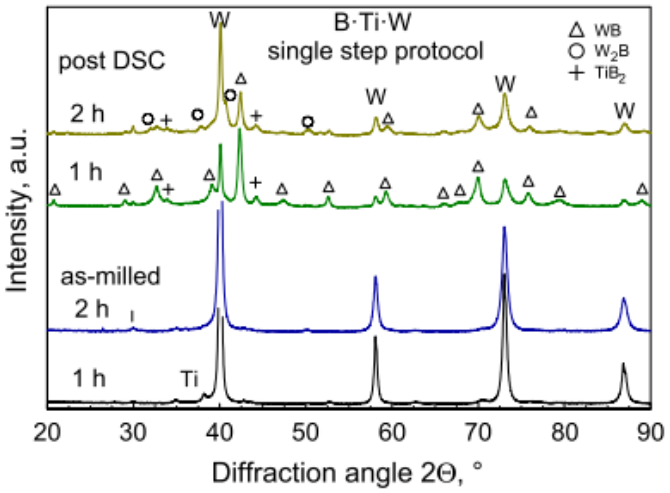

Figure 2.7 XRD of B·Ti·W composites in as-milled state, and after annealing to 1100 ˚C.

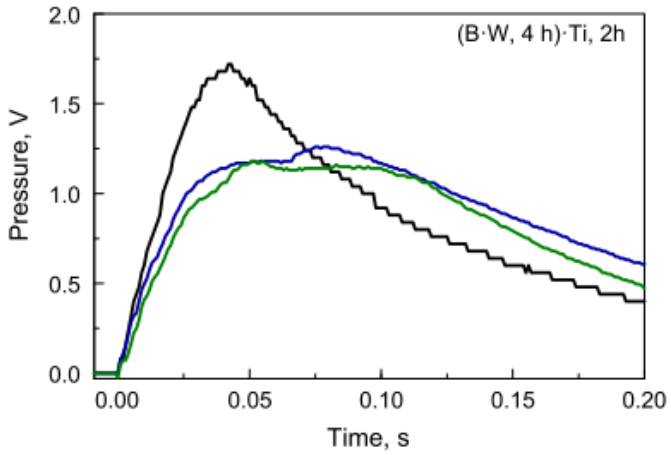

Figure 2.8 Examples pressure traces produced by a composite material ignited in oxygen by an electric spark. All three experiments used the same batch of the composite powder prepared by the two-stage milling protocol.

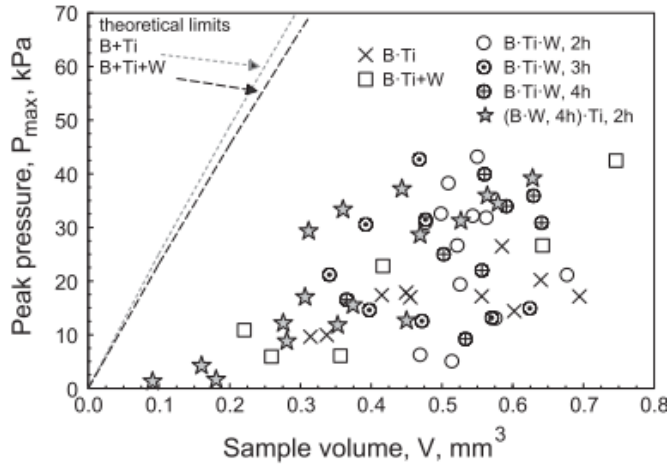

Figure 2.9 Peak pressure vs sample volume in constant-volume combustion tests.

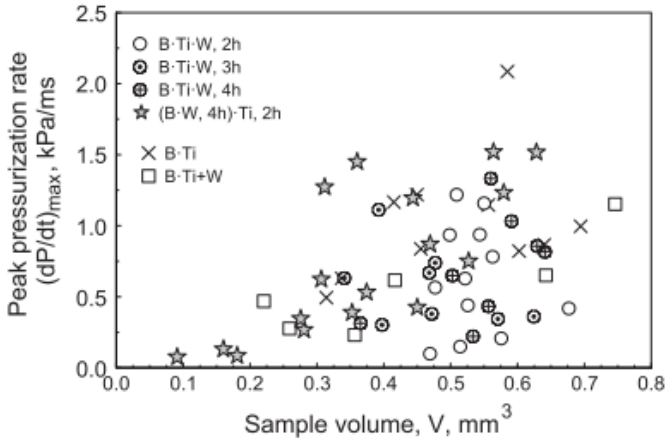

Figure 2.10 Maximum rate of pressure increase (dP/dt) in constant-volume combustion tests.

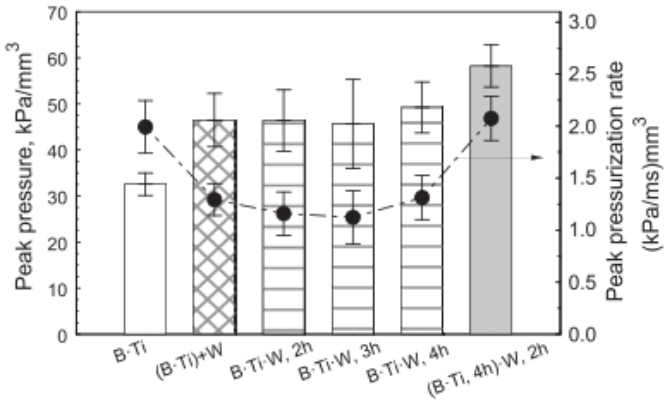

Figure 2.11 Summary of constant-volume combustion tests.

In order to meaningfully interpret the results shown in **Figure 2.9** and **Figure 2.10**, linear regression was performed for each material to obtain a value for the peak pressure generated per reference volume combusted. The pressures calculated by NASA CEA code shown in **Figure 2.9** are not strictly linear functions of the sample volume. However, the scatter in the measured data far exceeds the nonlinearity in the theoretical curve so that a linear fit for the pressure vs. sample volume was considered adequate for interpreting experimental data. The intercept value for the regression (that is, the pressure for zero amount of sample) was constrained to zero in the calculation. The peak pressurization rate

generated by a reference volume was obtained in an analogous way. These reduced results are shown in **Figure 2.11**.

This summary shows that the least pressure per reference volume is generated by the binary component B·Ti composite. All ternary composites prepared using the single-stage protocol, as well as the reference blend of tungsten and the binary B·Ti composite are virtually indistinguishable within their respective error bars. The peak pressure generated by the material prepared by the two-stage protocol is larger than all other values. The peak pressurization rate is high for the binary B·Ti composite. It is significantly lower for all single-stage ternary composites and the reference blend. The ternary composite prepared by the two-stage protocol shows a peak pressurization rate exceeding that of the binary composite and even slightly higher than that of the binary B·Ti powder.

2.4 Discussion

The heat flow data shown in **Figure 2.5**, and summarized in **Figure 2.6**, demonstrate that while binary B·W composites are mildly energetic in their own right due to the formation of B·W intermetallics, the bulk of the energy release from intermetallic reactions in the ternary composite is due to the boron-titanium reaction. The degree to which this intermetallic reaction enthalpy can be recovered to assist ignition depends on the material structure tuned using the milling protocol. The ideal structure would include fine inclusions of tungsten embedded into a nanocomposite of boron and titanium. The finer the scale of mixing, the more rapid reaction is expected. Presence of any borides (reacted phases) is undesirable, although a reduction in the overall combustion enthalpy may be relatively small if a fraction of the composite has reacted during milling. Structures with boron fully

embedded in tungsten or vice versa are also undesirable, because boron-titanium reaction may not occur while the material is being thermally initiated.

The material prepared using the single-stage protocol shows predictable behavior. At shorter milling times of less than 2 h, the composite is relatively coarse, diffusion distances are large, and the reaction is slow enough to not proceed to completion on the time scale of minutes used in thermal analysis. At milling times longer than 2 h, intermetallic reactions are induced during milling, reducing the enthalpy available to assist ignition. An optimum is observed here near 2 h milling time. Similar optimal conditions are observed for the initial and final stages of the two-stage milling protocol.

Under the respective optimal conditions for the ternary composites (**Figure 2.6**), less energy is recovered from the material prepared using the two-stage protocol compared to the single-stage milling protocol. These optima, however, apply to the specific time scale of the thermal analysis measurements. Ignition of particles with sizes on the order of 10 mm, and in typical combustion applications occur on time scales of milliseconds or less, requiring corresponding short diffusion distances. Maximizing the intermetallic reaction enthalpy on an absolute scale therefore may not be as important as high inclusion refinement in the composite, enabling recovery of intermetallic formation enthalpy on the time scale of ignition processes.

The above reasoning is supported by the combustion results summarized in **Figure 2.11**. All ternary composites prepared using the single-stage protocol, as well as the reference blend of B·Ti·W are indistinguishable on a time scale of less than 100 ms (**Figure 2.8**). Conversely, the ternary composite prepared using the two-stage protocol releases more combustion enthalpy and the energy release occurs faster compared to any other

material in **Figure 2.11**. This suggests that the degree of refinement in the composite is greater in the two-stage material, and therefore the recovery of the intermetallic reaction is effective on the time scale of this test.

It is reasonable to speculate that the better refinement is achieved by the effectively much longer cumulative milling time, 6 h for the two-stage material compared to 2-4 h for the single stage material. On the other hand, the thermoanalytical measurements (**Figure 2.5** and **Figure 2.6**) suggest that comparable milling times for the single-stage material would have resulted in near complete formation of the intermetallic compounds during milling, and removed any advantage they could provide for ignition. Therefore, the main advantage of the two-stage milling protocol is that it enables greater structural refinement of ternary B·Ti·W composites with limited sacrifices of intermetallic reaction enthalpy.

The pressures recovered from the combustion experiment are only fractions of calculated adiabatic pressures (see **Figure 2.9**). Given that this fraction is not drastically different between binary B·Ti and ternary B·Ti·W composites, and that binary B·Ti composites combust readily [25, 28, 244, 246-249], the major cause for the lower than calculated pressures are nonadiabatic losses, most likely due to radiation and heat transfer into the brass sample holder. Considering data shown in **Figure 2.11** and accounting for the relatively high reactivity of binary B·Ti composite, it can be concluded that tungsten was participating in combustion in all ternary materials. The results are shown in **Figure 2.11** for pressure per unit volume of the material, so assuming that all B·Ti composite present in the sample reacts to the same completeness, a lower pressure per unit volume would be expected for the ternary materials with the inert tungsten. Instead, all pressures for the ternary composites are higher than for B·Ti suggesting that tungsten is combusting

adding to the energy release by B·Ti. Taking the B·Ti·W blend, and all single-stage milled composites as reference, the increase in pressure is greater for the two-stage composite. This suggests combustion of a larger fraction of the contained tungsten in the two-stage composite, which contributes to the heat release in the ms time scale.

Regarding the constant-volume combustion test used here, the peak pressures shown in **Figure 2.9** as well as the peak pressurization rates shown in **Figure 2.10** exhibit substantial scatter. The greatest cause of experimental error in these measurements comes from uncertainties of the amount of material actually combusted. The tungsten bearing composites are heavy, and despite efforts to avoid any packing during sample placement, the amount of material actually aerosolized, and therefore effectively combusting, is not well known. A plot combining **Figure 2.9** and **Figure 2.10**, shown in **Figure 2.12**, eliminates this source of uncertainty. Here, the peak pressurization rate is directly related to the peak pressure, bypassing any uncertainty in the material amount. This plot shows substantially less scatter than **Figure 2.10**. Further, relations between the materials support the rate data shown in **Figure 2.11**: the trends for the peak pressurization rates of the binary B·Ti and two-stage ternary B·Ti·W composites are both above the trends for all other ternary composites, which are virtually indistinguishable.

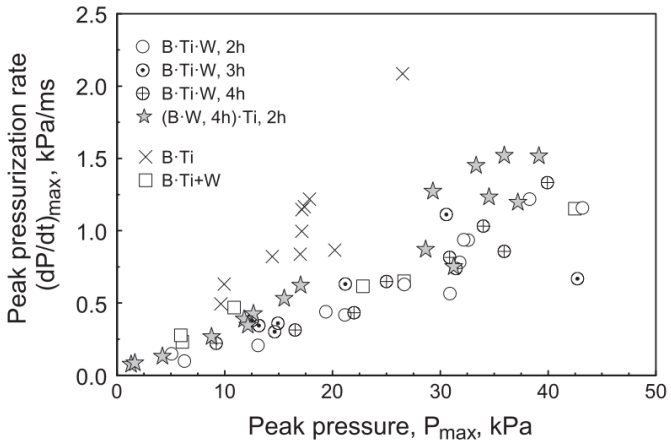

Figure 2.12 Maximum rate of pressure change vs. peak pressure, compensating for sample mass uncertainties

2.5 Conclusions

Ternary B·Ti·W composites were prepared by mechanical milling with the powder density matching that of steel. The milling protocol was varied and optimized to exploit intermetallic formation reactions to readily ignite and completely burn the prepared powders. The milling protocol consists of two stages: boron and tungsten are combined in an initial stage, while titanium is added in a second stage. The two-stage milling improves the scale of mixing while minimizing formation of borides in the prepared composites. Boron-titanium exothermic reaction releases most heat upon thermal initiation of the prepared materials; boron tungsten reaction is also sufficiently exothermic and needs to be accounted for. Both pressure and rate of pressure rise produced by the ternary material prepared following the optimized protocol and ignited in oxygen by an electric spark exceed those produced by reference materials with nominally the same composition but having different structures stemming from different preparation protocols. Tungsten combustion occurs for all prepared ternary materials. The optimized structure of the ternary nanocomposite materials prepared by two-stage milling enables tungsten contained in the powder to combust most effectively in millisecond time scales.

CHAPTER 3

ZIRCONIUM-BORON REACTIVE COMPOSITE POWDERS PREPARED BY ARRESTED REACTIVE MILLING

3.1 Introduction

Exothermic reactions accompanying formation of intermetallic or metal-metalloid compounds are often exploited for brazing [259] and in various munition components, e.g., penetrators [260], reactive liners [261], and weapons casings [262]. These reactions may also be used in illumination flares [263] and propellants [264]. Compounds typically formed in such reactions include borides, carbides, silicides, and aluminides [265]. Starting components can be mixed elemental powders, nanopowders, or prepared as differently structured nanocomposite materials [150]). It was shown that both sensitivity to initiation [266] and completeness of the ensuing reactions [25] can be substantially improved when reactive components are mixed on the nanoscale. Using fully-dense composite powders prepared by Arrested Reactive Milling (ARM) [267] combines the reactivity of nanocomposite reactive materials with the ease of handling associated with conventional micron scale powders. Among various reactive materials, ARM was used to prepare reactive composites combining boron and titanium [25, 28, 268]. These composites were ignited readily and burned rapidly and completely in different oxidizing media. A chemically similar system involving boron and zirconium has not been explored to date using similar experimental approaches. It was estimated to have a very high adiabatic flame temperature (3763 K) and high energy density [38]. Boron-zirconium composites also have a higher density than similar boron-titanium powders, making them more attractive in selected applications favoring high-density reactive materials, e.g., in reactive kinetic

penetrators. This study is aimed to prepare boron-zirconium composite powders by ARM and characterize their ignition and combustion behavior.

3.2 Adiabatic Flame Temperatures and Equilibrium Combustion Products for B-Zr Composites

Adiabatic flame temperatures and equilibrium combustion products predicted using NASA CEA code [257] are presented in **Figure 3.1**. These data are helpful when interpreting experimental results discussed below.

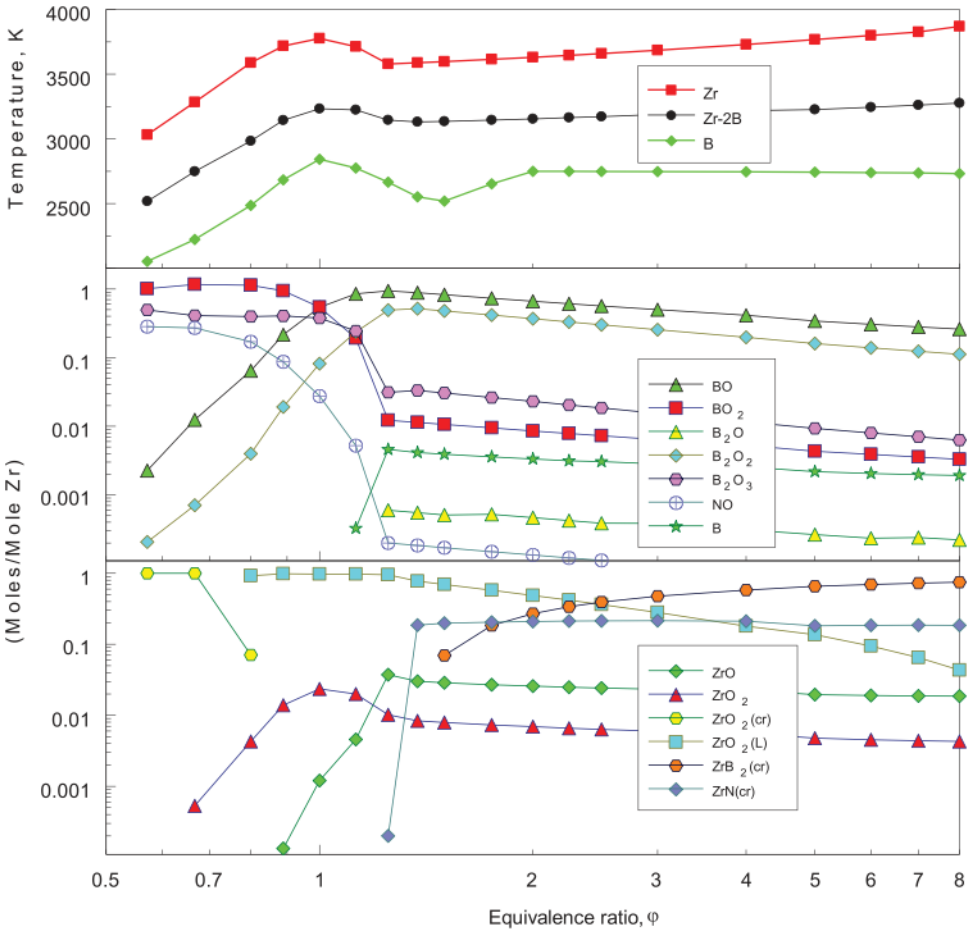

Figure 3.1 Predicted adiabatic flame temperature and main products formed for B·Zr composite burning in air at different equivalence ratios. Adiabatic flame temperatures for elemental B and Zr are also included for reference.

Calculations considered a mixture of elemental boron and zirconium (taken at a mole ratio of 2:1) exposed to air at different equivalence ratios, φ. Adiabatic flame temperatures are also shown for individual elemental boron and zirconium exposed to air with φ varied in the same range, while the products are only shown for the composite material. The predicted flame temperature for the composite generally is between those predicted for pure Zr and B.

It is expected that very fuel-rich conditions ($\varphi \gg 1$) exist at the surface of burning composite particles, while the equivalence ratio decreases with distance from the particle surface. Data describing ZrB_2 were taken from NIST Chemistry website [37] and included in the CEA database. The combustion products are shown in two plots, separating species containing oxidized boron and zirconium.

A local maximum reaction temperature of 3233 K is predicted for the composite material at $\varphi = 1$. The main products at that point are BO, BO_2, B_2O_3, and ZrO_2(L). Similarly, maxima in the adiabatic flame temperature at $\varphi = 1$ are observed for both B and Zr. At $\varphi > 1$, the adiabatic temperature for the composite first decreases as amounts of BO and B_2O_2 in the products increase, while amounts of BO_2 and B_2O_3 diminish. At continuously increasing values of φ, the adiabatic flame temperature increases again, primarily due to the preferential formation of ZrB_2 and because of formation of ZrN. Formation of ZrN also causes an increase in the adiabatic flame temperature for pure Zr at large equivalence ratios.

3.3 Material Preparation

Composite powders were prepared using high-energy ball milling of elemental boron and zirconium powders. Starting components were -325 mesh, nominally 95% pure boron (SB95 by SB Boron) and 2–3 μm zirconium (product 00847 by Alfa Aesar) powders. The powders were blended in a 2:1 mole ratio to yield a stoichiometric ZrB_2 with the reported heat of formation of 3.61 kJ/g or 14.06 kJ/cm^3 [38, 269]. A Spex Certiprep 8000 shaker mill was used with 65-ml hardened steel vials and 9.525-mm (3/8") diameter hardened steel balls. The powder mass loaded in each vial was 5 g, and the ball to powder mass ratio was 7. The milling vials were loaded and unloaded in an argon-filled glovebox. Hexane was used as a process control agent (PCA); 10 ml of hexane was added in each milling vial. Using liquid PCA prevented self-sustaining reaction from occurring during milling even if a fraction of the powder began reacting to form zirconium boride. Different milling times were used to prepare different powder batches. The milling times used were 0.5, 1, 2, and 3 hours.

3.4 Characterization of the Prepared Composites

Prepared samples were characterized by powder x-ray diffraction (XRD) using a PANalytical Empyrean x-ray diffractometer operated at 45 kV and 40 mA using unfiltered Cu Kα radiation (λ = 1.5438 Å) and scanning electron microscopy (SEM) using a LEO 1530 field emission SEM. Both as-milled powder samples and cross-sections of powder embedded in epoxy were examined using the SEM. Particle size distributions were measured first using a Malvern Panalytical Mastersizer 3000 with the hydro MV sampling unit. Powders were dispersed in ethylene glycol. In combustion experiments (discussed in more details further), powders were fed by a customized feeder delivering them either into

a focal point of a CO_2 laser beam or in the air-acetylene flame, where the powders were ignited. Because agglomeration and particle size-dependent settling could occur prior to ignition of the powders, separate measurements of the particle size distribution were made using particles collected after passing through the feeder. The powders were collected on a flat substrate coated with a double sided, conductive adhesive tape and examined using SEM. Images of the collected particles were taken at different magnifications and processed to obtain the particle size distributions following the method discussed in more detail elsewhere [270]. The particle size distributions obtained this way could be directly correlated with the measured distributions of the particle burn times, as discussed below.

Thermo-analytical measurements, including differential scanning calorimetry (DSC) and thermo-gravimetry (TG) were performed with selected samples of the prepared powders using a Netzsch Thermal Analyzer STA409PG. The samples were heated to 1273 K (1000°C) at 5 K/min in a flow of argon (99.998% pure by Airgas, flown at 50 mL/min). For each experiment, the heating program was repeated without removing the sample; the traces recorded during the second heating served as baselines. Some of the samples were recovered after the first heating and inspected using XRD.

3.5 Ignition and Combustion Experiments

Ignition of the prepared powders was characterized using an experimental setup employing an electrically heated filament. Following multiple previous studies, e.g., [171, 271, 272], a thin layer of the powder was coated onto a nickel-chromium filament (0.5 mm diameter). To prepare the coating, the powder was suspended in hexane and the suspension was deposited onto the filament using a small paintbrush. The hexane was allowed to dry prior to the ignition experiment. Only a 10-mm long portion of a 4.67 cm long filament was

coated. The filament was then heated using one or three 12-V (Kinetik HC600-Blue) batteries connected in series, resulting in the respective heating rates of approximately 2,000 or 20,000 K/s. The filament temperature was monitored in real time using an optical pyrometer comprising a germanium switchable gain detector (PDA30B2 by Thorlabs). The light to the detector came through a fiber optics cable equipped with a lens focused on an uncoated section of the wire. The pyrometer was calibrated using a black body (BB-4A by Omega Engineering). The pyrometer signal was recorded using a Rigol DS1054Z oscilloscope at rates above 1 kHz. The experiment was recorded at 500 frames per second using a high-speed camera, MotionPro 500 by Redlake. The recorded video was used to identify the instant of the powder ignition and thus determine the corresponding filament temperature. The camera is primarily sensitive in the visible light range with no significant sensitivity in the IR.

Combustion of the prepared powders was studied in air and in a heated flow of mixed CO_2 and H_2O generated by a fuel-lean, premixed air-acetylene flame. In both experiments, a customized powder feeder capable of feed rates in the range of 1 mg/min was used. Powders exiting the feeder moved vertically in a flow of a carrier gas. In air, particles were ignited by passing through a beam of a CO_2 laser (Synrad Evolution 125). Air served as a carrier gas. The laser operated at 50% of its maximum power ensuring reliable ignition of particles crossing the beam focused to about 250 μm diameter. Particles igniting in the combustion products of the hydrocarbon flame were injected coaxially at the flame's center. Nitrogen served as a carrier gas in those experiments. The flowrates of air, acetylene, and nitrogen were 6.5, 0.475, and 2.25 l/min, respectively (φflame = 0.53). Details of both experiments are available elsewhere [270, 273, 274]. In all combustion

tests, particle emission was monitored using two Hamamatsu R3896-03 photomultiplier tubes (PMT) equipped with interference filters at 700 and 800 nm. Each burning particle produced an emission pulse. Durations of such pulses were measured. Once overlapping pulses were removed from the collected data set, the distributions of the measured pulse durations was correlated with the measured particle size distribution for the powders passed through the feeder. Such correlations were interpreted as trends showing the effect of particle size on its burn time. Additionally, ratio of the optical signals measured at different wavelengths was used to evaluate the color temperature of the burning particles. For this processing, the particles were assumed to behave as gray body emitters. Preliminarily, the outputs of the filtered PMTs were calibrated using a tungsten lamp as a light source. The lamp's filament was heated to different temperatures in the range of 2000–2900 K, using an adjustable DC power supply and its temperature was measured using an externally calibrated BLACK-Comet StellarNet spectrometer serving as a standard.

3.6 Results and Discussion

3.6.1 Characteristics of the Prepared Materials

XRD patterns for different composite powders are shown in **Figure 3.2**. Only Zr peaks are seen in the composites milled less than 2 hours. It is not unexpected because SB95 boron is mostly amorphous. The amplitude of Zr peaks progressively diminishes with the milling time. For the sample milled for 3 hours, only very weak signatures of the strongest Zr peaks can still be distinguished. For samples milled for 2 and 3 hours, an additional peak at about $2\Theta \approx 44°$ is observed. This peak could not be unambiguously assigned, but could be an indication of iron contamination by the milling tools, or forming zirconium oxides or oxyborides.

Patterns shown in **Figure 3.2** were processed to roughly evaluate the crystallite size and lattice strain in zirconium. It was observed that within the first hour of milling, the nominal crystallite size decreases down to ca. 0.15 μm; it stabilizes at longer milling times. The lattice strain increases continuously with the milling time.

SEM images of the prepared powders and their cross-sections are shown in **Figure 3.3** and **Figure 3.4**, respectively. The sample milled for 30 min appeared poorly mixed containing multiple individual Zr and B particles. It was not examined in further experiments. Boron and zirconium appear to be mixed on the scale of about 1 μm in roughly equiaxial particles formed in the sample milled for 1 hour, as seen in **Figure 3.3** (top). The images taken using backscattered electrons show a clear compositional contrast between bright zirconium and dark boron parts of the composite. The mixing appears to become finer for the sample milled for 2 hours (**Figure 3.3**, center). Images of the sample milled for 3 hours (**Figure 3.3**, bottom) do not show a distinct compositional contrast between boron and zirconium. This suggests that the scale of mixing was reduced to become smaller than the resolution of these images. A large number of fine particles is also apparent in that sample.

A better assessment of mixing between boron and zirconium can be obtained observing cross sectioned composite particles, as shown in **Figure 3.4**. In each image, a fraction of a particle cross section is shown. As in **Figure 3.3** Backscattered electron SEM images of prepared composite powders milled for 1 h (top), 2 h (center), and 3 h (bottom)., images are taken with backscattered electrons highlighting the contrast between bright zirconium matrix and darker boron inclusions.

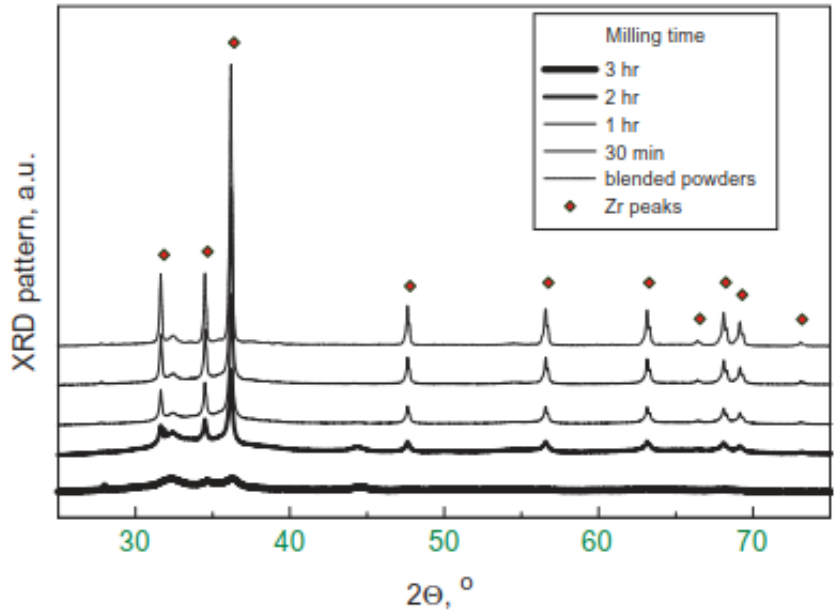

Figure 3.2 XRD patterns of the prepared composite powders as well as of the blended powder of the starting components.

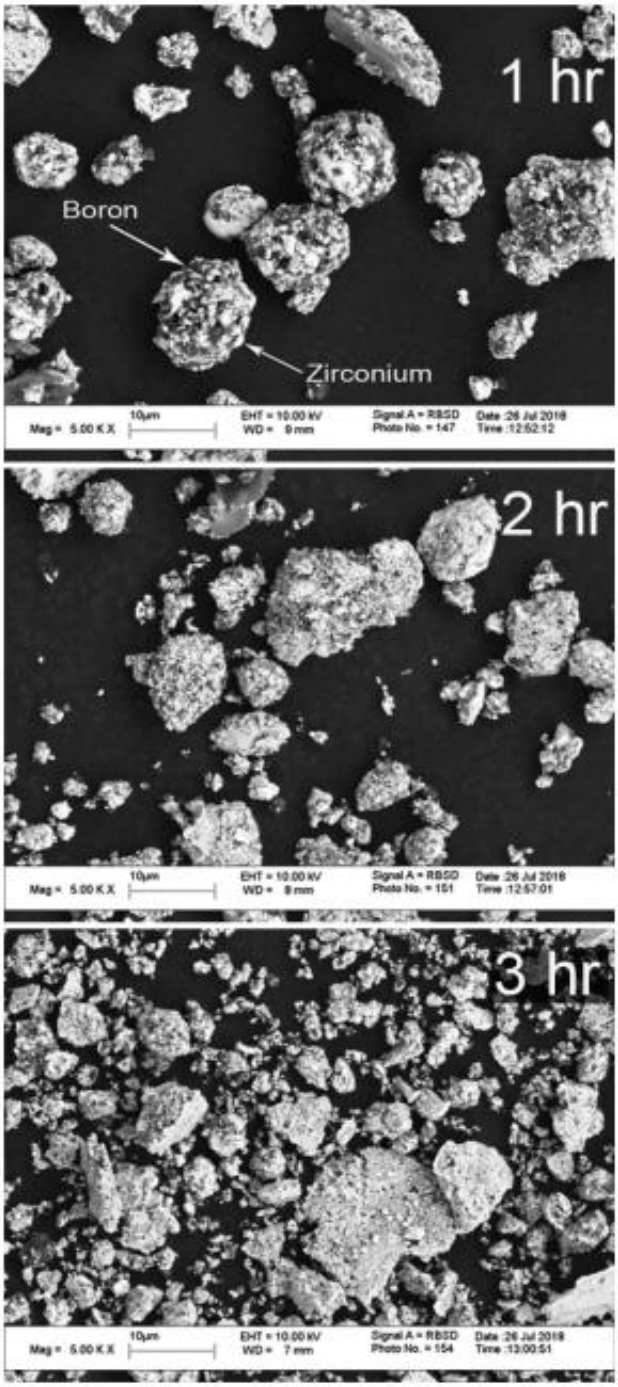

Figure 3.3 Backscattered electron SEM images of prepared composite powders milled for 1 h (top), 2 h (center), and 3 h (bottom).

Qualitatively, all three images shown in **Figure 3.4** look similar to each other. Each cross-section shows dark boron inclusions, ranging in size from 100 nm to almost 1 µm embedded rather uniformly in a zirconium matrix. The boron inclusions appear to have the

same sizes in all three cross-sections shown. A few micron-sized zirconium areas that contain no embedded boron are seen for the particles milled for 1 and 2 hours.

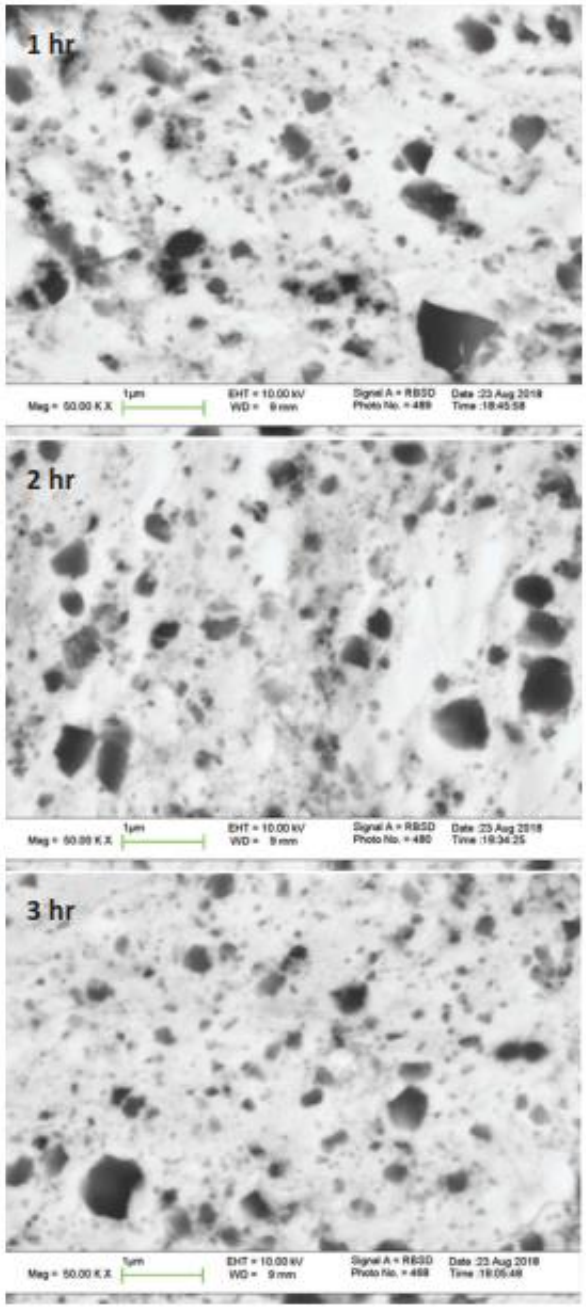

Figure 3.4 Backscattered electron SEM images of prepared composite powders milled for 1 h (top), 2 h (center), and 3 h (bottom). The particles are embedded in epoxy and cross-sectioned. Each image shows a portion of a typical cross-sectioned particle.

To evaluate the quality of mixing between components more quantitatively, such images as shown in **Figure 3.4** were processed using Fiji software [275]. Fifty cross sectional images were processed for each material. Processing included recursive median filtering, application of an unsharp mask and thresholding to produce a binary image. This binary image was processed to obtain Feret's diameter for all B inclusions. Further, a chamfer distance transform [276] was applied to the pixels representing the Zr matrix. This produced an image where the brightness of any matrix pixel corresponds to its distance to the nearest interface with B. A histogram of the brightness values therefore shows a distribution of separation distances between Zr and B. Lower distance values are taken as a measure of finer mixing of the components. A narrower distribution indicates more homogeneous mixing. This is shown in **Figure 3.5**. Corresponding B inclusion sizes are shown in **Figure 3.6**. There is a systematic reduction in distance between zirconium and boron inclusions as the milling time increases from 1 to 2 hours (**Figure 3.5**). This indicates an improvement in homogeneity of boron/zirconium mixing. In other words, boron inclusions become dispersed more uniformly. A further increase in the milling time results only a slight change in that distance, suggesting that the materials milled for 2 and 3 hours are nearly identical, in terms of mixing homogeneity between components. Boron inclusion sizes are effectively the same for all three samples (**Figure 3.6**). More than 90% of all boron inclusions have dimensions smaller than 0.1 μm.

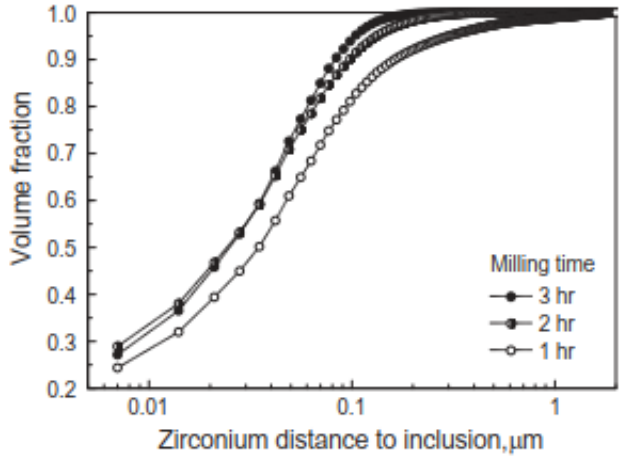

Figure 3.5 Distribution of distances from zirconium matrix to boron inclusions in composite materials prepared using different milling times.

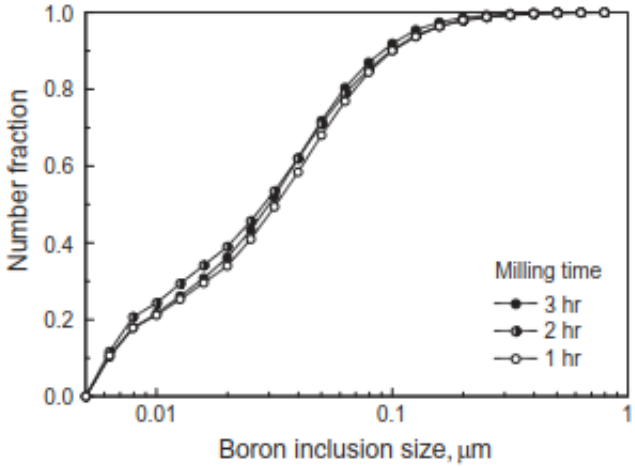

Figure 3.6 Size distributions of boron inclusions embedded in zirconium for composite materials prepared using different milling times.

Size distributions measured using low-angle light scattering for the composite powders suspended in ethylene glycol are shown in **Figure 3.7**. For each histogram, a dashed vertical line and associated label show an average particle size. Despite some difference in the average particle size, the size distributions are very similar to each other for the powders prepared using 1- and 2-hr milling. The particles are finer for the powder prepared using 3-hr milling. This is consistent with the qualitative observation made from **Figure 3.3** where multiple fine particles are observed for the latter sample.

The powder particle size distributions for the same powders carried from the customized feeder to the laser beam and to the flame are shown in **Figure 3.8**. The peaks of the size distributions clearly shifted compared to the sizes shown in **Figure 3.7**. Coarser average particle sizes for the powders passed through the feeder suggest that some of the particles agglomerated, or that finer particles were not effectively collected. Alternatively, the agglomerates could have been present in as prepared powders; such agglomerates could have been broken apart when the powders were suspended in ethylene glycol and subjected to ultrasonic excitation to obtain results shown in **Figure 3.7**, but they could pass through the feeder unaltered. If agglomerated particles are exposed to an ignition heat sources, such as laser beam or flame, they are expected to coalesce forming burning particles with dimensions close to those of the as fed agglomerates. Therefore, the particle size distributions shown in **Figure 3.8** were used to interpret the measured particle burn times. For all three powders prepared using different milling times, the particle size distributions are similar to one another when the powders were fed into the laser beam. For the powder fed into the burner, when nitrogen instead of air served as carrier gas and flowrates were slightly different, the particle size distribution shifted to smaller sizes, while still showing a noticeable change in the particle sizes compared to **Figure 3.7**.

For all particle size distributions shown in **Figure 3.8**, lognormal fit functions were obtained, as shown by solid lines in each plot. These lognormal functions were used to correlate the measured burn times with particle sizes. In such correlations, longer burn times are assigned to larger particles. Using lognormal functions rather than directly measured particle size distribution enables one to focus the interpretations on the particle sizes and, respectively, burn times that are most common in the present data sets. This

minimizes the errors that can occur if unwarranted significance is given to the tails of the measured particle size or burn time distributions. Such errors are expected, in particular, if the shapes of the measured distributions of particle sizes and their burn times are not similar to each other. For example, log-normal distributions shown in **Figure 3.8** under-represent super-fine particles, appearing in the measured histograms.

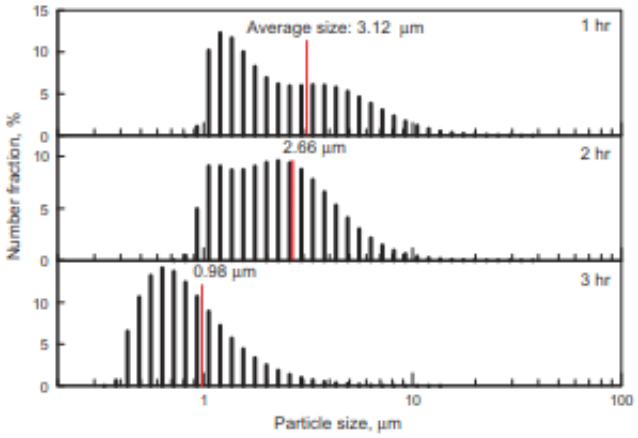

Figure 3.7 Size distributions of composite powder particles suspended in ethylene glycol measured by low-angle laser light scattering.

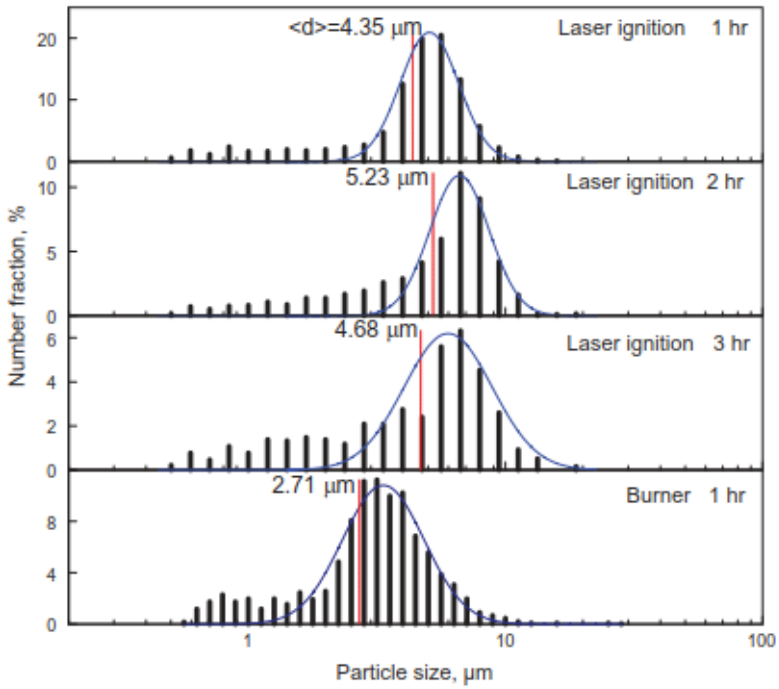

Figure 3.8 Size distributions composite powder particles fed by air to the laser beam and fed by nitrogen to the flame. The powders were collected at the exit from the feeder and examined using SEM.

However, as discussed later, the measured distributions of burn times are more similar in shape to log-normal functions and do not show "tails" for shorter burn times, that would be expected for such superfine particles. The most likely explanation for that is that the emission from burning super-fine particles is weaker than the optical detection threshold. This reasoning supports using the lognormal distribution fits rather than the directly measured histograms in this work.

DSC and TG traces for composites prepared using different milling times are shown in **Figure 3.9**. Traces are shifted vertically relative to one another for clarity. DSC traces show multiple, relatively broad exothermic features. The onset of an exothermic reaction occurs at a very low temperature, around 400 K; it is accompanied with a mass loss. The mass loss of less than 1% could be primarily due to removal of adsorbed hexane from the powder preparation. Exothermic events occurring just above 500 and under 700 K are

common for all three samples. The amplitude of the first event diminishes while the second one becomes stronger as milling time increases. A relatively sharp exothermic peak above 800 K (527°C) is only observed for the sample milled for 1 hr (bottom DSC curve). There is a broad endothermic feature observed for all samples above ca. 900 K. It is accompanied by a minor mass loss of about 0.33%, also for all samples. At higher temperatures, a broad exotherm is observed for all materials around 1000 K. As seen in **Figure 3.9**, exothermic features are overlapping with one another, making it difficult to separate them and identify the appropriate baseline. Because of these difficulties, integrals of the measured DSC signals are not reported.

One of the heated samples was quenched and examined by XRD. The results are shown in **Figure 3.10**. Comparing the pattern in **Figure 3.10** with that for as prepared material (**Figure 3.2**) it is noted that all original peaks of Zr disappeared; instead, multiple peaks are observed indicating formation of Zr_2B and ZrO_2. The latter phase is likely formed when zirconium fully or partially reduces boron oxide. The starting boron is specified as 95% pure; thus the most conservative estimate suggests that up to 5% of its mass is boron oxide or boric acid. This amount will clearly depend on the purity of boron used.

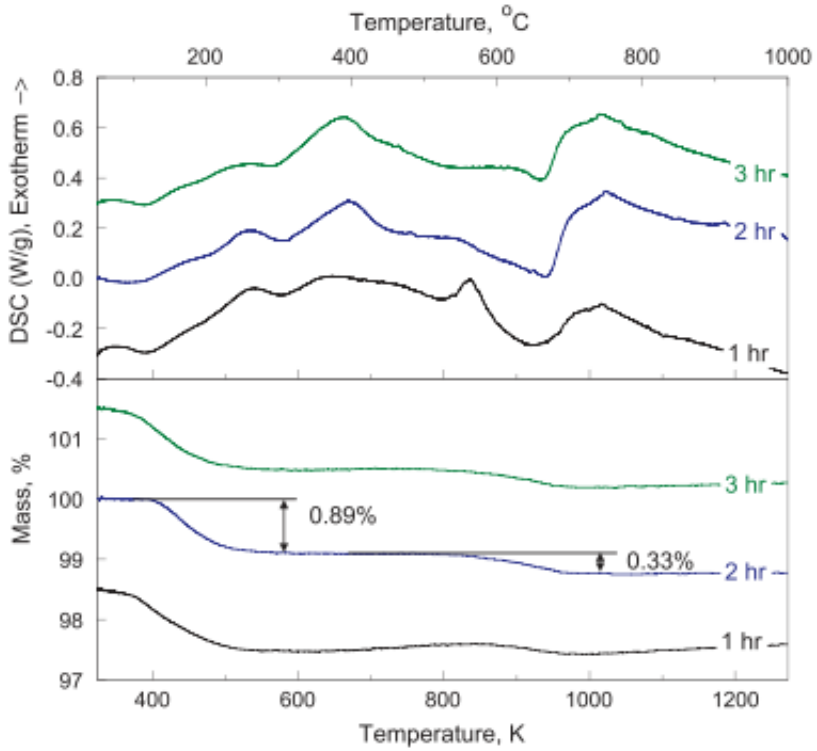

Figure 3.9 DSC and TG traces for the prepared composite powders heated in argon at 5 K/min.

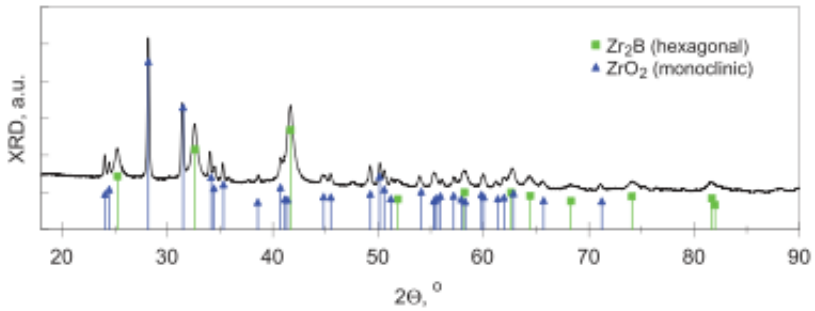

Figure 3.10 An XRD pattern for a composite material sample milled during 2 hours and heated in DSC up to 1273 K.

3.6.2 Ignition of Composite Powders

A sequence of video frames illustrating an ignition event is shown in **Figure 3.11**. The frames are cropped to focus on the igniting powder. Each image is labeled with the time elapsed from the instant the filament heating started. Qualitatively, all ignition experiments appeared similar to one another. The powder coating becomes luminous (see 122 ms frame in **Figure 3.11**) well before the filament itself. Following the initial luminosity, bright,

ignited powder particles are ejected from the wire and burn near its surface. Later on, as shown in the 238 ms frame, the filament becomes luminous while the leftover of the initial powder remaining on the filament surface continues to smolder.

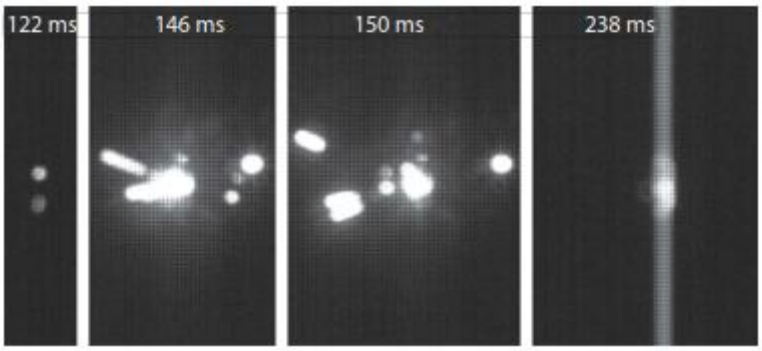

Figure 3.11 Sequence of high-speed video frames illustrating ignition of a composite material on an electrically heated filament. The heating rate is ca. 2000 K/s; material is milled for 2 hours.

Ignition temperatures defined at the instant the powder coating became luminous are plotted as a function of the heating rate for different materials in **Figure 3.12**. Note that the measured ignition temperatures are for powders coated on the heated filament. Thus, particle size distributions of the powders tested as well as the filament diameter affect the heat balance and resulting ignition temperature. Despite these effects, the measurements can be used to compare behaviors of different powders, especially for the powders with relatively similar particle size distributions as in the present study. In addition to the three composite powders prepared by milling for 1, 2, and 3 hours, experimental results for the starting zirconium powder are also shown. For all materials, the ignition temperature increases with the heating rate. However, the ignition temperatures are essentially the same for all materials, including reference zirconium. This suggests that the zirconium oxidation with surrounding air, and not any reaction between zirconium and boron, is the process driving ignition for these powders heated in an oxidizing environment. Considering that only part of zirconium is exposed to air in the composite powders, it can be concluded that

oxidation of only a small fraction of zirconium is sufficiently exothermic to cause the thermal runaway and ignition. The reactions detected in DSC (**Figure 3.9**) and likely associated with the formation of zirconium boride phases might be assisting ignition; they could become more significant if these composite powders are heated in an inert environment.

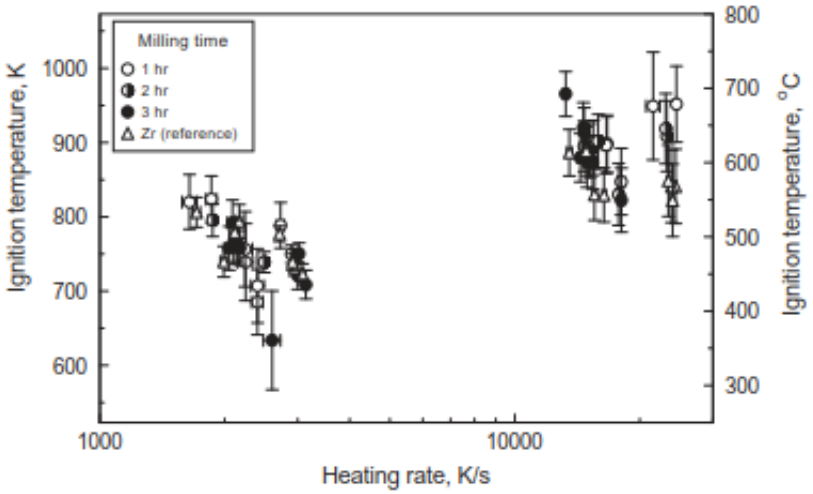

Figure 3.12 Ignition temperatures as a function of heating rate for the powder samples coated on an electrically heated filament.

3.6.3 Combustion of Composite Powders

Bulk Powder

Composite powders prepared using different milling times an.d a reference blend of starting component powders were burned in air by laying a 45 × 5 mm elongated pile of powder onto a flat ceramic block and initiating the powder by an electrically heated tungsten filament. Roughly, half of the powder burned and another half remained on the ceramic block following ignition. The optical emission from the burning powder was monitored using a BLACK-Comet Stellarnet Spectrometer with a field of view covering the entire burning sample. Spectra were taken every 50 ms; the integration time was 30 ms for each spectrum. Examples of three of such subsequently recorded spectra are shown in

Figure 3.13. A characteristic emission pattern of BO_2 is clearly observed between ca. 450 and 650 nm. Additional peaks produced by common sodium and potassium contaminations [277] are also clearly visible. An additional molecular emission peak has also been observed but not positively identified in the range of 345–380 nm. It is speculated that this peak could be produced by FeOH having several molecular emission bands in this range, and which could be a product formed from iron contaminants introduced during milling.

Portions of the spectra including 700–755 and 790–845 nm ranges, which were free of molecular or atomic emission signatures were selected for temperature measurements. Assuming that the emitters behave as gray bodies, these portions of spectra were fitted using Planck's formula, treating the temperature as an adjustable parameter. Note that overall signal intensity may not necessarily scale with temperature, and may be affected by the number of particles burning during the specific acquisition time. For example, in **Figure 3.13**, the spectrum acquired last (after a 150 ms delay) has a generally stronger emission, but represents a lower temperature compared to the spectrum acquired after a 100 ms delay.

Average measured temperatures and their standard deviations, shown as error bars are plotted in **Figure 3.14**. The reaction temperatures are comparatively high for the samples prepared using 0.5 and 1-hr milling times. For these samples, the measured flame temperatures are quite close to the previously calculated adiabatic flame temperatures (**Figure 3.1**) for Z-Br composites.

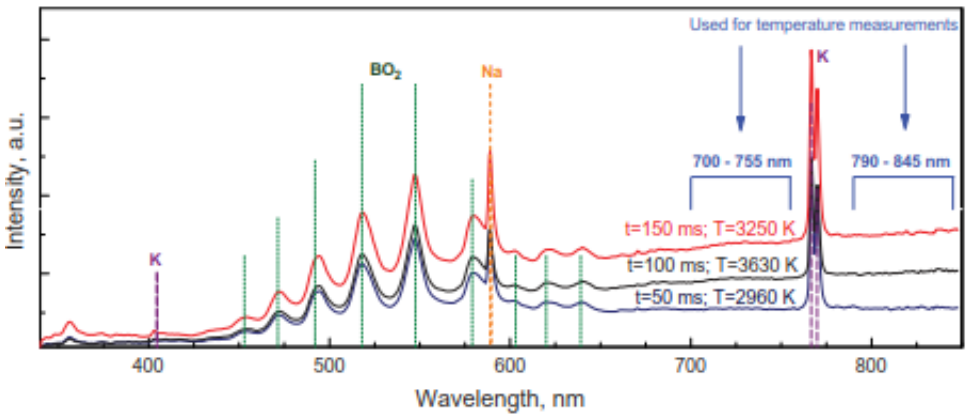

Figure 3.13 Characteristic optical emission spectra recorded for the composite powder burning in air. The powder was prepared using 1-hr milling time. A wavelength range used for Planck's emission fitting is marked.
Source: [277, 278]

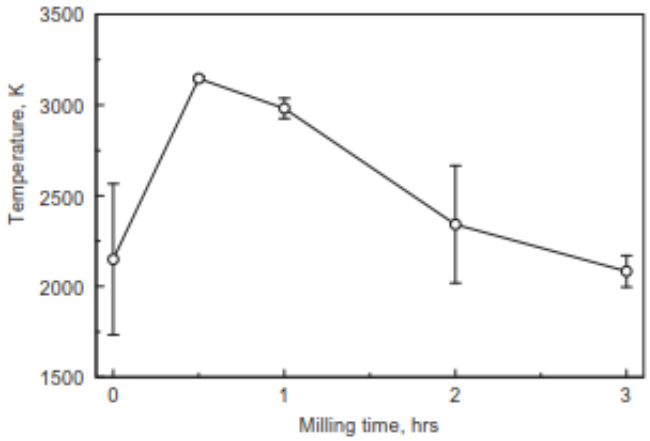

Figure 3.14 Average temperatures of combustion recovered from optical emission spectra for bulk composite powders prepared using different milling times and burning in air.

At longer milling times, reduced flame temperatures are observed. This suggests that a more homogeneous mixing achieved in composites milled longer than 1 hr, implied by results shown in **Figure 3.5**, is accompanied by some partial Zr-B reaction, which slows down the burn rate of bulk powders, and thus leads to a reduced flame temperature. Most directly, partially reacted boron and zirconium form a boride phase, which is harder to ignite in air than individual elemental components of the composite. A delayed ignition leads to slower flame propagation through the sample in contact with the heated tungsten

filament. During the slower bulk reaction, the effect of heat losses increases, leading to a reduced measured temperature. A partial reaction can also be inferred from the DSC measurements shown in **Figure 3.9**, where the intensity of the first exothermic peak diminishes for samples prepared with longer milling times.

Individual Particles

Durations of emission pulses produced by particles ignited after crossing a focused CO_2 laser beam interpreted as burn times were measured. Using data recorded by the PMT filtered at 700 nm, the pulse duration distributions for different composite powder samples are shown in **Figure 3.15**. The average burn times are shown using a dashed vertical line for each powder and labeled in the plots. All burn times are short. No clear difference between the burn times for powders prepared using different milling times is visible. As for particle size distributions, the present data were fit using lognormal functions, which are also shown in **Figure 3.15**. Although these materials have very similar distributions of the burn times, the emission brightness for the powder milled during 1 hour was greater than those for powders milled during 2 and 3 hours. The average emission pulse amplitude for the 1-hour sample was nearly 20% higher than those for the 2 and 3-hour milled samples.

Durations of the emission pulses produced by different material particles burning in the combustion products of an air-acetylene flame are shown in **Figure 3.16**. As for results in **Figure 3.15**, emission recorded by the PMT filtered at 700 nm was used. In addition to the three composite powders, experiments were performed with starting zirconium; respective results are also shown in **Figure 3.15**. The burn times for all powders are substantially longer than those observed in air by laser initiation (cf. **Figure 3.15**). Zirconium particle burn times in the products of the air-acetylene flame are shorter than

the burn times for all composites. For the powders milled for 1 and 2 hours, the burn time distributions are similar to each other, although longer burning particles appear more prominently for the sample milled for 2 hours. Substantially longer burn times are measured for the sample milled for 3 hours.

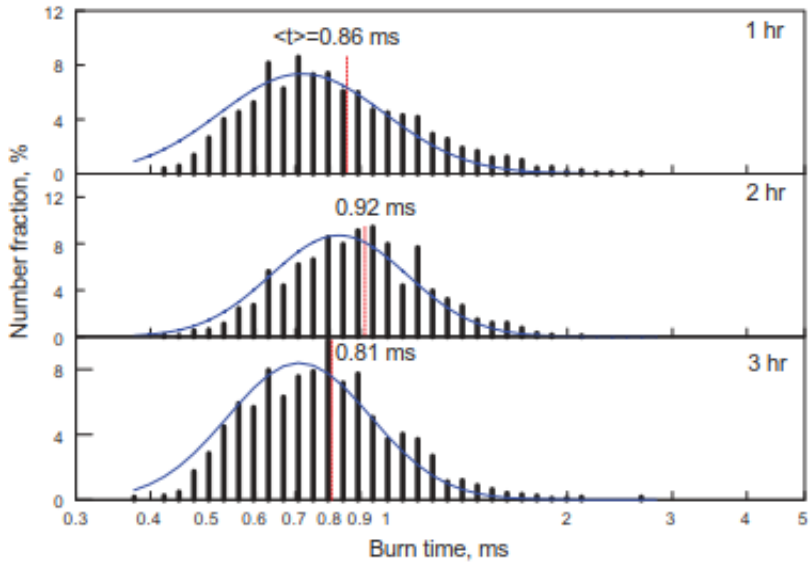

Figure 3.15 Distributions of burn times measured for different composite powder samples ignited in air by passing through a focused CO_2 laser beam.

Correlations of the burn times with particle sizes for composite Zr·2B powders are shown in **Figure 3.17** along with similar correlations for elemental zirconium and boron powders. The data for Zr in **Figure 3.17** come from the current measurements shown in **Figure 3.16**, and from earlier work [274]; the data for boron are from earlier work [270]. For all materials, separate trends are shown for combustion in air and in the products of the air-acetylene flame.

In air, all composite powders burn faster than similarly sized pure zirconium particles and much faster than boron particles. The difference in the burn times between different composite powders is relatively small. These differences can be attributed to changes in the heterogeneous reaction kinetics for the powders with different distributions

of boron inclusions and with somewhat different initial amounts of the partially reacted boron and zirconium. The effect of particle size on burn time is somewhat stronger for the particles milled for 1 hour; it becomes progressively weaker at longer milling times. **Table 3.1** includes parameters for coefficients a and n in the approximate, power-law description of the effect of particle size, d, on its burn time: $t = a \cdot d^n$. For all composite powders burning in air as well as for pure zirconium, the power n is close to 1, suggesting a kinetically limited reaction. This kinetics most likely describes the rate of heterogeneous surface oxidation of zirconium. For boron burning in air, the burn times are much longer. They are described better by a power law with $n \approx 2$. This implies a reaction controlled by the vapor-phase diffusion. In other words, surface oxidation of boron is slow, so that volatile suboxides, such as BO and BO_2 evaporate and continue oxidizing in a stand-off vapor phase flame. Presence of Zr in the composite powders accelerates the surface reaction rate, which makes the vapor phase oxidation of boron suboxides less relevant as rate-controlling processes.

For combustion in the products of an air-acetylene flame, the burn times of all materials except for pure boron are longer than in air. For boron, the effect of environment is more complex, suggesting a transition from a vapor phase diffusion controlled combustion in air ($n \approx 2$) to kinetics-controlled reaction in the products of a hydrocarbon flame ($n \approx 1$). For all composite powders, the burn times are longer than those of pure zirconium. For powders milled during 1 and 2 hours, the burn times are quite close to those of pure boron, while the powder milled for 3 hours burns longer. It is interesting that in this environment, the exponent in the power law increases from 0.7 for the powder milled for 1 hour to 1.4 and 2.2 for powders milled for 2 and 3 hours, respectively. This may suggest

that the effect of heterogeneous oxidation of Zr as a rate-limiting reaction diminishes in this environment at longer milling times. The heterogeneous reactions of Zr with CO_2 and H_2O as primary oxidizers slow down as zirconium is more and more actively reacting with boron in the powders prepared with longer milling times. Thus, presence of Zr noticeably accelerates combustion of only powders milled for 1 hour.

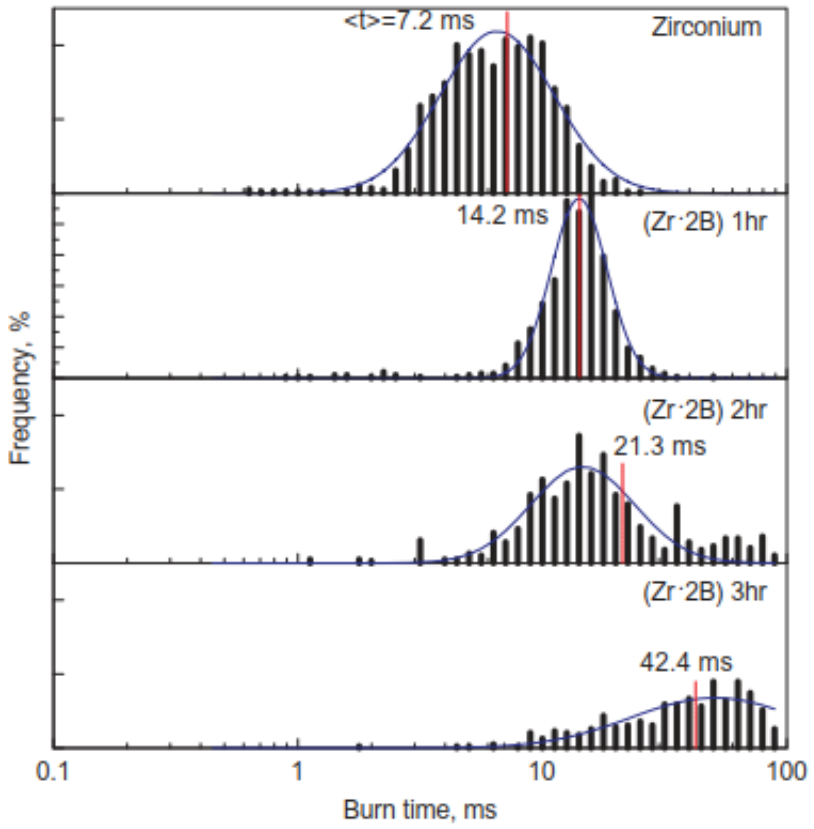

Figure 3.16 Distributions of burn times measured for different composite powder samples ignited in the products of an air-acetylene flame. Burn times for the starting Zr powder are also shown.

For each recorded emission pulse, the temperature as a function of time was determined using the ratio of the emission signals filtered at 700 and 800 nm. To assign one temperature to each particle, the temperatures measured for each pulse were averaged. The value of this average taken during the time, while the emission intensity exceeded 50% of the peak for each pulse was taken as one temperature value characterizing each burning

particle. Statistical distributions of temperatures determined that way for particles burning in air are shown in **Figure 3.18**. The average temperatures are marked by dashed vertical lines and labeled. The temperature distributions are very close to one another for all composite powders. The adiabatic flame temperature calculated using NASA CEA code [257] shown in **Figure 3.1** has a local maximum at 3233 K and can increase at the fuel-rich conditions (considering both boron and zirconium as fuels and oxygen as oxidizer), expected to exist near the surface of the particles burning in air. In the case of extremely fuel-rich situation, when only B-Zr reaction occurs the predicted flame temperature reaches 4138 K (not shown in **Figure 3.1**). The measured temperatures vary in the same general range as predicted by the code, suggesting that near-adiabatic conditions exist for burning particles of all composite materials. This is different from the situation observed for combustion of bulk powders (**Figure 3.14**), where oxygen transport to and heat losses from the entire burning powder pile affect the measured temperature.

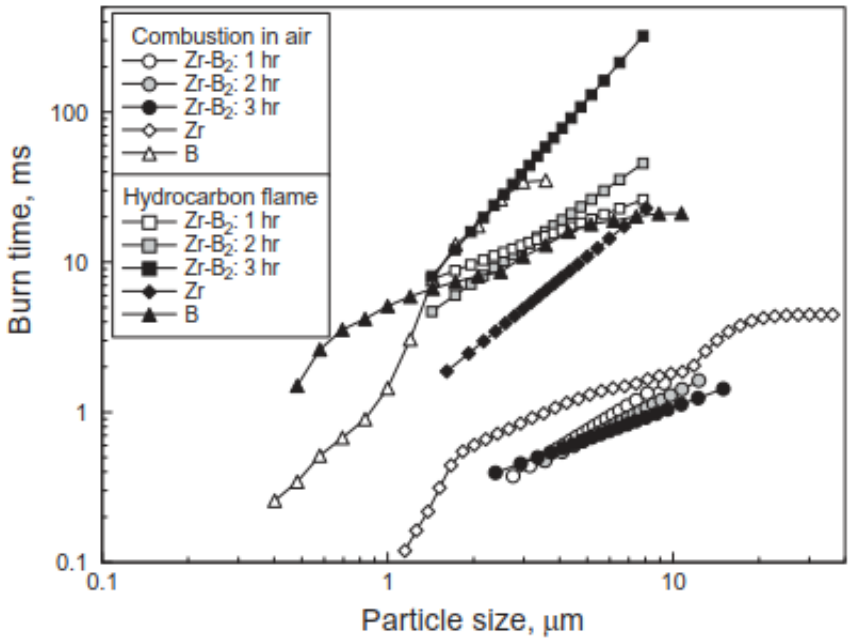

Figure 3.17 Correlations between burn times and particle sizes for different composite powders burning in different oxidizing environments. Burn times for elemental zirconium and boron powders
Source: [270, 274]

Table 3.1 Power Law Description for Burn Time vs. Particle Size for Different Materials in the Format $t=a \cdot d^n$, where t is Burn Time in ms and d is Particle Diameter in μm

Environment	Air		Hydrocarbon flame combustion products	
Material	*a*	*n*	*a*	*n*
Zr	0.4	0.7	0.9	1.6
B	3.5	2.1	5.1	0.7
Zr-B, milled 1 hr.	0.1	1.2	5.9	0.7
Zr-B, milled 2 hrs.	0.1	1.0	2.9	1.4
Zr-B, milled 3 hrs.	0.2	0.7	3.7	2.2

In that latter case, the differences between materials prepared with different milling times and having somewhat different extent of the initial B-Zr reaction are more significant. Such differences are thought to affect most noticeably ignition of the prepared powders, especially in the extremely fuel-rich conditions existing for the burning powder pile. For such conditions, the exothermic reaction between boron and zirconium is expected to be critical in raising the material temperature early on; the rate of this early reaction will be reduced for the powders milled longer than 1 hour, when some boride formation occurs

during milling. Conversely, when the oxygen is readily available, as in experiments with the heated filament involving a very thin powder layer in air (**Figure 3.12**), oxidation of zirconium is more important for ignition. The temperature measurements for individual particles shown in **Figure 3.18** are governed by the reaction occurring after ignition, when the particles reach their peak emission intensity. Thus, these particle flame temperatures are generally higher than those measured for the bulk powders, for which flame propagation across the pile and heat losses affect the thermal balance significantly.

Unfortunately, single particle combustion temperatures could not be measured for the powders burning in the air-acetylene flame. The intensity of the emission pulses was difficult to quantitatively separate from the background emission from the flame.

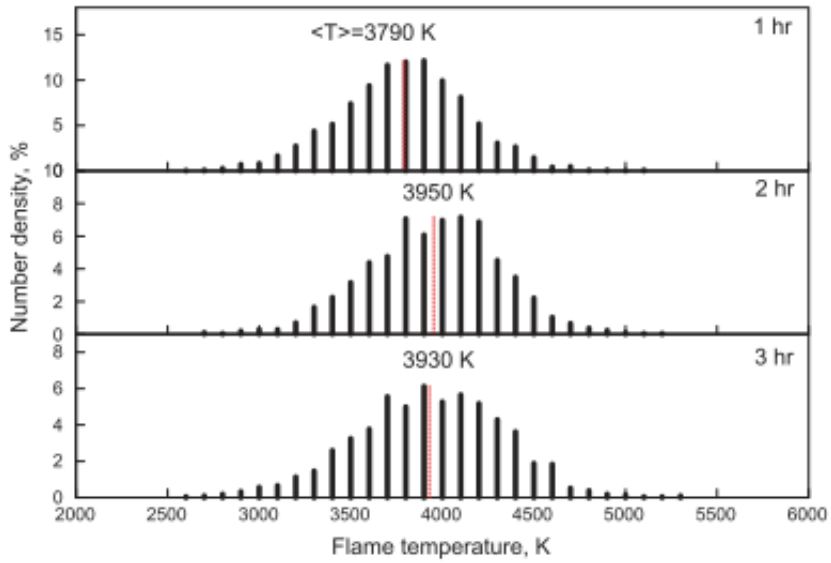

Figure 3.18 Statistical distributions of individual particle flame temperatures for composite powder particles burning in air.

3.7 Conclusions

Composite Zr-B powders with the composition of stoichiometric ZrB_2 were prepared by high energy milling in a shaker mill. The powder particles comprise a Zr matrix with embedded inclusions of B. Boron inclusions are mostly smaller than 100 nm in size; the size of these inclusions is unaffected by milling time varied in the range of 1–3 hours. The homogeneity of mixing between boron and zirconium was assessed by the average distances from zirconium matrix to boron inclusions obtained from processing images of cross-sectioned composite particles. This uniformity of boron distribution improves when the milling time increases from 1 to 2 hours; it is not affected by longer milling times. Results suggest that boron and zirconium start reacting during milling; the extent of this reaction becomes appreciable when the milling time reaches 2 hours. Ignition of the prepared powders in air occurs at the same temperatures as for pure zirconium. Thus, in presence of oxygen zirconium oxidation is the rate-controlling reaction, which affects ignition of these composite materials. However, in fuel-rich conditions, ignition of the prepared powders must be affected by the reaction between B and Zr. This reaction occurs less readily for powders milled for 2 hours or longer, where the components have partially reacted during milling. The inhibited boron-zirconium reaction is suggested to cause a slower flame propagation and respectively lower observed flame temperatures for bulk powders prepared with milling times longer than 1 hour.

In air, particles of the prepared composite powders burn faster than either pure boron or zirconium. It is suggested that heterogeneous oxidation of zirconium is the rate-limiting combustion process for all materials. Flame temperatures for individual composite particles burning in air are reasonably close to those predicted by the adiabatic flame temperature calculations at stoichiometric and fuel-rich conditions.

In combustion products of an air-acetylene flame, the burn rates of the prepared composites are lower than that of zirconium and are comparable to that of boron. It is suggested that the effect of preferred zirconium oxidation on burn rates of these materials in CO2/H2O oxidizers diminished compared to that in air. Powders prepared by 1-hour milling burn faster than powders prepared using longer milling times, most likely because of the absence of partially reacted zirconium boride phases formed during milling.

CHAPTER 4

STABILITY AND IGNITION OF A SILOXANE-COATED MAGNESIUM POWDER

4.1 Introduction

Magnesium powder is a common component of reactive and energetic materials used in pyrotechnics [279-282] and propellants [283, 284]. One advantage of magnesium is that it is readily ignited, and thus can serve to initiate the reaction of various energetic formulations. It generates a bright optical emission [285-289] and typically reacts in the vapor phase forming condensed MgO smoke as the main combustion product [61, 290-293]. The ease of ignition for magnesium is associated with the penetrable nature of the surface MgO film covering the metal [294]. The oxide film naturally grown on the metal is porous [295] and readily enables mass transport of evaporated Mg outside as well as oxygen to the metal surface [296]. Unfortunately, the same readily penetrable MgO film results in the poor stability of magnesium powders. They age rapidly in oxidizing environments [297-299], which causes difficulties associated with their long-term storage and handling. However, these issues can be mitigated through the modification of the surface with protective barrier coatings.

The surface modifying agents for these materials must also take into account the intended qualities of the magnesium powders. Ideally, coating materials would serve as protective layers at low temperatures, typically associated with storage, while not diminishing their ability to ignite upon heating. Additionally, given the reactive nature of magnesium, the modification process itself must not facilitate its premature ignition.

Finally, it is desirable to limit aggregation of particles while still preparing uniform coatings.

Over the last decade, siloxanes have found increased use as surface modifying agents, given their exceptional thermal stabilities, large temperature service range, and non-toxicity [300, 301]. Additionally, siloxanes have been shown to be a universal modifier of inorganic surfaces because the siloxane bond is reactive towards acids and bas-es, and inorganic interfaces have acid-base properties. More recently, poly(hydridomethyl-siloxane)s have also been shown to bond to a wide range of inorganic surfaces at mild temperatures through reaction with the hydridosilane (Si H) bond [302].

Despite their known versatility, to our knowledge, the use of siloxanes as coating materials for magnesium has hitherto been unexplored. This work describes preliminary results on the reactions of cyclic hydridomethylsiloxanes with magnesium powder surfaces to produce protective coatings. Particularly, a vapor-solid phase reaction is explored, which requires no solvents, minimal materials, and can be safely performed without the danger of premature ignition. The stability and ignition properties of siloxane-coated magnesium powders are also further investigated.

Table 4.1 Reaction Conditions and Yields of Siloxane-Modified Magnesium Powders

Sample	1	2	3	4	5	6	7
Temp (°C)	150	150	150	150	150	150	100
Vessel (mL)	100	100	100	100	100	500	500
Mg (g)	4.801	5.274	5.539	5.188	6.001	14.980	15.011
D_4^H (g)	1.550	1.553	1.468	1.674	1.657	5.031	5.007
Yield (g)	5.593	6.337	6.100	6.295	5.646	14.930	15.567
% D_4^H reacted	51.1	68.4	38.2	66.1	–	–	–

4.2 Materials and Methods

4.2.1 Materials

A spherical magnesium powder with nominal particle sizes ranging from 1 to 11 μm, 99.8% pure by Hart Metals was used. 1,3,5,7-Tetramethylcyclotetrasiloxane (D_4^H) was purchased from Gelest, Inc. (Morrisville, PA) and used as received.

4.2.2 Characterization

Powder surface morphology was characterized using a JEOL JSM 7900F field emission scanning electron microscope (SEM). Images were taken with back-scattered electrons to see possible phase contrast between coated and uncoated magnesium surface. Energy-dispersive spectroscopy was used to examine the coating composition and morphology. Fourier transform infrared spectroscopy (FTIR) of the modified powders was performed using a Shi-madzu IRTracer-100 with a QATR single reflection attachment.

4.2.3 Surface Modification of Mg Powders

A typical procedure for the modification of magnesium powders is as follows. In a 100 mL Kimax bottle with high temperature stable caps rated to 180 °C, 5.0 g magnesium powder is placed along with a 2 mL HPLC vial containing 1.5 g (6.24 mmol) of tetramethylcyclo-tetrasiloxane (D_4^H). Note that the siloxane and magnesium powder do not come into direct contact with one another. The contents of the vessel are sealed under nitrogen gas and placed in an oven at 100 or 150 °C for 72 hours. Following this, the vessel is removed from the oven and allowed to cool to room temperature. The HPLC vial is removed and the vessel is placed under vacuum for 24 hours to remove any excess and unreacted siloxanes. The modified magnesium powder is then stored in a 20 mL scintillation vial under nitrogen prior to characterization to prevent any unwanted oxidation. This procedure has also been

scaled up to 15 g of magnesium and a proportional amount of siloxane using a 500 mL reaction vessel.

4.2.4 Stability Tests

Stability of the prepared coated powders was assessed using their low-temperature oxidation at a constant temperature. The experiments employed TAM III analyzer by TA Instruments equipped with a perfusion ampoule. Both as received and coated Mg powders were heat-ed to 60 °C and exposed to a relative humidity of 80 %. These conditions were held in excess of 24 hours. An empty crucible in which only surface adsorption on the crucible surface occurred was used as baseline sample.

4.2.5 Ignition Tests

Prepared materials as well as the starting magnesium powder were ignited using an experimental setup involving an electrically heated filament. This setup was extensively discussed in earlier studies, e. g., [152, 160]. Briefly, a thin layer of powder is deposited on surface of a 0.5-mm diameter nickel-chromium wire. To deposit powder, it was mixed with hexane; a thin layer of a slurry was paint-ed on top of the wire and allowed to dry before the experiment. Only a small fraction of the wire length is coated with the powder. The wire was heated at a rate of approximately 8000 K/s using two 12-V (Kinetik HC600-Blue) batteries connected in series. The wire temperature was monitored using a high-speed infrared pyrometer with germanium switchable gain detector (Thorlabs PDA30B2) focused on an un-coated part of the wire surface. Simultaneously, a Redlake MotionPro 500 high-speed camera was focused on the coating. The ignition instant was identified when the coating became incandescent. The wire temperature at that instant is treated as the powder ignition temperature.

4.3 Results and Discussion

4.3.1 Preparation of Siloxane-Modified Magnesium Powders

Several different batches were made in order to determine the feasibility and reproducibility of this reaction. Conditions for each sample trial are given in **Table 4.1**. The reaction conditions attempted were based off previous reports [301] using liquid siloxane polymers and smooth inorganic oxide surfaces, and no significant effort was made in optimizing the conditions for magnesium powders. However, some small variations in conditions were made, which seemingly impact the resulting properties, suggesting that further optimization could provide additional improvement of the desired results. All reactions were performed at 150 °C for 72 hours, with the exception of Sample 7, which was heated to 100 °C.

The selection of tetramethylcyclotetrasiloxane (D_4^H) as a modifying agent was made for numerous reasons. The chemical structure is given in **Figure 4.1**, for reference. As a small molecule, it can easily be vaporized to perform reactions at the siloxane vapor-magnesium solid interface. This has the advantage of requiring no additional solvents, while also utilizing a minimal amount of reactant material. D_4^H also has a boiling point of 134 °C, which allows it to have significant vapor pressures well below the ignition point of magnesium. Finally, D_4^H contains reaction hydrido-silane (Si H) functional groups, which have been shown to react with a number of inorganic surfaces and do not produce any corrosive byproduct [302, 303].

Samples 1–5 were all prepared in similar small batches utilizing approximately 5 g of magnesium powder and 1.50 g of tetramethylcyclotetrasiloxane (D_4^H). With the exception of samples 5 and 6, the mass of the resulting modified powder increased, indicating a coating of the sample. A rough estimate of the percentage of D_4^H reacted with

each sample suggests that the amount of D_4^H used in these reactions is an excess quantity, although some material could have been lost from the vessel during transferring and sample isolation. These material losses explain the reduced mass of coated samples 5 and 6. Samples 6 and 7 were prepared at a greater scale using approximately 15 g of magnesium powder with a proportional amount of siloxane to provide an indication on the scalability of this process. Unfortunately, larger scale batches were not synthesized in a proportional vessel due to the availability of glassware. This likely has an effect on the resulting materials, which is discussed below.

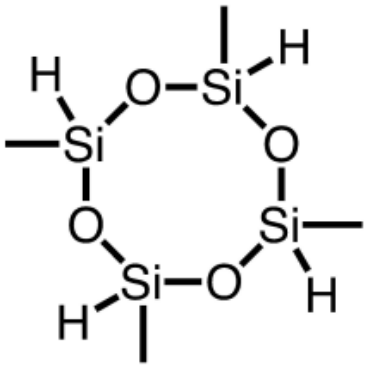

Figure 4.1 Chemical structure of 1,3,5,7-tetrameth-ylcyclotetrasiloxane (D_4^H).

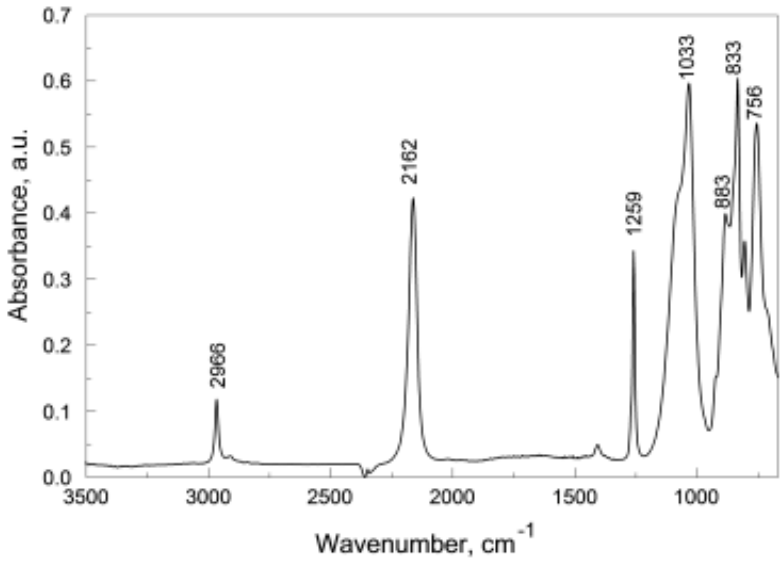

Figure 4.2 ATR-FTIR spectrum of tetramethylcyclotetrasiloxane (D_4^H)-modified magnesium powder.

4.3.2 Surface Properties and Morphologies of Coated Powders

Surfaces of the siloxane-modified magnesium were initially examined using FTIR of the powders using a single-reflectance ATR attachment. **Figure 4.2** shows a representative spectrum taken from Sample 6. No noticeable differences could be observed between the spectra of the different samples to distinguish the reaction parameters, and only the peaks relating to the siloxane coating could be observed: 2162 cm^{-1} (Si H), 1259 cm^{-1} (Si CH_3), and 1033 cm^{-1} (Si O Si). Additional peaks at 2966 cm^{-1}, 833 cm^{-1}, and 756 cm^{-1} are related to various C H vibrational modes associated with the methyl groups on D_4^H. A small shoulder appears at 921 cm^{-1} and may correspond to Si O Mg bonding, but this peak could not be fully resolved and is therefore difficult to define with certainty.

SEM images of the coated powders are shown in **Figure 4.3**. **Figure 4.3**a-b show images from the first attempted batch, Sample 1. Qualitatively, it was found to be the most agglomerated of the imaged samples, forming aggregates of approximately 50 μm in diameter. Within the aggregates, interparticle necking of the polymeric coating is clearly distinguishable. Similar results were found in Samples 2–5 (not shown). However, upon increasing the batch size a decrease in agglomeration could be observed, as seen in Sample 6 (**Figure 4.3**c,d). This decrease in agglomeration is attributed to the lower vapor pressure under which the reaction was performed due to the increase in the reaction vessel size rather than the upscaling of the materials. While not further investigated, it is suggested that this decrease in vapor pressure slows down the reaction kinetics, more readily allowing for uniform coatings without agglomeration or necking. This decrease in agglomeration is also observed in Sample 7, which was under the same conditions as Sample 6, but at a 100 °C. For the most part, no observable differences could be found between Samples 6 and 7,

although Sample 7 did appear to have some necking. Based on these results, it was determined that the conditions found in Sample 6 provided the best results for further study. In order to roughly evaluate the thickness of the resulting coating, energy-dispersive x-ray spectroscopy (EDX) mapping was performed on Sample 6. From **Figure 4.4**, a silicon-rich region can be clearly seen at the interface of the magnesium powder. This region also contains a significant amount of oxygen, which is unsurprising due to the structure of siloxanes. The carbon seen in **Figure 4.4** arises from the carbon tape mounting. A siloxane coating thickness of approximately 400 nm can be inferred from the maps shown. This thickness is much larger than expected for a monolayer coating and indicates that the coating is several monomers thick. D_4^H does not react with itself upon heating, but Si H bonds are known to react with magnesium, [304] similarly to Grignard reagent preparations. It is suggested that the magnesium substrate is catalyzing a cross coupling reaction between molecules of D_4^H, thereby creating coatings of these thicknesses.

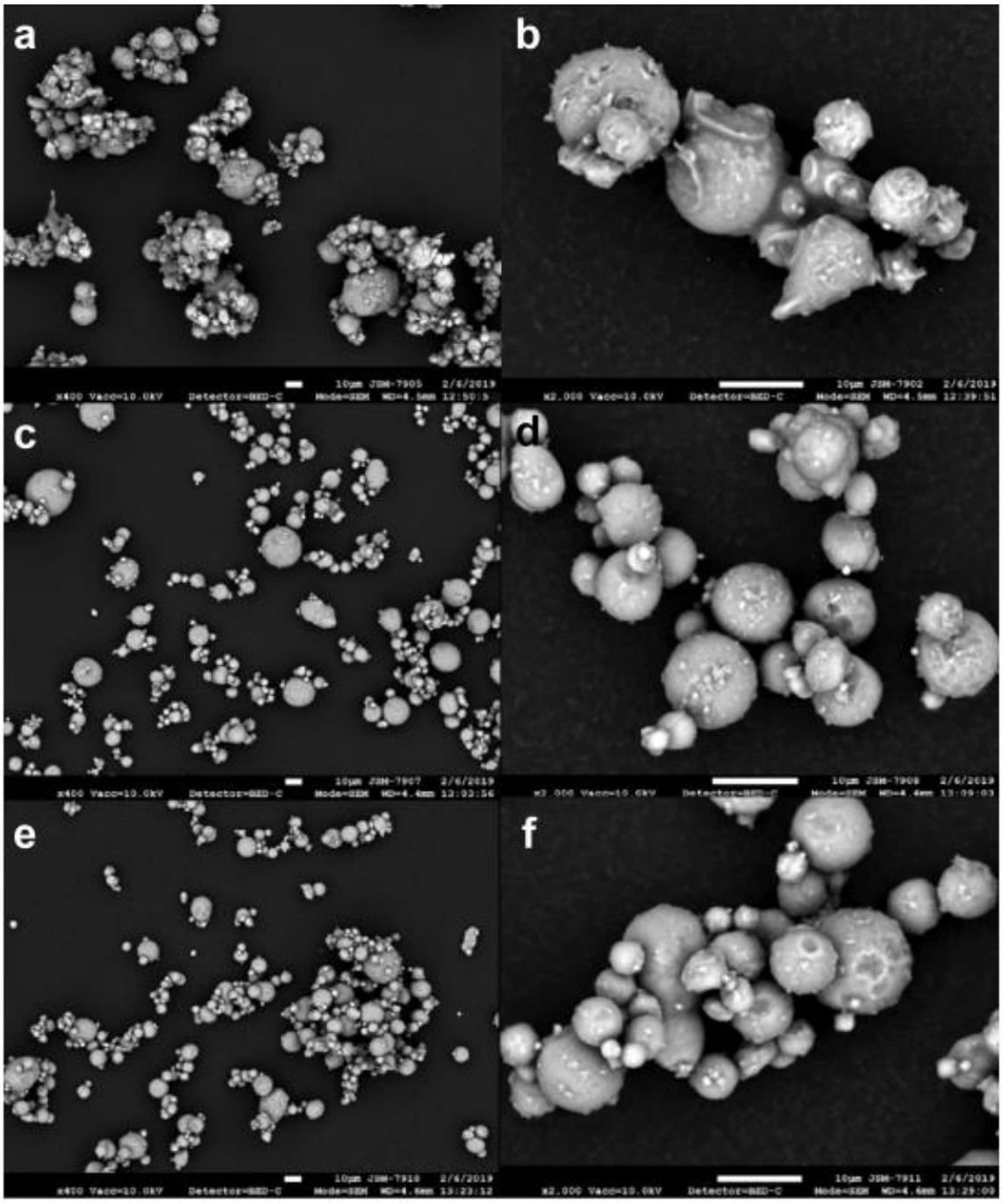

Figure 4.3 Backscattered electron scanning electron microscopy (SEM) images of a,b) Sample 1; c,d) Sample 6; and e,f) Sample 7.

Wire Ignition Testing. Results of wire ignition experiments are shown in **Figure 4.5** and **Figure 4.6**. **Figure 4.5** shows images of wires containing unmodified and siloxane-modified magnesium powders. A sequence of images is shown for each material. The first image shows the first frame when the emission from the powder became brighter than that

of the heated wire. These frames are labeled with Tig. Frames following 2, 5, and 10 ms after ignition are also shown and are labeled respectively. A continuing increase in brightness is observed with time for all materials. This increase appears to occur faster during the first 2 ms for both coated powders. At longer times, the flame formed around sample 6 appears to be greater than for other materials; however, this difference could be superficial and caused by a slightly greater coating thickness used in that particular experiment. In summary, the differences in ignition behavior between coated and uncoated samples are minor. If anything, the coating appears to accelerate rather than decelerate ignition of Mg upon heating.

Figure 4.6 shows ignition temperatures for unmodified magnesium and the modified magnesium powders. Overall, the average ignition temperatures for the siloxane-coated powders decreased by 25–50 °C. However, the standard deviations of these measurements significantly overlap those of the unmodified powders, indicating that the impact of the siloxane coating on the ignition temperature is rather minor. Most importantly, the protective coating does not increase the ignition temperature of magnesium.

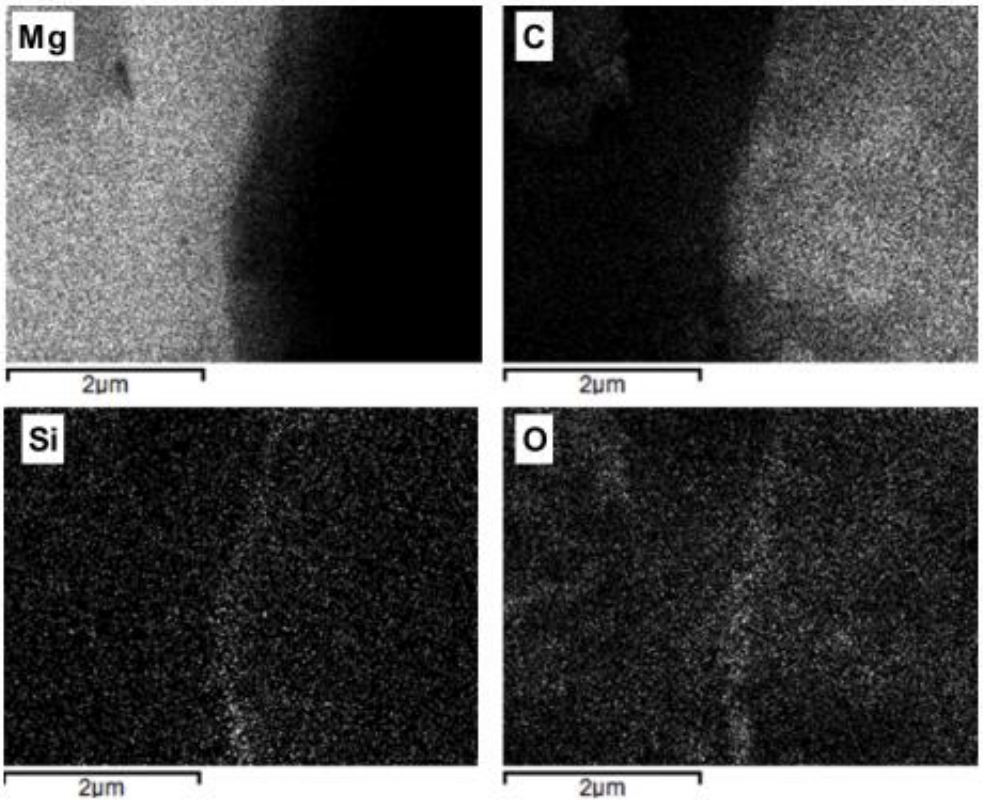

Figure 4.4 Energy-dispersive x-ray spectoscopy (EDX) elemental mapping of magnesium (Mg), carbon (C), silicon (Si) and oxygen (O) of siloxane-coated magnesium powder, sample 6.

4.3.3 Stability Testing

In order to determine the stability of the siloxane-modified magnesium coatings, micro-calorimetry experiments were performed using a TAM III at 60 °C with a relative humidity of 80 % for 24 hours. The results of these experiments are shown in **Figure 4.7**. For un-coated magnesium a small initial peak believed to be associated with water adsorption to particle and crucible surfaces is overlapped by a larger broad peak lasting in excess of ten hours from hydration. After twelve hours the sample stabilizes to a lower rate of reaction. Based on the integrated heat released after 24 hours, it is estimated that 1.18 % of the magnesium powder has reacted to form $Mg(OH)_2$. On the other hand, the samples with siloxane coatings did not show this trend, and appear to only adsorb water during a transient stage (when moisture is introduced or removed from the system). Steady state hydroxide

production is undetectable. This resilience in the presence of water is likely owed to the hydrophobic nature of the coating. Note that traces for two coated samples are shown, which effectively overlap with each other.

Crystal phases in the both uncoated and siloxane coated Mg powders after their exposure to water in TAM III experiment were examined via x-ray diffraction (XRD) operated at 45 kV and 40 mA using unfiltered Cu K Cu Kα radiation (λ=1.5438 Å). Results shown in **Figure 4.8** suggest $Mg(OH)_2$ as the primary reaction product on the order of 2% for uncoated magnesium. A noticeably smaller amount of hydroxide was observed in **Figure 4.6**, which may simply originate from the uncoated precursor.

4.4 Conclusions

Siloxane-coated magnesium powders demonstrate improved long-term stability, showing little oxidation at elevated temperature and in the presence of high humidity. Furthermore, modification of the powders does not negatively impact their ignition. Instead, a small decrease in the ignition temperature is noted. The ignited powder develop flame as fast as or faster than uncoated magnesium. Furthermore, the modification of the magnesium requires little material, no solvents, no corrosive byproducts, and easily produces conformal coatings on the powders.

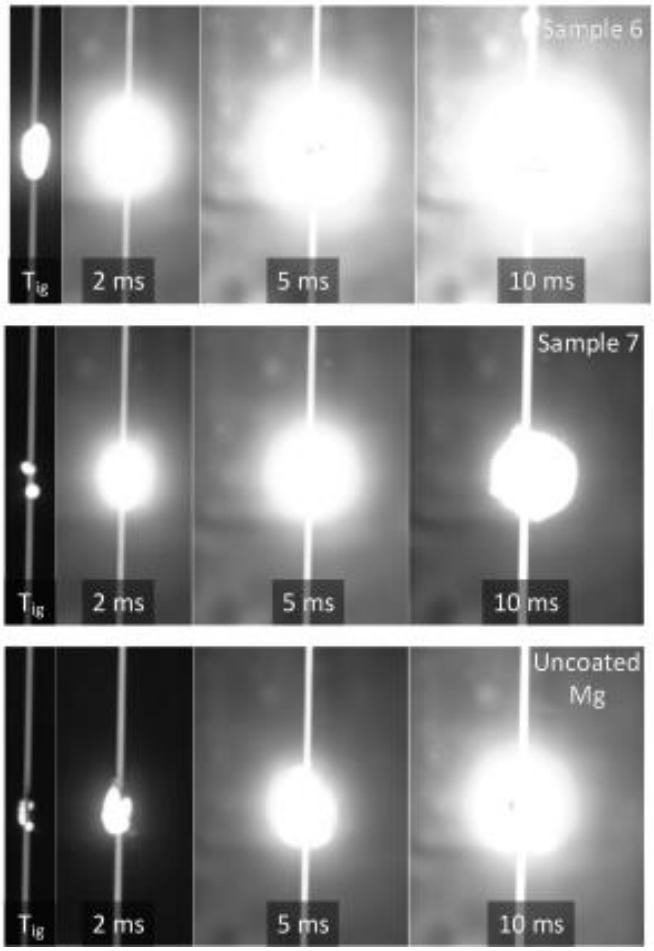

Figure 4.5 Coated samples 6, 7, and uncoated magnesium igniting on a heated nickel-chromium filament

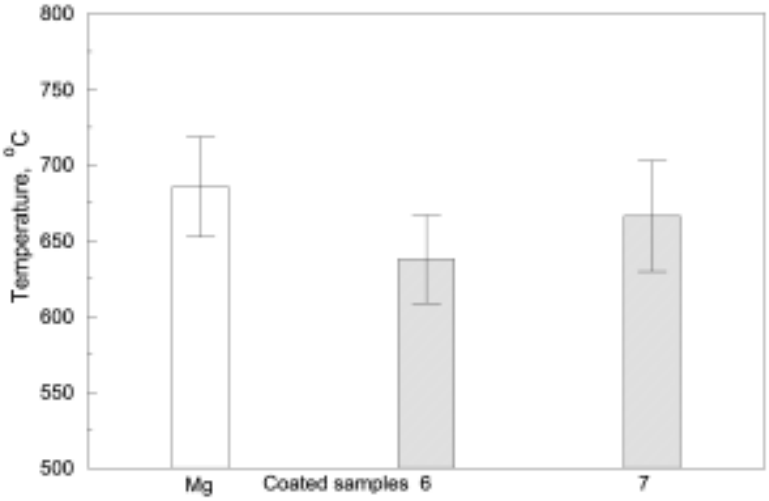

Figure 4.6 Ignition temperatures of unmodified magnesium powder and siloxane-coated magnesium powders.

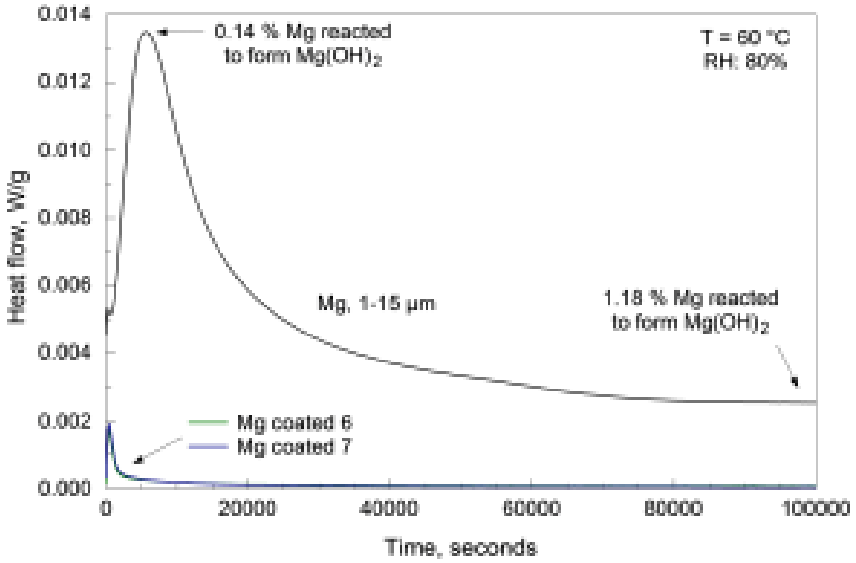

Figure 4.7 Experimental heat flow for unmodified and siloxane-coat-ed Mg powders measured using TAM III.

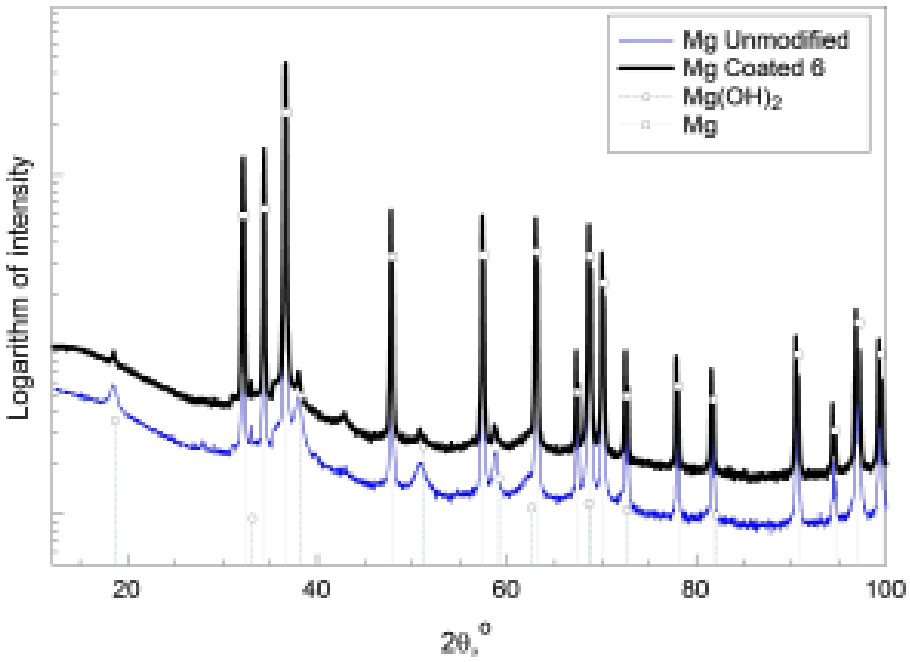

Figure 4.8 XRD scans of TAM III products for both uncoated Mg and coated sample 6 recovered after TAM III experiments. Both samples were kept at 60 °C under 80 % relative humidity during 48 hours.

CHAPTER 5

HIGHLY REACTIVE SPHEROIDAL MILLED ALUMINUM

5.1 Introduction

Aluminum powder is a common component of various energetic compositions, including solid propellants [52, 305-308] , explosives [309-311] , and pyrotechnics [312-314] because of its high volumetric and gravimetric energy density. In many cases, however, the low burn rate of aluminum particles leads to incomplete energy release [315]. One approach aimed at increased burn rates is to decrease the size of aluminum particles, leading to significant interest in aluminum nanopowders for advanced energetics [244, 316-319]. Such nanopowders contain a reduced amount of active aluminum because a significant fraction of the particle volume is occupied by the surface oxide shell [244, 317, 318, 320]. Nanopowders also age rapidly and are difficult to handle [320-324] . They tend to agglomerate[325-327] and mix poorly with other components of energetic formulations[319, 328, 329].

Production of consolidated items along with recent advances in additive manufacturing [330] emphasize the need for powders with improved flowability, in particular. This requirement limits the usable particle size range, as finer powders have generally poor flowability [331]. Mechanical milling has been used previously to prepare a variety of metal-based composite materials for use in energetic applications[332-335]. Although the resulting particles are generally equiaxed, they are not spherical and less flowable than spherical particles of comparable size prepared, e.g., by spray atomization [336]. For ductile aluminum, particles can be readily flattened into plate-like flakes by milling; this has been used to increase the aluminum reactivity [337], but it may negatively

affect the flowability. In related recent work, the mechanical milling method was expanded to use combinations of liquid immiscible process control agents (PCA). This results in the formation of emulsions during the milling process. If the liquid volume ratios are such that the liquid attracting the solids more forms droplets within the continuous phase formed by the second immiscible liquid, then the resulting particles accumulate inside droplets and yield particles that retain the droplet geometry [338, 339]. Such roughly spherical particles have been prepared in sizes from several to hundreds of micrometers. They consist of packed, finer primary particles of different shapes and show a degree of porosity. Thus, they combine the attractive handling and processing properties of micrometer sized spheres with the larger specific surface area and therefore enhanced reactivity of nanopowders. However, formation of flakes occurring during milling of aluminum may present a substantial challenge for packing them into spherical shapes.

The present work explores the feasibility of preparation of micronsized spheroidal aluminum powders comprising pure aluminum particles by mechanical milling regular aluminum powder in immiscible PCAs. Such spheroidal milled aluminum powders are expected to have improved reactivity and flowability.

5.2 Experimental

5.2.1 Material Preparation

The starting material was -325 mesh, 99.9% pure aluminum powder by Atlantic Equipment Engineers. It was processed using a Retsch PM400-MA planetary mill operated at 350 RPM employing custom-built 175-mL hardened steel vials (64 mm diameter, 55 mm height) with 9.525 mm (3/8 ”) diameter hardened steel balls. Each vial contained 25 g of powder. The ball-to-powder mass ratio was 3. All charges were loaded in an argon-filled

glovebox. Following earlier work[338, 339], the immiscible fluids, acetonitrile and hexane (both Alfa Aesar, 99.5 %) served as a PCA during milling. The volumes of aluminum powder and acetonitrile were equal to each other, 9.3 mL each. Hexane was added at three times the volume of acetonitrile, 27.8 mL, to form the continuous phase of the emulsion produced during milling. Altogether, the charge included 20 vol-% Al, 20 vol-% acetonitrile, and 60 vol-% of hexane. Milling times were 30, 60, 75, and 120 min. A reference sample was milled for 120 min using only 10 ml acetonitrile as the PCA to produce Al with the surface functionalized by milling it in acetonitrile, but not forming spherical particles.

5.2.2 Particle sizes and structures

Particle surface morphologies, as well as their internal structures were examined using a JEOL JSM-7900F scanning electron microscope (SEM). Particles were embedded in epoxy, cross-sectioned, and carbon coated. Particle sizes were determined by image analysis using Fiji software [275]. For each sample, the particle size distribution used more than 1000 particles. Particle sizes were also analyzed by laser light scattering using a Malvern Panalytical Mastersizer 3000 with a hydro MV sampling unit. Dry powder particles were poured directly into the unit loaded with ethylene glycol, serving to suspend the powder. The measurements were performed with a stirrer speed of 200 rpm and without sonication to provide modest agitation to maintain particle entrainment but minimize breakup of the clusters.

The spheroidal milled aluminum particles were characterized by powder x-ray diffraction (XRD) using a PANalytical Empyrean x-ray diffractometer operated at 45 kV and 40 mA with unfiltered Cu K α radiation (λ = 1.5438 Å). Crystallite sizes and lattice

strain were determined by Williamson-Hall analysis[340]. The coarse, -325 mesh starting Al powder was strain-relieved by annealing under vacuum at 350°C for 12 h.

Specific surface area and pore volume for the prepared powders were determined by nitrogen gas sorption analysis at 77 K using a Quantachrome Autosorb iQ-MP, Automated Gas Sorption Analyzer. Prior to analysis, samples were degassed near 1 torr at 300°C for 6 hours. Adsorption-desorption isotherms were recorded using 52 points for adsorption and 16 points for desorption. Following recommendations[341, 342], surface area and pore volume were determined using quenched solid density functional theory (QSDFT) [343]. Of the available QSDFT kernels, the measurements best fit the adsorption model of a carbonaceous material with a combination of cylindrical and spherical pores.

5.2.3 Thermal analysis and calorimetry

Oxidation of the prepared powders was characterized by Thermo-Gravimetric analysis (TG) using a TA Q5000-IR by TA Instruments. Samples of about 5.5 mg each were heated to 1100°C in an argon/oxygen gas mixture. Both oxygen and argon were flown at 20 mL/min each. The heating rate was varied from 2 to 20 K/min.

Aging of aluminum powders was characterized for one of the prepared spheroidal aluminum, for a sample milled in acetonitrile only, and for the starting aluminum powder. The 120-mg samples were placed into a perfusion ampoule in a microcalorimeter installed in a TAM III by TA Instruments. The samples were initially equilibrated in dry air at 60°C for 60 min, and then exposed to 80 % relative humidity for several days.

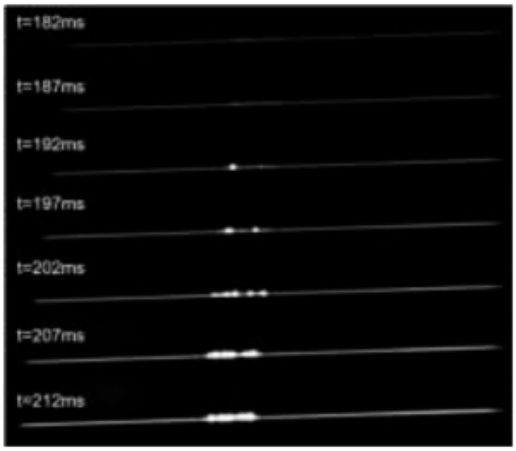

Figure 5.1 A sequence of high-speed video frames showing ignition of spheroidal milled aluminum coated ono a Kanthal® wire. Ignition is registered here at 187 ms. This sample was prepared by milling the starting powder in a blend of hexane and acetonitrile for 75 minutes.

5.2.4 Ignition experiments

Powders coated on an electrically heated filament were ignited, while the filament temperature was being monitored [344, 345]. Due to the approximately spherical shape, and resulting higher flowability the spheroidal powders prepared here did not adhere well to cylindrical Ni-Cr filaments used previously. Therefore, a flat Kanthal ribbon (TEMCo Industrial, 0.8 × 0.1 mm) was used instead. The ribbon was heated using a 12 V solid cell battery. Because of the ribbon shape, its temperature could not be reliably monitored optically with the pyrometer focused on its narrow side cross-section. Pyrometer also could not be placed above or below the filament because of the potential damage due to the generated smoke and fragments formed when the powder ignited. Instead, a reproducible heating protocol was established in preliminary experiments without powder, so that no smoke was produced. In these preliminary experiments, the ribbon temperature was monitored using a custom infrared pyrometer placed above it. The pyrometer was based on a PDA30B2 Thorlabs Germanium switchable gain detector calibrated using an Omega BB-4A black body source. Kanthal® was treated as a gray body with an emissivity of 0.7 based

on the product data sheet. The ribbon was heated up to about 1650 K at a rate of 3420 ± 80 K/s before it broke as a result of melting. The reproducibility of the time-dependent temperature reading was within ± 53 K. The obtained average time-dependent temperatures were used to evaluate the ribbon's temperature in subsequent experiments with powders, in which the instant of the powder ignition was determined from the recorded high-speed video. The videos were obtained using a Photron FASTCAM Nova S6 high speed camera operated at 6000 frames per second. A series of highspeed images illustrating the ignition for a prepared powder is shown in **Figure 5.1**. The time of ignition was identified as the frame where the brightness of the powder exceeded the brightness of the heated ribbon. The ribbon temperature corresponding to the time elapsed since the current was turned on was considered the ignition temperature.

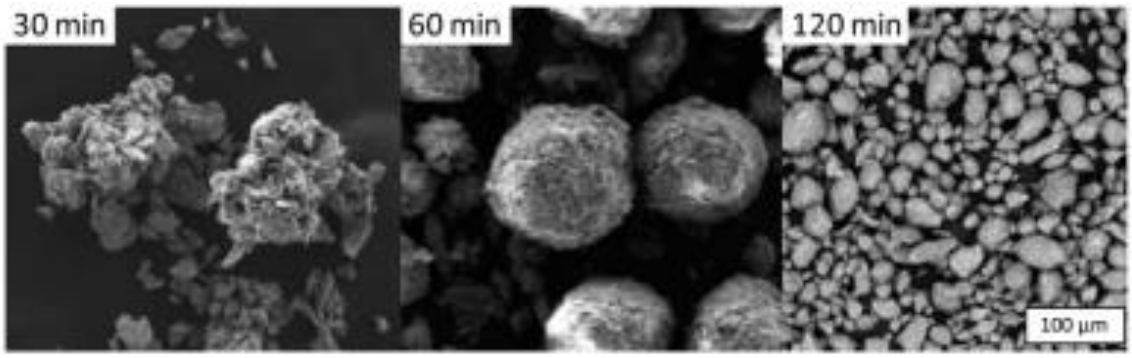

Figure 5.2 SEM images of spheroidal milled aluminum prepared with acetonitrile and hexane as PCA. Milling times are indicated. The scale bar is the same for all the images shown.

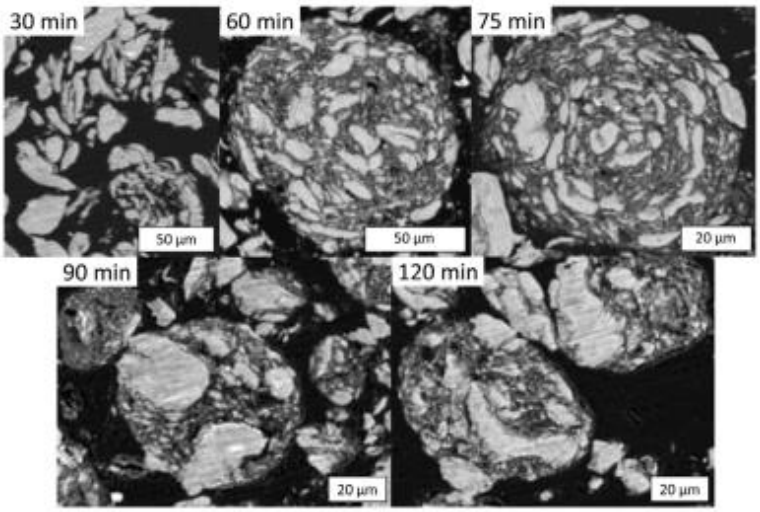

Figure 5.3 Cross-sections of spheroidal milled aluminum prepared with acetonitrile and hexane as PCA. Milling times are indicated.

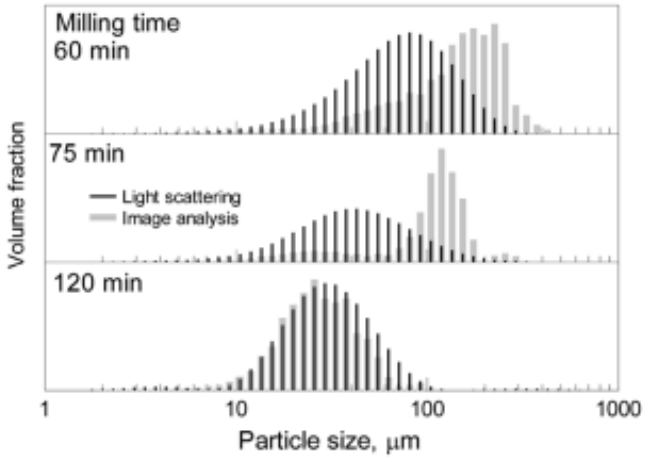

Figure 5.4 Particle size distributions determined by low-angle laser light scattering and image analysis.

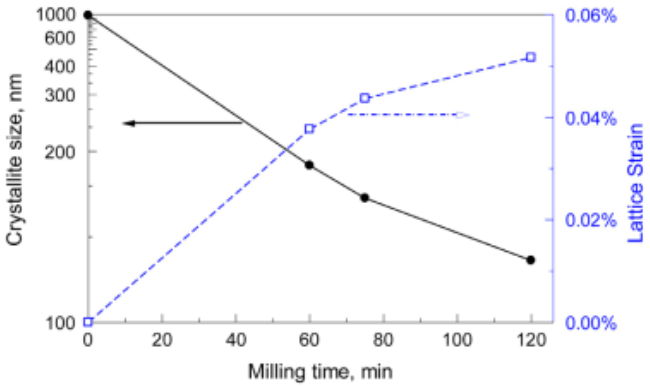

Figure 5.5 Changes in apparent crystallite size and lattice strain with milling time in spheroidal milled aluminum.

5.3 Results and Discussion

5.3.1 Particle morphology, size and structure

After milling with hexane and acetonitrile as PCA, the samples did not cake and exhibited high flowability making it easy to remove them from the vials. Particles with close to spherical shape were clearly observed in the liquid in samples placed under an optical microscope. As the liquid evaporated, some spheroidal particles were observed to break up, with the effect being most pronounced for materials prepared using shorter milling times. Characteristic SEM images of prepared spheroidal particles are shown in **Figure 5.2**. The material milled for 30 min consists of weakly agglomerated, large aluminum flakes, which likely represent fragments of particles broken up during drying. Relatively large spheroidal particles are observed for the powder milled for 60 min. Packed aluminum flakes are clearly observed at the surfaces of these particles. After 120 min of milling, the particle size is reduced substantially. However, spherical or spheroidal particle shapes remain.

Cross-sections in **Figure 5.3** further confirm that the particles are composed of aluminum flakes with various sizes. Some unattached flakes are visible as well, becoming less prevalent as milling time increases. Different magnifications are selected for different images to clarify the internal structures of the cross-sectioned particles. In the material recovered after 30 min of milling, the agglomerates are very loose and the spheroidal particles are not fully formed. After 60 and 75 min of milling flakes appear in a concentric pattern, aligned with the surface of the particles. This suggests some consolidation of the particles by rolling. The preferred orientation is less noticeable for the smaller particles recovered after 90 and 120 min of milling.

Particle size distributions determined by both SEM image analysis and low-angle laser light scattering are shown in **Figure 5.4**. As a general trend, the particle sizes decrease at longer milling times. For the milling times of 60 and 75 min, the sizes implied by image analysis are noticeably greater than those from the laser scattering measurements. It suggests that the larger particles obtained at shorter milling times and observed by SEM are breaking up while being agitated in a suspension used for the particle size measurements by laser light scattering. However, there is effectively no difference between the SEM and laser light scattering measurements for the particles milled for 120 min. Thus, such finer spheroidal milled aluminum particles obtained at a longer milling time are mechanically stronger.

The pattern assigned to the aluminum face-centered cubic (fcc) structure was the only one clearly observed in XRD. The observed fcc Al peaks broadened at longer milling times. The apparent crystallite sizes and lattice strains determined using Williamson-Hall analysis [39] are shown in **Figure 5.5**. The crystallite size decreases approximately from 1 μm down to 200 nm while the milling time increases to 120 min. Conversely, the lattice strain increases at longer milling times. No other crystalline phases were detected by XRD in the prepared particles at any milling time.

Example nitrogen adsorption-desorption curves of the spheroidal powder milled for 120 minutes and of reference -325 mesh Al are shown in **Figure 5.6**. The general shape of the isotherms matches that of a nonporous, or macroporous, material showing reversible adsorption, and identified as Type II in Ref. [342]. In addition, a small hysteresis is observed above a relative pressure of 0.5. This pattern, observed for all powders prepared here, matches materials described as non-rigid or macroporous aggregates of plate-like

particles, categorized as type H3 in Refs. [341, 342]. This morphology is consistent with the particle cross sections shown in **Figure 5.3**.

Specific surface area, pore volume, and pore half-width recovered from processing the nitrogen adsorption isotherms are shown for samples milled from 60 to 120 min in **Figure 5.7**. Both, specific surface area and pore volume exhibit a maximum after 75 min of milling. The pore half width increases slightly with the milling time and then decreases, varying around 1 nm.

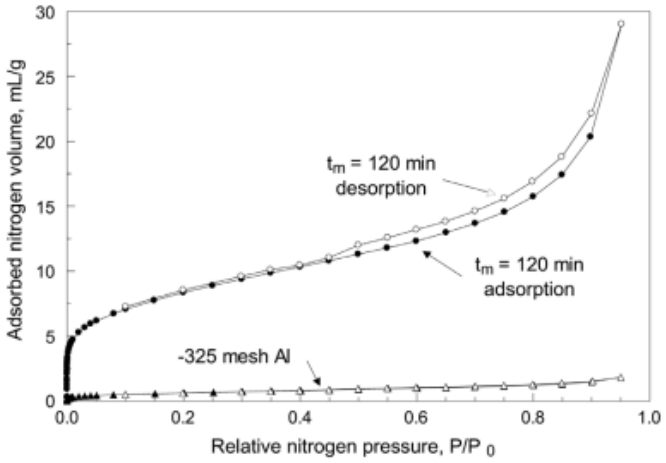

Figure 5.6 Nitrogen adsorption-desorption isotherm of spheroidal aluminum milled for 120 min and for the starting material, -325 mesh Al.

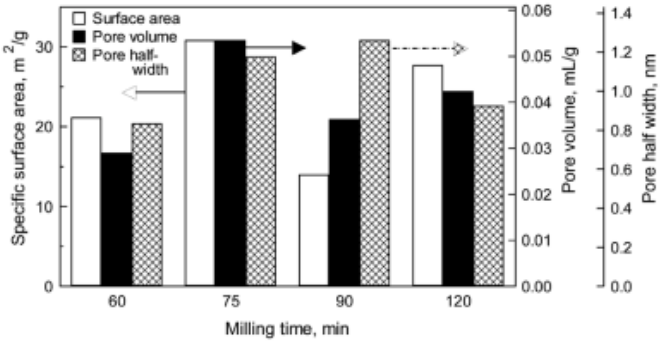

Figure 5.7 Surface area and pore volume for spheroidal aluminum prepared at different milling times measured using nitrogen adsorption.

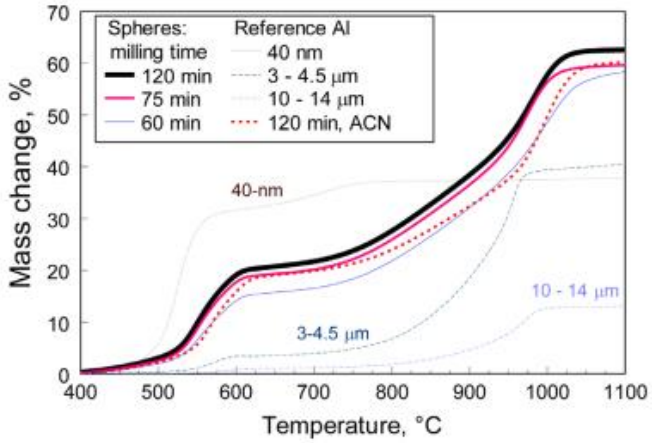

Figure 5.8 TG traces for the prepared spheroidal particles (solid lines) and for reference aluminum powders (dashed lines).
Source: Micron-sized Al [346] and nano-aluminum [347]

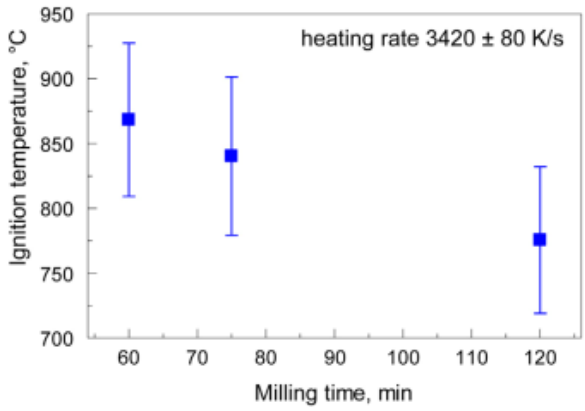

Figure 5.9 Ignition temperature vs milling time of spheroidal milled aluminum.

To interpret these observations, note that refining the starting aluminum powder into thin flakes is expected to lead to an increased surface area. Formation of the spheroidal shape generates a porous structure, with growing pore volume. Conversely, packing the generated particles at extended milling times should reduce their pore volume and surface area. The peak observed around 75-min milling may thus suggest that in early stages of milling, the particle refinement and initial formation of filled emulsion droplets are dominant processes. At longer milling times the formed particles become increasingly consolidated. Because the size of spheroidal particles decreases with the milling time, the surface area and accessible pore volume can increase again as the milling continues, despite

the reduction in the pore half width, as noted by an increase in the surface area and pore volume at 120 min vs. 90 min.

5.3.2 Thermal analysis and ignition

TG traces in argon-50 % oxygen atmosphere for the prepared spheroidal milled aluminum (solid lines) and for several reference aluminum powders (dashed lines) heated at 5 K/min are shown in **Figure 5.8**. The measurements for micron-sized powders are from Ref. [346] , and for the nano-aluminum from Ref. [347]. An additional dashed line shows aluminum milled only in acetonitrile for 120 min. All aluminum powders show a qualitatively similar sequence of oxidation steps at nearly the same temperatures, corresponding to the oxidation mechanism discussed in Refs. [348, 349]. The main difference between the powders is in the extent of mass gain observed for different oxidation steps. The strongest low-temperature mass gain associated with a polymorphic phase change from amorphous to γ-alumina occurs for the nano- aluminum powder with a nominal particle size of 40 nm. However, the mass gain for that powder at higher temperatures is limited, possibly due to the larger amount of initial oxide present, and therefore reduced amount of active aluminum. For regular aluminum powders with nominal particle sizes of 3-4.5 and 10-14 μm, the mass gains decrease with increasing particle size, as expected. For all powders milled in this work in presence of acetonitrile, including the spheroidal powders, the low-temperature mass gain is significantly greater than for micron-sized aluminum powders, approaching that observed for 40-nm aluminum. At higher temperatures, the mass gain observed for the powders milled in presence of acetonitrile increases above that observed for both nano-and micron-sized aluminum powders.

Among spheroidal powders prepared at different milling times, the mass gain is greater for powders milled longer, which show smaller particle size (cf. **Figure 5.4**), although not necessarily greater specific surface area (cf. **Figure 5.7**). Interestingly, the powder milled in acetonitrile only for 120 min, the trace overlaps with those for the spheroidal aluminum milled for 60 and 75 min. The mass gains observed at different temperatures for aluminum milled only in acetonitrile closely match those observed for the spheroidal particles milled for 75 min.

Ignition temperatures of the spheroidal milled aluminum are shown in **Figure 5.9**. Error bars show the uncertainty estimated from the calibration experiments, and resolution and repeatability of the actual ignition experiments, with i indicating the individual error sources. The ignition temperature decreases with increasing milling time, despite the observation that the material milled for 75 min exhibits greatest specific surface area. Regular aluminum powders with similar particle sizes could not be ignited in this experiment. Thus, although a direct comparison is not possible, it is clear that the conventional aluminum powder is less reactive than the prepared spheroidal milled powders.

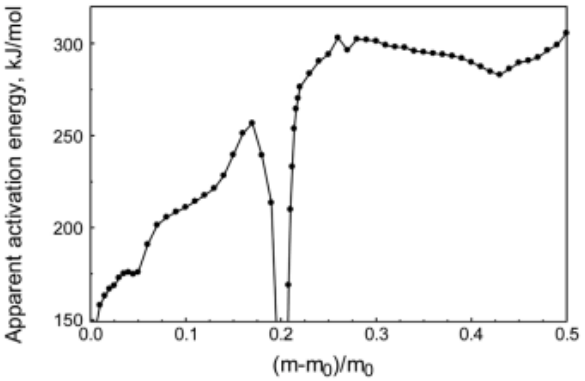

Figure 5.10 Apparent activation energy for oxidation of spheroidal aluminum milled for 120 min.

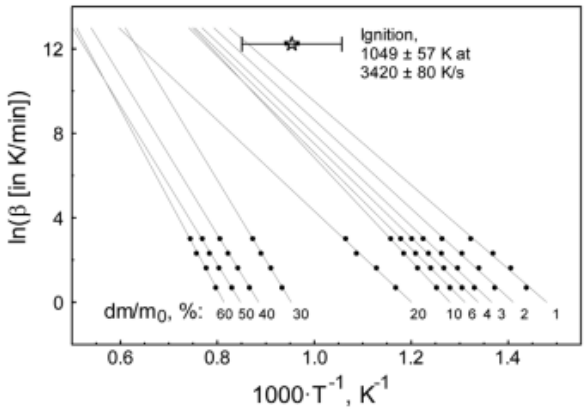

Figure 5.11 Arrhenius plot of TG measurements interpolated to specific degrees of oxidation, and of the ignition temperature shown in **Figure 5.10** for the spheroidal aluminum milled for 120 min.

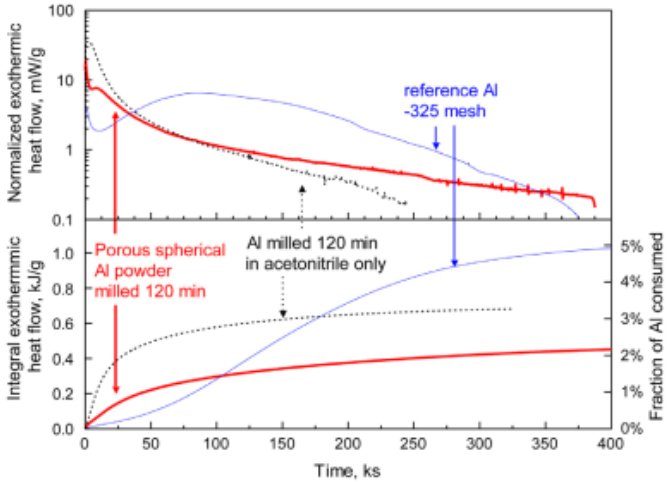

Figure 5.12 Heat flow and integrated heat flow generated by aging the spheroidal aluminum milled for 120 min at 60°C in air with 80 % relative humidity. Reference data are shown for starting Al powder and for Al milled in acetonitrile.

5.3.3 Kinetic Analysis

For spheroidal aluminum milled for 120 min, TG measurements at heating rates of 2, 5, 10, and 20 K/min were processed using an isoconversional method[350]. The result, apparent activation energies corresponding to specific degrees of oxidation, is shown in **Figure 5.10**. The initial stages of oxidation, below 5 % of mass gain and corresponding to temperatures below about 520°C in **Figure 5.8** are characterized by a relatively low apparent activation energy starting below 160 and increasing to 180 kJ/mol. At about 5 %

mass increase, the activation energy jumps to near 210-220 kJ/mol. This roughly corresponds to the steeper part of the first stepwise mass increase in **Figure 5.8**. The increase in the apparent activation energy continues to near 250 kJ/mol at the end of the first oxidation step. The behavior before the interval of nearly no mass change (600 – 700°C in **Figure 5.8**) is consistent with previously reported activation energies for early oxidation stages of aluminum[348] . The second main mass gain above 25 % (750°C in **Figure 5.8**) is characterized by an apparent activation energy near 300 kJ/mol. This is also consistent with previous reports for the second major oxidation step[346]. These comparisons suggest that the Al surface produced by milling in acetonitrile and/or hexane was not significantly changed to affect the nature of the oxidation process, and that the differences in mass change observed in **Figure 5.8** derive from the increased specific surface area of the spheroidal milled aluminum alone.

In order to relate the thermogravimetry to the ignition measurements shown in **Figure 5.9**, the oxidation measurements at different heating rates are shown in Arrhenius coordinates in **Figure 5.11**. Assuming that the reaction mechanism does not change with heating rate, points corresponding to a given mass gain at different heating rates fall on straight lines that can be extrapolated to the heating rates used in the heated filament ignition experiment. Data shown in **Figure 5.10** suggest, therefore, that at the point of ignition the spheroidal milled aluminum may have increased their mass by about 5-10 %, corresponding to the first oxidation step observed in **Figure 5.8**. This step, as noted above, is associated with the formation of γ-alumina. Without making assumptions about the specific geometry of the spheroidal particles, this mass change can be normalized by initial surface area, giving a range of 1.8-3.7 mg/m^2. Assuming an amorphous alumina density of

3.05 g/mL [349] and uniform oxidation over the entire internal surface, this corresponds to an increase of the oxide layer thickness by 0.6-1.2 nm. This estimate is likely too low, as the degree of oxidation is expected to decrease radially from the surface to the center of the porous particles. In other words, it is expected that a thicker oxide layer grows in the external shell of the igniting particles, whereas the particle core remains mostly unoxidized by the instant of the particle ignition.

5.3.4 Aging

Heat flows recorded for the spheroidal aluminum milled for 120 min, for aluminum milled only in acetonitrile, and for -325 mesh reference Al are shown in **Figure 5.12**. The Al milled only in acetonitrile shows the strongest initial heat flow, followed by the spheroidal milled aluminum, and the reference Al powder. The oxidation rate for both, the spheroidal powder and the material milled only in acetonitrile decreases strongly and at similar rates after about 50 ks. Conversely, the oxidation rate of the reference Al powder continues to increase, and only decreases after reaching a maximum near 80 ks. The integrated heat flow is shown in **Figure 5.12** as well, illustrating that despite the higher initial oxidation rate the total energy released is smallest for the spheroidal milled aluminum, and largest for the reference Al powder.

The integrated heat flow can be related to the amount of active aluminum consumed. The reaction $Al + 3\ H_2O(g) \rightarrow Al\ (OH)_3 + 1.5\ H_2$ produces approximately -21.0 kJ per gram of aluminum. This estimate uses the enthalpy of formation of the gibbsite polymorph of $Al(OH)_3$ [351] although the bayerite polymorph was observed here (verified by XRD, and included in Appendix A Figure S1). With this value, the second axis in **Figure 5.12** shows the fraction of Al consumed as a result of aging.

5.3.5 Reactions in spheroidal milled aluminum using a reactive shell/inert core model

To interpret thermal analysis measurements as well as aging in humid air, it is useful to model the oxidation of these porous particles by taking their unique geometry into account. With any external gaseous oxidizer that diffuses into the porous milled aluminum particles, the resulting oxide or hydroxide initially forms at the outer surface, and then continues to grow inward. During this process an oxidizer concentration gradient exists between the particle's environment and its interior. As a result, the oxide or hydroxide is nonuniformly distributed within partially oxidized particles. Simplifying, and at least for early stages of oxidation such particles can be described as having an outer layer, or shell, where oxidation occurs, and an unoxidized core. The heterogeneous oxidation can then be assumed to occur at a rate proportional to the available specific surface area within the shell, which is proportional to (but smaller than) the total specific surface area as determined by the nitrogen adsorption measurements shown in **Figure 5.7**. Introducing the thickness of the oxidizing shell, h_{shell}, is useful to describe the distribution of oxide or hydroxide in partially reacted particles. It can further be used to account for the morphology of the prepared spheroidal milled aluminum when analyzing ignition or aging.

As for any aluminum powders, ignition of the spheroidal milled particles prepared here is expected to be governed by heterogeneous oxidation of aluminum. The rate of this reaction needs to be predicted in order to describe ignition delays of such materials subjected to different ignition stimuli. The analysis of pre-ignition reactions can be based on the results obtained in the present TG measurements. The oxidation slows significantly above 600°C at the heating rates used for the TG measurements (**Figure 5.8**). This is likely the upper temperature limit for the proposed core-shell model. Aluminum melts at higher

temperatures and the initial morphology of the spheroidal particles may be destroyed, so that this model would no longer be useful in interpreting TG measurements. Based on ref. [349] [48] the thickness of alumina, h_{ox} , grown before the melting point of aluminum is reached is close to 15 nm. Taking h_{ox} = 15 nm to also be the oxide thickness grown on the aluminum surface within the reactive shell at the same temperature enables one to estimate h shell using the TG data shown in **Figure 5.8**.

The mass of a porous spherical Al particle, m_p, is the sum of the masses of its core, m_{core}, and shell, m_{shell}:

$$m_p = m_{core} + m_{shell} \tag{5.1}$$

The mass of the particle core is:

$$m_{core} = \rho_{Al}(1 - \Phi)\frac{4}{3}\pi(r_p - h_{shell})^3 \tag{5.2}$$

where ρ_{Al} is the aluminum density, Φ is the relative pore volume, and r_p is the particle radius. Similarly the mass of the oxidizing porous shell is initially:

$$m_{shell,0} = \rho_{Al}(1 - \Phi)\frac{4}{3}\pi\left(r_p{}^3 - (r_p - h_{shell})^3\right) \tag{5.3}$$

During the oxidation, the mass of the reacting, partially oxidized shell is calculated as

$$m_{shell} = m_{shell,0} - m_{Al,reacted} - m_{ox} = m_{shell,0} - m_{Al,reacted}\left(1 - \frac{M_{ox}}{M_{Al}}\right) \tag{5.4}$$

(4) where M_{Al} and M_{ox} are molar masses of aluminum and alumina, taken as AlO 1.5 , respectively, m_{ox} is the mass of newly formed oxide, and the mass of reacted aluminum, $m_{Al,reacted}$ is obtained as

$$m_{Al,reacted} = h_{ox} \cdot A_{shell} \cdot \frac{M_{Al}}{M_{ox}} \tag{5.5}$$

where A_{shell}=$SA\ m_{shell,0}$ is the total surface area of the oxidizing shell, assumed to be constant during this initial oxide growth. SA is the specific surface area determined from measurements shown in **Figure 5.7**. In Eq. (5) , the thickness of the oxide layer growing on the Al surface h_{ox}, is estimated without making specific assumptions about the surface geometry as

$$\mathrm{h_{ox}} = \frac{\mathrm{Vox}}{\mathrm{Ashell}} = \frac{\mathrm{m}_{ox}}{\rho_{ox} \cdot \mathrm{A_{shell}}} = \frac{\mathrm{m}_{Al,reacted} \cdot M_{ox}}{\rho_{ox} \cdot \mathrm{A_{shell}} \cdot M_{Al}} \tag{5.6}$$

Substituting Eqs. (2) , (3) and (4) into Eq. (1) , the mass of an oxidizing particle can be calculated as a function of both, h_{ox} and h_{shell} :

$$\mathrm{m_p} = \rho_{\mathrm{Al}}(1-\Phi)\frac{4}{3}\pi\left(\mathrm{r_p}^3 - \mathrm{h}_{ox} \cdot \rho_{\mathrm{Al}} \cdot \mathrm{SA} \cdot \left(\mathrm{r_p}^3 - \left(r_p - \mathrm{h}_{shell}\right)^3\right)\left(\frac{M_{Al}}{M_{ox}} - 1\right)\right) \tag{5.7}$$

and relative to the initial mass of the particle

$$\frac{\mathrm{m}_p}{\mathrm{m}_{p,0}} = 1 - \mathrm{h}_{ox} \cdot \rho_{\mathrm{ox}} \cdot \mathrm{SA} \cdot \left(1 - \frac{\left(r_p - \mathrm{h}_{shell}\right)^3}{\mathrm{r_p}^3}\right)\left(\frac{M_{Al}}{M_{ox}} - 1\right) \tag{5.8}$$

For $m\,p/m\,p$, 0 = 1 . 2 , representing the 20 % mass change observed for spheroidal milled aluminum at about 600°C after the first major mass gain (see **Figure 5.8**), and plugging in $h_{ox} \approx 15$ nm (and assuming that natural oxide had thickness of 3 nm) and $r_p \approx 15$ μm as the volume-averaged particle radius (see **Figure 5.4**) one solves for $h_{shell} \approx 2.2$ μm. This shell thickness describes the penetration depth of oxygen in the prepared particles during their oxidation in TG experiments.

Considering that reaction rates are higher during ignition than in TG experiments, the shell thickness is expected to be smaller due to stronger oxygen concentration gradients developing in igniting spherical particles. Thus, 2.2 μm can serve as the upper bound of the reactive shell thickness enabling one to estimate the rate of pre-ignition reactions in the prepared spheroidal milled aluminum accounting for the measured specific surface and kinetics of heterogeneous oxidation of aluminum. This estimate characterizes only powders prepared in these reported experiments; it is expected that varying milling conditions can yield spheroidal particles with different sizes and morphologies, which would respectively change the thickness of the reactive shell that needs to be considered to predict the rates of pre-ignition reactions. The approach outlined above and relying on the measured SA and TG traces can be used universally.

The same core-shell model can be used to interpret the aging experiments shown in **Figure 5.12**. Analogous to oxide formation during thermal analysis, hydroxide formation occurs only in the outer shell. The point at which the measured heat flow drops to the noise level, at about 390 ks for the spheroidal aluminum milled for 2 h and at about 370 ks for the nonporous reference Al (**Figure 5.12**), serves as a convenient reference point for comparison, representing a state where aging has slowed to comparable low rates. In the analysis below, bayerite $Al(OH)_3$ is the hydroxide reaction product and the molar enthalpy of its formation is $\Delta H_{f,hyd}$. The bayerite molar mass and its thickness grown on the aluminum surface are referred to as M_{hyd} and h_{hyd} respectively. The reaction enthalpy is obtained as:

$$\Delta H_r = \Delta H_{f,hyd} \cdot \frac{m_{Al,reacted}}{m_{Al,0}} = \Delta H_{f,hyd} \frac{h_{hyd} \cdot \rho_{hyd} \cdot \mathrm{SA} \cdot \mathrm{m}_{shell,0}}{M_{hyd}} \cdot \frac{M_{Al}}{m_{Al,0}} \qquad (5.9)$$

Substituting Eq. (3) for the initial shell mass and similarly expressing the initial total mass of Al in a porous spherical particle, $m_{Al,0}$, one obtains:

$$\Delta H_r = \Delta H_{f,hyd} \cdot \frac{h_{hyd} \cdot \rho_{hyd} \cdot \mathrm{SA} \cdot \mathrm{M}_{Al}}{M_{hyd}} \cdot \frac{\rho_{Al}(1-\Phi)\frac{4}{3}\pi\left({r_p}^3 - \left(r_p - h_{shell}\right)^3\right)}{\rho_{Al}(1-\Phi)\frac{4}{3}\pi \cdot {r_p}^3} \quad (5.10)$$

Simplifying, the reaction enthalpy for a porous spherical particle is expressed as

$$\Delta H_r = \Delta H_{f,hyd} \cdot \frac{h_{hyd} \cdot \rho_{hyd} \cdot \mathrm{SA} \cdot \mathrm{M}_{Al}}{M_{hyd}} \cdot \left(1 - \left(1 - \frac{h}{r_p}\right)^3\right) \quad (5.11)$$

Conversely, for the reference -325 mesh Al, which is not porous, and has an experimentally determined surface area of SA_{Al} = 2.0 m 2 /g, the heat of reaction is

$$\Delta H_r = \Delta H_{f,hyd} \cdot \frac{h_{hyd} \cdot \rho_{hyd} \cdot \mathrm{SA}_{Al} \cdot \mathrm{M}_{Al}}{M_{hyd}} \quad (5.12)$$

The heat flow drops to the noise level for -325 mesh Al at a total evolved heat of 1.055 kJ/g = 28.5 kJ/mol. Therefore, the thickness of the hydroxide on the particle surface, calculated by rearranging Eq. (12), evaluates to h_{hyd} = 29 nm for this reference powder. This can be taken as a reference state, where the hydroxide layer is thick enough to slow the reaction rate to the measurement noise level. For the spheroidal milled aluminum, this state is reached at a total evolved heat of 0.478 kJ/g = 12.9 kJ/mol (**Figure 5.12**). If h_{hyd} is thus known, the thickness of the shell where the hydroxide grows is estimated from Eq. (11) as

$$h_{shell} = \mathrm{r}_p \cdot \left(1 - \left(1 - \frac{\Delta H_r}{\Delta H_{f,hyd}} \frac{M_{hyd}}{h_{hyd} \cdot \rho_{hyd} \cdot \mathrm{SA}_{Al} \cdot \mathrm{M}_{Al}}\right)^{\frac{1}{3}}\right) \quad (5.13)$$

For a 30-μm particle, it is obtained that h shell = 0.17 μm. This is likely a lower limit, and the fraction of the particle participating in reaction is higher. The nitrogen adsorption

measurements (**Figure 5.7**) suggest that the average pore half-width of these materials is on the order of 1 nm, less than the 29 nm of hydroxide growing on the nonporous reference material. Therefore, there is not enough space to grow 29 nm of hydroxide on the Al surface in the shell, even accounting for changes in pore shape and size due to the hydroxide growth. If one were to assume 1 nm as an upper limit for the hydroxide layer thickness within the spheroidal milled aluminum, the reacted shell on a 30 μm particle would evaluate to $h_{shell} \approx 6$ μm according to Eq. (13) . The actual shell thickness is within these upper and lower bounds of 6 μm and 0.17 μm, respectively, and likely with nonuniform hydroxide distribution, i.e., the complete reaction close to the particle surface, and decreasing hydroxide amounts deeper in the particle. Regardless of these details, the density of the growing hydroxide is less than that of the unreacted aluminum, ensuring that the pores of spheroidal milled aluminum are blocked soon after the material's exposure to a humid oxidizing environment, well before the hydroxide thickness reaches 29 nm, as required to slow down aging for regular aluminum. The blocked pores provide an effective protective barrier for the remaining unreacted core of the spheroidal milled aluminum, preventing further rapid aging.

If all aluminum inside a reacting shell with a lower-limit estimate thickness of 0.17 μm were fully reacted, ca. 3.4% of all available aluminum in a 30-μm diameter particle would have been consumed. However, the results shown in **Figure 5.12** show that only about 2.2% of aluminum was consumed, which would comprise approximately 65% of aluminum within the shell. This relatively high fraction of aluminum consumed within the porous shell reflects the high specific surface area of the spheroidal milled aluminum.

While additional detailed studies involving cross-sectioned partially reacted powders are necessary to further describe processes occurring during oxidation and aging for the prepared spheroidal aluminum, it is clear that the approach involving a reacting shell and inert core is fruitful and can be used to describe reactions in such powders in the future.

5.4 Conclusions

Spheroidal aluminum particles were produced by mechanical milling of non-spherical commercial aluminum powder in a hexane-acetonitrile emulsion serving as process control agent. The average particle size decreased as the milling time was increased from 1 to 2 h. The resulting spheroidal particles consisted of packed plate-like aluminum flakes. The spheroidal milled aluminum ignited on an electrically heated Kanthal strip at about 750 – 900°C, whereas no ignition could be achieved for regular micron-sized aluminum powders in similar experiments. Oxidation of the spheroidal milled aluminum in TG experiments proceeded significantly faster than for micron-sized aluminum; the early stages of oxidation approached the behavior expected of nano-sized aluminum powders. The reaction for spheroidal milled aluminum proceeded to a greater completeness than for nano-powder, in agreement with the expected much greater content of active aluminum. Thermoanalytical experiments suggested that the overall oxidation stages and their respective activation energies for spheroidal milled aluminum are similar to those of other aluminum powders. However, their oxidation is accelerated because of the particle morphology and an available specific surface area significantly exceeding that of micron-sized aluminum. For the purpose of modeling reactions leading to ignition, these particles can be described as having a reactive shell and an inert core. The results suggest that the

ignition can be triggered when the oxidation is accelerated by the polymorphic phase change from amorphous to γ-alumina in the growing oxide layer. The same core-shell model needs to be considered to describe aging of these powders. At 60°C and air with 80% relative humidity, the aging of spheroidal milled aluminum effectively stops when only ca. 2.2 % of the available aluminum is consumed; for the commercial non-porous aluminum aged at the same conditions, almost 5% of the active aluminum is consumed before the reaction slows to the same rate. The results are interpreted to suggest that the aging of spheroidal milled aluminum in humid environments at low temperatures is controlled by sealing the pores in the reactive shell by the growing layer of hydroxide effectively protecting the core from further reaction.

CHAPTER 6

TITANIUM-BORON REACTIVE COMPOSITE POWDERS WITH VARIABLE MORPHOLOGY PREPARED BY ARRESTED REACTIVE MILLING

6.1 Introduction

The superior thermodynamic potential of metals and metalloids, which readily oxidize in air, has been well established in the literature [38, 246]. Common high-energy density fuels include aluminum, titanium, and boron[352-355]. Respective elemental powders possess inherent limitations in reaction completeness and sensitivity, as has been extensively studied previously[356-358]. Successful methodologies to improve their performance include an increase in the reactive surface area (or use of nano-materials[359, 360]) and the use of preliminary solid phase (intermetallic) reactions to preheat the fuel up to a more kinetically favorable reaction temperature [156, 361-363]. Boron-titanium composite powders are among the most attractive based on their thermodynamic properties illustrated in **Figure 6.1**. For both nominal compositions, Ti·B and Ti·2B, the heats of formation of respective borides are substantial, although they are always much less than heats of oxidation. For comparison, heats of oxidation for elemental aluminum are also shown in **Figure 6.1**. It is apparent that the boron-titanium composites are expected to outperform aluminum based on the volumetric heat of oxidation. The composite containing more boron, Ti·2B, is also expected to outperform aluminum based on the gravimetric heat of oxidation. For boron-titanium composites, ignition can be governed by the exothermic formation of borides. Thus, unlike aluminum, these materials can ignite in oxidizer-deprived environments, as exist, for example, inside a fireball produced by an explosive. Once ignited, these materials are expected to burn when exposed to oxidizer. Indeed,

formation of borides raises the composite particle temperature sufficiently high for it to oxidize readily when it reaches the periphery of the fireball and becomes exposed to air. As a result, complete theoretical heat release is expected as shown in **Figure 6.1**. The attractive energetics for boron-titanium composites motivates interest in such materials as potential replacement of aluminum in various energetic formulations.

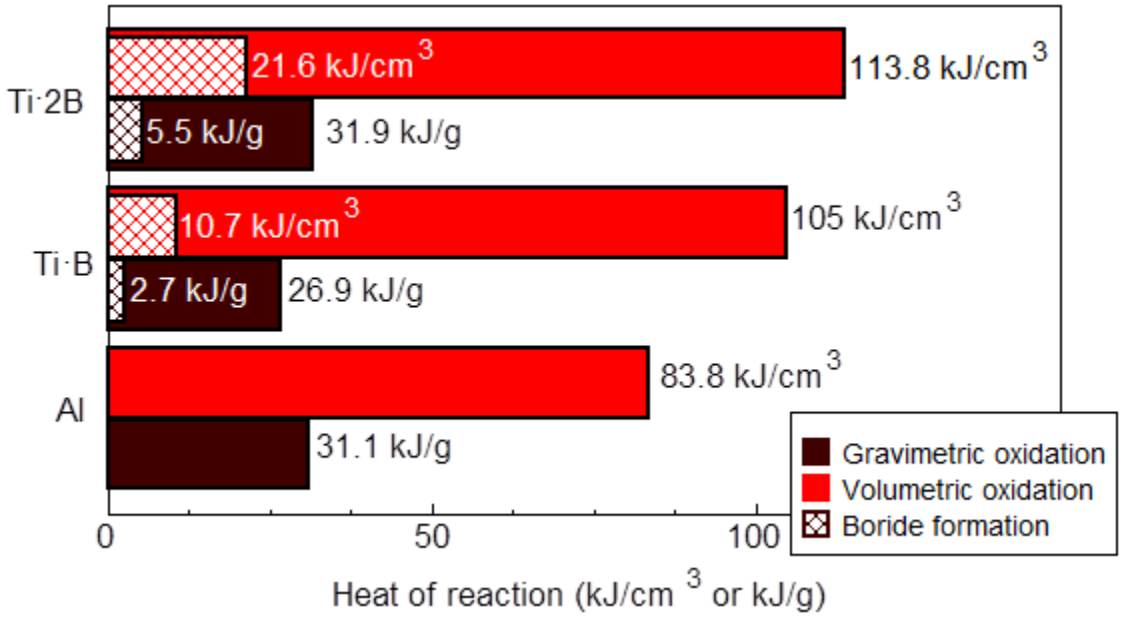

Figure 6.1 Theoretical heats of intermetallic reaction in prepared composite powders as well as heats of oxidation for both the prepared composites and aluminum.

Arrested reactive milling (ARM) [364] was previously used to prepare reactive composites of boron and titanium [25, 28, 268]. However, the broad ranges of particle sizes it produced made it difficult to tune their combustion performance. Adjusting particle size distributions of the powders prepared by mechanical milling proved to be difficult when the material structure should be optimized along with the particle morphology.

Recently it has been demonstrated that mechanical milling can produce narrowly sized spherical powders using a variety of materials including aluminum, boron, iron oxide, melamine, and sucrose [365, 366]. Spherical powders are formed when starting

components are milled in the presence of two immiscible liquids serving as process control agent (PCA) [367]. The immiscible liquids form an emulsion, which also contains a suspension of the powder being milled. Mechanical activation causes solid particles to aggregate in the droplet phase, ultimately forming composite spherical powders with the size distribution controlled by the size of the emulsified droplets. Produced spherical powders are attractive for formulators of energetic compositions[368] and as feedstock for additive manufacturing[369-371]. Here this mechanical milling-based approach is explored for preparation of boron-titanium reactive composites. Both spherical and irregularly shaped powders are prepared by ARM with liquid PCAs and their characteristics are compared using thermal analysis and ignition measurements.

6.2 Material Preparation

Composite powders were prepared using high-energy ball milling of elemental boron and titanium powders. Starting components were powders: boron (SB95, 95% purity by SB Boron) and -325 mesh titanium (-325 mesh, 99.8% purity by Atlantic Equipment Engineers). The powders were blended in a 2:1 or 1:1 molar ratio to yield, respectively, stoichiometric TiB_2 and TiB reaction products.

A Retsch PM 400 planetary mill was used with both standard 500 mL as well as custom built 180 mL hardened steel vials. The mill was equipped with an air conditioner used to chill the milling compartment. The mill was operated at 350 rpm with the rotation direction switching every 15 minutes. The milling media were hardened steel balls, 3/8 inch (9.52 mm) diameter.

A schematic diagram illustrating the steps involved during preparation of different composite powders is shown in **Figure 6.2**. Further details are given in Table 1 showing also the resulting powder particle shapes and average sizes (see details below). Milling process characteristics shown in **Table 6.1** were selected following a preliminary study, in which these characteristics varied. The products obtained were evaluated using x-ray powder diffraction, particle size analysis and scanning electron microscopy (SEM). The parameters leading to the powders with most spherical shapes as observed by SEM were selected and used in further experiments.

Irregularly shaped composites were prepared using one milling stage. Boron and titanium powders were loaded into the milling vials, a liquid process control agent (PCA) was added, and the powders were milled for a prescribed time. In most cases, hexane (Hex. in **Table 6.1**) served as the PCA in this milling stage. Milled powders were dried under vacuum. For preparing spherical powders, dried irregular composite powders remained in the milling vial. Two liquids, hexane and acetonitrile (ACN in **Table 6.1**), were added for the second milling stage. The ball to powder mass ratio (BPR) was changed and the second stage of milling was performed. Sizes of the prepared spherical powders were altered varying the amounts of hexane and acetonitrile used during stage 2 milling and BPR.

For both Ti·B and Ti·2B composites, samples of powders prepared with one-stage milling (4 h milling time) and serving as precursors for preparing spherical powders were recovered and characterized. In addition, for Ti·2B composites, irregularly shaped powders were prepared using an extended milling time during stage 1 milling to match the milling dose used to prepare spherical powders. Milling dose [372] serves as a measure of energy transferred from milling tools to the powder being milled and can be roughly considered

to be proportional to the product of charge ratio and milling time. Two such Ti·2B composite powders were prepared using both hexane and acetonitrile as PCA (see **Table 6.1** for details). Particle compositions, shapes, and average particle sizes listed in **Table 6.1** are used to identify different powder samples in further discussion.

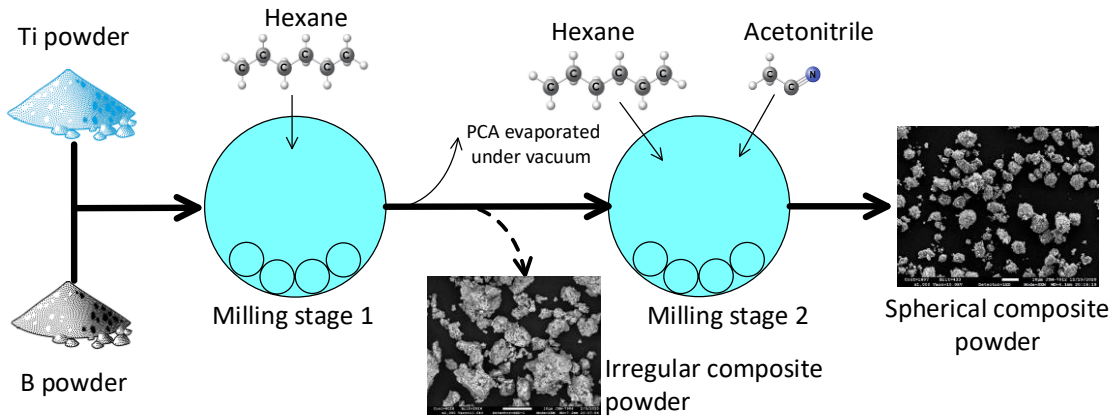

Figure 6.2 Process diagram illustrating preparation of composite powders.

Table 6.1 Milling Conditions used to Prepare Composite Powders

Product powder			Milling vial volume, mL	Batch mass, g	Stage 1				Stage 2			
					Volume, mL		BPR	Mill. time, h	Volume, mL		BPR	Mill. time, h
Material	Shape	Avg. size, μm			ACN	Hex.			ACN	Hex.		
Ti·B	Irregular	18	500	25	0	20	3	4	-	-	-	-
	Spheres	93	180	15.4	0	12.3	3	4	4	20	5.94	1.5
		20	180	7.7	0	6	9	4	2	10	11.87	2
Ti·2B	Irregular	11	500	25	0	20	3	4	-	-	-	-
		5.6	180	7	0	15	12.5	5	-	-	-	-
		7.8	180	7	15	0	12.5	5	-	-	-	-
	Spheres	160	180	14	0	11.2	3	4	4	20	6.53	1.5
		7.5*	180	7	0	6	9	4	2	10	11.87	2

*Seven batches of the fine spherical Ti·2B were prepared with some variation in size distribution as shown in Appendix B, Fig. S1. These variations are relatively small and represent reproducibility of the experiment.

6.3 Characterization of the Prepared Composite Powders

Particle size distributions were measured using a Malvern Panalytical Mastersizer 3000 with a hydro MV sampling unit. Powders were dispersed in ethylene glycol.

Electron microscopy was performed using a JEOL JSM-7900F field emission SEM. Both as prepared and cross-sectioned powder samples embedded in epoxy were examined. Images were taken with a secondary electron detector at 10 kV for full particle images, a backscattered electron detector at 3 kV for high magnification cross sections and at 7kV for wider field of view cross sections of entire particles. Transmission electron microscopy (TEM) was performed using a JEM-F200, operated at 200 kV. As-milled particles were deposited dry on a copper grid.

Prepared materials as well as materials recovered after thermo-analytical measurements were characterized by powder x-ray diffraction (XRD) using a PANalytical Empyrean x-ray diffractometer operated at 45 kV and 40 mA using Cu Kα radiation (λ= 1.5438 Å). Samples were mounted on a zero-background sample holder cut from a Si single crystal.

Specific surface of the prepared powders was measured by nitrogen gas sorption analysis at 77 K using a Quantachrome Autosorb iQ-MP, Automated Gas Sorption Analyzer. A 52 point adsorption/16 point desorption full isotherm was measured after degassing samples for 390 minutes at 115 ºC.

Thermo-analytical measurements, including differential scanning calorimetry and thermo-gravimetry (DSC/TG) were performed using a Netzsch Thermal Analyzer STA409PG. The samples were heated at 5 and 40 ºC/min in a flow of argon (99.998 % pure by Airgas, flown at 50 mL/min). For each experiment, the heating program was repeated without removing the sample; the traces recorded during the second heating

served as baselines. Samples heated at 5 ºC/min were recovered after the second heating and inspected using XRD. Using a Netzsch Thermal Analyzer STA449F3, samples were also heated at 10 ºC /min in a mixed flow of argon and oxygen (respective flowrates were 55 and 15 mL/min). For a baseline, these samples were heated at the same rate for the second time in pure argon flown at 70 mL/min. In initial experiments, samples were heated up to 1100 ºC; however, evaporating boron oxide was found to damage the sample carriers. Respectively, in following experiments the maximum temperature was reduced to 800 or 900 ºC, for which the evaporation of boron oxide was noted to be nearly negligible.

Ignition of the prepared powders was characterized using an experimental setup employing an electrically heated filament similar in configuration to those described previously [152, 171, 373, 374]. Unlike previous experiments, powders were deposited onto a rectangular nickel-chromium wire with a cross-section of 0.8 × 0.1 mm. The flat wire had to be used to enable measurements for the produced spherical powders, which could not be retained on cylindrical wires used in most previous experiments.

The wire temperature as a function of time was measured using an optical pyrometer comprised of a germanium switchable gain detector (Thorlabs PDA30B2) calibrated using a black body emission source BB-4A by Omega. The optical pyrometer was equipped with a fiber optics cable with a lens. It was used to measure temperature of an uncoated wire heated using a fully charged 12-V battery. Because the pyrometer lens was placed above the heated wire, it could not be used with the powder coatings, generating rising combustion products, which could damage the lens. Thus, after preliminary experiments using pyrometer established the wire temperature history, the pyrometer was removed. Powder coatings were then applied and heated using the same battery. The instant

of ignition was registered using a RedLake MotionPro 500 high-speed camera. The time reference indicating the beginning of the wire heating was obtained using the same video, recording emission of an LED lit at the onset of the heating. It was observed that the wire was heated at approximately 3,200 ºC/s in the temperature range of 500 to 1100 ºC. Correlating the preliminarily obtained temperature histories of the heated wires with the times of ignition measured in separate experiments enabled us to determine the ignition temperature for each powder tested.

6.4 Results and Discussion

6.4.1 Characteristics of the prepared materials

Preliminary observations showed distinct difference in flowability of the prepared powders. Spherical powders were observed to flow much better. Qualitatively, the improved flowability is illustrated in the photo showing both spherical and irregularly shaped powders filling a glass bottle (Appendix B, Fig. S2). The surface of the spherical powder is characteristically smoother.

SEM images of the prepared irregularly shaped and spherical composite powders are shown in **Figure 6.3** Irregularly shaped powder particles are roughly equiaxial. For both Ti·B and Ti·2B composites, the material surface is mostly bright, representing titanium matrix. Dark inclusions observed for both powders represent boron particles. Spherical particles obtained with two distinct size ranges for each composition. Surface of spherical particles appears to include multiple small pores. Thus, the spheres appear to be dense compacts of much finer particles, which cannot be distinguished clearly at the sphere surfaces.

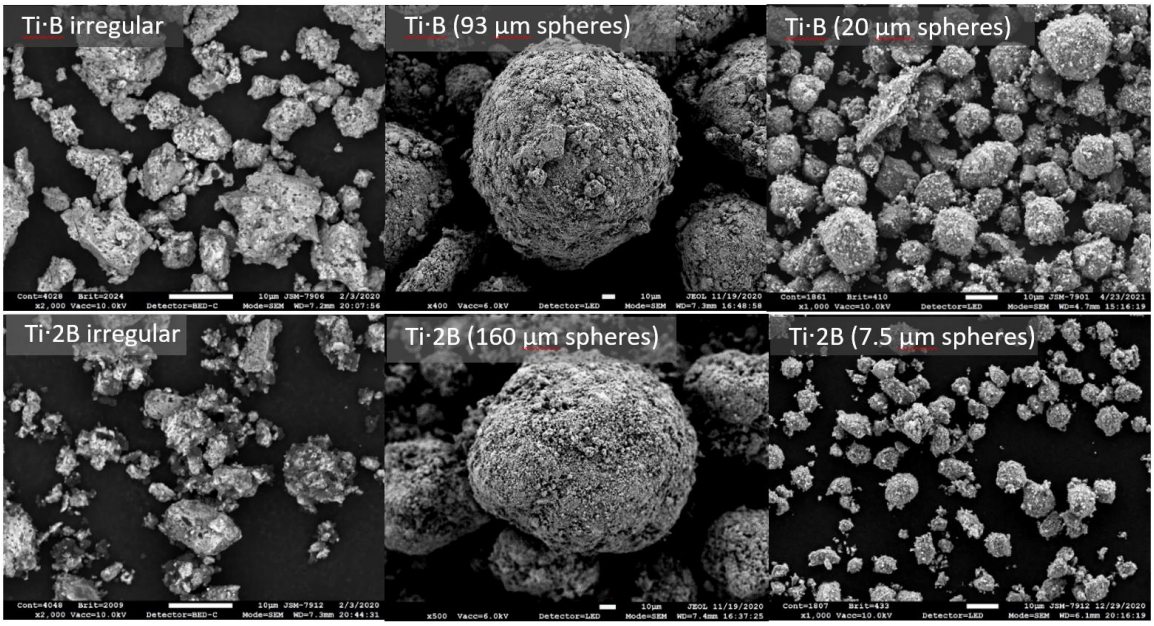

Figure 6.3 Backscattered electron images of as-prepared irregular composite powders, and secondary electron images of as-prepared spherical composite powders.

Particle size distributions of different composite powders are shown in **Figure 6.4** and **Figure 6.5**, for Ti·B and Ti·2B composites, respectively. Average particle sizes and half widths of the distributions are shown for each material. Particle shapes and average size for each sample can serve as identifiers for respective milling conditions shown in **Table 6.1** Milling Conditions used to Prepare Composite Powders. Irregularly shaped powders have relatively broad particle size distributions with the ratios of half width to the average size close to 1.9 for both materials. Narrower size distributions are observed for all spherical powders. The ratios of half width to the average size vary from 1 to 1.38 for different samples. Particle size distributions shown in **Figure 6.4** and **Figure 6.5** were obtained before sonication of the suspended powder samples. It was observed that the sizes of irregularly shaped powders were not affected by sonication. For smaller spherical powders, sonication destroyed large agglomerates, such as clearly seen for Ti·B spheres with average size of 20 µm (particles greater than ca. 50 µm in **Figure 6.4**). However, the mode of the particle size distribution for fine spherical powders remained unaffected by

sonication. Conversely, larger size spherical powders could not withstand the agitation of the suspension subject to sonication. The particle size distributions shifted significantly as shown in Appendix B, Fig. S3.

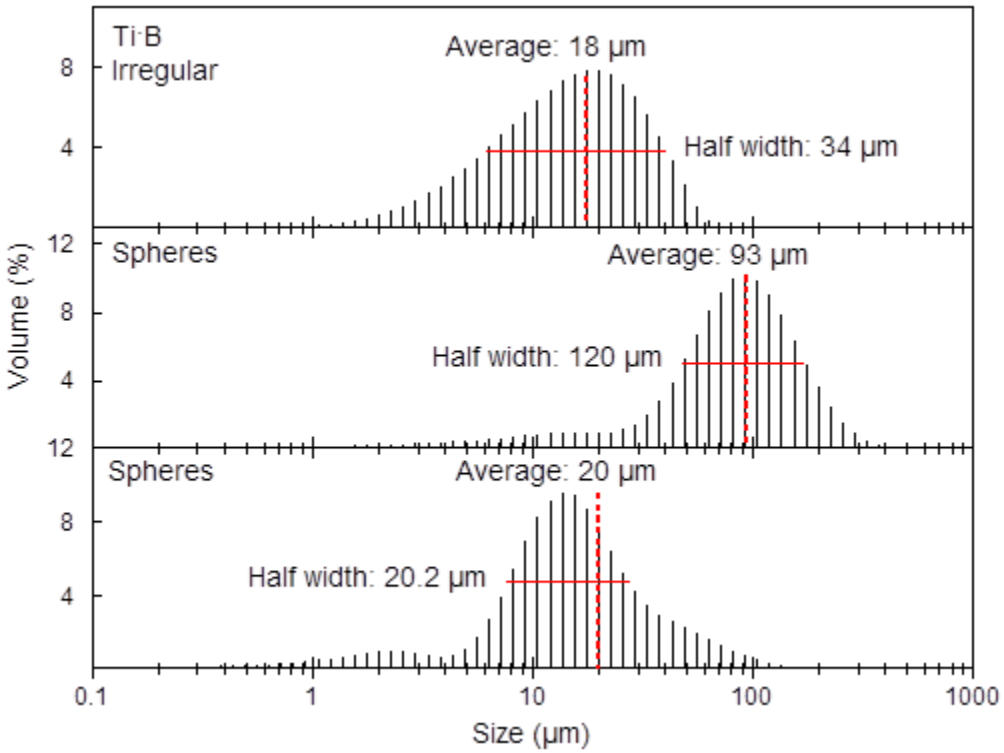

Figure 6.4 Particle size distribution of Ti·B composite powders.

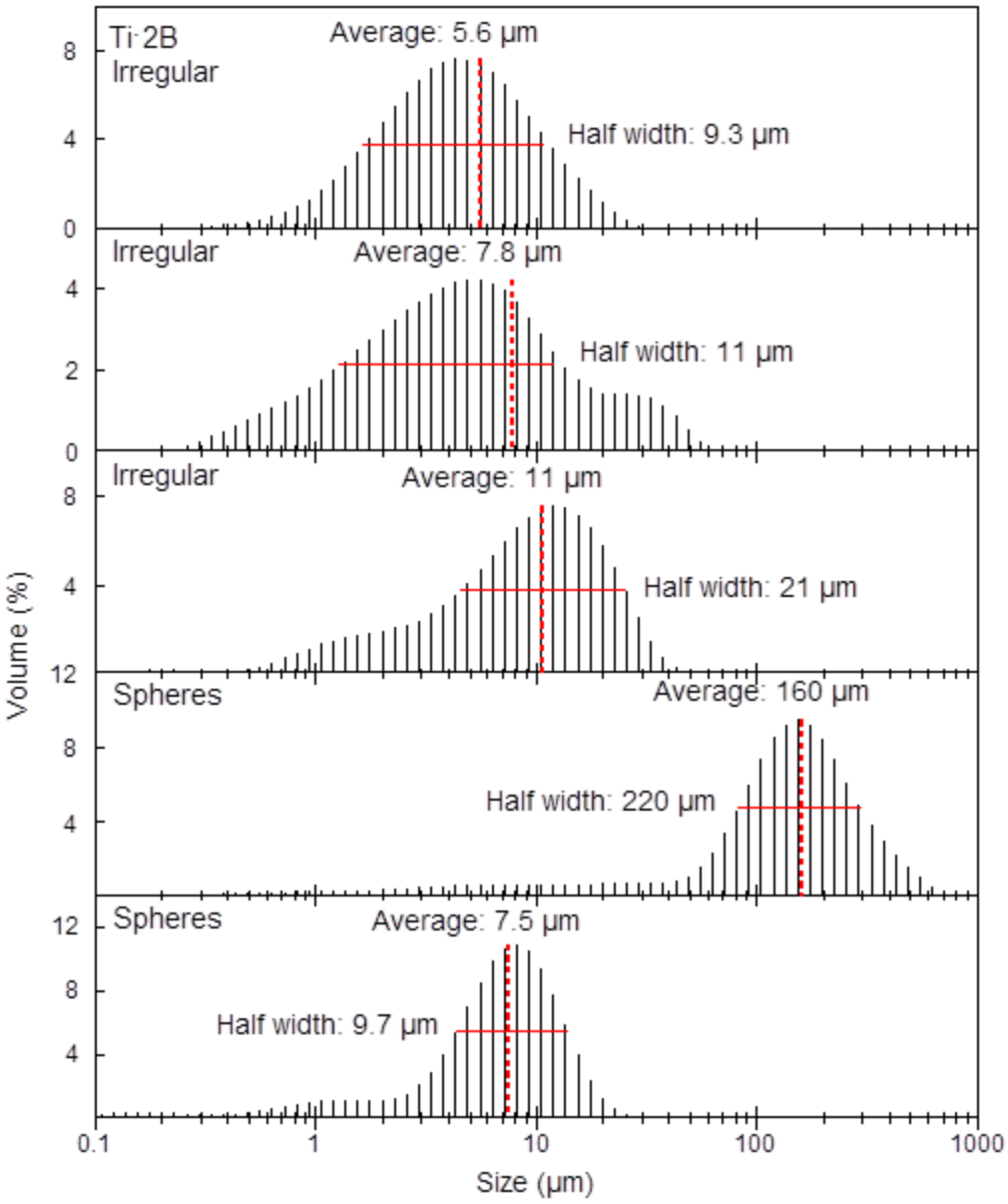

Figure 6.5 Particle size distribution of Ti·2B composite powders.

SEM images of different composite powders embedded in epoxy and cross-sectioned to observe their internal structure are shown in **Figure 6.6** through **Figure 6.10**. For each material, two images taken at different magnifications are shown. Cross sections of irregularly shaped powders for both composites (**Figure 6.6**, **Figure 6.7**) show a fully dense structure with a bright titanium matrix and dark (almost black) boron inclusions. Most boron inclusions are substantially smaller than 1 µm, although some large boron

inclusions are also observed. The structures are qualitatively similar for both irregularly shaped materials. Some dark grey particles are observed; both separated from and embedded into composite structures. These particles are likely representing contamination by iron coming from the milling media.

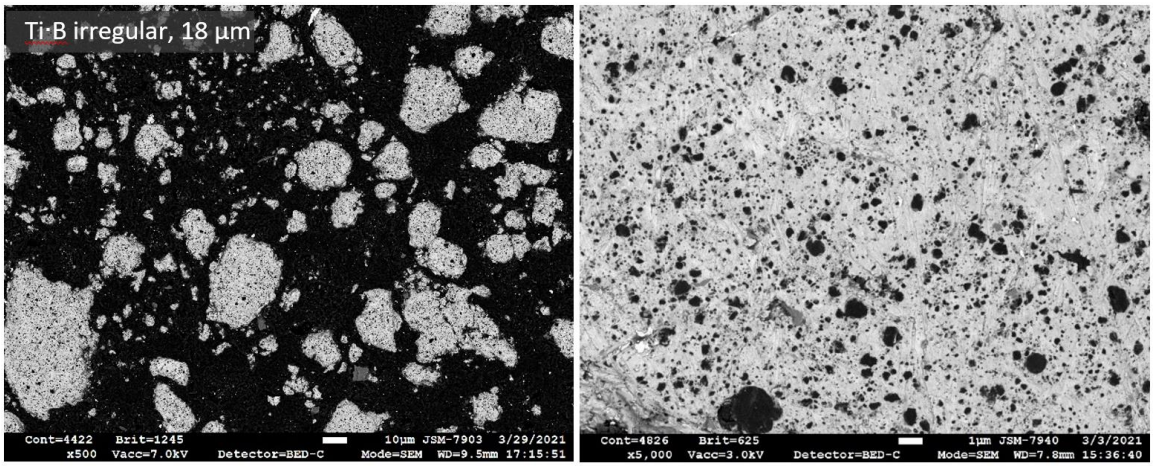

Figure 6.6 Backscattered electron images of cross-sectioned Ti·B irregular powders.

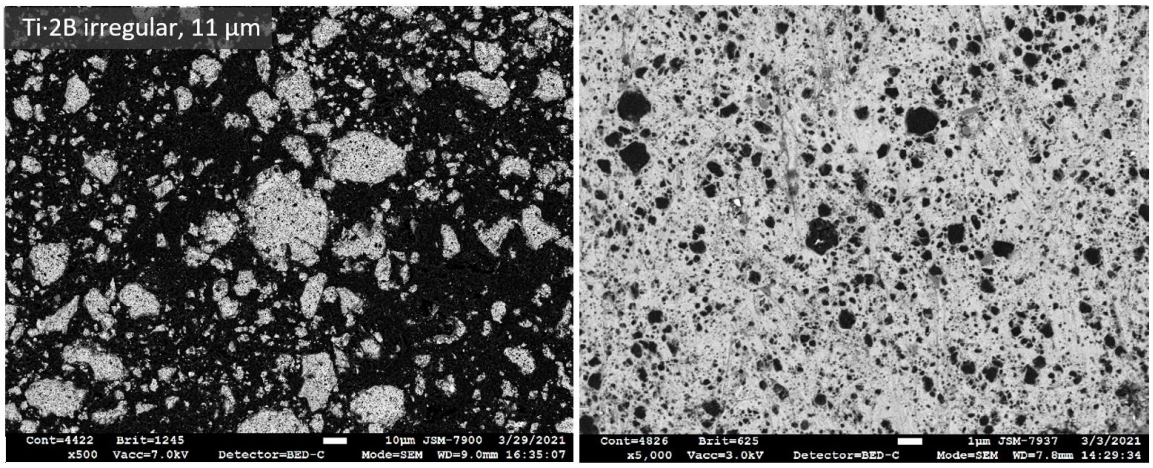

Figure 6.7 Backscattered electron images of cross-sectioned Ti·2B irregular powders.

Cross-sections of spherical composite powders are shown in **Figure 6.8** - **Figure 6.10**. The interiors of the particles images at a lower magnification are distinctly darker than those of the irregularly shaped powders with the same compositions. The close-up images show that the titanium matrix is discontinuous. Because the bulk compositions of the materials are the same as for irregularly shaped powders, this suggests substantial

porosity of the prepared spheres. Boron is difficult to separate in the images from the background epoxy, which could have been embedded into porous particles. Characteristic porous structures with discontinuous titanium particles are observed for all prepared spherical powders. The dimensions of titanium inclusions vary broadly; however, it is apparent that these dimensions are smaller for the finer spherical powder.

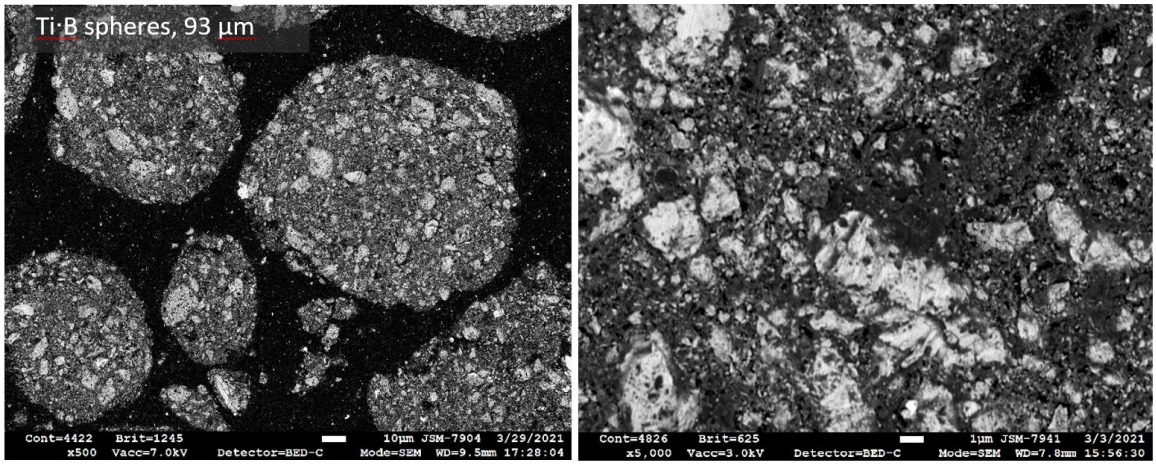

Figure 6.8 Backscattered electron images of cross-sectioned Ti·B spherical powders (93 µm average diameter).

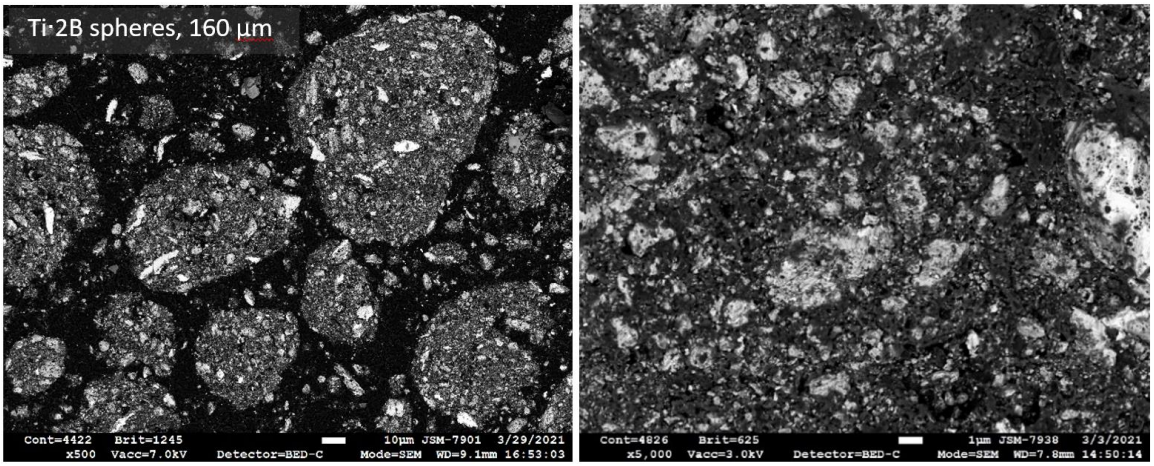

Figure 6.9 Backscattered electron images of cross-sectioned Ti·2B spherical powders (160 µm average diameter).

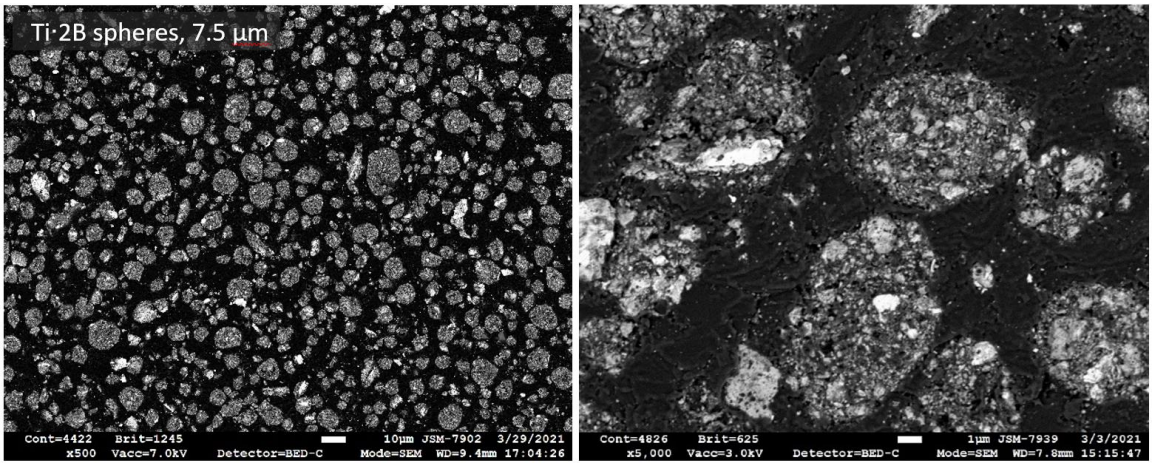

Figure 6.10 Backscattered electron images of cross-sectioned Ti·2B spherical powders (7.5 µm average diameter).

Results of specific surface measurements for different composite powders are shown in **Figure 6.11**. Spherical powders have consistently greater surface areas than irregularly shaped powders. This is consistent with the porosity observed for the spherical particles in their cross-sections (**Figure 6.8** - **Figure 6.10**). No correlation between the size of spherical particles and their surface area is observed.

The surface areas of different powders can be used to roughly estimate their average surface-based particle diameters. These diameters are obtained from the ratio of the theoretical specific volume and the measured specific surface area. For irregular powders, the estimated diameters are close to 1 and 0.6 µm for Ti·2B and Ti·B, respectively. From particle size distributions, (**Figure 6.4** and **Figure 6.5**) their respective surface area based average particle sizes are 3.7 and 9.6 µm. This suggests some porosity in the prepared powders, which is more significant for Ti·B composite. A similar estimate for spheres, with greater specific surface area (**Figure 6.11**) yields the estimated size for fully-dense particles in the range of 100 – 130 nm, which is much smaller than the surface average particle sizes measured by light scattering, varied from 2.5 (for finer spherical Ti·2B) to 31.5 (for coarse Ti·B spheres). The larger discrepancy between the particle sizes implied

by light scattering and nitrogen adsorption measurements is consistent with significant porosity in the prepared spherical powders.

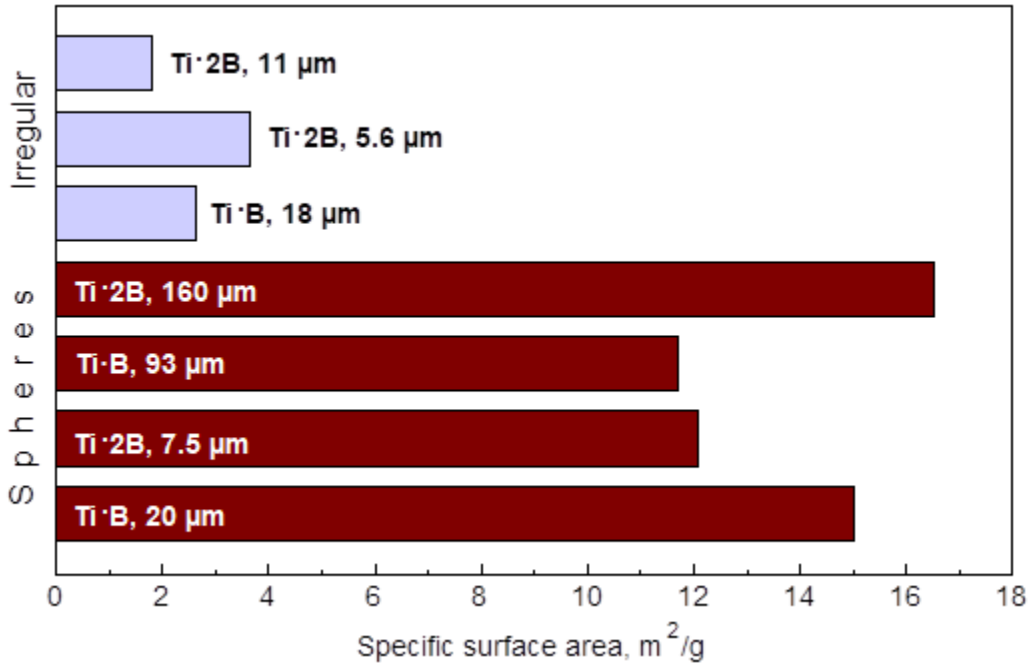

Figure 6.11 Specific surface measured by nitrogen adsorption for the prepared composite powders.

XRD patterns of different prepared composite powders are shown in **Figure 6.12**. A pattern for the starting blended (unmilled) powders of boron and titanium with the composition Ti·2B is shown for comparison. The vertical scale for the blend was adjusted down for the pattern to fit in **Figure 6.12**. Peaks observed for the milled powders are generally broad, weak, and the intensity drops rapidly at higher diffraction angles. Phases identified with reasonable confidence are α-Ti with hcp structure, a cubic phase matching TiB with fcc structure, and Fe that was introduced by the milling tools as a significant contamination. The Ti phase remains recognizable in the irregular powders and the large spheres for both, Ti·B and Ti·2B compositions. Titanium can no longer be clearly distinguished in the small sphere powders, and in the irregular powder with Ti·2B composition milled with the same milling dose as the corresponding small sphere powder.

The TiB phase is clearly present in all powders. The amount of iron as a distinct phase increases with increasing milling dose for both, Ti·B and Ti·2B compositions. No peaks corresponding to TiB_2 were detected in any of the patterns. Amorphous boron is not detectable by XRD, as expected. Only a trace of boric acid can be seen in the reference powder blend.

Not clearly identifiable from the peaks shown in **Figure 6.12** is a phase that appears to be cubic and was tentatively attributed to α-Ti with bcc structure. Without introducing this phase, the intensities for at least the Ti·2B irregular powder in the range 35° - 45° 2θ cannot be reconciled with the other identified phases. The bcc phase of Ti is nominally unstable below 882 °C, but iron stabilizes it to lower temperatures under equilibrium conditions [375]. Still, the presence of this phase here is speculative, and the derived phase compositions must therefore be considered semi-quantitative.

Phase compositions of the as-milled materials were determined by whole-pattern refinement, using nominal compositions of the phases. The results are shown in **Figure 6.13**. Minor differences can be seen between the irregular powders and the larger spheres for both, Ti·B and Ti·2B compositions. The amount of metallic Ti in the larger spheres is slightly less than in the irregular powder for Ti·B, but slightly more for the Ti·2B composition. Because the larger spheres were prepared by further milling of the irregular powders, this is an unexpected result, and likely illustrates the uncertainty of the quantification in general, and of the assignment of the α-Ti phase. The cubic TiB phase increases significantly for both smaller spheres and for the irregular powder milled with the same milling dose as the smaller spheres. Consistent with expectations, the amount of metallic Fe continuously increases with continued milling.

In a separate experiment, not shown for brevity, the small sphere powder for the Ti·2B composition was blended with a known amount of γ-alumina as an internal standard. This allowed determining the amount of metallic iron using the reference intensity ratio method to 11.8 wt-%. This value is distinctly smaller than the approximately 28 wt-% obtained by whole pattern fitting, and shown in **Figure 6.13**. This is consistent with the presence of about 50 wt-% of amorphous material in this powder. The other powders likely contain significant amounts of amorphous material as well.

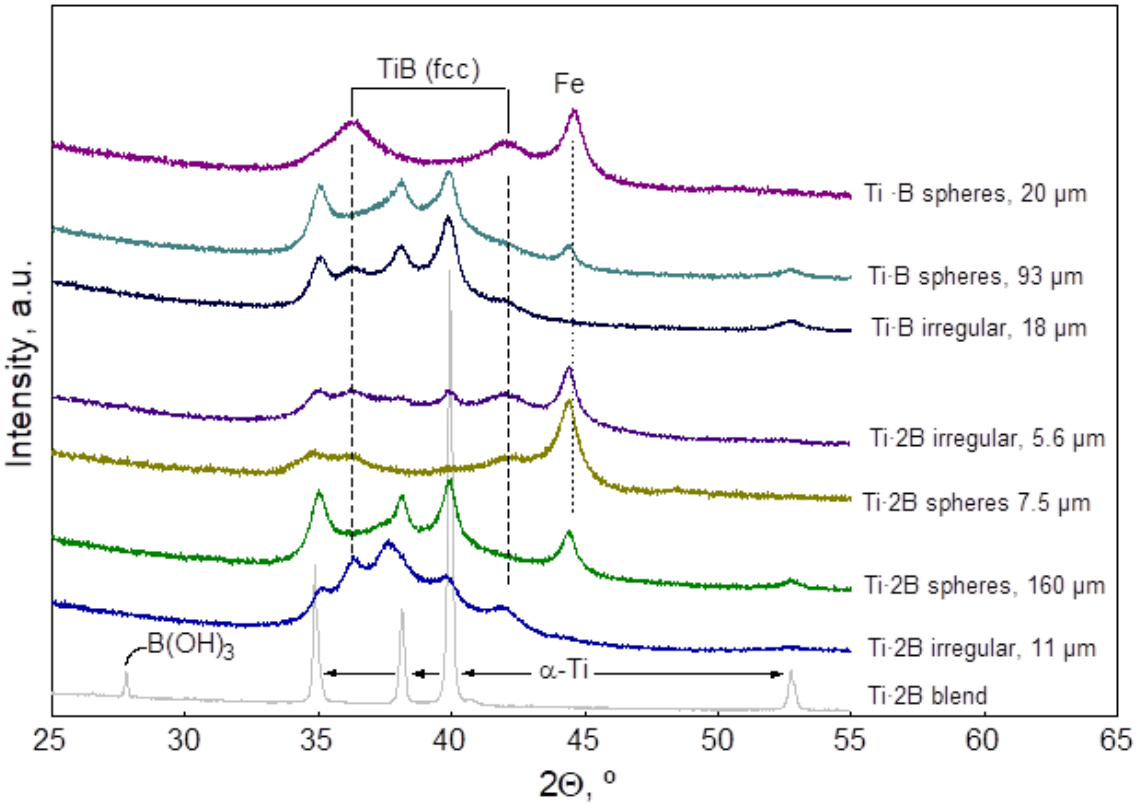

Figure 6.12 XRD patterns for the prepared composite powders. For reference, an XRD pattern for the Ti·2B powder blend is also shown.

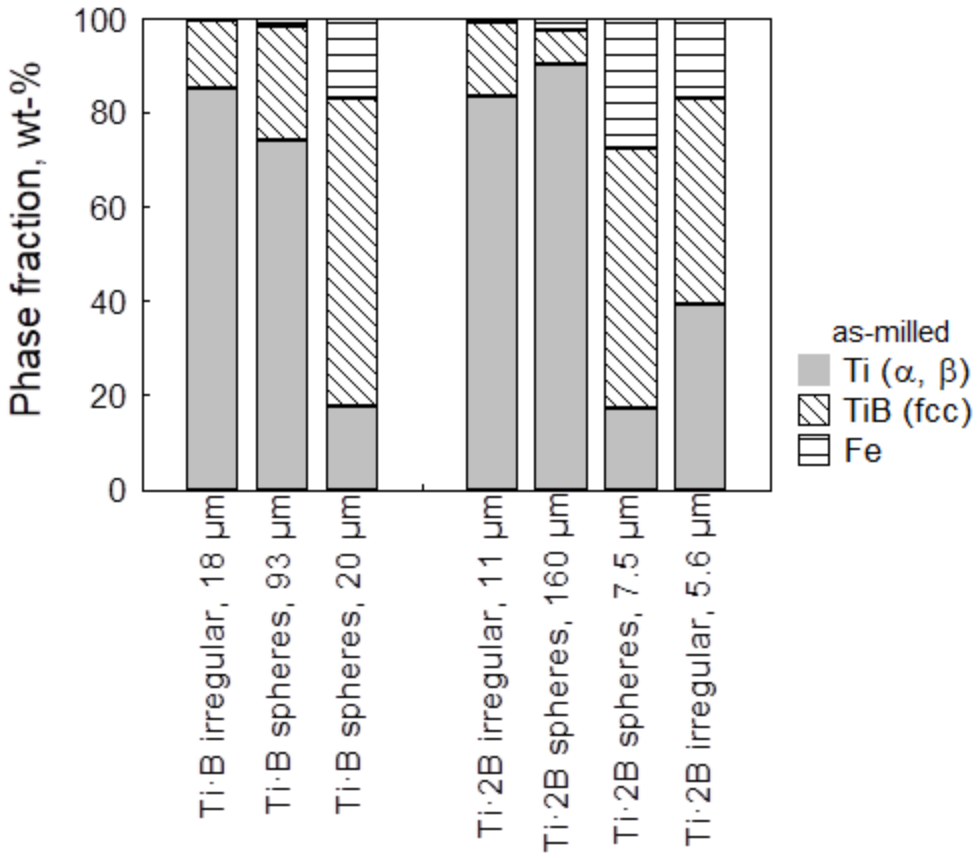

Figure 6.13 Phase compositions of the crystalline phases in prepared composite powders from the whole pattern fitting for XRD; the presence of amorphous phases is not accounted for.

6.4.2 Reactivity of the Prepared Materials

Baseline-corrected DSC and TG traces for four composite Ti·2B powders are shown in **Figure 6.14**. Only DSC traces are shown for the powders heated in argon; respective TG traces showing minor mass loss due to evaporation of adsorbed PCA are omitted for brevity. For both spherical powders heated in argon, DSC traces show an immediately rising background. Both traces show a broad exothermic hump with peak around 570 ºC. For spheres with 160 µm average size, the broad exothermic hump overlaps with a second broad peak around 850 ºC. Integration of the entire DSC signals measured in argon for spherical powders yields values that exceed, roughly by a factor of two, the total heat release expected for the formation of TiB_2. Because no other exothermic reactions are

expected for these materials heated in argon, it is concluded that the effect of baseline could not be eliminated from these measurements, despite subtracting a trace measured during the second heating. The same conclusion was made for the DSC traces recorded for the samples heated in argon-oxygen environment. Nevertheless, the obtained DSC traces can serve to compare qualitatively the reactive behaviors of different composite powders.

Qualitatively, the DSC traces recorded in argon for spherical powders are different from those obtained for both irregularly shaped powders. Both irregular powders (one, 11 μm prepared using a lower milling dose than used preparing spheres, and the other, prepared with the same milling dose as fine spheres, 5.6 μm) show no early exothermic reactions. Broad and weak exothermic features are observed to begin around 470 and 520 ºC for the 5.6- and 11-μm powders, respectively. Integrating an exothermic peak observed for 11-μm irregular powder around 670 ºC gives about 10% of the energy expected for the formation of TiB_2. It is thus apparent that the heat release observed for both irregularly shaped powders heated in argon is insignificant.

The rising background observed for both spherical powders heated in argon suggests an early onset of an exothermic reaction. These exothermic reactions could include rearranging B-Ti bonds in the initially formed amorphous TiB compound and formation of a new TiB phase. It is interesting that the early parts of DSC traces for both spherical powders are very similar to each other despite a substantial difference in the composition identified between these powders from XRD (**Figure 6.13**). This further confirms that most of the material in the prepared composite powders is x-ray amorphous. The second exothermic feature observed only for 160-μm spheres could be attributed to the detected composition difference between coarser and finer spherical powders (**Figure**

6.13). As prepared, coarser spheres contained almost no detectable TiB phase; thus, formation of new TiB could cause the additional exothermic peak observed for 160-µm spheres.

Both DSC and TG traces are shown for the composite powders heated in argon-oxygen flow. DSC shows a much stronger heat effect, associated with oxidation of the powders. As was the case for experiments in argon, there is a strong rising background observed in all experiments. This background cannot be usefully assigned to a specific reaction. For example, it is observed for both spherical and irregularly shaped powders at low temperatures; however, the mass increase is only observed initially for spherical powders in the respective TG traces. Additional experiments (Appendix B, Fig. S4) with pure titanium powder also showed a rising background in the DSC traces using the same heating program; however, the mass gain associated with oxidation began much later, similar to the additional trace for the blended Ti·2B powders shown in **Figure 6.14**. Because of spurious background effects, integration of DSC traces is not useful. Instead, positions of the peaks for the observed exothermic features can be compared for different composite powders. Although the exothermic humps observed for all materials are broad, they systematically peak at lower temperatures for spherical powders compared to both irregularly shaped powders shown in **Figure 6.14**. Note that DSC and TG experiments were also performed with the 7.8-µm irregularly shaped Ti·2B powder (cf. Table 6.1). As the 5.6-µm powder represented in **Figure 6.14**, it was prepared with the same milling dose as the 7.5-µm spherical powder. Its DSC and TG traces are not shown because they were effectively the same as those presented for the 5.6-µm irregular powder.

The difference in oxidation behavior between different materials appears most clearly from the TG traces shown in **Figure 6.14**. The blend of boron and titanium powders shown in **Figure 6.14** for comparison does not exhibit any mass gain due to oxidation up until 500 ºC. Similarly, oxidation for pure titanium and boron powders (Appendix B, Fig. S4) begins only after 500 ºC. Conversely, all milled powders begin oxidizing as soon as the heating program starts. This low-temperature oxidation occurs faster for both spherical powders. The difference between TG traces for finer and coarser spheres is minor for the entire temperature range. Irregular powder with the average particle size of 5.6 µm, which was prepared using the same milling dose as fine spheres, exhibit faster initial oxidation than 11-µm irregular powder, which was prepared with a lower milling dose than respective spheres. A faster oxidation step is observed for all materials at elevated temperatures. This step occurs between 600 and 900 ºC for both blended elemental powders and for the irregularly shaped powder with the average size of 11 µm. The oxidation rate peaks for both powders around 750 ºC. This strong oxidation step shifts to lower temperatures and occurs between 500 and 800 ºC for the 5.6-µm irregularly shaped powder. It shifts to still lower temperatures, ca. 450 – 650 ºC, for both spherical powders. The peaks in the differential TG curves (not shown in **Figure 6.14**) correlate well with the observed peaks in the respective DSC traces shown.

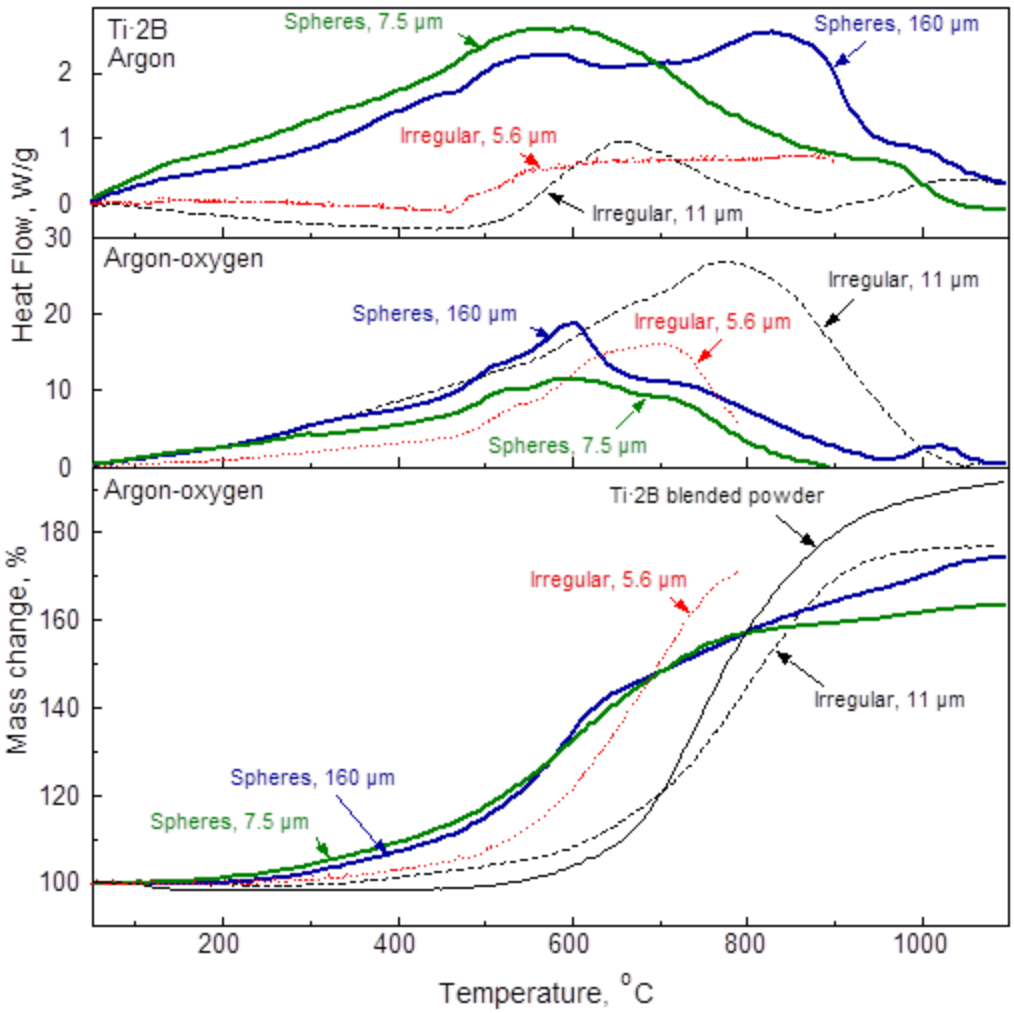

Figure 6.14 DSC and TG traces for Ti·2B composite powders heated in argon and argon-oxygen environments at 10 K/min.

TG traces for Ti·B composite powders are shown in **Figure 6.15**. Similar to **Figure 6.14**, the oxidation of spherical powders begins at a lower temperature than for its irregularly shaped counterpart. Respective DSC traces are also qualitatively similar to those shown in **Figure 6.14** and are omitted for brevity.

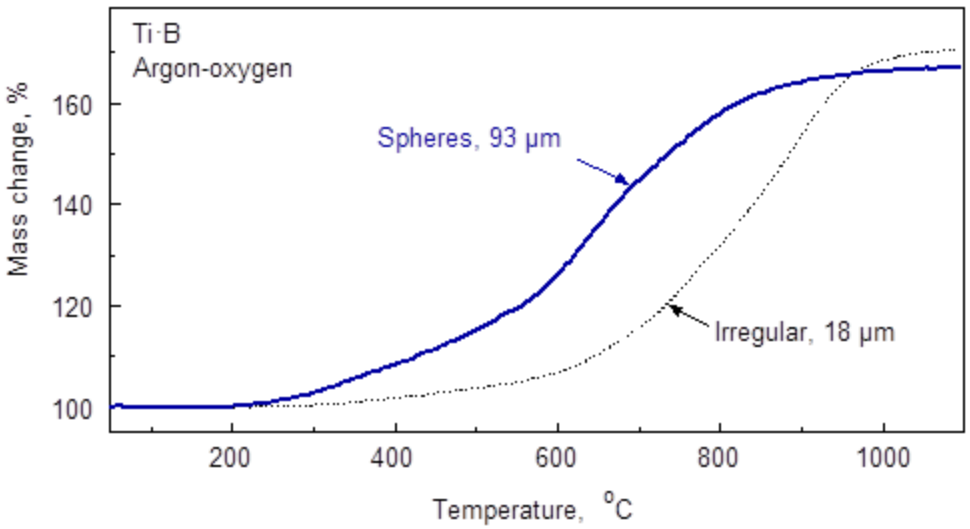

Figure 6.15 TG traces for Ti·B composite powders heated in the argon-oxygen environment at 10 K/min.

XRD patterns of selected powders heated to 800 °C during the DSC experiments are shown in **Figure 6.16**. Detectable phases are α-Ti, cubic TiB, Fe, and Fe_2B. No TiB_2 is detectable. Peaks are generally sharper than in the as-milled material (**Figure 6.12**), although still relatively broad. Phase compositions were determined by whole-pattern refinement, and are shown in **Figure 6.17**. Less Ti, and more TiB is detected in the large sphere powder compared to the irregular powder for both, Ti·B and Ti·2B compositions. The Ti·2B 7.5-µm spherical powder shows no detectable Ti. No systemic difference could be identified between spherical and irregularly shaped powders heated to 800 ºC in argon in terms of the reduced amount of Ti or increased amount of TiB. The iron boride is only detected for the Ti·2B composition, and has a higher amount for the 7.5-µm spherical powder.

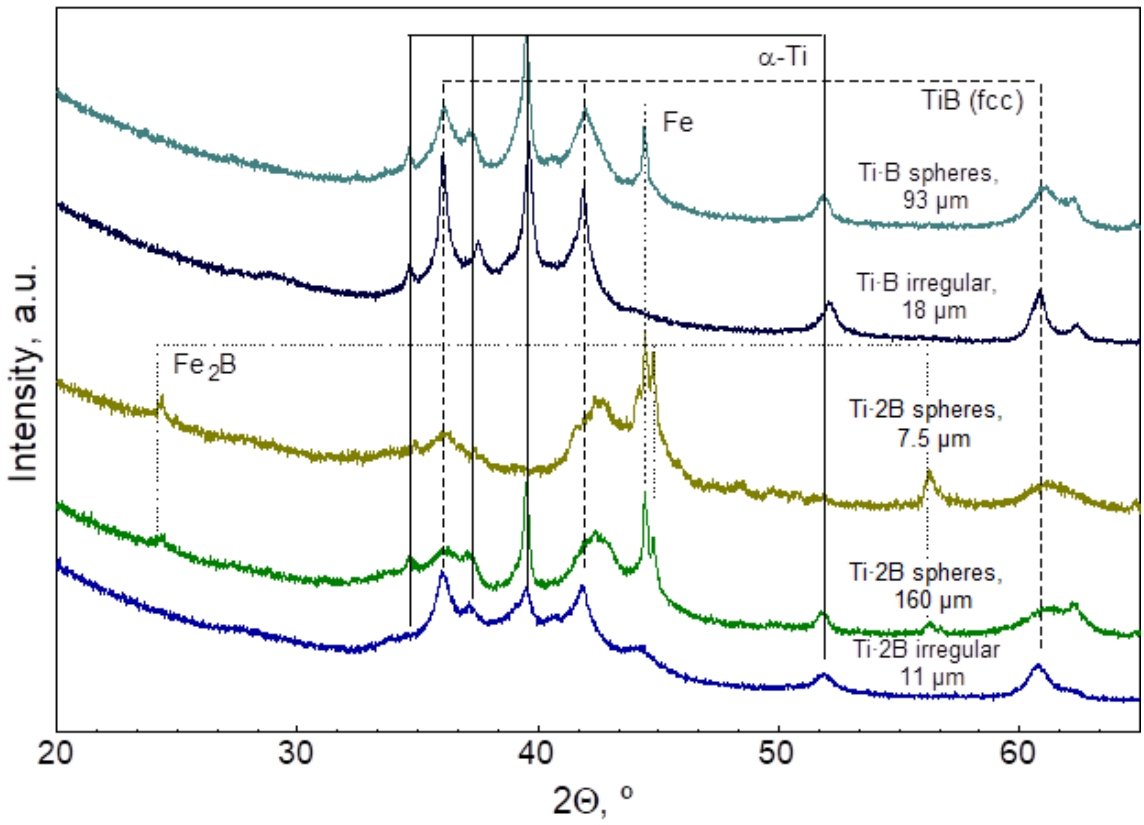

Figure 6.16 XRD patterns of Ti·2B and Ti·B composites heated to 800 °C under argon.

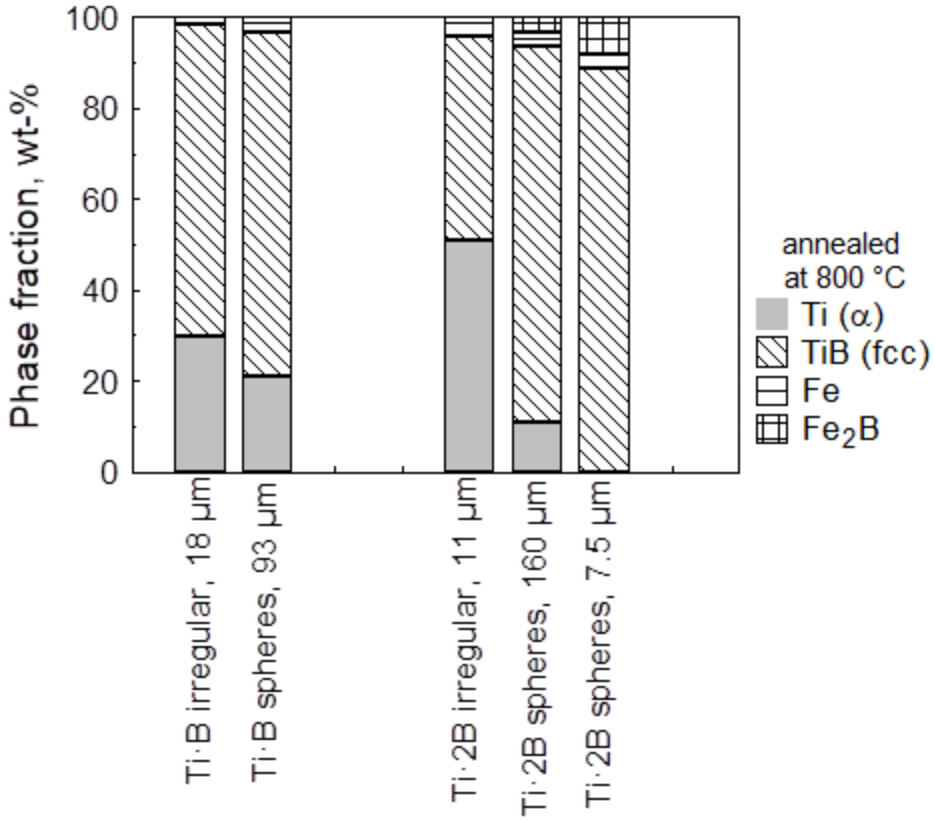

Figure 6.17 Phase compositions of the crystalline phases in composite powders after heating to 800 °C in argon.

Ignition temperatures for different powders measured using an electrically heated filament are reported in **Figure 6.18**. For comparison, results are also shown for elemental boron, which could not be ignited in this experiment, aluminum powder with nominal size of 3 µm (H3 aluminum by Valimet) and -325 mesh titanium powder used as a starting material for the prepared composites. Aluminum powder was observed to ignite just before the filament melted. Titanium ignited at a lower temperature, ca. 810 ºC, which was well quantified by the present experiments. It is reasonable to correlate ignition, observed in experiments with the heating rates of about 3,200 ºC/s with the oxidation, observed to begin just above 500 ºC at much lower heating rates used in thermo-analytical measurements (**Figure 6.14**, S4 and S5).

Both Ti·B and Ti·2B irregularly shaped composite powders ignited at 620 – 660 ºC, that is at lower temperatures than elemental titanium. The difference in the ignition temperature between the irregularly shaped powders with different compositions was insignificant. All spherical powders ignited at still lower temperatures. For all spherical powders, independently of composition or average particle size, the ignition occurred around 500 ºC. This temperature is close to the temperature at which the oxidation rate peaked in thermo-analytical experiments with the same powders. Because of significant difference in the heating rates in the wire ignition and thermo-analytical measurements, it is reasonable to assign ignition to the reaction occurring in the DSC/TG experiments at lower temperatures. It is most likely, therefore, that ignition of spherical powders was governed by the low-temperature oxidation, clearly registered by the respective TG measurements. Indeed, because of the high specific surface area for the spherical powders observed in **Figure 6.11**, it is expected that even a relatively slow, low-temperature oxidation can lead to the thermal runaway and ignition.

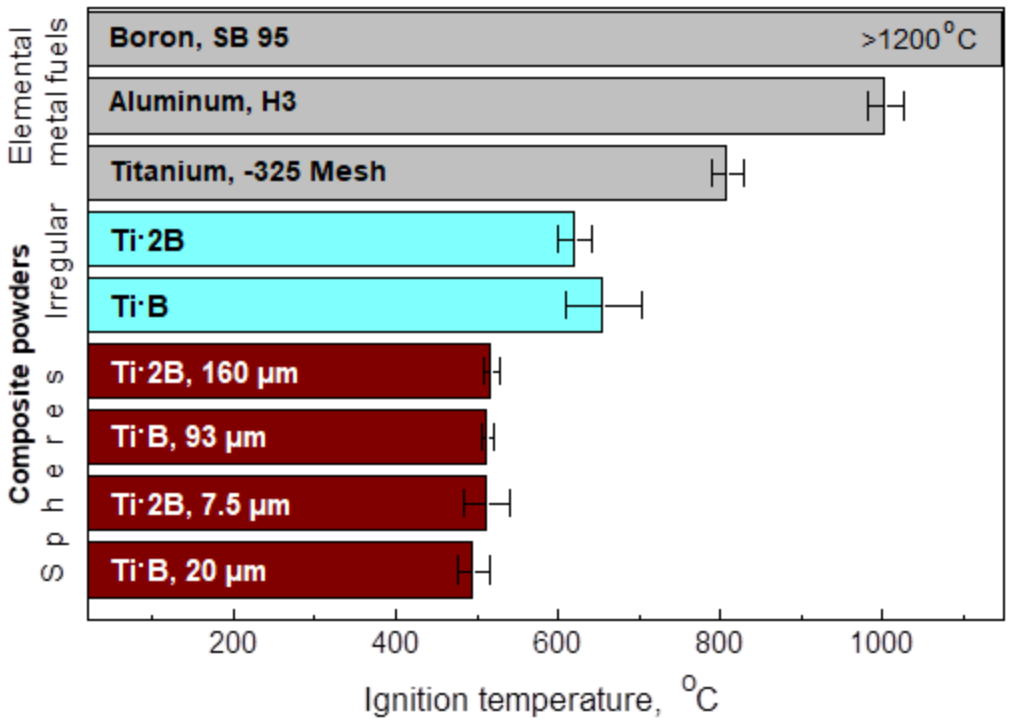

Figure 6.18 Ignition temperatures measured using a heated filament ignition for different composite powders and for elemental metal powders.

6.5 Conclusions

Both irregularly shaped and spherical powders with compositions Ti·B and Ti·2B were prepared using arrested reactive milling and characterized. Spherical powders were prepared using two immiscible liquids, hexane and acetonitrile, as process control agent during milling. In both types of materials, boron and titanium were mixed on the nanoscale. Average volumetric particle sizes for spherical powders could be controlled in a broad range selecting milling conditions. Spherical powders with different particle sizes were found to be porous, unlike reference irregularly shaped composite powders. Despite porosity, spherical powders packed at nearly the same bulk density as irregularly shaped powders. It was also observed that milling led to formation of poorly crystalline TiB in all milled materials. The amount of observed TiB as well as contamination by Fe from the milling tools increased at greater milling dose (e.g., energy transferred to the powders being

milled from the milling tools). Substantial portion of the prepared composite materials (more than half) was amorphous. The amount of the formed TiB did not correlate with the reactivity of the prepared materials. All composite materials exhibited exothermic reactions at low temperatures when heated in both inert and oxidizing environments. The exothermic reactions were always stronger for spherical powders. Oxidation for spherical powders started sooner (at lower temperatures) compared to the irregularly shaped composites or to elemental metal fuels, boron and titanium. Similarly, spherical powders ignited at a lower temperature than irregularly shaped powders with the same compositions when coated on an electrically heated wire.

CHAPTER 7

CONCLUSIONS

Preparation of metal based reactive structural materials capable of highly exothermic self-sustaining reactions have been discussed and explored. The most promising of these reaction pathways leading to formation of oxides, fluorides, carbides, borides, silicides and aluminides were reviewed in literature. The methods of the reaction initiation and characterization were also discussed as the understanding of these techniques and respective experimental outcomes are fundamental to relative comparison of prepared materials for end use applications.

Further discussion dealt with the preparation of composites focusing on non-trivial processes leading to the fine scales of mixing between reactive material components necessary for rapid reaction, typically in the 10 – 100 nm range. Dissimilar materials with potential for reaction have been found to require interface areas greater that achievable with conventional powder mixing; respectively, the work focused on preparing composite powders, for which each particle contains components mixed on the nanoscale. Once composite powders are prepared further processing may also be required to consolidate them by one of various methods to achieve a material that is not just reactive but also capable of serving a structural purpose. Although not a primary focus of this work, these methods of consolidation were considered and materials were contributed towards uniaxial compression as well as additive manufacturing methods which were believed among the most straightforward in incorporating powdered materials.

Of those materials available, metal-based systems composed of boron, tungsten, titanium, zirconium, and aluminum were explored as materials that possessed high

thermodynamic potential, tunable density and the ability to subsequently react with an oxidizing environment. Boron-titanium intermetallic reaction was explored most extensively, this highly reactive composite can be combined with tungsten to achieve greater material density. Binary boron-titanium exothermic reaction releases the most heat upon thermal initiation of the prepared materials; boron-tungsten reaction was also sufficiently exothermic to potentially contribute to the heat release by the reactive structure. Both pressure and rate of pressure rise produced by binary and ternary materials prepared here by high energy milling were investigated in an oxidizing gas environment. Promising improvements in reactivity were found. Boron-zirconium composite powders were also explored with an expectation of similar capabilities with a higher theoretical density than boron-titanium (without tungsten). Theoretical calculations using the thermodynamic equilibrium NASA CEA code were explored in detail to describe the system combustion. Combustion of the prepared composites was characterized experimentally igniting them in air and an air-acetylene flame.

In addition to the preparation of composites, surface modification and a novel method of spherical powder production was explored. An effort to demonstrate the viability of siloxane-coated magnesium powders was successful. It demonstrated an improved long-term stability, showing little oxidation at elevated temperature and in the presence of high humidity. Furthermore, modification of the powders did not negatively impact its ignition. Likewise, improvement in aluminum fuel was achieved via the production of spheroidal particles consisted of packed plate-like aluminum flakes. This form was found to exhibit higher ignition sensitivity and to possess a more protected surface from hydroxide formation than equivalent spherical commercial powders. Additionally, spherical or

spheroidal powders are expected to be beneficial as feedstock for consolidation and additive manufacturing necessary to prepare reactive structural components. By the milling of boron and titanium powders in two immiscible liquids, spherical composite powders were produced as well and were found to exhibit similarly enhanced ignition characteristics. Examination of the prepared materials showed that nanoscale levels of intermixing was achieved combined with a high porosity. It is proposed that combination of these attributes was important for their observed enhanced energetic performance.

Future anticipated work needed to be explored would include the extension of staged milling procedures to additional formulations of interest. Foundational material works such as the production of spherical boron and aluminum can be extended to the respective composites of interest. From the work conducted it can be concluded that mechanical milling to tune reactivity and morphology can be affected, both in semi-independent stages, as well as together. However, the mechanisms by which morphology changes occurs in particular is not entirely understood. Works to achieve formation of spheres have been to date highly experimental without strong foundation in the mechanisms by which the particle stabilized emulsions produce them. To effectively form spheres, a polar and non-polar liquid with specific interface interactions for a given rate of agitation must be achieved. To date most work has effectively used hexane and acetonitrile however other solvents including mixtures of hydrocarbons, alcohols, water, and oils could represent viable alternatives.

Simulation of immiscible liquids stabilized by particles to predict milling conditions is a non-trivial task as the size of particles, the complex dynamics of emulsion formation, and droplet-particle stabilization are all anticipated to affect the result. Some

experimental results referenced which pertain to the formation of oil-particle aggregates[376] and emulsifiers[377] may help interpret these effects. Because of the complexity it could be suggested that perhaps control of liquid interface parameters could be exerted based on experimental results to produce equivalent pseudo liquids from which CFD simulation should be more readily achieved. In spite of this, there will be complexities associated with change in state of materials during milling, and packing for which a solution is not well known. Ultimately, the tuning of properties by variation in milling material as well as the solvents used to produce emulsions would increase the versatility of mechanical milling tremendously and advance this work into more widespread use for the production of on demand, tunable reactive structural materials.

APPENDIX A

Highly Reactive Spheroidal Milled Aluminum

Image Analysis

Image analysis was performed by despeckling to remove image graininess, thresholding to generate a binary image, and a feature capturing full particle sizes. Further, particles containing fewer than 4 pixels which was well below minimum particle size were removed to reduce the effect of digital noise. A watershed feature was used to separate particles that might have been contacting one another. Finally, the identification of particles with "analyze particles" protocol was performed using a circularity of 0.3-1.0 and aspect ratio of less than 3.

X-ray diffraction of aging product

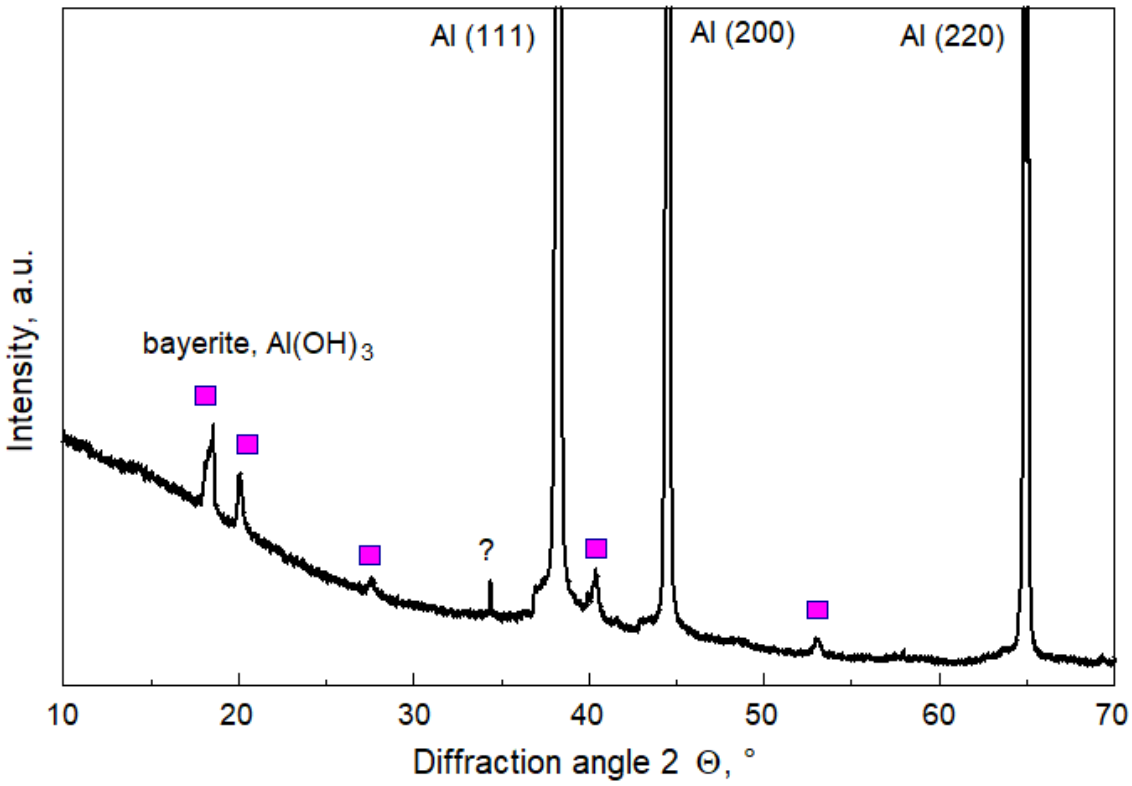

Figure B.1: XRD of aged commercial aluminum, identifying the Aluminum hydroxide

APPENDIX B

Titanium boron reactive composite powders with variable morphology prepared by arrested reactive milling

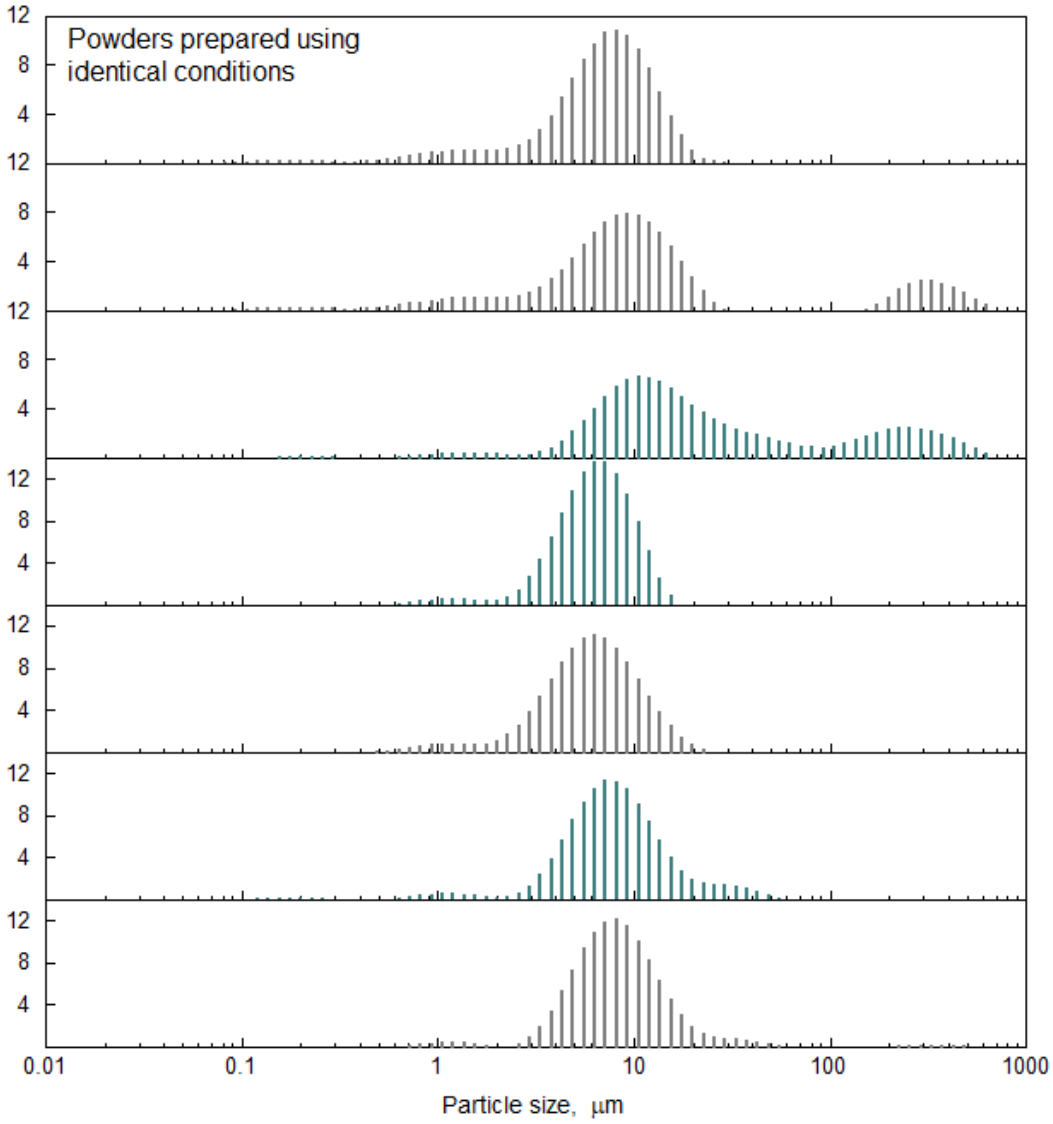

Figure B.1 Particle size distributions for different Ti·2B powder batches prepared at the same conditions as spheres, 7.5 μm (see Table 6.1). Agglomerates (particles greater than 20 μm) are readily broken down by sonication.

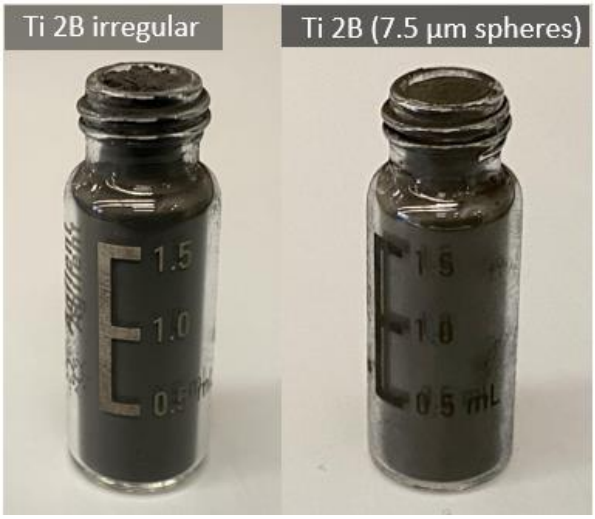

Figure B.2 Glass bottles filled with different powder samples (details on samples). Approximate Ti·2B bulk densities of 11-µm irregular and 7.5-µm spherical powders were respectively 1.93 and 1.80 g/mL. Bulk densities for 18-µm irregular and 93-µm spherical Ti·B powders were 2.22 and 1.77 g/mL, respectively. A slight decrease in bulk density for spherical powders is likely associated with their much greater porosity.

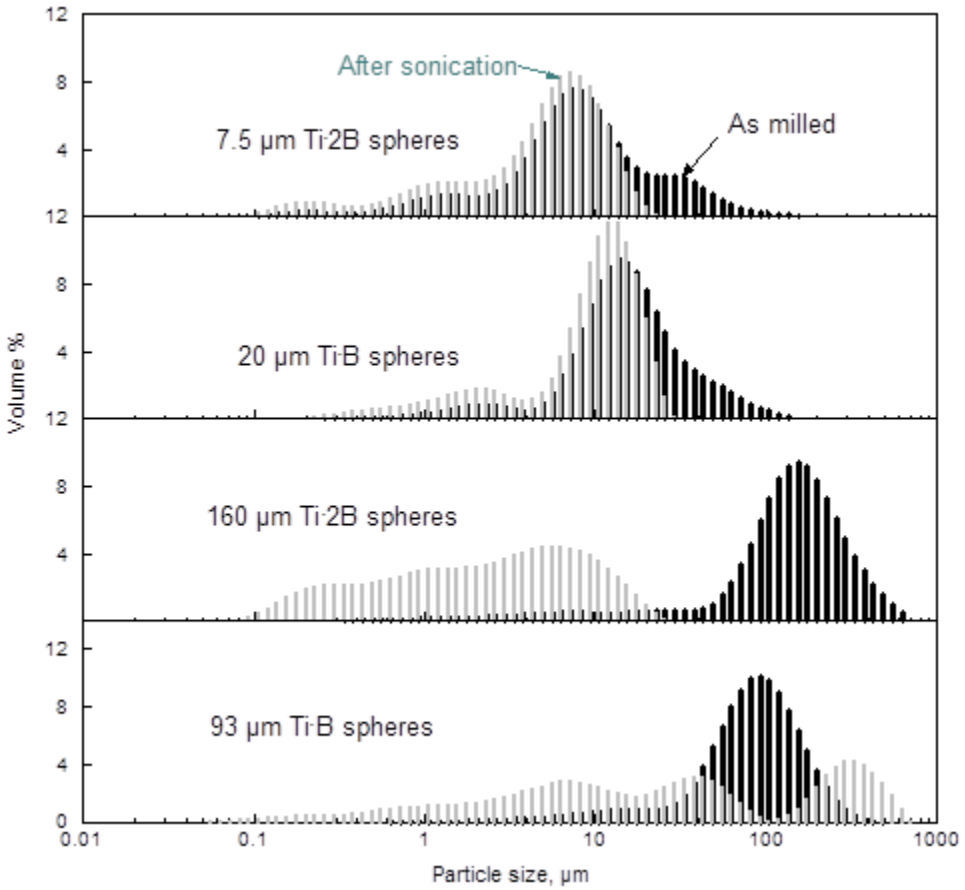

Figure B.3 Particle size distributions of different prepared spherical powders before and after sonication.

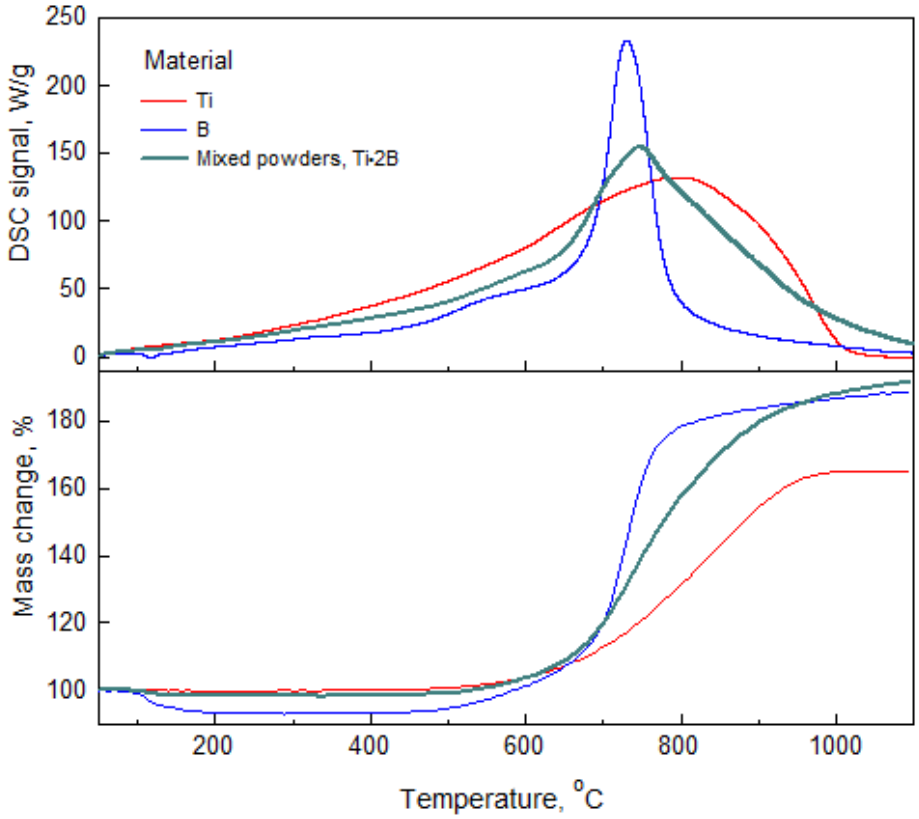

Figure B.4 DSC and TG traces for mixed and pure Ti and B powders heated in oxidizing environment

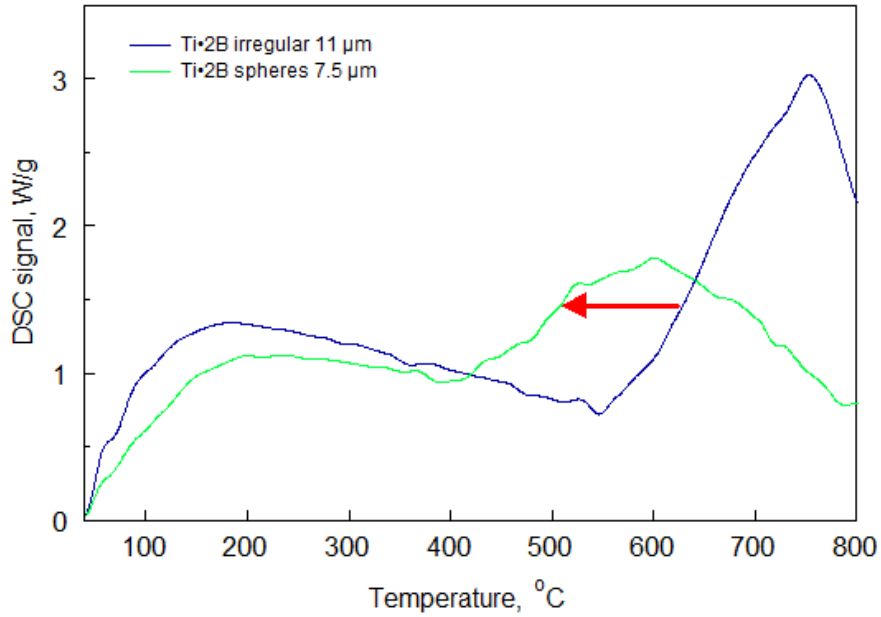

Figure B.5 DSC traces of Ti·2B irregular and spherical powders measured at a heating rate of 40 K/min

REFERENCES

[1] T. Ackerman, D. R. Crofts, K. Gulia, and M. M. M. Attallah, "Composite reactive material for use in a munition," Patent GB2526262A, 2015.

[2] J. Chen, B. H. Yuan, Z. F. Liang, C. Xiao, and Y. J. Chen, "An experimental evaluation method of energy release characteristics of reactive materials," *Huozhayao Xuebao/Chinese Journal of Explosives and Propellants,* vol. 38, no. 3, pp. 49-53, 2015, doi: 10.14077/j.issn.1007-7812.2015.03.009.

[3] J. P. Hooper, "Impact fragmentation of aluminum reactive materials," *Journal of Applied Physics,* Article vol. 112, no. 4, 2012, Art no. 043508, doi: 10.1063/1.4746788.

[4] R. J. Lee, W. Mock Jr., J. R. Carney, W. H. Holt, G. I. Pangilinan, R. M. Gamache, J. M. Boteler, D. G. Bohl, J. Drotar, and G. W. Lawrence, "Reactive materials studies," *AIP Conf. Proc.,* vol. 845, no. Copyright (C) 2015 American Chemical Society (ACS). All Rights Reserved., pp. 169-174, 2006.

[5] D. B. Nielson, R. M. Truitt, and B. N. Ashcroft, "Reactive material-enhanced projectiles and munitions containing incendiaries and explosives," Patent EP1780494A2 Patent Appl. Copyright (C) 2017 American Chemical Society (ACS). All Rights Reserved., 2007.

[6] M. D. Tucker, "Characterization of Impact Initiation of Aluminum Based Intermetallic Forming Reactive Materials," Master of Science, Mechanical Engineering, Georgia Institute of Technology, Atlanta, GA, 2011.

[7] F. Zhang, M. Gauthier, and C. Cojocaru, "Sub-fragmentation of structural reactive material casings under explosion," in *AIP Conference Proceedings*, 2017, vol. 1793, doi: 10.1063/1.4971532.

[8] W. Q. Wan, D. Q. Yu, F. Peng, W. M. Wang, and T. H. Yang, "Formation and terminal effect of an explosively-formed penetrator made by energetic materials," *Baozha Yu Chongji/Explosion and Shock Waves,* Article vol. 34, no. 2, pp. 235-240, 2014.

[9] J. Liou, G.-H. Huang, Y.-Y. You, and M.-T. Hsu, "Preliminary study on the reactive fragment warhead," *Huoyao Jishu*, vol. 28, no. 1, pp. 35-46, // 2012.

[10] V. L. Bucharskiy and P. V. Frolov, "Assessment of use of active-reactive munition charge by method of integral approximation," *Bulletin of Dnepropetrovsk University; Series: Space rocket technology (In Ukrainian)*, vol. 20, no. 15(1), pp. 38-43, 2012.

[11] M. Mayseless, "Effectiveness of explosive reactive armor," *Journal of Applied Mechanics, Transactions American Society of Mechanical Engineers,* Article vol. 78, no. 5, 2011, Art no. 051006, doi: 10.1115/1.4004398.

[12] H. N. G. Wadley, K.P. Dharmasena, M.Y. He, R.M. McMeeking, A.G. Evans, T. Bui-Thanh, R. Radovitzky, "An active concept for limiting injuries caused by air blasts," *International Journal of Impact Engineering*, Article vol. 37, no. 3, pp. 317-323, 2010, doi: 10.1016/j.ijimpeng.2009.06.006.

[13] F. Zhang, Wilson, W., "The Effect of Charge Reactive Metal Cases on Air Blast," *Shock Compression of Condensed Matter*, vol. CP1195, 2009.

[14] F. Zhang, R. Ripley, and W. H. Wilson, "Air blast characteristics of laminated al and NI-AL casings," in *AIP Conference Proceedings*, 2012, vol. 1426, pp. 275-278, doi: 10.1063/1.3686272.

[15] S. P. Li, G. Y. Huang, S. S. Feng, C. Wang, and H. Zou, "Research on combustion effect of depleted uranium alloys subjected to impact," *Binggong Xuebao/Acta Armamentarii*, Article vol. 32, no. SUPPL. 2, pp. 57-60, 2011. [Online]. Available: https://www.scopus.com/inward/record.uri?eid=2-s2.0-84863278601&partnerID=40&md5=cd550d1821b460795aa7cc34e6d0409f.

[16] C. Mitsakou, K. Eleftheriadis, C. Housiadas, and M. Lazaridis, "Modeling of the dispersion of depleted uranium aerosol," *Health Physics*, Article vol. 84, no. 4, pp. 538-544, 2003, doi: 10.1097/00004032-200304000-00014.

[17] R. J. Lee, W. Mock Jr., J. R. Carney, W. H. Holt, G. I. Pangilinan, R. M. Gamache, J. M. Boteler, D. G. Bohl, J. Drotar, and G. W. Lawrence, "Reactive materials studies," in *AIP Conference Proceedings*, 2006, vol. 845 I, pp. 169-174, doi: 10.1063/1.2263291. [Online]. Available: https://www.scopus.com/inward/record.uri?eid=2-s2.0-33846204408&doi=10.1063%2f1.2263291&partnerID=40&md5=bb586e2821f5624c00a7bc7c69065b9a

[18] B. Zygmunt, "Explosive properties of the Mg-Al/PTFE composition," *Hanneng Cailiao/Chinese Journal of Energetic Materials*, Article vol. 15, no. 6, pp. 592-596, 2007. [Online]. Available: https://www.scopus.com/inward/record.uri?eid=2-s2.0-38349014278&partnerID=40&md5=8ee3338bb9ac73b61c71ea941697111c.

[19] A. Bacciochini, M. I. Radulescu, M. Yandouzi, G. Maines, J. J. Lee, and B. Jodoin, "Reactive structural materials consolidated by cold spray: Al-CuO thermite," *Surface and Coatings Technology*, vol. 226, pp. 60-67, 2013. [Online]. Available: http://www.scopus.com/inward/record.url?eid=2-s2.0-84878011706&partnerID=40&md5=e168c580a28a37c2bd31f8f881e9a37f.

[20] A. Ermoline, Y. Aly, M. A. Trunov, M. Schoenitz, and E. L. Dreizin, "Preparation and characterization of granular hybrid reactive materials," *International Journal of Energetic Materials and Chemical Propulsion*, vol. 9, no. 3, pp. 267-284, 2010, doi: 10.1615/IntJEnergeticMaterialsChemProp.v9.i3.60.

[21] P. Dupiano, D. Stamatis, and E. L. Dreizin, "Hydrogen production by reacting water with mechanically milled composite aluminum-metal oxide powders," *International Journal of Hydrogen Energy*, vol. 36, no. 8, pp. 4781-4791, 2011, doi: 10.1016/j.ijhydene.2011.01.062.

[22] S. W. Du, B. Aydelotte, D. Fondse, C. T. Wei, F. Jiang, E. Herbold, K. Vecchio, M. A. Meyers, N. N. Thadhani, "Explosive compations of intermetallic-forming powder mixtures for fabricating structural energetic materials," in *AIP Conference Proceedings*, 2009, vol. 1195, pp. 498-501, doi: 10.1063/1.3295183. [Online]. Available: http://www.scopus.com/inward/record.url?eid=2-s2.0-74949089308&partnerID=40&md5=0efd958b2f3e179045e130f3fb378dd2

[23] B. Aydelotte and N. N. Thadhani, "A comparison of different Ni+Al structural energetic materials," in *Materials Research Society Symposium Proceedings*, 2013, vol. 1521, pp. 13-18, doi: 10.1557/opl.2013.48. [Online]. Available: https://www.scopus.com/inward/record.uri?eid=2-s2.0-84900329143&doi=10.1557%2fopl.2013.48&partnerID=40&md5=29b3f7c422da16a16d1245cb3c7bff7a

[24] A. Bacciochini, S. Bourdon-Lafleur, C. Poupart, M. Radulescu, and B. Jodoin, "Ni-Al Nanoscale Energetic Materials: Phenomena Involved During the Manufacturing of Bulk Samples by Cold Spray," *Journal of Thermal Spray Technology*, vol. 23, no. 7, pp. 1142-1148, 2014, doi: 10.1007/s11666-014-0078-1.

[25] M. D. Clemenson, S. Johnson, H. Krier, and N. Glumac, "Explosive Initiation of Various Forms of Ti/2B Reactive Materials," *Propellants, Explosives, Pyrotechnics*, vol. 39, no. 3, pp. 454-462, 2014, doi: doi:10.1002/prep.201300114.

[26] N. A. Kochetov and S. G. Vadchenko, "Effect of the time of mechanical activation of a Ti + 2B mixture on combustion of cylindrical samples and thin foils," *Combustion, Explosion and Shock Waves*, Article vol. 51, no. 4, pp. 467-471, 2015, doi: 10.1134/S0010508215040103.

[27] V. Rosenband, B. Natan, and A. Gany, "Ignition of boron particles coated by a thin titanium film," *Journal of Propulsion and Power*, Article vol. 11, no. 6, pp. 1125-1131, 1995, doi: 10.2514/3.23950.

[28] M. A. Trunov, V. K. Hoffmann, M. Schoenitz, and E. L. Dreizin, "Combustion of boron-titanium nanocomposite powders in different environments," *Journal of Propulsion and Power*, vol. 24, no. 2, pp. 184-191, 2008, doi: 10.2514/1.30483.

[29] I. Song, L. Wang, M. Wixom, and L. T. Thompson, "Self-propagating high temperature synthesis and dynamic compaction of titanium diboride/titanium carbide composites," *Journal of Materials Science*, Article vol. 35, no. 10, pp. 2611-2617, 2000, doi: 10.1023/A:1004731532616.

[30] H. Ren, X. Liu, and J. Ning, "Microstructure and mechanical properties of W-Zr reactive materials," *Materials Science and Engineering A*, Article vol. 660, pp. 205-212, 2016, doi: 10.1016/j.msea.2016.02.009.

[31] H. Ren, X. Liu, and J. Ning, "Impact-initiated behavior and reaction mechanism of W/Zr composites with SHPB setup," *AIP Advances*, Article vol. 6, no. 11, 2016, Art no. 115205, doi: 10.1063/1.4967340.

[32] L. Z. Xu and Z. H. Du. *Experimental study on damage effect of PELE with new structure and composite material against multi-layered plates, Key Engineering Materials*, vol. 723 KEM, pp. 202-206, 2017.

[33] H. Zhang, J. Yin, and Z. Wang. *Influence of jacket and filling materials characteristics on PELE effects, Applied Mechanics and Materials*, vol. 217-219, pp. 358-361, 2012.

[34] J. S. Zhu, Z. Fan, and B. Gao. *Influences of material parameters on terminal effect of PELE with tungsten fiber composite jacket, Advanced Materials Research*, vol. 936, pp. 1927-1932, 2014.

[35] A. Coverdill, C. Delaney, A. Jennrich, H. Krier, and N. G. Glumac, "Tungsten Combustion in Explosively Initiated W/Zr Mechanical Alloys," *Journal of Energetic Materials*, vol. 32, pp. 135-145, 2014.

[36] L. J. Kecskes and K. A. Darling, "Formation of HfW2 and ZrW2 in the W-Hf and W-Zr binary systems," in *Proceedings of the 8th International Conference on Tungsten, Refractory and Hardmaterials*, 2011, pp. 936-945, doi: N/A. [Online]. Available: https://www.scopus.com/inward/record.uri?eid=2-s2.0-84883294222&partnerID=40&md5=dd976d816c25050432517ec736900e59

[37] M. W. Chase, "NIST-JANAF Themochemical Tables, Fourth Edition.," *J. Phys. Chem. Ref. Data, Monograph 9*, pp. 1-1951, 1998.

[38] S. H. Fischer and M. C. Grubelich, "Theoretical energy release of thermites, intermetallics, and combustible metals," *Proc. Int. Pyrotech. Semin.*, vol. 24th, no. Copyright (C) 2015 American Chemical Society (ACS). All Rights Reserved., pp. 231-286, 1998.

[39] K. T. Jacob, A. Kumar, G. Rajitha, and Y. Waseda, "Thermodynamic data for Mn 3O 4, Mn 2O 3 and MnO 2," *High Temperature Materials and Processes*, Article vol. 30, no. 4, pp. 459-472, 2011, doi: 10.1515/HTMP.2011.069.

[40] S. V. Meschel and O. J. Kleppa, "Standard enthalpies of formation of some 3d transition metal carbides by high temperature reaction calorimetry," *Journal of Alloys and Compounds*, Article vol. 257, no. 1-2, pp. 227-233, 1997. [Online]. Available: https://www.scopus.com/inward/record.uri?eid=2-s2.0-0031175894&partnerID=40&md5=0ac85c7950029442edad906f4ecff23f.

[41] E. S. Domalski and G. T. Armstrong, "Heats of Formation of Metallic Borides by Fluorine Bomb Calorimetry," in "Report APL-TDR-64-39," Air Force Aero Propulsion Laboratory, Research and Technology Division, Air Force Systems Command Wright-Patterson Air Force Base, Ohio, 1964.

[42] E. Rudzitis, R. Terry, H. M. Feder, and W. N. Hubbard, "Fluorine bomb calorimetry. VIII. The enthalpy of formation of zinc difluoride," *Journal of Physical Chemistry*, Article vol. 68, no. 3, pp. 617-619, 1964. [Online]. Available: https://www.scopus.com/inward/record.uri?eid=2-s2.0-33947488748&partnerID=40&md5=4b8a99155263de9d5264def23135c9c4.

[43] B. E. Douda, "Survey of Military Pyrotechnics," in "Report NSWC/CR/RDTR-595," Naval Weapons Support Center Ordnance Engineering Department Crane, IN, May 24, 1991 1991, vol. NSWC/CR/RDTR-595.

[44] M. L. Chan and G. W. Meyers, "Advanced Thermobaric Explosive Compositions," USA Patent Appl. US 10/779,545, 2005.

[45] W. S. d. Rossett, "An Overview of Novel Penetrator Technology," in "Report ARL-TR-2395," Army Research Laboratory, Aberdeen Proving Ground, MD, ARL-TR-2395, 2001, vol. Report ARL-TR-2395.

[46] J. Askill, *Tracer diffusion data for metals, alloys, and simple oxides*. New York, IFI/Plenum, 1970., 1970.

[47] H. Nakajima, W. Sprengel, and K. Nonaka, "Diffusion in intermetallic compounds," *Intermetallics,* no. 4, pp. S17-S28, 1996.

[48] S. Frank, S. V. Divinski, U. Sodervall, and C. Herzig, "Ni Tracer Diffusion in the B2 Compound NiAl influence of temperature and composition," *Acta materialia,* no. 49, pp. 1399-1411, 2001.

[49] M. Keddam, S. Taktak, and S. Tasgetiren, "A diffusion model for the titanium borides on pure titanium," *Surface Engineering,* vol. 32, no. 11, pp. 802-808, 2016, doi: 10.1080/02670844.2016.1180845.

[50] Q. Fu and T. Wagner, "Interaction of nanostructured metal overlayers with oxide surfaces," *Surface Science Reports,* vol. 62, no. 11, pp. 431-498, 2007. [Online]. Available: http://www.scopus.com/inward/record.url?eid=2-s2.0-35348933734&partnerID=40&md5=6350dfd3088acd31bcee82165460722e.

[51] A. Atkinson, "Transport processes during the growth of oxide films at elevated temperature," *Reviews of Modern Physics,* vol. 57, no. 2, pp. 437-470, 04/01/ 1985. [Online]. Available: https://link.aps.org/doi/10.1103/RevModPhys.57.437.

[52] M. W. Beckstead, "Correlating aluminum burning times," *Combustion, Explosion and Shock Waves,* vol. 41, no. 5, pp. 533-546, 2005, doi: 10.1007/s10573-005-0067-2.

[53] Y. Aly, V. K. Hoffman, M. Schoenitz, and E. L. Dreizin, "Preparation, ignition, and combustion of mechanically alloyed Al-Mg powders with customized particle sizes," in *Materials Research Society Symposium Proceedings*, 2013, vol. 1521, pp. 43-48, doi: 10.1557/opl.2013.145. [Online]. Available: http://www.scopus.com/inward/record.url?eid=2-s2.0-84900332552&partnerID=40&md5=f30f6b64ccbace4ab5de4bf4a0be8e3d

[54] A. Maček and J. M. Semple, "Combustion of boron particles at elevated pressures," *Symposium (International) on Combustion,* vol. 13, no. 1, pp. 859-868, 1971/01/01/ 1971, doi: http://dx.doi.org/10.1016/S0082-0784(71)80087-5.

[55] K.-L. Chintersingh, Q. Nguyen, M. Schoenitz, and E. L. Dreizin, "Combustion of boron particles in products of an air–acetylene flame," *Combustion and Flame,* vol. 172, pp. 194-205, 10// 2016, doi: http://dx.doi.org/10.1016/j.combustflame.2016.07.014.

[56] G. Young, K. Sullivan, M. R. Zachariah, and K. Yu, "Combustion characteristics of boron nanoparticles," *Combustion and Flame,* Article vol. 156, no. 2, pp. 322-333, 2009, doi: 10.1016/j.combustflame.2008.10.007.

[57] I. E. Molodetsky, E. P. Vicenzi, E. L. Dreizin, and C. K. Law, "Phases of titanium combustion in air," *Combustion and Flame,* vol. 112, no. 4, pp. 522-532, 1998, doi: 10.1016/s0010-2180(97)00146-6.

[58] E. Shafirovich, S. K. Teoh, and A. Varma, "Combustion of levitated titanium particles in air," *Combustion and Flame,* vol. 152, no. 1-2, pp. 262-271, 2008, doi: 10.1016/j.combustflame.2007.05.008.

[59] S. Wang, S. Mohan, and E. L. Dreizin, "Effect of flow conditions on burn rates of metal particles," *Combustion and Flame,* vol. 168, pp. 10-19, 6// 2016, doi: http://dx.doi.org/10.1016/j.combustflame.2016.03.014.

[60] X. Huang, Z.-x. Xia, L.-y. Huang, and J.-x. Hu, "Progress in combustion characteristics of Mg particles in oxidation gases," *Hanneng Cailiao,* 10.3969/j.issn.1006-9941.2013.03.021 vol. 21, no. Copyright (C) 2014 American Chemical Society (ACS). All Rights Reserved., pp. 379-386, 2013, doi: 10.3969/j.issn.1006-9941.2013.03.021.

[61] H. M. Cassel and I. Liebman, "Combustion of magnesium particles I," *Combustion and Flame,* vol. 6, no. C, pp. 153-156, 1962. [Online]. Available: http://www.scopus.com/inward/record.url?eid=2-s2.0-0039725943&partnerID=40&md5=b8cca28045d9899cb03cb5ac8650bf63.

[62] E. L. Dreizin, C. H. Berman, and E. P. Vicenzi, "Condensed-phase modifications in magnesium particle combustion in air," *Combustion and Flame,* vol. 122, no. 1-2, pp. 30-42, 2000, doi: 10.1016/s0010-2180(00)00101-2.

[63] S. Wang, A. L. Corcoran, and E. L. Dreizin, "Combustion of magnesium powders in products of an air/acetylene flame," *Combustion and Flame,* vol. 162, no. 4, pp. 1316-1325, April 2015 2015, doi: http://dx.doi.org/10.1016/j.combustflame.2014.10.016.

[64] A. Saigal and V. S. Joshi, "Strength and stiffness of aluminum/PTFE reactive composites," *American Society of Mechanical Engineers, Pressure Vessels and Piping Division (Publication) PVP,* vol. 432, pp. 107-111, 2000. [Online]. Available: http://www.scopus.com/inward/record.url?eid=2-s2.0-0346685323&partnerID=40&md5=432b2fbf9a496346788a2c91aed4b6fa.

[65] V. S. Joshi, "Process for making polytetrafluoroethylene-aluminum composite and sintered product made," Patent US6547993B1 Patent Appl. Copyright (C) 2017 American Chemical Society (ACS). All Rights Reserved., 2003.

[66] J. Wu, M. Li, S. Zhang, Y. Mei, and Z. Gao, "Research on sintering polytechnic of of PTFE/Al reactive materials," *Adv. Mater. Res. (Durnten-Zurich, Switz.)*, vol. 820, no. Metallic Materials and Manufacturing Technology, pp. 25-29, 6 pp., 2013, doi: 10.4028/www.scientific.net/AMR.820.25.

[67] S.-q. Yang, S.-l. Xu, and T. Zhang, "Preparation and performance of PTFE/Al reactive materials," *Guofang Keji Daxue Xuebao*, vol. 30, no. 6, pp. 39-42, 62, // 2008.

[68] C. Ge, W. Maimaitituersun, Y. Dong, and C. Tian, "A study on the mechanical properties and impact-induced initiation characteristics of brittle PTFE/Al/W reactive materials," *Materials*, Article vol. 10, no. 5, 2017, Art no. 452, doi: 10.3390/ma10050452.

[69] Z. Lu, D. Jiang, and P. Tang, "Experimental study of energy release effect of PTFE based reactive material rod striking at spaced plates," in *International Symposium on Ballistics*, Atlanta, GA, 2014, vol. 2: DEStech Publications, Inc., pp. 1129-1133.

[70] J. Cai, V.F. Nesterenko, K.S. Vecchio, E.B. Herbold, D.J. Benson, F. Jiang, J.W. Addiss, S.M. Walley, and W.G. Proud, "The influence of metallic particle size on the mechanical properties of PTFE-Al-W powder composites," *Los Alamos Natl. Lab., Prepr. Arch., Condens. Matter*, no. Copyright (C) 2015 American Chemical Society (ACS). All Rights Reserved., pp. 1-18, arXiv:0709.2172v1 [cond-mat.soft], 2007. [Online]. Available: http://arxiv.org/ftp/arxiv/papers/0709/0709.2172.pdf.

[71] G. Young, C. A. Stoltz, D. H. Mayo, C. W. Roberts, and C. L. Milby, "Combustion behavior of solid fuels based on PTFE/boron mixtures," *Combustion Science and Technology*, vol. 185, no. 8, pp. 1261-1280, 2013, doi: 10.1080/00102202.2013.787417.

[72] D. B. Nielson, R. M. Truitt, R. D. Poore, and B. N. Ashcroft, "Reactive material compositions for shot shells ammunition consisting of metal fuels, inorganic oxidants, epoxy resins, and fluoropolymer binders," Patent US20070272112A1 Patent Appl. Copyright (C) 2017 American Chemical Society (ACS). All Rights Reserved., 2007.

[73] B. E. Homan, K. L. McNesby, J. Ritter, J. Colburn, and A. Brant, "Characterization of the Combustion Behavior of Aluminum-Nickel Based Reactive Materials," in "Report ARL-TR-4917," Weapons and Material Research Directorate, ARL, Aberdeen Proving Ground, MD 21005, August 2009 2009, vol. ARL-TR-4917.

[74] J. D. Gibbins, A. K. Stover, N. M. Krywopusk, K. Woll, and T. P. Weihs, "Properties of reactive Al: Ni compacts fabricated by radial forging of elemental and alloy powders," *Combustion and Flame*, Article vol. 162, no. 12, pp. 4408-4416, 2015, doi: 10.1016/j.combustflame.2015.08.003.

[75] T. F. Zahrah, R. Rowland, and L. Kecskes, "High-density Hf-base and Fe-based metallic-glass-alloy powders and their composite derivatives," Patent US20060062684A1 Patent Appl. Copyright (C) 2015 American Chemical Society (ACS). All Rights Reserved., 2006.

[76] S. W. Dean, J. K. Potter, R. A. Yetter, T. J. Eden, V. Champagne, and M. Trexler, "Energetic intermetallic materials formed by cold spray," *Intermetallics,* vol. 43, pp. 121-130, 2013, doi: 10.1016/j.intermet.2013.07.019.

[77] V. F. Nesterenko, C. H. Braithwaite, A. Collins, K. L. Olney, and D. Benson, "Dynamic behavior of particulate/porous energetic materials," in *AIP Conference Proceedings,* 2012, vol. 1426, pp. 533-538, doi: 10.1063/1.3686334. [Online]. Available: https://www.scopus.com/inward/record.uri?eid=2-s2.0-84861976345&doi=10.1063%2f1.3686334&partnerID=40&md5=4d5cb9bb7009ae5a031019f9109a269d

[78] P. H. Chiu and V. F. Nesterenko, "Processing and mechanical properties of novel Al-W composites with ordered mesostructure," *Journal of Composite Materials,* Article vol. 50, no. 28, pp. 4015-4022, 2016, doi: 10.1177/0021998316630802.

[79] P.-H. Chiu, K. S. Vecchio, and V. F. Nesterenko, "Dynamic compressive strength and mechanism of failure of Al-W fiber composite tubes with ordered mesostructure," *International Journal of Impact Engineering,* vol. 100, pp. 1-6, 2// 2017, doi: https://doi.org/10.1016/j.ijimpeng.2016.10.003.

[80] E. S. Collins, B. R. Skelton, M. L. Pantoya, F. Irin, M. J. Green, and M. A. Daniels, "Ignition sensitivity and electrical conductivity of an aluminum fluoropolymer reactive material with carbon nanofillers," *Combustion and Flame,* Article vol. 162, no. 4, pp. 1417-1421, 2015, doi: 10.1016/j.combustflame.2014.11.008.

[81] M. L. Pantoya and S. W. Dean, "The influence of alumina passivation on nano-Al/Teflon reactions," *Thermochimica Acta,* vol. 493, no. 1-2, pp. 109-110, 2009, doi: 10.1016/j.tca.2009.03.018.

[82] C. D. Yarrington, S. F. Son, T. J. Foley, S. J. Obrey, and A. N. Pacheco, "Nano aluminum energetics: The effect of synthesis method on morphology and combustion performance," *Propellants, Explosives, Pyrotechnics,* vol. 36, no. 6, pp. 551-557, 2011, doi: 10.1002/prep.201000156.

[83] R. A. Yetter, G. A. Risha, and S. F. Son, "Metal particle combustion and nanotechnology," *Proceedings of the Combustion Institute,* vol. 32 II, pp. 1819-1838, 2009, doi: 10.1016/j.proci.2008.08.013.

[84] D. Erdeniz, G. Gulsoy, D. Colanto, and T. Ando, "Ignition characteristics of aluminum-nickel heterostructures produced by ultrasonic powder consolidation," in *TMS 2010, Annual Meeting & Exhibition*, Seattle, WA, 2010, vol. 1: Minerals, Metals & Materials Society, pp. 729-736.

[85] S. Gheybi Hashemabad and T. Ando, "Ignition characteristics of hybrid Al-Ni-Fe2O3 and Al-Ni-CuO reactive composites fabricated by ultrasonic powder consolidation," *Combustion and Flame,* Article vol. 162, no. 4, pp. 1144-1152, 2015, doi: 10.1016/j.combustflame.2014.10.006.

[86] S. K. Pillai, A. Hadjiafxenti, C. C. Doumanidis, T. Ando, and C. Rebholz, "Ultrasonic consolidation and ignition characteristics of thermite composites," *International Journal of Applied Ceramic Technology*, Article vol. 9, no. 1, pp. 206-213, 2012, doi: 10.1111/j.1744-7402.2011.02655.x.

[87] B. J. Clapsaddle, L. Zhao, A. E. Gash, J, H. Satcher Jr., K. J. Shea, M. L. Pantoya & R. L. Simpson, "Synthesis and characterization of mixed metal oxide nanocomposite energetic materials," in *MRS Proceedings*, Boston, MA., R. Armstrong, N. Thadhani, W. Wilson, J. Gilman, and R. Simpson, Eds., 2003, vol. 800: Materials Research Society, in Synthesis, Characterization and Properties of Energetic/Reactive Nanomaterials, pp. 91-96, doi: 10.1557/PROC-800-AA2.7. [Online]. Available: http://www.scopus.com/inward/record.url?eid=2-s2.0-2442568657&partnerID=40&md5 =d65dd499fef5cc73e9e241fe62cd87f7

[88] A. E. Gash, J. H. Satcher Jr, R. L. Simpson, and B. J. Clapsaddle, "Nanostructured energetic materials with sol-gel methods," in *MRS 2003*, Boston, MA., R. Armstrong, N. Thadhani, W. Wilson, J. Gilman, and R. Simpson, Eds., 2003, vol. 800, in Synthesis, Characterization and Properties of Energetic/Reactive Nanomaterials, pp. 55-66, doi: 10.1557/PROC-800-AA2.2. [Online]. Available: http://www.scopus.com/inward/record.url?eid=2-s2.0-2442539008&partnerID=40&md5=b470b899d6115bcffd4d47f7 53fdb420

[89] K. B. Plantier, M. L. Pantoya, and A. E. Gash, "Combustion wave speeds of nanocomposite Al/Fe2O3: The effects of Fe2O3 particle synthesis technique," *Combustion and Flame*, vol. 140, no. 4, pp. 299-309, 2005, doi: 10.1016/j.combustflame.2004.10.009.

[90] D. Prentice, M. L. Pantoya, and A. E. Gash, "Combustion wave speeds of sol-gel-synthesized tungsten trioxide and nano-aluminum: The effect of impurities on flame propagation," *Energy and Fuels*, vol. 20, no. 6, pp. 2370-2376, 2006, doi: 10.1021/ef060210i.

[91] J. L. Cheng, H. H. Hng, H. Y. Ng, P. C. Soon, and Y. W. Lee, "Synthesis and characterization of self-assembled nanoenergetic Al–Fe2O3 thermite system," *Journal of Physics and Chemistry of Solids*, vol. 71, no. 2, pp. 90-94, 2010, doi: http://dx.doi.org/10.1016/j.jpcs.2009.08.017.

[92] R. Thiruvengadathan, S. W. Chung, B. Balasubramanian, C. S. Staley, K. Gangopadhyay, and S. Gangopadhyay, "A versatile self-assembly approach toward high performance nanoenergetic composite using functionalized graphene," *Langmuir*, vol. 30, no. 22, pp. 6556-6564, 2014, doi: 10.1021/la500573e.

[93] J. L. Cheng, H. H. Hng, Y. W. Lee, S. W. Du, and N. N. Thadhani, "Kinetic study of thermal- and impact-initiated reactions in Al-Fe2O3 nanothermite," *Combustion and Flame*, vol. 157, no. 12, pp. 2241-2249, 2010, doi: https://doi.org/10.1016/j.combustflame.2010.07.012

[94] J. L. Cheng, H. H. Hng, H. Y. Ng, P. C. Soon, and Y. W. Lee, "Synthesis and characterization of self-assembled nanoenergetic Al-Fe2O3 thermite system," *Journal of Physics and Chemistry of Solids*, Article vol. 71, no. 2, pp. 90-94, 2010, doi: 10.1016/j.jpcs.2009.08.017.

[95] X. Li, P. Guerieri, W. Zhou, C. Huang, and M. R. Zachariah, "Direct deposit laminate nanocomposites with enhanced propellent properties," *ACS Applied Materials and Interfaces,* Article vol. 7, no. 17, pp. 9103-9109, 2015, doi: 10.1021/acsami.5b00891.

[96] X. Zhou, M. Torabi, J. Lu, R. Shen, and K. Zhang, "Nanostructured energetic composites: Synthesis, ignition/combustion modeling, and applications," *ACS Applied Materials and Interfaces,* Article vol. 6, no. 5, pp. 3058-3074, 2014, doi: 10.1021/am4058138.

[97] K. T. Sullivan, C. Zhu, E. B. Duoss, A. E. Gash, D. B. Koleshy, J. D. Kuntz, J. A. Lewis and C. M. Spadaccini, "Controlling Material Reactivity Using Architecture," *Advanced materials (Deerfield Beach, Fla.),* Article vol. 28, no. 10, pp. 1934-1939, 2016, doi: 10.1002/adma.201504286.

[98] K. T. Sullivan, C. Zhu, D. J. Tanaka, J. D. Kuntz, E. B. Duoss, and A. E. Gash, "Electrophoretic deposition of thermites onto micro-engineered electrodes prepared by direct-ink writing," *Journal of Physical Chemistry B,* Article vol. 117, no. 6, pp. 1686-1693, 2013, doi: 10.1021/jp306440t.

[99] A. M. Marquez, C. H. Braithwaite, T. P. Weihs, N. M. Krywopusk, D. J. Gibbins, K. S. Vecchio, and M. A. Meyers, "Fragmentation and constitutive response of tailored mesostructured aluminum compacts," *Journal of Applied Physics,* Article vol. 119, no. 14, 2016, Art no. 145903, doi: 10.1063/1.4945813.

[100] D. P. Adams, "Reactive multilayers fabricated by vapor deposition: A critical review," *Thin Solid Films,* 10.1016/j.tsf.2014.09.042 no. Copyright (C) 2014 American Chemical Society (ACS). All Rights Reserved., p. Ahead of Print, 2014, doi: 10.1016/j.tsf.2014.09.042.

[101] M. E. Reiss, C. M. Esber, D. Van Heerden, A. J. Gavens, M. E. Williams, and T. P. Weihs, "Self-propagating formation reactions in Nb/Si multilayers," *Materials Science and Engineering A,* vol. 261, no. 1-2, pp. 217-222, 1999. [Online]. Available: http://www.scopus.com/inward/record.url?eid=2-s2.0-0000408365&partnerID=40&md5=94fe48cc7f601434b674d982644e624d.

[102] A. J. Gavens, D. Van Heerden, A. B. Mann, M. E. Reiss, and T. P. Weihs, "Effect of intermixing on self-propagating exothermic reactions in Al/Ni nanolaminate foils," *Journal of Applied Physics,* vol. 87, no. 3, pp. 1255-1263, 2000.

[103] S. C. Barron, S. T. Kelly, J. Kirchhoff, R. Knepper, K. Fisher, K. J. T. Livi, E. M. Dufresne, K. Fezzaa, T. W. Barbee, T. C. Hufnagel, and T. P. Weihs, "Self-propagating reactions in Al/Zr multilayers: Anomalous dependence of reaction velocity on bilayer thickness," *Journal of Applied Physics,* vol. 114, no. 22, 2013, Art no. 223517, doi: 10.1063/1.4840915.

[104] G. M. Fritz, S. J. Spey, Jr., M. D. Grapes, and T. P. Weihs, "Thresholds for igniting exothermic reactions in Al/Ni multilayers using pulses of electrical, mechanical, and thermal energy," *J. Appl. Phys. (Melville, NY, U. S.),* 10.1063/1.4770478 vol. 113, no. Copyright (C) 2014 American Chemical Society (ACS). All Rights Reserved., pp. 014901/1-014901/11, 2013, doi: 10.1063/1.4770478.

[105] K. J. Blobaum, M. E. Reiss, J. M. Plitzko Lawrence, and T. P. Weihs, "Deposition and characterization of a self-propagating CuOx/Al thermite reaction in a multilayer foil geometry," *Journal of Applied Physics,* vol. 94, no. 5, pp. 2915-2922, 2003. [Online]. Available: http://www.scopus.com/inward/record.url?eid=2-s2.0-0141633891&partnerID=40&md5=1ccd892afb31efede4c05e2bb6b4db6c.

[106] K. J. Blobaum, A. J. Wagner, J. M. Plitzko, D. Van Heerden, D. H. Fairbrother, and T. P. Weihs, "Investigating the reaction path and growth kinetics in CuOx/Al multilayer foils," *Journal of Applied Physics,* vol. 94, no. 5, pp. 2923-2929, 2003. [Online]. Available: http://www.scopus.com/inward/record.url?eid=2-s2.0-0141745984&partnerID=40&md5=77fbe9c0b8afd08f7ce63a348a929998.

[107] J. Kwon, J. M. Ducéré, P. Alphonse, M. Bahrami, M. Petrantoni, J. Veyan, C Tenailleau, A Estève, C Rossi, and Y. J. Chabal, "Interfacial chemistry in Al/CuO reactive nanomaterial and its role in exothermic reaction," *ACS Applied Materials and Interfaces,* vol. 5, no. 3, pp. 605-613, 2013. [Online]. Available: http://www.scopus.com/inward/record.url?eid=2-s2.0-84873621574&partnerID=40&md5=b46fd6531aa763ab134504a8bcc82a73.

[108] A. Nicollet, G. Lahiner, A. Belisario, S. Souleille, M. Djafari-Rouhani, A. Estève, and C. Rossi, "Investigation of Al/CuO multilayered thermite ignition," *Journal of Applied Physics,* Article vol. 121, no. 3, 2017, Art no. 034503, doi: 10.1063/1.4974288.

[109] M. Petrantoni, C. Rossi, L. Salvagnac, V. Conédéra, A. Estève, C. Tenailleau, P. Alphonse, and Y. J. Chabal, "Multilayered Al/CuO thermite formation by reactive magnetron sputtering: Nano versus micro," *Journal of Applied Physics,* vol. 108, no. 8, 2010. [Online]. Available: http://www.scopus.com/inward/record.url?eid=2-s2.0-78149448143&partnerID=40&md5=e70f71d8c1a5fb7ec5da9285d3c48b11.

[110] C. Lanthony, M. Guiltat, J. Ducéré, A. Verdier, A. Hémeryck, M. Djafari-Rouhani, C. Rossi, Y. J. Chabal, and A. Estève, "Elementary surface chemistry during CuO/Al nanolaminate-thermite synthesis: Copper and oxygen deposition on aluminum (111) surfaces," *ACS Applied Materials and Interfaces,* Article vol. 6, no. 17, pp. 15086-15087, 2014, doi: 10.1021/am503126k.

[111] L. Marín, C. E. Nanayakkara, J. Veyan, B. Warot-Fonrose, S. Joulie, A. Estève, C. Tenailleau, Y. J. Chabal, and C. Rossi, "Enhancing the Reactivity of Al/CuO Nanolaminates by Cu Incorporation at the Interfaces," *ACS Applied Materials and Interfaces,* Article vol. 7, no. 22, pp. 11713-11718, 2015, doi: 10.1021/acsami.5b02653.

[112] L. Marín, B. Warot-Fonrose, A. Estève, Y. J. Chabal, L. Alfredo Rodriguez, and C. Rossi, "Self-Organized Al2Cu Nanocrystals at the Interface of Aluminum-Based Reactive Nanolaminates to Lower Reaction Onset Temperature," *ACS Applied Materials and Interfaces,* Article vol. 8, no. 20, pp. 13104-13113, 2016, doi: 10.1021/acsami.6b02008.

[113] D. Xu, Y. Yang, H. Cheng, Y. Y. Li, and K. Zhang, "Integration of nano-Al with Co 3O 4 nanorods to realize high-exothermic core-shell nanoenergetic materials on a silicon

substrate," *Combustion and Flame,* Article vol. 159, no. 6, pp. 2202-2209, 2012, doi: 10.1016/j.combustflame.2012.01.022.

[114] Y. Yang, D. Xu, and K. Zhang, "Effect of nanostructures on the exothermic reaction and ignition of Al/CuOx based energetic materials," *Journal of Materials Science,* Article vol. 47, no. 3, pp. 1296-1305, 2012, doi: 10.1007/s10853-011-5903-z.

[115] X. Zhou, D. Xu, J. Lu, and K. Zhang, "CuO/Mg/fluorocarbon sandwich-structure superhydrophobic nanoenergetic composite with anti-humidity property," *Chemical Engineering Journal,* Article vol. 266, pp. 163-170, 2015, doi: 10.1016/j.cej.2014.12.087.

[116] X. Zhou, D. Xu, G. Yang, Q. Zhang, J. Shen, J. Lu, and K. Zhang, "Highly exothermic and superhydrophobic Mg/fluorocarbon core/shell nanoenergetic arrays," *ACS Applied Materials and Interfaces,* Article vol. 6, no. 13, pp. 10497-10505, 2014, doi: 10.1021/am502078e.

[117] E. L. Dreizin and M. Schoenitz, "Mechanochemically prepared reactive and energetic materials: a review," *Journal of Materials Science,* Article in Press pp. 1-21, 2017, doi: 10.1007/s10853-017-0912-1.

[118] E. L. Dreizin and M. Schoenitz, "Reactive and Metastable Nanomaterials Prepared by Mechanical Milling," in *Metal Nanopowders*: Wiley-VCH Verlag GmbH & Co. KGaA, 2014, pp. 227-278.

[119] C. Suryanarayana, "Mechanical alloying and milling," *Progress in Materials Science,* vol. 46, no. 1-2, pp. 1-184, 2001, doi: 10.1016/s0079-6425(99)00010-9.

[120] C. Suryanarayana, "Recent developments in mechanical alloying," *Reviews on Advanced Materials Science,* vol. 18, no. 3, pp. 203-211, 2008. [Online]. Available: http://www.scopus.com/inward/record.url?eid=2-s2.0-61549087540&partnerID=40 &md5=798e0582cb64524f9e2c3e1494df1562.

[121] A. Y. Dolgoborodov, "Mechanically activated oxidizer-fuel energetic composites," *Combustion, Explosion and Shock Waves,* Article vol. 51, no. 1, pp. 86-99, 2015, doi: 10.1134/S0010508215010098.

[122] A. N. Sterletskii, A. Yu. Dolgoborodov, I. V. Kolbanev, M. N. Makhov, S. F. Lomaeva, A. B. Borunova and V. E. Fortov, "Structure of mechanically activated high-energy Al + polytetrafluoroethylene nanocomposites," *Colloid Journal,* vol. 71, no. 6, pp. 852-860, 2009, doi: 10.1134/s1061933x09060155.

[123] A. N. Streletskii, I. Kolbanev, A. Leonov, A. Dolgoborodov, G. A. Vorob'eva, M. V. Sivak, and D. G. Permenov, "Defective structure and reactivity of mechanoactivated magnesium/fluoroplastic energy-generating composites," *Colloid Journal,* Article vol. 77, no. 2, pp. 213-225, 2015, doi: 10.1134/S1061933X15020180.

[124] D. Stamatis, X. Zhu, M. Schoenitz, E. L. Dreizin, and P. Redner, "Consolidation and mechanical properties of reactive nanocomposite powders," *Powder Technology*, vol. 208, no. 3, pp. 637-642, 2011, doi: 10.1016/j.powtec.2011.01.002.

[125] K. Komvopoulos, *Mechanical Testing of Engineering Materials: Second Edition*. Cognella, Incorporated, 2016.

[126] D. Stamatis, X. Zhu, A. Ermoline, M. Schoenitz, E. L. Dreizin, and P. Redner, "Consolidation of reactive nanocomposite powders," in *45th AIAA/ASME/SAE/ASEE Joint Propulsion Conference and Exhibit*, Denver, CO, 2009, in 45th AIAA/ASME/SAE/ASEE Joint Propulsion Conference and Exhibit, doi: N/A. [Online]. Available: http://www.scopus.com/inward/record.url?eid=2-s2.0-77957841896&partnerID=40&md5=73f4c638dac3d3fb29e334704464e410

[127] W. G. Proud, D. M. Williamson, J. E. Field, and S. M. Walley, "Diagnostic techniques in deflagration and detonation studies," *Chemistry Central Journal*, vol. 9, no. 1, 2015, Art no. 52, doi: 10.1186/s13065-015-0128-x.

[128] B. A. Gama, S. L. Lopatnikov, and J. W. Gillespie Jr, "Hopkinson bar experimental technique: A critical review," *Applied Mechanics Reviews*, Review vol. 57, no. 1-6, pp. 223-250, 2004, doi: 10.1115/1.1704626.

[129] B. Feng, X. Fang, H. X. Wang, W. Dong, and Y. C. Li, "The effect of crystallinity on compressive properties of Al-PTFE," *Polymers*, Article vol. 8, no. 10, 2016, Art no. 356, doi: 10.3390/polym8100356.

[130] S. Xu, S. Yang, P. Zhao, J. Li, and F. Lu, "The study on the compressive behavior of PTFE/Al energetic composite," *Lixue Xuebao/Chinese Journal of Theoretical and Applied Mechanics*, Article vol. 41, no. 5, pp. 708-712, 2009. [Online]. Available: https://www.scopus.com/inward/record.uri?eid=2-s2.0-70350532315&partnerID=40&md5=c487f841f64bab555483571934f86f8f.

[131] X. F. Zhang, J. Zhang, L. Qiao, S. Shi, Y. G. Zhang, Y He, Z. Guan, "Experimental study of the compression properties of Al/W/PTFE granular composites under elevated strain rates," *Mater. Sci. Eng., A*, 10.1016/j.msea.2013.05.063 vol. 581, no. Copyright (C) 2015 American Chemical Society (ACS). All Rights Reserved., pp. 48-55, 2013, doi: 10.1016/j.msea.2013.05.063.

[132] P. D. Zhao, F. Y. Lu, J. L. Li, R. Chen, S. L. Xu, and S. Q. Yang, "The dynamic compressive properties of PTFE/Al reactive materials," *Hanneng Cailiao/Chinese Journal of Energetic Materials*, Article vol. 17, no. 4, pp. 459-462, 2009. [Online]. Available: https://www.scopus.com/inward/record.uri?eid=2-s2.0-70349389372&partnerID=40&md5=aba8730fdb81c3e94be412e17690ed35.

[133] P.-d. Zhao, F.-y. Lu, J.-l. Li, R. Chen, S.-l. Xu, and S.-q. Yang, "The dynamic compressive properties of PTFE/Al reactive materials," *Hanneng Cailiao*, vol. 17, no. 4, pp. 459-462, // 2009.

[134] J. E. Field, S. M. Walley, W. G. Proud, H. T. Goldrein, and C. R. Siviour, "Review of experimental techniques for high rate deformation and shock studies," *International Journal of Impact Engineering,* Conference Paper vol. 30, no. 7, pp. 725-775, 2004, doi: 10.1016/j.ijimpeng.2004.03.005.

[135] E. P. Fahrenthold and C. H. Yew, "Hydrocode simulation of hypervelocity impact fragmentation," *International Journal of Impact Engineering,* Article vol. 17, no. 1-3, pp. 303-310, 1995, doi: 10.1016/0734-743X(95)99856-M.

[136] B. O'Toole, M. Trabia, R. Hixson, S. K. Roy, M. Pena, S. Becker, E. Daykin, E. Machorro, R. Jennings, and M. Matthes, "Modeling plastic deformation of steel plates in hypervelocity impact experiments," in *Procedia Engineering*, 2015, vol. 103, pp. 458-465, doi: 10.1016/j.proeng.2015.04.060. [Online]. Available: https://www.scopus.com/inward/record.uri?eid=2-s2.0-84991408303&doi=10.1016%2fj.proeng.2015.04.060&partnerID=40&md5=7ed977e764899202ec03ae3bb2918243

[137] M. Martin, S. Hanagud, and N. N. Thadhani, "Mechanical behavior of nickel + aluminum powder-reinforced epoxy composites," *Materials Science and Engineering A,* Article vol. 443, no. 1-2, pp. 209-218, 2007, doi: 10.1016/j.msea.2006.08.106.

[138] J. L. Breidenich, J. Turner, G. Kennedy, and N. N. Thadhani, "Impact initiated combustion of aluminum exposed to mechanical pre-activation," *Journal of Physics: Conference Series,* vol. 500, no. PART 18, 2014, Art no. 182006, doi: 10.1088/1742-6596/500/18/182006.

[139] M. Gonzales, A. Gurumurthy, G. B. Kennedy, A. M. Gokhale, and N. N. Thadhani, "Shock compression response of Ti+B reactive powder mixtures," *Journal of Physics: Conference Series,* vol. 500, no. PART 5, 2014, Art no. 052013, doi: 10.1088/1742-6596/500/5/052013.

[140] Q. An, S. V. Zybin, W. A. Goddard, A. Jaramillo-Botero, M. Blanco, and S. N. Luo, "Elucidation of the dynamics for hot-spot initiation at nonuniform interfaces of highly shocked materials," *Physical Review B - Condensed Matter and Materials Physics,* vol. 84, no. 22, 2011, Art no. 220101, doi: 10.1103/PhysRevB.84.220101.

[141] T. L. Jackson, D. E. Hooks, and J. Buckmaster, "Modeling the microstructure of energetic materials with realistic constituent morphology," *Propellants, Explosives, Pyrotechnics,* vol. 36, no. 3, pp. 252-258, 2011. [Online]. Available: http://www.scopus.com/inward/record.url?eid=2-s2.0-79959219734&partnerID=40&md5=0a429a2f82bfd1fc0ffe330994bf75ac.

[142] R. Menikoff, "Hot spot formation from shock reflections," *Shock Waves,* vol. 21, no. 2, pp. 141-148, 2011, doi: 10.1007/s00193-011-0303-5.

[143] S. You, M. W. Chen, D. D. Dlott, and K. S. Suslick, "Ultrasonic hammer produces hot spots in solids," *Nature Communications,* vol. 6, 2015, Art no. 6581, doi: 10.1038/ncomms7581.

[144] J. E. Field, "Hot spot ignition mechanisms for explosives," *Accounts of Chemical Research,* Article vol. 25, no. 11, pp. 489-496, 1992. [Online]. Available: https://www.scopus.com/inward/record.uri?eid=2-s2.0-0001513469&partnerID=40&md5=97724cda87762636923e9ad85cdc49e6.

[145] X. J. Gu, D. R. Emerson, and D. Bradley, "Modes of reaction front propagation from hot spots," *Combustion and Flame,* Article vol. 133, no. 1-2, pp. 63-74, 2003, doi: 10.1016/S0010-2180(02)00541-2.

[146] C. M. Tarver, S. K. Chidester, and A. L. Nichols Iii, "Critical conditions for impact- and shock-induced hot spots in solid explosives," *Journal of Physical Chemistry,* Article vol. 100, no. 14, pp. 5794-5799, 1996. [Online]. Available: https://www.scopus.com/inward/record.uri?eid=2-s2.0-0030568455&partnerID=40&md5=503f1317bc8fdf20b16cbfa40ebe6790.

[147] E. L. Dreizin and M. Schoenitz, "Correlating ignition mechanisms of aluminum-based reactive materials with thermoanalytical measurements," *Progress in Energy and Combustion Science,* vol. 50, pp. 81-105, 2015.

[148] S. Vyazovkin, A. K. Burnham, J. M. Criado, L. A. Pérez-Maqueda, C. Popescu, and N. Sbirrazzuoli, "ICTAC Kinetics Committee recommendations for performing kinetic computations on thermal analysis data," *Thermochimica Acta,* vol. 520, no. 1-2, pp. 1-19, 2011, doi: 10.1016/j.tca.2011.03.034.

[149] S. Vyazovkin, K. Chrissafis, M. L. Di Lorenzo, N. Koga, M. Pijolat, B. Roduit, N. Sbirrazzuoli, J. J. Suñol, "ICTAC Kinetics Committee recommendations for collecting experimental thermal analysis data for kinetic computations," *Thermochimica Acta,* Article vol. 590, pp. 1-23, 2014, doi: 10.1016/j.tca.2014.05.036.

[150] E. L. Dreizin, "Metal-based reactive nanomaterials," *Progress in Energy and Combustion Science,* vol. 35, no. 2, pp. 141-167, 2009, doi: 10.1016/j.pecs.2008.09.001.

[151] P. Swaminathan, M. D. Grapes, K. Woll, S. C. Barron, D. A. Lavan, and T. P. Weihs, "Studying exothermic reactions in the Ni-Al system at rapid heating rates using a nanocalorimeter," *Journal of Applied Physics,* Article vol. 113, no. 14, 2013, Art no. 143509, doi: 10.1063/1.4799628.

[152] T. S. Ward, M. A. Trunov, M. Schoenitz, and E. L. Dreizin, "Experimental methodology and heat transfer model for identification of ignition kinetics of powdered fuels," *International Journal of Heat and Mass Transfer,* vol. 49, no. 25-26, pp. 4943-4954, 2006, doi: 10.1016/j.ijheatmasstransfer.2006.05.025.

[153] R. J. Jacob, D. L. Ortiz-Montalvo, K. R. Overdeep, T. P. Weihs, and M. R. Zachariah, "Incomplete reactions in nanothermite composites," *Journal of Applied Physics,* Article vol. 121, no. 5, 2017, Art no. 054307, doi: 10.1063/1.4974963.

[154] G. Jian, S. Chowdhury, J. Feng, and M. R. Zachariah, "The ignition and combustion study of nano-Al and iodine pentoxide thermite," in *US National Combustion Meeting, 8th*, Park City, UT, 2013, vol. 2: Combustion Institute, Western States Section, pp. 1287-1299.

[155] A. Abraham, S. Zhang, Y. Aly, M. Schoenitz, and E. L. Dreizin, "Aluminum-iodoform composite reactive material," *Advanced Engineering Materials*, vol. 16, no. 7, 2014. [Online]. Available: http://www.scopus.com/inward/record.url?eid=2-s2.0-84892456549&partnerID=40&md5=794208c4d6723373b48c73d41cdd7eb7.

[156] Y. Aly, M. Schoenitz, and E. L. Dreizin, "Aluminum-metal reactive composites," *Combustion Science and Technology*, vol. 183, no. 10, pp. 1107-1132, 2011, doi: 10.1080/00102202.2011.584090.

[157] S. M. Umbrajkar, S. Seshadri, M. Schoenitz, V. K. Hoffmann, and E. L. Dreizin, "Aluminum-rich Al-MoO3 nanocomposite powders prepared by arrested reactive milling," *Journal of Propulsion and Power*, vol. 24, no. 2, pp. 192-198, 2008, doi: 10.2514/1.31762.

[158] R. A. Williams, J. V. Patel, A. Ermoline, M. Schoenitz, and E. L. Dreizin, "Correlation of optical emission and pressure generated upon ignition of fully-dense nanocomposite thermite powders," *Combustion and Flame*, vol. 160, no. 3, pp. 734-741, 2013. [Online]. Available: http://www.scopus.com/inward/record.url?eid=2-s2.0-84872831258&partnerID=40&md5=519a230add98566680f563b4540acbe4.

[159] S. M. Umbrajkar, M. Schoenitz, and E. L. Dreizin, "Heterogeneous processes leading to metal ignition in reactive nanocomposite materials," in *45th AIAA Aerospace Sciences Meeting*, Reno, NV, 2007, vol. 6, in 45th AIAA Aerospace Sciences Meeting 2007, pp. 3582-3589, doi: 10.2514/6.2007-294. [Online]. Available: http://www.scopus.com/inward/record.url?eid=2-s2.0-34250889452&partnerID=40&md5=2e7e6c28326f180d0bc01553f2273a83

[160] Y. L. Shoshin, M. A. Trunov, X. Zhu, M. Schoenitz, and E. L. Dreizin, "Ignition of aluminum-rich Al-Ti mechanical alloys in air," *Combustion and Flame*, vol. 144, no. 4, pp. 688-697, 2006, doi: 10.1016/j.combustflame.2005.08.037.

[161] G. C. Egan, E. J. Mily, J. P. Maria, and M. R. Zachariah, "Probing the Reaction Dynamics of Thermite Nanolaminates," *Journal of Physical Chemistry C*, Article vol. 119, no. 35, pp. 20401-20408, 2015, doi: 10.1021/acs.jpcc.5b04117.

[162] G. Young, R. Jacob, and M. R. Zachariah, "High pressure ignition and combustion of aluminum hydride," *Combustion Science and Technology*, Article vol. 187, no. 9, pp. 1335-1350, 2015, doi: 10.1080/00102202.2015.1038383.

[163] G. Young, G. Jian, R. Jacob, and M. R. Zachariah, "Decomposition and ignition characteristics of titanium hydride at high heating rates," *Combustion Science and Technology*, Article vol. 187, no. 8, pp. 1182-1194, 2015, doi: 10.1080/00102202.2015.1019619.

[164] W. Zhou, J. B. DeLisio, X. Wang, G. C. Egan, and M. R. Zachariah, "Evaluating free vs bound oxygen on ignition of nano-aluminum based energetics leads to a critical reaction rate criterion," *Journal of Applied Physics,* Article vol. 118, no. 11, 2015, Art no. 114303, doi: 10.1063/1.4930889.

[165] G. Young, N. Piekiel, S. Chowdhury, and M. R. Zachariah, "Ignition behavior of α-AlH3," *Combustion Science and Technology,* vol. 182, no. 9, pp. 1341-1359, 2010, doi: 10.1080/00102201003694834.

[166] G. Jian, S. Chowdhury, K. Sullivan, and M. R. Zachariah, "Nanothermite reactions: Is gas phase oxygen generation from the oxygen carrier an essential prerequisite to ignition?," *Combustion and Flame,* vol. 160, no. 2, pp. 432-437, 2013.

[167] B. J. Henz, T. Hawa, and M. R. Zachariah, "On the role of built-in electric fields on the ignition of oxide coated nanoaluminum: Ion mobility versus fickian diffusion," *Journal of Applied Physics,* vol. 107, no. 2, 2010, doi: 10.1063/1.3247579.

[168] L. Zhou, N. Piekiel, S. Chowdhury, D. Lee, and M. R. Zachariah, "Transient ion ejection during nanocomposite thermite reactions," *Journal of Applied Physics*, vol. 106, no. 8, 2009. [Online]. Available: http://www.scopus.com/inward/record.url?eid=2-s2.0-70350721451&partnerID=40&md5=5a356ec571b12715d53949894948d3c4.

[169] L. Zhou, N. Piekiel, S. Chowdhury, and M. R. Zachariah, "Time-resolved mass spectrometry of the exothermic reaction between nanoaluminum and metal oxides: The role of oxygen release," *Journal of Physical Chemistry C,* vol. 114, no. 33, pp. 14269-14275, 2010, doi: 10.1021/jp101146a.

[170] S. Mohan, M. A. Trunov, and E. L. Dreizin, "Heating and ignition of metallic particles by a CO2 laser," *Journal of Propulsion and Power,* vol. 24, no. 2, pp. 199-205, 2008, doi: 10.2514/1.30195.

[171] Y. Aly and E. L. Dreizin, "Ignition and combustion of Al·Mg alloy powders prepared by different techniques," *Combustion and Flame,* vol. 162, no. 4, pp. 1440-1447, 2015, doi: 10.1016/j.combustflame.2014.11.010.

[172] D. Stamatis, E. L. Dreizin, and K. Higa, "Thermal initiation of Al-MoO3 nanocomposite materials prepared by different methods," *Journal of Propulsion and Power,* vol. 27, no. 5, pp. 1079-1087, 2011, doi: 10.2514/1.b34179.

[173] E. Beloni and E. L. Dreizin, "Model of heating and ignition of conductive polydisperse powder in electrostatic discharge," *Combustion Theory and Modelling,* vol. 16, no. 6, pp. 976-993, 2012, doi: 10.1080/13647830.2012.689010.

[174] I. Monk, R. Williams, X. Liu, and E. L. Dreizin, "Electro-static discharge ignition of monolayers of nanocomposite thermite powders prepared by arrested reactive milling," *Combustion Science and Technology,* vol. 187, no. 8, pp. 1276-1294, 2015, doi: 10.1080/00102202.2015.1035373.

[175] R. A. Williams, J. V. Patel, and E. L. Dreizin, "Ignition of fully dense nanocomposite thermite powders by an electric spark," *Journal of Propulsion and Power,* vol. 30, no. 3, pp. 765-774, 2014, doi: 10.1016/0304-3886(85)90041-5.

[176] W. L. Shaw, D. D. Dlott, R. A. Williams, and E. L. Dreizin, "Ignition of nanocomposite thermites by electric spark and shock wave," *Propellants, Explosives, Pyrotechnics,* vol. 39, no. 3, pp. 444-453, 2014. [Online]. Available: http://www.scopus.com/inward/record.url?eid=2-s2.0-84902497708&partnerID=40&md5=810067dbc24d33bf400b4c037db9e1fc.

[177] I. Monk, M. Schoenitz, and E. L. Dreizin, "Modes of Ignition of Powder Layers of Nanocomposite Thermites by Electrostatic Discharge," *Journal of Energetic Materials,* Article in Press vol. 35, no. 1, pp. 29-43, 2016, doi: 10.1080/07370652.2016.1150366.

[178] Y. Yang, S. Wang, Z. Sun, and D. D. Dlott, "Near-infrared and visible absorption spectroscopy of nano-energetic materials containing aluminum and boron," *Propellants, Explosives, Pyrotechnics,* vol. 30, no. 3, pp. 171-177, 2005, doi: 10.1002/prep.200500001.

[179] Y. Yang, S. Wang, Z. Sun, and D. D. Dlott, "Near-infrared laser ablation of poly tetrafluoroethylene (Teflon) sensitized by nanoenergetic materials," *Applied Physics Letters,* vol. 85, no. 9, pp. 1493-1495, 2004, doi: 10.1063/1.1785291.

[180] Y. Yang, S. Wang, Z. Sun, and D. D. Dlott, "Propagation of shock-induced chemistry in nanoenergetic materials: The first micrometer," *Journal of Applied Physics,* vol. 95, no. 7, pp. 3667-3676, 2004, doi: 10.1063/1.1652250.

[181] M. A. Zamkov, R. W. Conner, and D. D. Dlott, "Ultrafast chemistry of nanoenergetic materials studied by time-resolved infrared spectroscopy: Aluminum nanoparticles in teflon," *Journal of Physical Chemistry C,* vol. 111, no. 28, pp. 10278-10284, 2007, doi: 10.1021/jp072662h.

[182] R. W. Conner and D. D. Dlott, "Ultrafast condensed-phase emission from energetic composites of teflon and nanoaluminum," *Journal of Physical Chemistry A,* vol. 114, no. 25, pp. 6731-6741, 2010, doi: 10.1021/jp101539u.

[183] A. Plummer, V. A. Kuznetsov, J. Gascooke, J. Shapter, and N. H. Voelcker, "Laser shock ignition of porous silicon based nano-energetic films," *Journal of Applied Physics,* vol. 116, no. 5, 2014, Art no. 054912, doi: 10.1063/1.4892444.

[184] X. Zheng, A. D. Curtis, W. L. Shaw, and D. D. Dlott, "Shock initiation of nano-Al + Teflon: Time-resolved emission studies," *Journal of Physical Chemistry C,* vol. 117, no. 9, pp. 4866-4875, 2013, doi: 10.1021/jp312637g.

[185] K. E. Brown, W. L. Shaw, X. X. Zheng, and D. D. Dlott, "Simplified laser-driven flyer plates for shock compression science," (in English), *Rev Sci Instrum,* vol. 83, no. 10, Oct 2012, Doi 10.1063/1.4754717.

[186] J. Wang, W. P. Bassett, and D. D. Dlott, "Shock initiation of nano-Al/Teflon: High dynamic range pyrometry measurements," *Journal of Applied Physics,* Article vol. 121, no. 8, 2017, Art no. 085902, doi: 10.1063/1.4977109.

[187] C. M. Berg and D. D. Dlott, "Picosecond dynamics of shock compressed and flash-heated nanometer thick films of δ-HMX," *Journal of Physics: Conference Series,* vol. 500, no. PART 14, 2014, Art no. 142004, doi: 10.1088/1742-6596/500/14/142004.

[188] G. C. Egan, T. Lagrange, and M. R. Zachariah, "Time-resolved nanosecond imaging of nanoscale condensed phase reaction," *Journal of Physical Chemistry C,* Article vol. 119, no. 5, pp. 2792-2797, 2015, doi: 10.1021/jp5084746.

[189] M. D. Grapes, T. LaGrange, K. Woll, B. W. Reed, G. H. Campbell, D. A. LaVan, and T. P. Weihs, "In situ transmission electron microscopy investigation of the interfacial reaction between Ni and Al during rapid heating in a nanocalorimeter," *APL Mater.,* 10.1063/1.4900818 vol. 2, no. Copyright (C) 2014 American Chemical Society (ACS). All Rights Reserved., pp. 116102/1-116102/7, 2014, doi: 10.1063/1.4900818.

[190] J. C. Trenkle, L. J. Koerner, M. W. Tate, Noël Walker, S. M. Gruner, T. P. Weihs, and T. C. Hufnagel, "Time-resolved x-ray microdiffraction studies of phase transformations during rapidly propagating reactions in Al/Ni and Zr/Ni multilayer foils," *Journal of Applied Physics,* vol. 107, no. 11, p. 113511, 2010, doi: 10.1063/1.3428471.

[191] Y. Aly, M. Schoenitz, and E. L. Dreizin, "Ignition and combustion of mechanically alloyed Al-Mg powders with customized particle sizes," *Combustion and Flame,* vol. 160, no. 4, pp. 835-842, 4// 2013, doi: 10.1016/j.combustflame.2012.12.011.

[192] S. Wang, X. Liu, M. Schoenitz, and E. L. Dreizin, "Nanocomposite Thermites with Calcium Iodate Oxidizer," *Propellants, Explosives, Pyrotechnics,* Article vol. 42, no. 3, pp. 284-292, 2017, doi: 10.1002/prep.201600213.

[193] X. Liu, M. Schoenitz, and E. L. Dreizin, "Boron-based reactive materials with high concentrations of iodine as a biocidal additive," *Chemical Engineering Journal,* Article vol. 325, pp. 495-501, 2017, doi: 10.1016/j.cej.2017.05.100.

[194] S. Wang, A. Abraham, Z. Zhong, M. Schoenitz, and E. L. Dreizin, "Ignition and combustion of boron-based Al·B·I2 and Mg·B·I2 composites," *Chemical Engineering Journal,* Article vol. 293, pp. 112-117, 2016, doi: 10.1016/j.cej.2016.02.071.

[195] R. J. Jacob, B. Wei, and M. R. Zachariah, "Quantifying the enhanced combustion characteristics of electrospray assembled aluminum mesoparticles," *Combustion and Flame,* Article vol. 167, pp. 472-480, 2016, doi: 10.1016/j.combustflame.2015.09.032.

[196] T. Bazyn, P. Lynch, H. Krier, and N. Glumac, "Combustion measurements of fuel-rich aluminum and molybdenum oxide nano-composite mixtures," *Propellants, Explos., Pyrotech.,* 10.1002/prep.200900016 vol. 35, pp. 93-99, 2010, doi: 10.1002/prep.200900016.

[197] T. Bazyn, N. Glumac, H. Krier, T. S. Ward, M. Schoenitz, and E. L. Dreizin, "Reflected shock ignition and combustion of aluminum and nanocomposite thermite powders," *Combustion Science and Technology,* vol. 179, no. 3, pp. 457-476, 2007, doi: 10.1080/00102200600637261.

[198] B. Aaron Mason, L. J. Groven, S. F. Son, and R. A. Yetter, "Combustion performance of several nanosilicon-based nanoenergetics," *Journal of Propulsion and Power,* vol. 29, no. 6, pp. 1435-1444, 2013, doi: 10.2514/1.b34902.

[199] S. F. Son, B. W. Asay, T. J. Foley, R. A. Yetter, M. H. Wu, and G. A. Risha, "Combustion of nanoscale Al/MoO3 thermite in microchannels," *Journal of Propulsion and Power,* vol. 23, no. 4, pp. 715-721, 2007, doi: 10.2514/1.26090.

[200] V. K. Patel, J. R. Saurav, K. Gangopadhyay, S. Gangopadhyay, and S. Bhattacharya, "Combustion characterization and modeling of novel nanoenergetic composites of Co3O4/nAl," *RSC Advances,* Article vol. 5, no. 28, pp. 21471-21479, 2015, doi: 10.1039/c4ra14751k.

[201] S. W. Dean, M. L. Pantoya, A. E. Gash, S. C. Stacy, and L. J. Hope-Weeks, "Enhanced convective heat transfer in nongas generating nanoparticle thermites," *Journal of Heat Transfer,* vol. 132, no. 11, 2010, doi: 10.1115/1.4001933.

[202] J. M. Densmore, K. T. Sullivan, A. E. Gash, and J. D. Kuntz, "Expansion behavior and temperature mapping of thermites in burn tubes as a function of fill length," *Propellants, Explosives, Pyrotechnics,* vol. 39, no. 3, pp. 416-422, 2014. [Online]. Available: http://www.scopus.com/inward/record.url?eid=2-s2.0-84902551222&partnerID=40&md5=bf2bd7fca03081ddeab00ab033dac21e.

[203] K. T. Sullivan, O. Cervantes, J. M. Densmore, J. D. Kuntz, A. E. Gash, and J. D. Molitoris, "Quantifying dynamic processes in reactive materials: An extended burn tube test," *Propellants, Explosives, Pyrotechnics,* vol. 40, no. 3, pp. 394-401, 2015, doi: 10.1002/prep.201400267.

[204] I. Monk, M. Schoenitz, R. J. Jacob, E. L. Dreizin, and M. R. Zachariah, "Combustion Characteristics of Stoichiometric Al-CuO Nanocomposite Thermites Prepared by Different Methods," (in English), *Combustion Science and Technology,* Article vol. 189, no. 3, pp. 555-574, 2017, doi: 10.1080/00102202.2016.1225731.

[205] Y. Aly, V. K. Hoffman, M. Schoenitz, and E. L. Dreizin, "Reactive, mechanically alloyed Al · Mg powders with customized particle sizes and compositions," *Journal of Propulsion and Power,* vol. 30, no. 1, pp. 96-104, 2014. [Online]. Available: http://www.scopus.com/inward/record.url?eid=2-s2.0-84892580955&partnerID=40&md5=78e88400494f304e9420d58581307f28.

[206] A. Abraham, Z. Zhong, R. Liu, S. A. Grinshpun, M. Yermakov, R. Indugula, M. Schoenitz and E. L. Dreizin, "Preparation, Ignition and Combustion of Mg·S Reactive Nanocomposites," *Combustion Science and Technology,* vol. 188, no. 8, pp. 1345-1364, 2016.

[207] S. A. Grinshpun, M. Yermakov, R. Indugula, A. Abraham, M. Schoenitz, and E. L. Dreizin, "Aluminum-based materials for inactivation of aerosolized spores of Bacillus anthracis surrogates," *Aerosol Science and Technology*, Article vol. 51, no. 2, pp. 224-234, 2017, doi: 10.1080/02786826.2016.1257109.

[208] E. M. Hunt and M. L. Pantoya, "Impact sensitivity of intermetallic nanocomposites: A study on compositional and bulk density," *Intermetallics*, vol. 18, no. 8, pp. 1612-1616, 2010, doi: 10.1016/j.intermet.2010.04.015.

[209] M. T. Beason, I. E. Gunduz, and S. F. Son, "The role of fracture in the impact initiation of Ni-Al intermetallic composite reactives during dynamic loading," *Acta Materialia*, Article vol. 133, pp. 247-257, 2017, doi: 10.1016/j.actamat.2017.05.042.

[210] B. A. Mason, L. J. Groven, and S. F. Son, "The role of microstructure refinement on the impact ignition and combustion behavior of mechanically activated Ni/Al reactive composites," *J. Appl. Phys. (Melville, NY, U. S.)*, 10.1063/1.4821236 vol. 114, no. Copyright (C) 2014 American Chemical Society (ACS). All Rights Reserved., pp. 113501/1-113501/7, 2013, doi: 10.1063/1.4821236.

[211] R. V. Reeves, A. S. Mukasyan, and S. F. Son, "Thermal and impact reaction initiation in Ni/Al heterogeneous reactive systems," *Journal of Physical Chemistry C*, vol. 114, no. 35, pp. 14772-14780, 2010. [Online]. Available: http://www.scopus.com/inward/record.url?eid=2-s2.0-79951641727&partnerID=40&md5=5bd77d0db6f4bb62bbd9aa99501c69c6.

[212] B. B. Aydelotte and N. N. Thadhani, "Mechanistic aspects of impact initiated reactions in explosively consolidated metal+aluminum powder mixtures," *Materials Science and Engineering A*, vol. 570, pp. 164-171, 2013. [Online]. Available: http://www.scopus.com/inward/record.url?eid=2-s2.0-84874398538&partnerID=40&md5=bfe0cae7a0cbc0ba86903d467fa3338d.

[213] R. G. Ames, "Vented chamber calorimetry for impact-initiated energetic materials," in *43rd AIAA Aerospace Sciences Meeting and Exhibit - Meeting Papers*, 2005, pp. 15391-15403, doi: N/A. [Online]. Available: http://www.scopus.com/inward/record.url?eid=2-s2.0-30744438073&partnerID=40&md5=57cd248692fb2c68fe62e693385a58e9

[214] R. G. Ames, "Energy release characteristics of impact-initiated energetic materials," in *Materials Research Society Symposium Proceedings*, 2006, vol. 896, pp. 123-132, doi: N/A. [Online]. Available: http://www.scopus.com/inward/record.url?eid=2-s2.0-33646941665&partnerID=40&md5=7253aa43d542c03f0f0468b2014bd743

[215] B. Sorensen, "High-velocity impact of encased Al/PTFE projectiles on structural aluminum armor," in *Procedia Engineering*, 2015, vol. 103, pp. 569-576, doi: 10.1016/j.proeng.2015.04.074. [Online]. Available: https://www.scopus.com/inward/record.uri?eid=2-s2.0-84991387381&doi=10.1016%2fj.proeng.2015.04.074&partnerID=40&md5=7f245bb0346941b5838381b3fb7b7da7

[216] B. Feng, X. Fang, Y. C. Li, S. Z. Wu, Y. M. Mao, and H. X. Wang, "Influence of processing techniques on mechanical properties and impact initiation of an Al-PTFE reactive material," *Central European Journal of Energetic Materials,* Article vol. 13, no. 4, pp. 989-1004, 2016, doi: 10.22211/cejem/61496.

[217] Y. Li, C. Jiang, Z. Wang, and P. Luo, "Experimental study on reaction characteristics of PTFE/Ti/W energetic materials under explosive loading," *Materials,* Article vol. 9, no. 11, 2016, Art no. 936, doi: 10.3390/ma9110936.

[218] C. Ge, Y. Dong, W. Maimaitituersun, Y. Ren, and S. Feng, "Experimental Study on Impact-induced Initiation Thresholds of Polytetrafluoroethylene/Aluminum Composite," *Propellants, Explosives, Pyrotechnics,* Article vol. 42, no. 5, pp. 514-522, 2017, doi: 10.1002/prep.201600216.

[219] Y. Li, Z. Wang, C. Jiang, and H. Niu, "Experimental study on impact-induced reaction characteristics of PTFE/Ti composites enhanced by W particles," *Materials,* Article vol. 10, no. 2, 2017, Art no. 175, doi: 10.3390/ma10020175.

[220] F. Y. Xu, Y. F. Zheng, Q. B. Yu, X. P. Zhang, and H. F. Wang, "Damage effects of aluminum plate by reactive material projectile impact," *International Journal of Impact Engineering,* Article vol. 104, pp. 38-44, 2017, doi: 10.1016/j.ijimpeng.2017.02.010.

[221] X. F. Zhang, A. S. Shi, L. Qiao, J. Zhang, Y. G. Zhang, and Z. W. Guan, "Experimental study on impact-initiated characters of multifunctional energetic structural materials," *J. Appl. Phys. (Melville, NY, U. S.),* 10.1063/1.4793281 vol. 113, no. Copyright (C) 2015 American Chemical Society (ACS). All Rights Reserved., pp. 083508/1-083508/10, 2013, doi: 10.1063/1.4793281.

[222] J. Zhou, Y. He, Y. He, and C. T. Wang, "Investigation on Impact Initiation Characteristics of Fluoropolymer-matrix Reactive Materials," *Propellants, Explosives, Pyrotechnics,* Article vol. 42, no. 6, pp. 603-615, 2017, doi: 10.1002/prep.201700003.

[223] A. Y. Dolgoborodov, M. N. Makhov, I. V. Kolbanev, A. N. Streletskiĭ, and V. E. Fortov, "Detonation in an aluminum-teflon mixture," *JETP Letters,* vol. 81, no. 7, pp. 311-314, 2005, doi: 10.1134/1.1944069.

[224] D. L. Gur'ev, Y. A. Gordopolov, S. S. Batsanov, A. G. Merzhanov, and V. E. Fortov, "Solid-state detonation in the zinc-sulfur system," *Applied Physics Letters,* vol. 88, no. 2, pp. 1-3, 2006, Art no. 024102, doi: 10.1063/1.2164411.

[225] J. H. S. Lee, S. Goroshin, A. Yoshinaka, M. Romano, J. Jiang, I. Hooton and F. Zhang, "Attempts to initiate detonations in metal-sulphur mixtures," in *Shock Compression of Condensed Matter - 1999: Proceedings of the Conference of the American Physical Society Topical Group on Shock Compression of Condensed Matter held at Snowbird, Utah, June 27-July 2, 1999,* M. D. Furnish, L. C. Chhabildas, and R. S. Hixson Eds.: American Inst. of Physics, 2000, pp. 775-778.

[226] F. X. Jetté, S. Goroshin, A. J. Higgins, and J. J. Lee, "Experimental investigation of gasless detonation in metal-sulfur compositions," *Combustion, Explosion and Shock Waves,* vol. 45, no. 2, pp. 211-217, 2009, doi: 10.1007/s10573-009-0028-2.

[227] F. X. Jetté, A. J. Higgins, S. Goroshin, D. L. Frost, Y. Charron-Tousignant, M. I. Radulescu, and J. J. Lee, "In-situ measurements of the onset of bulk exothermicity in shock initiation of reactive powder mixtures," *Journal of Applied Physics,* vol. 109, no. 8, 2011, doi: 10.1063/1.3553861.

[228] F. X. Jetté, S. Goroshin, D. L. Frost, A. J. Higgins, and J. J. Lee, "On the relationship between shock and thermal initiating conditions for various reactive powder mixtures," *Propellants, Explosives, Pyrotechnics,* vol. 37, no. 3, pp. 345-358, 2012. [Online]. Available: http://www.scopus.com/inward/record.url?eid=2-s2.0-84862511091&partnerID=40&md5=eff92d5db1af5eee5bd24b5a3121a377.

[229] P. H. Chiu, K. L. Olney, A. Higgins, M. Serge, D. J. Benson, and V. F. Nesterenko, "The mechanism of instability and localized reaction in the explosively driven collapse of thick walled Ni-Al laminate cylinders," *Applied Physics Letters,* vol. 102, no. 24, 2013, Art no. 241912, doi: 10.1063/1.4811837.

[230] K. L. Olney, P. H. Chiu, A. Higgins, M. Serge, T. P. Weihs, G. M. Fritz, A. K. Stover, D. J. Benson & V. F. Nesterenko, "The mechanisms of plastic strain accommodation during the high strain rate collapse of corrugated Ni-Al laminate cylinders," *Philosophical Magazine,* 2014, doi: 10.1080/14786435.2014.948523.

[231] J. Guadarrama, E. L. Dreizin, and N. Glumac, "Reactive Liners Prepared Using Powders of Aluminum and Aluminum-Magnesium Alloys," *Propellants, Explosives, Pyrotechnics,* Article vol. 41, no. 4, pp. 605-611, 2016, doi: 10.1002/prep.201500230.

[232] D. L. Frost, J. Loiseau, S. Goroshin, F. Zhang, A. Milne, and A. Longbottom, "Fracture of explosively compacted aluminum particles in a cylinder," in *AIP Conference*, 2017, vol. 1793, doi: 10.1063/1.4971701. [Online]. Available: https://www.scopus.com/inward/record.uri?eid=2-s2.0-85017035539&doi=10.1063%2f1.4971701&partnerID=40&md5=9c9aa6f5ad219413defb68e735a70ff8

[233] P.-d. Zhao, F.-y. Lu, J.-l. Li, R. Chen, S.-l. Xu, and S.-q. Yang, "The dynamic compressive properties of PTFE/Al reactive materials," *Hanneng Cailiao,* vol. 17, no. Copyright (C) 2015 American Chemical Society (ACS). All Rights Reserved., pp. 459-462, 2009.

[234] J. Guadarrama, E. L. Dreizin, and N. Glumac, "Reactive liners prepared using powders of aluminum and aluminum-magnesium alloys," *Propellants Explosives Pyrotechnics,* vol. In Press, 2015.

[235] P. D. Church, R. P. Claridge, P. J. Gould, and R. G. Townsley, "Improvements in and relating to oil well perforators," Patent WO2012013926A1 Patent Appl. Copyright (C) 2015 American Chemical Society (ACS). All Rights Reserved., 2012.

[236] T. R. Sippel, S. F. Son, and L. J. Groven, "Altering reactivity of aluminum with selective inclusion of polytetrafluoroethylene through mechanical activation," *Propellants, Explosives, Pyrotechnics,* Article vol. 38, no. 2, pp. 286-295, 2013, doi: 10.1002/prep.201200102.

[237] A. Coverdill, C. Delaney, A. Jennrich, H. Krier, and N. G. Glumac, "Tungsten Combustion in Explosively Initiated W/Zr Mechanical Alloys," *Journal of Energetic Materials,* vol. 32, no. 3, pp. 135-145, 2013, doi: 10.1080/07370652.2013.795203.

[238] G. D. Hugus, E. W. Sheridan, and G. W. Brooks, "Dispersed metal-metal binder matrix structural materials for incorporation into reactive fragmentation weapons," Patent EP1864961A2 Patent Appl. Copyright (C) 2016 American Chemical Society (ACS). All Rights Reserved., 2007.

[239] F. Zhang and W. H. Wilson, "The effect of charge reactive metal cases on air blast," 2009, vol. 1195, pp. 149-152, doi: 10.1063/1.3295089. [Online]. Available: https://www.scopus.com/inward/record.uri?eid=2-s2.0-74949121034&doi=10.1063%2f1.3295089&partnerID=40&md5=36602d467edb3478ec893587c2690e99

[240] A. Duckham, S. J. Spey, J. Wang, M. E. Reiss, and T. P. Weihs, "Reactive nanostructured foil used as a heat source for joining titanium," *Journal of Applied Physics,* vol. 96, no. 4, pp. 2336-2342, 2004, doi: 10.1063/1.1769097.

[241] R. W. Nelson, "Nuclear Bunker Busters, Mini-Nukes, and the US Nuclear Stockpile," *Physics Today,* vol. 56, no. 11, pp. 32-37, 2003. [Online]. Available: http://www.scopus.com/inward/record.url?eid=2-s2.0-0345330200&partnerID=40&md5=9b33d6e954f210fd5089ca57a0519073.

[242] Y. Li, B. Zhou, Z. C. Qin, S. Ruiqi, F. Chen, P. and K. Du, "Development of composite semiconductor bridge technique for electrical-explosive device," *Hanneng Cailiao/Chinese Journal of Energetic Materials,* vol. 21, no. 3, pp. 387-393, 2013, doi: 10.3969/j.issn.1006-9941.2013.03.022.

[243] S. P. Andrew, R. D. Caligiuri, and L. E. Eiselstein, "Review of penetration mechanisms and dynamic properties of tungsten and depleted uranium penetrators," in *Tungsten and Tungsten Alloys*, 1991, pp. 141-149, doi: N/A. [Online]. Available: http://www.scopus.com/inward/record.url?eid=2-s2.0-0026383754&partnerID=40&md5=5df66f93e96c7032d5d1022bd0526a89

[244] A. Pivkina, P. Ulyanova, Y. Frolov, S. Zavyalov, and J. Schoonman, "Nanomaterials for Heterogeneous Combustion," *Propellants, Explosives, Pyrotechnics,* vol. 29, no. 1, pp. 39-49, 2004, doi: N/A.

[245] B. E. Schuster, J. P. Ligda, Z. L. Pan, and Q. Wei, "Nanocrystalline refractory metals for extreme condition applications," *JOM*, vol. 63, no. 12, pp. 27-31, 2011, doi: 10.1007/s11837-011-0202-3.

[246] E. W. Price, *Combustion of Metallized Propellants* (Progress in Astronautics and Aeronautics, no. 90). New York: AIAA, 1984, pp. 479-513.

[247] S. H. F. a. M. C. Grubelich, "A Survey of Combustible Metals Thermites and Intermetallics for Pyrotechnic Applications," presented at the 32nd AIAA/ASME/SAE/ASEE Joint Propulsion Conference, Lake Buena Vista, FL, July 1-3, 1996, 1996.

[248] A. Gany, "Comprehensive Consideration of Boron Combustion in Airbreathing Propulsion," *42nd AIAA/ASME/SAE/ASEE Joint Propulsion Conference & Exhibit*, 2006.

[249] M. L. Chan and G. W. Meyers, "Solid fuel-air thermobaric explosives containing oxidizer grains surrounded by fuel grains," Patent US6955732B1 Patent Appl. Copyright (C) 2013 American Chemical Society (ACS). All Rights Reserved., 2005.

[250] T. Kottke, L. J. Kecskes, and A. Niiler, "Control of TiB2 SHS reactions by inert dilutions and mechanical constraint," *AIChE Journal*, vol. 36, no. 10, pp. 1581-1584, 1990. [Online]. Available: http://www.scopus.com/inward/record.url?eid=2-s2.0-0025508837&partnerID=40&md5=ab32509df56fb82b79c5c21e0a6aee98.

[251] S. J. Bless, K. Tarcza, R. Chau, E. Taleff, and C. Persad, "Dynamic fracture of tungsten heavy alloys," *International Journal of Impact Engineering*, Article vol. 33, no. 1-12, pp. 100-108, 2006, doi: 10.1016/j.ijimpeng.2006.09.028.

[252] W. D. Cai, Y. Li, R. J. Dowding, F. A. Mohamed, and E. J. Lavernia, "A review of tungsten-based alloys as kinetic energy penetrator materials," *Rev. Part. Mater.*, vol. 3, no. Copyright (C) 2015 American Chemical Society (ACS). All Rights Reserved., pp. 71-132, 1995.

[253] L. Magness, L. Kecskes, F. Biancianello, S. Ridder, M. Chung, and D. Kapoor, "The performance of a nanocrystalline tungsten composite in ballistic impacts," in *Proceedings of SPIE - The International Society for Optical Engineering*, 2002, vol. 4608, pp. 216-224, doi: 10.1117/12.465225. [Online]. Available: http://www.scopus.com/inward/record.url?eid=2-s2.0-0036028875&partnerID=40&md5=ea902e11af236110c870bc531ee5280f

[254] Z. Xiaoqing, L. Shukui, L. Jinxu, W. Yingchun, and W. Xing, "Self-sharpening behavior during ballistic impact of the tungsten heavy alloy rod penetrators processed by hot-hydrostatic extrusion and hot torsion," *Materials Science and Engineering A*, Article vol. 527, no. 18-19, pp. 4881-4886, 2010, doi: 10.1016/j.msea.2010.04.050.

[255] G. V. Ivanov, A. A. Reshetov, A. M. Viktorenko, V. G. Surkov, and L. N. Karmadonov, "Combustion of tungsten powder in pyrotechnic mixtures," *Fiz. Goreniya Vzryva*, vol. 18, no. 2, pp. 20-3, // 1982.

[256] Y. Lao and P. Wang, "A study of pyrotechnic delay system and analysis of temperature profile," *Proc. Int. Pyrotech. Semin.*, vol. 13th, pp. 537-44, // 1988.

[257] B. J. McBride and S. Gordon, "Computer Program for Calculation of Complex Chemical Equilibrium Compositions and Applications II. User's Manual and Program Description," *NASA RP 1311,* Report p. 55, 1996.

[258] D. Stamatis and E. L. Dreizin, "Fully dense Al-CuO nanocomposite powders for energetic formulations," in *46th AIAA Aerospace Sciences Meeting and Exhibit*, Reno, NV, January 7-10, 2008 2008, vol. 46th AIAA Aerospace Sciences Meeting and Exhibit: AIAA, pp. AIAA2008-1425, [Online]. Available: http://www.scopus.com/inward/record.url?eid=2-s2.0-78149441458&partner ID=40&md5=0bd1be4c1b5e50128698ee6333ef9655

[259] R. A. Long, R. A. Caughey, and G. H. Sievert, "Method and fillings for exothermic brazing," United States Patent 3,308,532, 1967.

[260] R. S. Storm, V. Shapovalov, J. C. Withers, and R. Loutfy, "Multi component reactive metal penetrators and their method of manufacture," United States Patent 8,573,128 B2, 2013.

[261] L. R. Bates and B. Bourne, "Improvements in and related to oil well perforators," Great Britain Patent EP 1671013, 2011.

[262] G. D. Hugus, E. W. Sheridan, and G. W. Brooks, "Structural metallic binders for reactive fragmentation weapons," United States Patent 8,746,145 B2, 2014.

[263] H. W. Kruse, "Flare composition comprising dry blend of metal fuel and eutectic mixture of oxidizer salts," United States Patent 3729351, 1969.

[264] H. Singh, "Studies on decomposition and combustion mechanism of solid fuel rich propellants," PUNE UNIV (INDIA), 2010.

[265] A. P. Hardt, "Incendiary potential of exothermic intermetallic reactions," LOCKHEED MISSILES AND SPACE CO INC PALOALTO CA PALO ALTO RESEARCH LAB, 1971.

[266] M. Schoenitz, T. Ward, and E. L. Dreizin, "Preparation of energetic metastable nano-composite materials by arrested reactive milling," *MRS Online Proceedings Library (OPL),* vol. 800, 2003, doi: 10.1557/PROC-800-AA2.6.

[267] E. L. Dreizin and M. Schoenitz, "Nano-composite energetic powders prepared by arrested reactive milling," Patent 7,524,355 B2, 2009.

[268] E. Beloni, V. K. Hoffmann, and E. L. Dreizin, "Combustion of decane-based slurries with metallic fuel additives," *J Propul Power,* vol. 24, no. 6, pp. 1403-1411, 2008, doi: 10.2514/1.28042.

[269] S. Fischer and M. Grubelich, "A survey of combustible metals, thermites, and intermetallics for pyrotechnic applications," in *32nd Joint Propulsion Conference and Exhibit,* 1996, p. 3018.

[270] K.-L. Chintersingh, M. Schoenitz, and E. L. Dreizin, "Combustion of boron and boron–iron composite particles in different oxidizers," *Combustion and Flame*, vol. 192, pp. 44-58, 2018/06/01 2018, doi: https://doi.org/10.1016/j.combustflame.2018.01.043.

[271] D. Stamatis, Z. Jiang, V. K. Hoffmann, M. Schoenitz, and E. L. Dreizin, "Fully dense, aluminum-rich Al-CuO nanocomposite powders for energetic formulations," *Combustion Science and Technology*, vol. 181, no. 1, pp. 97-116, 2008.

[272] S. K. Valluri, I. Monk, M. Schoenitz, and E. L. Dreizin, "Fuel Rich Aluminum-Metal Fluoride Thermites," *International Journal of Energetic Materials and Chemical Propulsion*, vol. 16, no. 1, 2017.

[273] X. Liu, M. Schoenitz, and E. L. Dreizin, "Combustion of Mg and composite Mg·S powders in different oxidizers," *Combustion and Flame*, vol. 195, pp. 292-302, 2018/09/01/ 2018, doi: https://doi.org/10.1016/j.combustflame.2018.03.036.

[274] I. Monk, M. Schoenitz, and E. L. Dreizin, "The Effect of Heating Rate on Combustion of Fully Dense Nanocomposite Thermite Particles," *Combustion Science and Technology*, vol. 190, no. 2, pp. 203-221, 2018/02/01 2018, doi: 10.1080/00102202.2017.1380002.

[275] J. Schindelin, I. Arganda-Carreras, E. Frise, V. Kaynig, M. Longair, T. Pietzsch, S. Preibisch, C. Rueden, S. Saalfeld, B. Schmid, J. Tinevez, D. J. White, V. Hartenstein, K. Eliceiri, P. Tomancak & A. Cardona, "Fiji: an open-source platform for biological-image analysis," *Nature Methods*, vol. 9, no. 7, pp. 676-682, 2012/07/01 2012, doi: 10.1038/nmeth.2019.

[276] D. Legland, I. Arganda-Carreras, and P. Andrey, "MorphoLibJ: integrated library and plugins for mathematical morphology with ImageJ," (in eng), *Bioinformatics*, vol. 32, no. 22, pp. 3532-3534, Nov 15 2016, doi: 10.1093/bioinformatics/btw413.

[277] J. A. Dean and N. A. Lange, *Lange's handbook of chemistry*. Toronto: McGraw-Hill (in English), 1985.

[278] R. W. B. Pearse and A. G. Gaydon, "The identification of molecular spectra," (in English), 1976. [Online]. Available: http://catalog.hathitrust.org/api/volumes/oclc/2630075.html.

[279] E. C. Koch, "Metal-fluorocarbon-pyrolants IV: Thermochemical and combustion behaviour of magnesium/Teflon/Viton (MTV)," *Propellants, Explosives, Pyrotechnics*, Article vol. 27, no. 6, pp. 340-351, 2002, doi: 10.1002/prep.200290004.

[280] E. C. Koch, "Metal-fluorocarbon-pyrolants: III. Development and application of Magnesium/Teflon/Viton (MTV)," *Propellants, Explosives, Pyrotechnics*, Article vol. 27, no. 5, pp. 262-266, 2002, doi: 10.1002/1521-4087(200211)27:5<262::AID-PREP262>3.0.CO;2-8.

[281] I. M. Tuukkanen, E. L. Charsley, P. G. Laye, J. J. Rooney, T. T. Griffiths, and H. Lemmetyinen, "Pyrotechnic and thermal studies on the magnesium-strontium nitrate

pyrotechnic system," *Propellants, Explosives, Pyrotechnics,* Article vol. 31, no. 2, pp. 110-115, 2006, doi: 10.1002/prep.200600012.

[282] C. G. Zhu, H. Z. Wang, and L. Min, "Ignition Temperature of Magnesium Powder and Pyrotechnic Composition," *Journal of Energetic Materials,* Article vol. 32, no. 3, pp. 219-226, 2014, doi: 10.1080/07370652.2013.812162.

[283] E. Y. Shafirovich, A. A. Shiryaev, and U. I. Goldshleger, "Magnesium and carbon dioxide: A rocket propellant for Mars missions," *Journal of Propulsion and Power,* Article vol. 9, no. 2, pp. 197-203, 1993, doi: 10.2514/3.23609.

[284] L. Zheng, G. P. Pan, X. Chen, and L. Qiao, "Effect of magnesium powder particle size on combustion properties of Mg/PTFE fuel-rich propellant," *Hanneng Cailiao/Chinese Journal of Energetic Materials,* Article vol. 18, no. 2, pp. 180-183, 2010, doi: 10.3969/j.issn.1006-9941.2010.02.012.

[285] E. C. Koch and A. Dochnahl, "IR emission behaviour of magnesium/Teflon/Viton (MTV) compositions," *Propellants, Explosives, Pyrotechnics,* Article vol. 25, no. 1, pp. 37-40, 2000, doi: 10.1002/(SICI)1521-4087(200001)25:1<37::AID-PREP37>3.0.CO;2-#.

[286] R. N. Newman and J. F. B. Payne, "The anomalous brightness of magnesium-Air flames," *Combustion and Flame,* Article vol. 68, no. 1, pp. 31-41, 1987, doi: 10.1016/0010-2180(87)90063-0.

[287] A. V. Florko, V. V. Golovko, N. A. Okhrimenko, and V. G. Shevchuk, "Structure of the magnesium particle combustion zone. I. Optico-spectrum investigations," *Combustion, Explosion, and Shock Waves,* vol. 27, no. 1, pp. 32-37, 1991. doi: https://doi.org/10.1007/BF00785352

[288] A. V. Florko and V. V. Golovko, "Characteristics of the radiation emitted by and the conditions for nucleation of submicron oxide particles during combustion of magnesium," *Combustion, Explosion, and Shock Waves,* vol. 29, no. 5, pp. 562-567, 1994. doi: https://doi.org/10.1007/BF00783707

[289] A. E. Valov, Y. A. Kustov, and V. I. Shevtsov, "Spectroscopic study of the combustion of solitary magnesium particles in air and in carbon dioxide," *Combustion, Explosion, and Shock Waves,* Article vol. 30, no. 4, pp. 431-436, 1994, doi: 10.1007/BF00790146.

[290] G. K. Ezhovskii, A. S. Mochalova, E. S. Ozerov, and A. A. Yurinov, "Ignition and combustion of a magnesium particle," 1972: "Nauka", pp. 234-40.

[291] A. V. Florko, S. V. Kozitskii, A. N. Pisarenko, and A. M. Matsko, "Study of combustion of single magnesium particles at low pressure," *Combustion, Explosion, and Shock Waves,* Article vol. 22, no. 2, pp. 159-163, 1986, doi: 10.1007/BF00749260.

[292] B. Legrand, E. Shafirovich, M. Marion, C. Chauveau, and I. Gökalp, "Ignition and combustion of levitated magnesium particles in carbon dioxide," *Symposium*

(International) on Combustion, Conference Paper vol. 27, no. 2, pp. 2413-2419, 1998, doi: 10.1016/S0082-0784(98)80093-3.

[293] R. Lomba, S. Bernard, P. Gillard, C. Mounaïm-Rousselle, F. Halter, C. Chauveau, T. Tahtouh and O. Guézet, "Comparison of Combustion Characteristics of Magnesium and Aluminum Powders," *Combustion Science and Technology*, Article vol. 188, no. 11-12, pp. 1857-1877, 2016, doi: 10.1080/00102202.2016.1211871.

[294] F. Czerwinski, "Controlling the ignition and flammability of magnesium for aerospace applications," *Corrosion Science*, Review vol. 86, pp. 1-16, 2014, doi: 10.1016/j.corsci.2014.04.047.

[295] J. H. Nordlien, S. Ono, N. Masuko, and K. Nisancioglu, "A tem investigation of naturally formed oxide films on pure magnesium," *Corrosion Science,* Article vol. 39, no. 8, pp. 1397-1414, 1997, doi: 10.1016/S0010-938X(97)00037-1.

[296] H. Nie, M. Schoenitz, and E. L. Dreizin, "Oxidation of Magnesium: Implication for Aging and Ignition," (in English), *Journal of Physical Chemistry C*, Article vol. 120, no. 2, pp. 974-983, 2016, doi: 10.1021/acs.jpcc.5b08848.

[297] S. D. Brown, E. L. Charsley, S. J. Goodall, P. G. Laye, J. J. Rooney, and T. T. Griffiths, "Studies on the ageing of a magnesium-potassium nitrate pyrotechnic composition using isothermal heat flow calorimetry and thermal analysis techniques," *Thermochimica Acta*, Conference Paper vol. 401, no. 1, pp. 53-61, 2003, doi: 10.1016/S0040-6031(03)00055-8.

[298] I. Tuukkanen, S. D. Brown, E. L. Charsley, S. J. Goodall, J. J. Rooney, T. T. Griffiths, and H. Lemmetyinen, "Studies on the ageing of a magnesium-strontium nitrate pyrotechnic composition using isothermal microcalorimetry and thermal analysis techniques," *Thermochimica Acta*, Article vol. 417, no. 2, pp. 223-229, 2004, doi: 10.1016/ j.tca.2003.07.021.

[299] W. P. C. De Klerk, W. Colpa, and P. J. Van Ekeren, "Ageing studies of magnesium-sodium nitrate pyrotechnic compositions," *Journal of Thermal Analysis and Calorimetry*, Conference Paper vol. 85, no. 1, pp. 203-207, 2006, doi: 10.1007/s10973-005-7422-0.

[300] J. W. Krumpfer and T. J. McCarthy, "Contact angle hysteresis: A different view and a trivial recipe for low hysteresis hydrophobic surfaces," *Faraday Discussions,* Article vol. 146, pp. 103-111, 2010, doi: 10.1039/b925045j.

[301] J. W. Krumpfer and T. J. McCarthy, "Rediscovering silicones: "unreactive" silicones react with inorganic surfaces," *Langmuir,* Article vol. 27, no. 18, pp. 11514-11519, 2011, doi: 10.1021/la202583w.

[302] A. Hozumi, D. F. Cheng, and M. Yagihashi, "Hydrophobic/superhydrophobic oxidized metal surfaces showing negligible contact angle hysteresis," *Journal of Colloid and Interface Science,* Article vol. 353, no. 2, pp. 582-587, 2011, doi: 10.1016/j.jcis.2010.09.075.

[303] A. Y. Fadeev and T. J. McCarthy, "A new route to covalently attached monolayers: Reaction of hydridosilanes with titanium and other metal surfaces [1]," *Journal of the American Chemical Society,* Letter vol. 121, no. 51, pp. 12184-12185, 1999, doi: 10.1021/ja9931269.

[304] L. E. Lemmerz, V. Leich, D. Martin, T. P. Spaniol, and J. Okuda, "Silyl-Hydrosilane Exchange at a Magnesium Triphenylsilyl Complex Supported by a Cyclen-Derived NNNN-Type Macrocyclic Ligand," *Inorganic Chemistry,* Article vol. 56, no. 24, pp. 14979-14990, 2017, doi: 10.1021/acs.inorgchem.7b02233.

[305] S. J. Brotton, M. J. Malek, S. L. Anderson, and R. I. Kaiser, "Effects of Acetonitrile-Assisted Ball-Milled Aluminum Nanoparticles on the Ignition of Acoustically Levitated exo-Tetrahydrodicyclopentadiene (JP-10) Droplets," *Chemical Physics Letters,* p. 137679, 2020/06/02/ 2020, doi: https://doi.org/10.1016/j.cplett.2020.137679.

[306] C. Carmicino and A. R. Sorge, "Experimental investigation into the effect of solid-fuel additives on hybrid rocket performance," *Journal of Propulsion and Power,* Article vol. 31, no. 2, pp. 699-713, 2015, doi: 10.2514/1.B35383.

[307] J. C. Melcher, H. Krier, and R. L. Burton, "Burning aluminum particles inside a laboratory-scale solid rocket motor," *Journal of Propulsion and Power,* Article vol. 18, no. 3, pp. 631-640, 2002, doi: 10.2514/2.5977.

[308] J. F. Widener and M. W. Beckstead, "Aluminum combustion modeling in solid propellant combustion products," in *34th AIAA/ASME/SAE/ASEE Joint Propulsion Conference and Exhibit*, 1998, doi: https://doi.org/10.2514/6.1998-3824

[309] F. Zhang, "Detonation in reactive solid particle-gas flow," *Journal of Propulsion and Power,* Article vol. 22, no. 6, pp. 1289-1309, 2006, doi: 10.2514/1.18210.

[310] F. Zhang, K. Gerrarc, and R. C. Ripley, "Reaction mechanism of aluminum-particle-air detonation," *Journal of Propulsion and Power,* Article vol. 25, no. 4, pp. 845-858, 2009, doi: 10.2514/1.41707.

[311] F. Zhang, S. B. Murray, and K. B. Gerrard, "Aluminum particles-air detonation at elevated pressures," *Shock Waves,* Article vol. 15, no. 5, pp. 313-324, 2006, doi: 10.1007/s00193-006-0027-0.

[312] J. S. Lee and C. K. Hsu, "The DSC studies on the phase transition, decomposition and melting of potassium perchlorate with additives," *Thermochimica Acta,* Article vol. 367-368, pp. 367-370, 2001, Art no. 6397, doi: 10.1016/S0040-6031(00)00683-3.

[313] S. M. Pourmortazavi, S. S. Hajimirsadeghi, I. Kohsari, M. Fathollahi, and S. G. Hosseini, "Thermal decomposition of pyrotechnic mixtures containing either aluminum or magnesium powder as fuel," *Fuel,* Article vol. 87, no. 2, pp. 244-251, 2008, doi: 10.1016/j.fuel.2007.04.022.

[314] X. G. Wu, Q. L. Yan, X. Guo, X. F. Qi, X. J. Li, and K. Q. Wang, "Combustion efficiency and pyrochemical properties of micron-sized metal particles as the components of modified double-base propellant," *Acta Astronautica,* vol. 68, no. 7-8, pp. 1098-1112, 2011, doi: 10.1016/j.actaastro.2010.09.028.

[315] E. W. Price, "Combustion of Metalized Propellants," in *Progress in Astronautics and Aeronautics 90* vol. 90, ed, 1984, pp. 479-513.

[316] L. T. De Luca, L. Galfetti, F. Maggi, G. Colombo, C. Paravan, A. Reina, S. Dossi, M. Fassina and A. Sossi, "Characterization and Combustion of Aluminum Nanopowders in Energetic Systems," in *Metal Nanopowders: Production, Characterization, and Energetic Applications,* vol. 9783527333615, 2014, pp. 301-410.

[317] A. A. Gromov, U. Förter-Barth, and U. Teipel, "Aluminum nanopowders produced by electrical explosion of wires and passivated by non-inert coatings: Characterisation and reactivity with air and water," *Powder Technology,* Article vol. 164, no. 2, pp. 111-115, 2006, doi: 10.1016/j.powtec.2006.03.003.

[318] M. Kearns, "Development and applications of ultrafine aluminium powders," *Materials Science and Engineering A,* Article vol. 375-377, no. 1-2 SPEC. ISS., pp. 120-126, 2004, doi: 10.1016/j.msea.2003.10.160.

[319] J. A. Puszynski, "Processing and characterization of aluminum-based nanothermites," *Journal of Thermal Analysis and Calorimetry,* Article vol. 96, no. 3, pp. 677-685, 2009, doi: 10.1007/s10973-009-0037-0.

[320] Q. S. M. Kwok, C. Badeen, K. Armstrong, R. Turcotte, D. E. G. Jones, and V. Y. Gertsman, "Hazard characterization of uncoated and coated aluminium nanopowder compositions," *Journal of Propulsion and Power,* Article vol. 23, no. 4, pp. 659-668, 2007, doi: 10.2514/1.25181.

[321] J. Bouillard, A. Vignes, O. Dufaud, L. Perrin, and D. Thomas, "Ignition and explosion risks of nanopowders," *Journal of Hazardous Materials,* Article vol. 181, no. 1-3, pp. 873-880, 2010, doi: 10.1016/j.jhazmat.2010.05.094.

[322] D. E. G. Jones, R. Turcotte, R. C. Fouchard, Q. S. M. Kwok, A. M. Turcotte, and Z. Abdel-Qader, "Hazard characterization of aluminum nanopowder compositions," *Propellants, Explosives, Pyrotechnics,* Article vol. 28, no. 3, pp. 120-131, 2003, doi: 10.1002/prep.200390018.

[323] Y. Li, W. Song, C. Xie, D. Zeng, A. Wang, and M. Hu, "Influence of humidity on the thermal behavior of aluminum nanopowders," *Materials Chemistry and Physics,* Article vol. 97, no. 1, pp. 127-131, 2006, doi: 10.1016/j.matchemphys.2005.07.064.

[324] C. Paravan, F. Maggi, S. Dossi, G. Marra, G. Colombo, and L. Galfetti, "Pre-burning Characterization of Nanosized Aluminum in Condensed Energetic Systems," in *Energetic Nanomaterials: Synthesis, Characterization, and Application,* 2016, pp. 341-368.

[325] A. Gany and L. H. Caveny, "Agglomeration and ignition mechanism of aluminum particles in solid propellants," (in English), *Symposium (International) on Combustion,* Article vol. 17, no. 1, pp. 1453-1461, 1979, doi: 10.1016/S0082-0784(79)80137-X.

[326] V. Rosenband and A. Gany, "A microscopic and analytic study of aluminum particles agglomeration," *Combustion Science and Technology,* Article vol. 166, no. 1, pp. 91-108, 2001, doi: 10.1080/00102200108907821.

[327] T. R. Sippel, S. F. Son, and L. J. Groven, "Aluminum agglomeration reduction in a composite propellant using tailored Al/PTFE particles," *Combustion and Flame,* Article vol. 161, no. 1, pp. 311-321, 2014, doi: 10.1016/j.combustflame.2013.08.009.

[328] L. T. De Luca, L. Galfetti, F. Severini, L. Meda, G. Marra, A. B. Vorozhtsov, V. S. Sedoi and V. A. Babuk, "Burning of nano-aluminized composite rocket propellants," *Combustion, Explosion and Shock Waves,* vol. 41, no. 6, pp. 680-692, 2005, doi: 10.1007/s10573-005-0080-5.

[329] Q. S. M. Kwok, R. C. Fouchard, A. M. Turcotte, P. D. Lightfoot, R. Bowes, and D. E. G. Jones, "Characterization of aluminum nanopowder compositions," *Propellants, Explosives, Pyrotechnics,* Article vol. 27, no. 4, pp. 229-240, 2002, doi: 10.1002/1521-4087(200209)27:4<229::AID-PREP229>3.0.CO;2-B.

[330] K. E. Neely, K. C. Galloway, and A. M. Strauss, "Additively Manufactured Reactive Material Architectures as a Programmable Heat Source," *3D Printing and Additive Manufacturing,* Article vol. 6, no. 4, pp. 210-216, 2019, doi: 10.1089/3dp.2018.0077.

[331] J. Tomas, "Fundamentals of cohesive powder consolidation and flow," *Granular Matter,* Conference Paper vol. 6, no. 2-3, pp. 75-86, 2004, doi: 10.1007/s10035-004-0167-9.

[332] A. Abraham, N. A. MacDonald, and E. L. Dreizin, "Reactive Materials for Evaporating Samarium," *Propellants, Explosives, Pyrotechnics,* vol. 41, no. 5, pp. 926-935, 2016, doi: 10.1002/prep.201500263.

[333] A. Abraham, Z. Zhong, R. Liu, S. A. Grinshpun, M. Yermakov, R. Indugula, M. Schoenitz and E. L. Dreizin, "Preparation, Ignition, and Combustion of Mg·S Reactive Nanocomposites," *Combustion Science and Technology,* vol. 188, no. 8, pp. 1345-1364, 2016/08/02 2016, doi: 10.1080/00102202.2016.1190347.

[334] E. L. Dreizin and M. Schoenitz, "Mechanochemically prepared reactive and energetic materials: a review," *Journal of Materials Science,* vol. 52, no. 20, pp. 11789-11809, 2017/10/01 2017, doi: 10.1007/s10853-017-0912-1.

[335] D. Hastings, M. Schoenitz, and E. L. Dreizin, "Zirconium-boron reactive composite powders prepared by arrested reactive milling," *Journal of Energetic Materials,* pp. 1-20, 2019, doi: 10.1080/07370652.2019.1679279.

[336] A. Ünal, "Effect of processing variables on particle size in gas atomization of rapidly solidified aluminium powders," *Materials Science and Technology*, vol. 3, no. 12, pp. 1029-1039, 1987/12/01 1987, doi: 10.1179/mst.1987.3.12.1029.

[337] B. André, M. V. Coulet, P. H. Esposito, B. Rufino, and R. Denoyel, "High-energy ball milling to enhance the reactivity of aluminum nanopowders," *Materials Letters*, Article vol. 110, pp. 108-110, 2013, doi: 10.1016/j.matlet.2013.07.101.

[338] M. Mursalat, D. L. Hastings, M. Schoenitz, and E. L. Dreizin, "Microspheres with Diverse Material Compositions Can be Prepared by Mechanical Milling," *Advanced Engineering Materials*, Article vol. 22, no. 3, p. 1901204, 2020, Art no. 1901204, doi: 10.1002/adem.201901204.

[339] M. Mursalat, M. Schoenitz, and E. L. Dreizin, "Custom particle morphology in energetic nanocomposites prepared by arrested reactive milling in immiscible liquids," *Powder Technology*, Article vol. 359, pp. 238-246, 2020, doi: 10.1016/j.powtec.2019.10.006.

[340] G. K. Williamson and W. H. Hall, "X-ray line broadening from filed aluminium and wolfram," *Acta Metallurgica*, vol. 1, no. 1, pp. 22-31, 1953/01/01/ 1953, doi: https://doi.org/10.1016/0001-6160(53)90006-6.

[341] K. S. W. Sing D. H. Everett, R. A. W. Haul, L. Moscou, R. A. Pierotti, J. Rouquerol, and T. Siemieniewska, "Reporting Physisorption Data for Gas/Solid Systems with Special Reference to the Determination of Surface Area and Porosity," *International Union of Pure & Applied Chemistry*, pp. 603-619, 1985.

[342] M. Thommes, K. Kaneko, A. V. Neimark, J. P. Olivier, F. Rodriguez-Reinoso, J. Rouquerol and K. S. W. Sing, "Physisorption of gases, with special reference to the evaluation of surface area and pore size distribution (IUPAC Technical Report)," in *Pure and Applied Chemistry* vol. 87, ed, 2015, p. 1051. doi: 10.1515/pac-2014-1117

[343] J. Landers, G. Y. Gor, and A. V. Neimark, "Density functional theory methods for characterization of porous materials," *Colloids and Surfaces A: Physicochemical and Engineering Aspects*, Article vol. 437, pp. 3-32, 2013, doi: 10.1016/j.colsurfa.2013.01.007.

[344] Y. L. Shoshin, M. A. Trunov, X. Zhu, M. Schoenitz, and E. L. Dreizin, "Ignition of aluminum-rich Al–Ti mechanical alloys in air," *Combustion and Flame*, vol. 144, no. 4, pp. 688-697, 2006/03/01/ 2006, doi: https://doi.org/10.1016/j.combustflame.2005.08.037.

[345] T. S. Ward, M. A. Trunov, M. Schoenitz, and E. L. Dreizin, "Experimental methodology and heat transfer model for identification of ignition kinetics of powdered fuels," *International Journal of Heat and Mass Transfer*, vol. 49, no. 25, pp. 4943-4954, 2006/12/01/ 2006, doi: https://doi.org/10.1016/j.ijheatmasstransfer.2006.05.025.

[346] M. A. Trunov, M. Schoenitz, X. Zhu, and E. L. Dreizin, "Effect of polymorphic phase transformations in Al2O3 film on oxidation kinetics of aluminum powders," *Combustion and Flame*, vol. 140, no. 4, pp. 310-318, 2005, doi: 10.1016/j.combustflame.2004.10.010.

[347] M. A. Trunov, S. M. Umbrajkar, M. Schoenitz, J. T. Mang, and E. L. Dreizin, "Oxidation and melting of aluminum nanopowders," *Journal of Physical Chemistry B,* vol. 110, no. 26, pp. 13094-13099, 2006, doi: 10.1021/jp0614188.

[348] H. Nie, M. Schoenitz, and E. L. Dreizin, "Initial stages of oxidation of aluminum powder in oxygen," *Journal of Thermal Analysis and Calorimetry,* vol. 125, no. 1, pp. 129-141, 2016/07/01 2016, doi: 10.1007/s10973-016-5369-y.

[349] M. A. Trunov, M. Schoenitz, and E. L. Dreizin, "Effect of polymorphic phase transformations in alumina layer on ignition of aluminium particles," *Combustion Theory and Modelling,* vol. 10, no. 4, pp. 603-623, 2006, doi: 10.1080/13647830600578506.

[350] S. Vyazovkin, "Modification of the integral isoconversional method to account for variation in the activation energy," *Journal of Computational Chemistry,* vol. 22, no. 2, pp. 178-183, 2001/01/30 2001, doi: 10.1002/1096-987X(20010130)22:2<178::AID-JCC5>3.0.CO;2-#.

[351] R. A. Robie and B. S. Hemingway, "Thermodynamic properties of minerals and related substances at 298.15 K and 1 bar (105 Pascals) pressure and at higher temperatures," *US Geological Survey Bulletin,* Article vol. 2131, 1995. [Online]. Available: https://www.scopus.com/inward/record.uri?eid=2-s2.0-0029512134&partnerID=40&md5=0d2ad5a6a400239f86c0a4b10a13a589.

[352] R. A. Yetter, G. A. Risha, and S. F. Son, "Metal particle combustion and nanotechnology," *Proceedings of the Combustion Institute,* vol. 32, no. 2, pp. 1819-1838, 2009/01/01/ 2009, doi: https://doi.org/10.1016/j.proci.2008.08.013.

[353] X. Huang, C. Cao, J. Ma, B. Wang, and Y. Gao, "Titanium combustion in aeroengines and fire-resistant titanium alloys," *Cailiao Gongcheng/Journal of Materials Engineering,* Article no. 8, pp. 11-15, 1997. [Online]. Available: https://www.scopus.com/inward/record.uri?eid=2-s2.0-0031197736&partnerID=40&md5=0d76f87568c195a3b6d80a33ade268df.

[354] J. Yu, X. Zhang, Q. Zhang, L. Wang, K. Ji, L. Peng, and W. Gao, "Combustion behaviors and flame microstructures of micro- and nano-titanium dust explosions," *Fuel,* Article vol. 181, pp. 785-792, 2016, doi: 10.1016/j.fuel.2016.05.085.

[355] M. K. King, "Ignition and combustion of boron particles and clouds," in *Journal of Spacecraft and Rockets*, 1982, vol. 19, no. 4, 4 ed., pp. 294-306, doi: N/A. [Online]. Available: http://www.scopus.com/inward/record.url?eid=2-s2.0-0020155290&partnerID=40&md5=aedcff817291d89aabaf841a8a7474f3

[356] M. K. King, "Metal combustion efficiency predictions for low L* rocket motors," *Journal of Spacecraft and Rockets,* Article vol. 22, no. 5, pp. 512-513, 1985, doi: 10.2514/3.25061.

[357] V. A. Babuk and V. A. Vasilyev, "Model of aluminum agglomerate evolution in combustion products of solid rocket propellant," (in English), *Journal of Propulsion and Power,* Article vol. 18, no. 4, pp. 814-823, 2002, doi: 10.2514/2.6005.

[358] C. L. Yeh and K. K. Kuo, "Ignition and combustion of boron particles," *Progress in Energy and Combustion Science,* vol. 22, no. 6, pp. 511-541, 1996, doi: 10.1016/s0360-1285(96)00012-3.

[359] M. G. Zaky, A. Elbeih, and T. Elshenawy, "Review of Nano-thermites: a Pathway to Enhanced Energetic Materials," *Central European Journal of Energetic Materials,* Article vol. 18, no. 1, pp. 63-85, 2021, doi: 10.22211/cejem/134953.

[360] A. Gromov, L. T. DeLuca, A. P. Il'in, U. Teipel, A. Petrova, and D. Prokopiev, "Nanometals in energetic systems: achievements and future," *Int. J. Energ. Mater. Chem. Propul.,* 10.1615/IntJEnergeticMaterialsChemProp.2014011255 vol. 13, no. Copyright (C) 2015 American Chemical Society (ACS). All Rights Reserved., pp. 399-419, 2014, doi: 10.1615/IntJEnergeticMaterialsChemProp.2014011255.

[361] B. A. Mason, T. R. Sippel, L. J. Groven, I. E. Gunduz, and S. F. Son, "Combustion of mechanically activated Ni/Al reactive composites with microstructural refinement tailored using two-step milling," *Intermetallics,* vol. 66, pp. 88-95, 2015, doi: 10.1016/j.intermet.2015.06.009.

[362] D. L. Hastings, M. Schoenitz, and E. L. Dreizin, "High density reactive composite powders," *Journal of Alloys and Compounds,* Article vol. 735, pp. 1863-1870, 2018, doi: 10.1016/j.jallcom.2017.11.345.

[363] D. Hastings, M. Schoenitz, and E. L. Dreizin, "Zirconium-boron reactive composite powders prepared by arrested reactive milling," *Journal of Energetic Materials,* Article vol. 38, no. 2, pp. 142-161, 2020, doi: 10.1080/07370652.2019.1679279.

[364] E. L. Dreizin and M. Schoenitz, "Nano-composite energetic powders prepared by arrested reactive milling," Patent Appl. Patent record available from the World Intellectual Property Organization (WIPO), 2009. [Online]. Available: http://v3.espacenet.com/textdoc?DB=EPODOC&IDX=WO2005049658&F=0

[365] M. Mursalat, D. L. Hastings, M. Schoenitz, and E. L. Dreizin, "Microspheres with Diverse Material Compositions Can be Prepared by Mechanical Milling," *Advanced Engineering Materials,* Article vol. 22, no. 3, 2020, Art no. 1901204, doi: 10.1002/adem.201901204.

[366] D. Hastings, M. Schoenitz, and E. L. Dreizin, "Highly reactive spheroidal milled aluminum," *Materialia,* Article vol. 15, 2021, Art no. 100959, doi: 10.1016/j.mtla.2020.100959.

[367] M. Mursalat, M. Schoenitz, and E. Dreizin, L., "Spherical composite spheres," United States of America Patent Appl. 62/738,046, 2018.

[368] U. Teipel, *Energetic Materials: Particle Processing and Characterization*. Wiley, 2006.

[369] D. Bourell, J. P. Kruth, M. Leu, G. Levy, D. Rosen, A. M. Beese, A. Clare, "Materials for additive manufacturing," *CIRP Annals - Manufacturing Technology,* Article vol. 66, no. 2, pp. 659-681, 2017, doi: 10.1016/j.cirp.2017.05.009.

[370] P. Sun, Z. Z. Fang, Y. Zhang, and Y. Xia, "Review of the Methods for Production of Spherical Ti and Ti Alloy Powder," *JOM*, Review vol. 69, no. 10, pp. 1853-1860, 2017, doi: 10.1007/s11837-017-2513-5.

[371] J. H. Tan, W. L. E. Wong, and K. W. Dalgarno, "An overview of powder granulometry on feedstock and part performance in the selective laser melting process," *Additive Manufacturing*, Review vol. 18, pp. 228-255, 2017, doi: 10.1016/j.addma.2017.10.011.

[372] T. S. Ward, W. Chen, M. Schoenitz, R. N. Dave, and E. L. Dreizin, "A study of mechanical alloying processes using reactive milling and discrete element modeling," *Acta Materialia*, vol. 53, no. 10, pp. 2909-2918, 2005, doi: 10.1016/j.actamat.2005.03.006.

[373] D. Stamatis, Z. Jiang, V. K. Hoffmann, M. Schoenitz, and E. L. Dreizin, "Fully dense, aluminum-rich Al-CuO nanocomposite powders for energetic formulations," *Combustion Science and Technology*, vol. 181, no. 1, pp. 97-116, 2009, doi: 10.1080/00102200802363294.

[374] S. K. Valluri, I. Monk, M. Schoenitz, and E. Dreizin, "Fuel-rich aluminum–metal fluoride thermites," *International Journal of Energetic Materials and Chemical Propulsion*, Article vol. 16, no. 1, pp. 81-101, 2017, doi: 10.1615/IntJEnergeticMaterialsChemProp. 2018021842.

[375] J. L. Murray, *Phase Diagrams of Binary Titanium Alloys*. ASM International, 1987.

[376] W. Ji, M. Boufadel, L. Zhao, B. Robinson, T. King, C. An, B. Zhang, K. Lee, "Formation of oil-particle aggregates: Impacts of mixing energy and duration," *Science of The Total Environment*, vol. 795, p. 148781, 2021/11/15, doi: https://doi.org/10.1016/ j.scitotenv.2021.148781.

[377] I. Burgaud and E. Dickinson, "Emulsifying Effects of Food Macromolecules In Presence of Ethanol," *Journal of Food Science*, vol. 55, no. 3, pp. 875-876, 1990, doi: https://doi.org/10.1111/j.1365-2621.1990.tb05257.x.